Investigating Directional Proton Transfer in Rhodopsins by Novel Time-Resolved Infrared Spectroscopies

Dissertation

zur Erlangung des Grades eines
Doktors der Naturwissenschaften
(*Dr. rer. nat.)*

am Fachbereich Physik
der Freien Universität Berlin

vorgelegt von
Luiz Schubert

Berlin, 2024

Erstgutachter: Prof. Dr. Joachim Heberle

Zweitgutachter: Prof. Dr. Holger Dau

Tag der Disputation: 25.10.2024

Publications presented in this thesis (chronological order):

- Schubert, L., Langner, P., Ehrenberg, D., Lorenz-Fonfria, V., Heberle, J. Protein conformational changes and protonation dynamics probed by a single shot using quantum-cascade-laser-based IR spectroscopy, *J. Chem. Phys*. **2022**, 156, 204201
- Baserga, F. Vorkas, A., Crea, F., Schubert, L., Chen, J.L., Redlich, A., La Greca, M., Storm, J., Oldemeyer, S., Hoffmann, K., Schlesinger, R., Heberle, J. Membrane Protein Activity Induces Specific Molecular Changes in Nanodiscs Monitored by FTIR Difference Spectroscopy, *Front. Mol. Biosci*. **2022**, 9, 915328
- Schubert, L$^{\#}$., Chen, J-L.$^{\#}$, Fritz, T., Marxer, F., Langner, P., Hoffmann, K., Gamiz-Hernandez, A., Kaila, V.R.I., Schlesinger, R., Heberle, J. Proton Release Reactions in the Inward H^+ Pump *Ns*XeR, *J. Phys. Chem. B* **2023**, 127, 8358-8369
$^{\#}$these authors contributed equally to the work.

Publications related to the work performed during the doctoral thesis (chronological order):

- Harris, A.; Lazaratos, M.; Siemers, M.; Watt, E.; Hoang, A.; Tomida, S.; Schubert, L.; Saita, M.; Heberle, J.; Furutani, Y.; Kandori, H.; Bondar, A. N.; Brown, L. S., Mechanism of Inward Proton Transport in an Antarctic Microbial Rhodopsin. *J. Phys. Chem. B* **2020,** *124*, 4851-4872.
- La Greca, M.$^{\#}$; Chen, J-L.$^{\#}$; Schubert, L.; Kozuch, J.; Berneiser, T.; Terpitz, U.; Heberle, J.; Schlesinger, R., The Photoreaction of the Proton-Pumping Rhodopsin 1 From the Maize Pathogenic Basidiomycete Ustilago maydis. *Front. Mol. Biosci.* **2022,** *9*, 826990.
- Walter, M.; Schubert, L.; Heberle, J.; Schlesinger, R.; Losi, A., Time-resolved photoacoustics of channelrhodopsins: early energetics and light-driven volume changes. *Photochem. & Photobiol. Sci.* **2022**, 22, 477-486
- Saliminasab, M.; Yamazaki, Y.; Palmateer, A.; Harris, A.; Schubert, L.; Langner, P.; Heberle, J.; Bondar, A.-N.; Brown, L. S., A Proteorhodopsin-Related Photosensor Expands the Repertoire of Structural Motifs Employed by Sensory Rhodopsins. *J. Phys. Chem. B* **2023**, *127*, 7872-7886.

Manuscripts in preparation:

- Schubert, L., Bartl, F., Heberle, J. Probing Rhodopsin Activation by Single-Shot IR Spectroscopy, in preparation
- Baserga, F.$^{\#}$, Langner, P.$^{\#}$, Schubert, L., Storm, J., Schlesinger, R., Heberle, J., Electron transfer to heme a is coupled to the deprotonation of E286 in the cytochrome *c* oxidase from *Rhodobacter sphaeroides*, in preparation.
$^{\#}$these authors contributed equally to the work.

Contributions at International Conferences:

- Biennial Meeting of the German Biophysical Society, September 2018, Düsseldorf, Germany
  (Poster contribution)
- European Conference on the Spectroscopy of Biological Molecules, August 2019, Dublin, Ireland
  (Poster contribution)
- Time Resolved Vibrational Spectroscopy, June 2021, online attendance (Oral contribution)
- Proton Transfer in Biology (Telluride Meeting), June 2021, online attendance (Oral contribution)
- 19th International Conference on Retinal Proteins, November 2022, Sapporo, Japan (Oral contribution)
- European Biophysical Society Association Meeting, August 2023, Stockholm, Sweden (Oral contribution)

Abstract

Directional proton transport across the lipid bilayer of a biological membrane is a process of fundamental importance in nature. Due to the protons' small size, the study of proton transfer in biological macromolecules such as proteins, is a challenging task. One of the few techniques, that allows one to observe protonation reactions is infrared (IR) difference spectroscopy. Its chemical sensitivity sheds insight into the changes in protonation state of single moieties within proteins but is at the same time sensitive to all other molecular alterations accompanying proton transfer. IR difference spectroscopy is therefore a powerful tool to study the functional mechanism of proton-translocating proteins.

A very intriguing question is how proteins that act as membrane-bound proton pumps achieve vectorial proton transport. The first part of this thesis aims to address this question by the spectroscopic investigation of a novel microbial rhodopsin acting as an inward proton pump. I characterized the sequence of protonation reactions with a focus on the cytoplasmic half channel of the protein. Here, deprotonation of an aspartic acid located on the cytoplasmic side is correlated to the deprotonation of the distantly located retinal Schiff base. The sequence of these protonation events has important implications on the functional mechanism of inward proton transport, which is compared to the mechanism of a prototypical outward proton pump. The structural changes associated with inward proton transfer are not only localized within the protein itself but are also transmitted to the surrounding lipid bilayer. Photoactivation of this microbial rhodopsin is sensed by the surrounding lipid molecules by two different processes occurring on a fast (< 100 ns) and a slow time scale (> µs).

While time-resolved IR spectroscopy is an established tool to monitor light-induced absorption changes of reversible processes, it has found only limited application in the study of irreversible and light-insensitive reactions. In the second part of this thesis, I showcase two novel IR absorption techniques based on quantum cascade lasers (QCL) to study protein reactions. Both techniques were used to monitor protein conformational changes as well as protonation dynamics by single-shot experiments, i.e. without the need to average multiple acquisitions. After a thorough comparison of both techniques, I applied them to the study of the irreversible activation process of the G-protein-coupled receptor rhodopsin. This approach demonstrates that QCL-based IR spectroscopy is a powerful tool for the spectroscopic study of irreversible and, in the future, also light-insensitive (protein) reactions.

Kurzfassung

Protonentransfer über die Lipiddoppelschicht einer biologischen Membran ist ein Prozess von höchster Relevanz in der Natur. Da Protonen sehr klein sind, stellt die experimentelle Untersuchung von Protonentransferreaktionen eine große Herausforderung dar. Eine der wenigen Methoden, die es ermöglicht, Protonentransfer nachzuweisen, ist Infrarot (IR) Differenzspektroskopie. Die chemische Sensitivität der IR-Spektroskopie ermöglicht es, Protonierungszustände von funktionellen Gruppen innerhalb eines Proteins zu bestimmen und liefert gleichzeitig Erkenntnisse über anderweitige strukturelle Änderungen, die ggf. simultan ablaufen. Daher ist IR-Spektroskopie eine geeignete Methode, um Funktionsmechanismen jener Proteine zu untersuchen, die in biologischem Protonentransfer involviert sind.

Für das Verständnis von Membranproteinen, die als Protonenpumpen fungieren, ist es wichtig zu verstehen, was die Richtung des Transports bestimmt. Im ersten Teil dieser Arbeit soll diese Frage adressiert werden, indem ein mikrobielles Rhodopsin untersucht wird, das Protonen in das Innere der Zelle pumpt. Mittels zeitaufgelöster Spektroskopie konnte gezeigt werden, dass die Deprotonierung einer Asparaginsäure zeitlich mit der Deprotonierung der Schiff'schen Base am Retinalchromophor korreliert ist. Die Abfolge dieser Protonentransferreaktionen hat relevante Implikationen für den Funktionsmechanismus dieser inwärts gerichteten Protonenpumpe, welcher mit den bereits bekannten Mechanismen für auswärts gerichtete Protonenpumpen verglichen werden kann. Die lichtgetriebenen Strukturänderungen, sind nicht nur im Protein selbst lokalisiert, sondern beeinflussen auch die Struktur der umgebenden Lipidmoleküle in der Membran. Die Aktivierung dieses mikrobiellen Rhodopsins führt zu einer strukturellen Änderung in der umgebenden Membran in einem schnellen (< 100 ns) und einem langsamen Prozess (> µs).

Konventionelle zeitaufgelöste IR-Spektroskopie ist eine gängige Methode, um reversible, lichtgetriebene Prozesse zu untersuchen, aber kann nur selten verwendet werden, um irreversible oder gar licht-unabhängige Prozesse zu untersuchen. Im zweiten Teil dieser Arbeit vergleiche ich zwei neuartige IR-spektroskopische Methoden basierend auf Quantenkaskadenlasern (QCL) im Hinblick auf ihre Anwendung zur Untersuchung von Protonierungsdynamiken und Konformationsänderungen in Proteinen. Beide Methoden ermöglichen die Datenerfassung mit hohem Signal-zu-Rausch Verhältnis bei jeder einzelnen Acquisition, was das Mitteln mehrerer Experimente erspart. Aufgrund dieser Tatsache konnte ich die irreversible Aktivierung des G-protein-gekoppelten Rezeptors Rhodopsin zeitaufgelöst messen. Dies zeigt, dass IR-Spektrometer basierend auf QCLs eine geeignete Möglichkeit darstellen, irreversible und in der Zukunft auch lichtunabhängige (Protein)-Reaktionen IR-spektroskopisch zu untersuchen.

List of Abbreviations

AC	alternating current
ADC	analog-to-digital converter
AntR	antarctic rhodopsin
ATP	adenosine triphosphate
***Bc*XeR**	*Bacillus coahuilensis* rhodopsin
BR_{548}	dark-adapted bacteriorhodopsin from *Halobacterium salinarum*
BR_{568}	light-adapted bacteriorhodopsin from *Halobacterium salinarum*
BTP	1,3-bis(tris(hydroxymethyl)methylamino)propane
Cryo-EM	cryogenic electron microscopy
DADS	decay-associated difference spectrum
DC	direct current
DCS	dual-comb spectroscopy
DDM	n-dodecyl-β-maltoside
DHPDS	6,8-dihydroxy-1,3-pyrenedisulfonic acid
DMA	dimethylacetamide
DMPC	1,2-dimyristoyl-sn-glycero-3-phosphocholine
DPPC	1,2-dipalmitoyl-sn-glycero-3-phosphocholine
EADS	evolution-associated difference spectrum
E. coli	*Escherichia coli*
EC-QCL	external cavity quantum cascade laser
FT	Fourier transformation
FTIR	Fourier-transform Infrared
FWHM	full width at half maximum
FWM	four-wave mixing
GLA	global lifetime analysis
GPCR	G-protein-coupled receptor
GTA	global target analysis
GVD	group velocity dispersion
He-Ne	helium neon laser
HOOP	hydrogen out-of-plane
***Hs*BR**	bacteriorhodopsin from *Halobacterium salinarum*
IR	infrared
IRF	instrument response function
IST	isomerization switch transfer
KIE	kinetic isotope effect
LDA	lifetime density analysis
LED	light-emitting diode
Low-T	low temperature
LP	long pass
MCT	mercury cadmium telluride
MD	molecular dynamics
MES	2-(N-Morpholino)ethansulfonsäure

***Ns*XeR**	*Nanosalina* sp. xenorhodopsin
OPO	optical parametric oscillator
PDB	protein data bank
PMT	photomultiplier tube
***Po*XeR**	*Parvularcula oceani* xenorhodopsin
PRG	proton release group
QCL	quantum cascade laser
***Rm*XeR**	*Rubricoccus marinus* xenorhodopsin
ROS	rod outer segments
RR	resonance Raman
RSB	retinal Schiff base
SADS	species-associated difference spectrum
SNR	signal-to-noise ratio
SVD	singular value decomposition
SzR	Schizorhodopsin
UV/vis	ultraviolett/visible
Wt	wild type
XeR	xenorhodopsin
XFEL	X-ray free electron laser

Contents

1 Introduction

Proton Transfer in Biology

Proton transfer plays a fundamental role in many biological processes. By coupling to an external source of energy, protons can be translocated unidirectionally across a biological membrane and establish an electrochemical gradient. This electrochemical energy can be utilized and coupled to the generation of energy-rich molecules such as adenosine triphosphate (ATP). This process is of central importance for bioenergetics and is described by Peter Mitchell's chemiosmotic theory.[1] Here, integral membrane proteins couple proton transport across the lipid bilayer to other processes, that provide the energy to overcome the energetic barrier for establishing a proton gradient. Both in photosynthesis and respiration, proton transport is coupled to electron transfer reactions, whereas the primary source of energy is light and nutrients, respectively.[2, 3] Apart from its exemplary importance for bioenergetics due to unidirectional transport across biological membranes, proton transfer processes play an important role in other biological processes, too. For example in the enzyme carbonic anhydrase, which catalyzes the hydration/dehydration reaction of CO_2, protons are engaged as substrates in the catalytic turnover where intramolecular proton transfer can be rate-limiting in certain cases.[4] Even in proteins or enzymes, whose primary function is not associated with proton translocation or catalytic turnover of protons, internal proton transfer reactions can be essential for the protein's functional mechanism. A prominent example is the G-protein-coupled receptor rhodopsin, where the deprotonation of the retinal Schiff base is a prerequisite for receptor activation and initiation of the visual phototransduction.[5] Also in phytochromes, which are red-light sensitive photoreceptors that activate output domains such as histidine kinases, internal protonation steps and even transient proton release to the environment have been observed.[6] The aforementioned examples illustrate that regardless of the fact whether proton transport itself defines the basic function of the protein, proton transfer reactions are of central importance for protein function.

The Study of Proton Transfer in Proteins

The fact that a proton does not contain electrons and its radius is 10^5 times smaller than that of any other ions, promotes proton transfer, but renders its direct observation with experimental techniques a challenging task. Nevertheless, the combination of a plethora of biophysical experiments allowed to derive mechanistic concepts about proton transfer in proteins.[4] One technique which enables to localize changes in protonation states within a protein is Infrared (IR) difference spectroscopy. Ideally the experiment is conducted in a time-resolved manner, where the dynamics of proton transfer reactions are monitored in real time.

Such experiments revealed detailed information about proton transfer in proteins. Yet, because of the experimental design of state-of-the-art IR spectrometers, the reaction of interest needs to be probed repeatedly to obtain spectro-temporal data with sufficiently high signal-to-noise ratio (SNR). Therefore, most experiments were conducted on light-driven proteins that undergo strictly reversible reactions. Among these proteins, microbial rhodopsins have been studied extensively as they are intrinsically light-sensitive and undergo a cyclic photoreaction.[7] Because of their large functional variety, including ion pumps of different ion selectivity and pumping direction, they have been used as model systems to study directional ion transport. In this respect, an intriguing question about the directionality of proton transport arose. How do ion pumps, which unlike ion channels translocate ions unidirectionally, achieve strictly vectorial proton transport?[8]

1.1 Microbial Rhodopsins

Rhodopsins are retinylidene proteins, i.e. they covalently bind a retinal chromophore to a conserved lysine of the apoprotein opsin via a protonated Schiff base (RSB). Microbial (or type I) rhodopsins occur in prokaryotes and lower eukaryotes. In nature, their physiological roles range from energy conversion in e.g. bacteriorhodopsin, to signaling in e.g. sensory rhodopsin. In contrast, animal (or type II) rhodopsins likewise display a seven-transmembrane α-helical fold and harbor a retinal chromophore, but function as G-protein-coupled receptors (GPCRs) involved in light sensation (Figure 1-1).[9] The discovery of channelrhodopsins, which belong to the family of microbial rhodopsins and are responsible for the photophobic response or phototaxis in green algae, led to the development of optogenetics. In optogenetics light-driven ion transporters are used to activate or silence specific neuronal cells. This method is an elegant way to study for example neuronal circuits by light stimulation, but also medical applications are explored.[9, 10] In a pioneering study, the vision of a blind patient was partially recovered by optogenetic therapy.[11] This illustrates that the study of microbial rhodopsins is motivated not only by the desire to understand structure-function relationships in these proteins but also leads to applications in biomedical research. In turn, a profound mechanistic understanding may enable the optimization and further development of optogenetic applications.

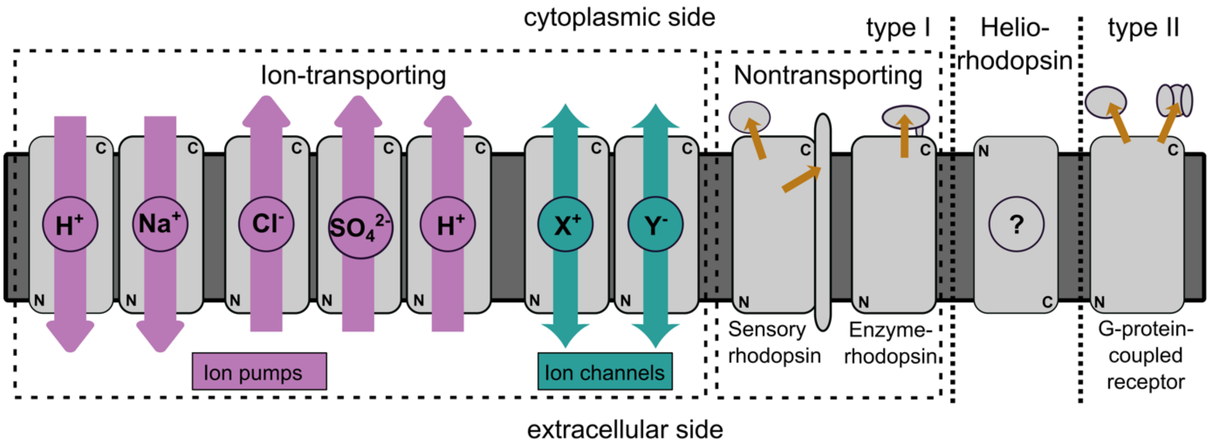

Figure 1-1: The functional diversity of retinal proteins. The family of type I rhodopsins can be subdivided into ion-transporting and non-transporting proteins. For ion-transporting rhodopsins, the colored arrows indicate the direction of ion transport. In nontransporting and type II rhodopsins the yellow arrow indicates the interaction of the receptor with the transducer (or the functional domain in the case of enzymerhodopsins). N and C mark the location of the N- and C-termini, respectively. Note the inverted membrane topology of heliorhodopsin, whose function is still unknown. The orientation of type II rhodopsins is kept analogously to type I rhodopsins (C-terminus up) in this thesis, while it is usually drawn with C-terminus down in the literature. Figure adapted from refs.[9, 12].

Microbial rhodopsins display a large functional diversity (Figure 1-1). They can be subdivided into ion-transporting and nontransporting microbial rhodopsins. In the latter case, sensory rhodopsins and enzymerhodopsins are involved in photoreception while the functional role of heliorhodopsins is still unknown. Within the class of ion-transporting rhodopsins, ion pumps and ion channels need to be distinguished. While ion pumps translocate ions without or even against an ion gradient, ion channels are not able to do so. In both cases, cation- and anion-specific proteins have been discovered. While channelrhodopsins are involved in photoreception, ion pumps are involved mostly in bioenergetics. The variety of pumped ions ranges from protons to chloride and sodium ions.[12] Also, the transport of larger ions such as sulfate has been reported.[13] An essential feature of ion pumps is the directionality of ion transport. Sodium pumps achieve net outward transport, while chloride pumps were found to transport halides into the cell. In the case of proton pumps, both outward and inward proton pumps have been discovered.[12] Even a proton pump with variable vectoriality depending on the surrounding pH has been described.[14] As the focus of this thesis is on the vectoriality of proton translocation, current knowledge on outward and inward proton transport is summarized in the following chapters.

1.1.1 Outward Proton Transport in *Hs*BR

In 1971, Dieter Oesterhelt and Walther Stoeckenius discovered a retinal binding protein in the purple membrane fragment of *Halobacterium salinarum*, formerly known as *Halobacterium halobium*.[15] Two years later, the same authors showed that this protein, termed bacteriorhodopsin (*Hs*BR), pumps protons across the cell membrane upon light activation and can establish a proton gradient, playing a central role in the halobacterial metabolism.[16] A minimal system consisting of lipid vesicles with reconstituted bacteriorhodopsin and ATPase univocally demonstrated that bacteriorhodopsin couples light absorption to the generation of ATP. These experiments not only revealed the function of bacteriorhodopsin itself, but also served as a simple model system for the chemiosmotic theory proposed by Mitchell.[17] Since its discovery, *Hs*BR has been studied in great detail by a large variety of methods. These efforts led to a profound understanding of the functional mechanism leading to net outward proton transport. For a detailed overview on *Hs*BR the reader is referred to recent review articles, e.g.[9, 18-20]. The key findings with a focus on the protonation steps are summarized below (Figure 1-2):

The functionally active form of *Hs*BR contains exclusively all-*trans* retinal. It is formed upon exposure to light and is the therefore often referred to as light-adapted BR. In the dark, *Hs*BR is present in a mixture of molecules containing either all-*trans* or 13-*cis*, 15-*syn* retinal. Its absorption maximum is slightly blue-shifted to 548 nm (BR_{548}) as compared to light-adapted *Hs*BR, which absorbs maximally at 568 nm (BR_{568}). Vectorial proton transport in *Hs*BR can be discussed as a sequence of individual steps leading to net outward proton transport. Light absorption by light-adapted *Hs*BR leads to all-*trans* to 13-*cis,* 15-*anti* isomerization within 500 fs forming the K_{590} intermediate via the J_{625} intermediate. About 30% of the absorbed energy is stored in the K intermediate, which drives the transition through the subsequent intermediates. The energy stored in K is discussed in terms of a distorted retinal chromophore as well as weakened hydrogen bonds at the RSB. The L intermediate received a lot of attention as this intermediate precedes the first proton transfer step from the protonated RSB to the counter ion D85. Structural studies did not observe any large conformational changes, but NMR and FTIR spectroscopy suggest changes in hydrogen bonding mainly between the RSB, D85, D212 and a water molecule. These minute changes are expected to lead to the simultaneous and opposite change in pK_a of D85 and the RSB, enabling proton transfer between the two residues. In M, the RSB is deprotonated and the proton has been transferred to D85. Protonation of D85 leads to a conformational change of R82, triggering the proton release from the so-called proton release group (PRG) to the bulk surface. In this context, it should be noted that the exact nature of the conformational change of R82 is still a matter of controversy[21]. The proton release group consists of protonated water molecules arranged close to E194 and E204. Proton removal from this group causes the disappearance of a broad infrared absorption band, known as the continuum band.

In the second stage of the photocycle, another proton needs to be translocated from the cytoplasmic side back to the RSB. Therefore, the RSB needs to change its accessibility to the cytoplasmic side prior to reprotonation. At least two spectrally hardly distinguishable sub-states of M exist, and it is believed that the transition between the two M states marks the step where the RSB changes its accessibility from the extracellular to the cytoplasmic side. This reorientation is discussed in the context of the isomerization switch transfer (IST) model as the switch. However, the exact molecular origin of the switch has not been elucidated as the sub-states are experimentally difficult to distinguish. In this context, protein conformational changes as well as changes at the retinal chromophore have been discussed.

Early on, evidence arose that D96 is involved in the reprotonation of the RSB. However, the interpretation of Fourier-transform Infrared (FTIR) data led to some controversy about the exact timings of proton transfer involving D96 (see ref.[22] for a summary). A negative band, indicating a deprotonation of D96, has already been observed in L, but later it was demonstrated that this negative band is caused by a combination of differential bands stemming from D115 and D96[23]. It is now established, that protonated D96 undergoes an environmental change during L, but deprotonates during the M→N transition leading to RSB reprotonation. The high pK_a of D96 in BR_{568} may be explained by its hydrophobic environment of several leucines and phenylalanines. In order to reprotonate the RSB, the pK_a of D96 drops from >12 to 7.1 during the M→N transition[24]. Given the large distance of ~11 Å between the RSB and D96, direct proton transfer is unlikely to occur. Spectroscopic data in combination with molecular dynamics (MD) simulations suggested that reorientations of W182, L93 and F219 create space for three water molecules bridging the gap between

D96 and the RSB, enabling Grotthuss-type proton transfer[25]. This arrangement of water molecules has later been verified by crystallographic data[26].

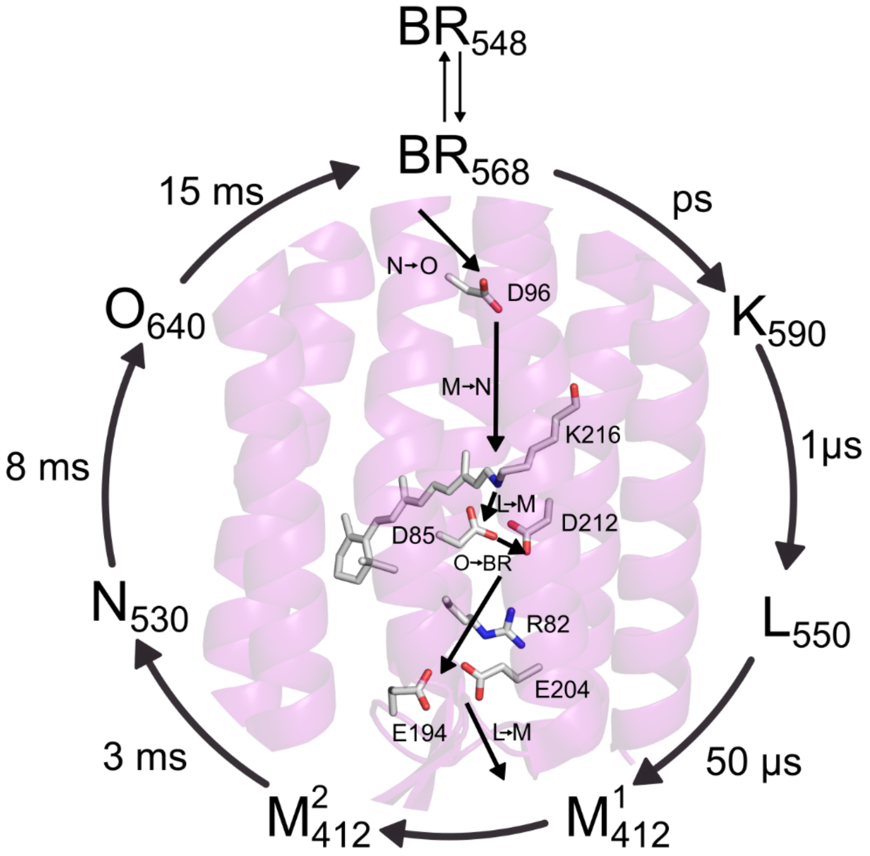

Figure 1-2: Photocycle of bacteriorhodopsin from *Halobacterium salinarum*, adapted from ref.[7]. Crystal structure of *Hs*BR (PDB: 1C3W) with amino acids involved in protonation steps shown as sticks. Proton transfer steps leading to a net outward proton translocation are shown with arrows. More elaborate models of the photocycle with multiple sub-states have been suggested, but are omitted here.

D96 gets reprotonated during the N→O (or N→N') transition from the cytoplasmic surface. The exact proton pathway is not elucidated yet, but it was shown that mutation of D38 has a strong impact on RSB reprotonation. D38 is one out of six acidic residues on the cytoplasmic surface, probably acting as proton antennas by attracting protons from the bulk solution. Reprotonation of D96 happens simultaneously with thermal isomerization from 13-*cis*,15-*anti* to a strained all-*trans* retinal during the N→O transition. These two processes are believed to be coupled by perturbation of the hydrogen bond network between D96 and the RSB upon reprotonation of D96. In the final steps of the photocycle D85 transfers its proton to the PRG via D212 and R82 adopts its dark-state conformation[27, 28].

1.1.2 Inward Proton Transport

In 2016, the first naturally occurring inward proton pumping microbial rhodopsin was described.[29] It was found in the deep-ocean marine bacterium *Parvularcula oceani* and belongs to the class of xenorhodopsins, first described in 2011[30], and was therefore named

*Po*XeR. Pumping assays and electrophysiological recordings revealed that *Po*XeR, when heterologously expressed in *Escherichia coli* (*E. coli)* or mouse cells, acts as a light-driven inward proton pump. During the photocycle of *Po*XeR, prototypical K, L, and M intermediates are formed as well as a long-lived species containing 13-*cis*, 15-*syn* retinal. As in outward proton pumps, proton release to the bulk solution precedes proton uptake. D216, which is located in a similar position as D96 in *Hs*BR, was shown to act as proton acceptor of the RSB proton, but the proton transfer is expected to be mediated by other residues, given the large distance between the RSB and D216.[29] A small kinetic isotope effect (KIE) on the M decay suggests that the reprotonation itself is not rate limiting. It was therefore concluded that reprotonation occurs directly from the bulk solution and is rate-limited by the (branched) reisomerization of the retinal upon M decay.[31] A similar observation was made for another inward proton pump, schizorhodopsin (SzR) found in Asgard archaea. Proton release and uptake occur simultaneously with the rise and decay of the M intermediate. As FTIR experiments did not show changes in protonation states of carboxylic amino acids, it was concluded that proton transfer between the bulk and the RSB happens without any intermediate protonation steps.[32] Such an untrapped proton pathway may be rationalized by proton transfer via water molecules which were observed in the crystal structure of SzR4.[33] In addition, a resonance Raman study suggests that in SzR4, 13-*cis* to all-*trans* reisomerization precedes RSB reprotonation and plays a major role for the vectoriality of proton transport.[34] Another microbial rhodopsin, whose gene was found in an Antarctic freshwater lake, was shown to act as an inward proton pump when expressed in *E. coli* (termed AntR). Its peculiar pH-dependent photochemistry renders a thorough spectroscopic investigation difficult, but a cysteine residue (C75) was shown to be involved in the protonation pathway.[35] Xenorhodopsin from *Rubricoccus marinus* (*Rm*XeR) acts as an inward proton pump, too, but pH indicator experiments indicate that proton uptake precedes proton release[36], which is unique among microbial rhodopsins around neutral pH, but has likewise been observed for *Hs*BR at pH<6[37]. Recent structural data of a bacterial xenorhodopsin from *Bacillus coahuilensis (Bc*XeR*)*, revealed a very detailed insight into the mechanism of inward proton pumping by providing the crystal structures of the ground, L and M states.[38] It was shown that the RSB orientation toward helix G is stabilized by a hydrogen bond to S206 in M, which is different as compared to *Hs*BR, where the RSB is oriented towards helix C. In L, a hydrogen bond network extends from the protonated RSB towards the proton transit group (PTG), which consists of two carboxylic amino acids (E34 and D214) in a similar position as compared to D96 in *Hs*BR. This network is believed to facilitate efficient proton transfer towards the cytoplasmic side. Upon M formation a central gate is closed, which disconnects the RSB from the cytoplasmic side and the RSB is prepared for reprotonation from the extracellular side. A structurally flexible binding pocket of *Bc*XeR is believed to avoid steric conflict, which otherwise could cause large protein conformational changes. The absence of protein conformational changes in *Bc*XeR might be essential to maintain a hydrophobic gate after proton release from the RSB and to avoid proton backflow.[38]

Xenorhodopsin from *Nanosalina* sp. (*Ns*XeR) was the first inward proton pump which was structurally characterized in 2017.[39] The crystal structure revealed the similarity of the fold as compared to *Hs*BR, but at the same time highlighted differing motifs (Figure 1-3). The electrostatic environment of the RSB is very different as compared to *Hs*BR (Table A. 1). While the aspartic acid in position 85 (*Hs*BR) is conserved among xenorhodopsins, D212 is replaced by a proline (P209 in *Ns*XeR). R82 is conserved among xenorhodopsins, but is replaced by W73 in *Ns*XeR. Y57 is conserved among xenorhodopsins. A carboxylic amino acid is conserved in the position of D115 in *Hs*BR. Additional unique features of *Ns*XeR sequence are F174 (W182 in *Hs*BR) and Y216 (F219 in *Hs*BR). D96 in *Hs*BR is replaced by A87 in *Ns*XeR, but D220 is located in a similar position.

Based on the structural basis and the absence of proton pumping upon D220N mutation, D220 was suggested to act as the proton acceptor, possibly together with H48. D76 was suggested to be transiently protonated during the photocycle of *Ns*XeR and to act as the internal proton donor to the RSB. Time-resolved UV/vis experiments led to a photocycle model comprising K, L, and two spectrally distinct M intermediates, but no N- or O-like intermediates.[39] Another spectroscopic study introduced an additional long-lived intermediate with absorption characteristics close to those of *Ns*XeR ground state, termed GS*.[40] The same study reported perturbed photocycle kinetics in the D220E and D220N variants, underlining the functionally important role of this residue. Moreover, the nature of the two spectrally distinct M intermediates was investigated by electrophysiological experiments. It was shown that upon yellow background illumination, a mixture of the two blue-light-absorbing species was accumulated. Applying a blue light flash, led to either an additional inward or an outwardly directed current, depending on the applied membrane potential. It was concluded that the applied membrane potential shifts the equilibrium to either of the two M states, where in MI the RSB is accessible to the cytoplasmic side (M_{CP}) and in MII to the extracellular side (M_{EC}). Therefore, the two spectrally distinct M intermediates with different RSB accessibilities were interpreted as the two species before and after the switch with respect to the IST model.[40] Although the structure of *Ns*XeR is known since 2017 and it has been characterized by means of UV/vis spectroscopy, a direct observation of protonation steps has not been performed and therefore the proton pathway remains elusive to a large extent.

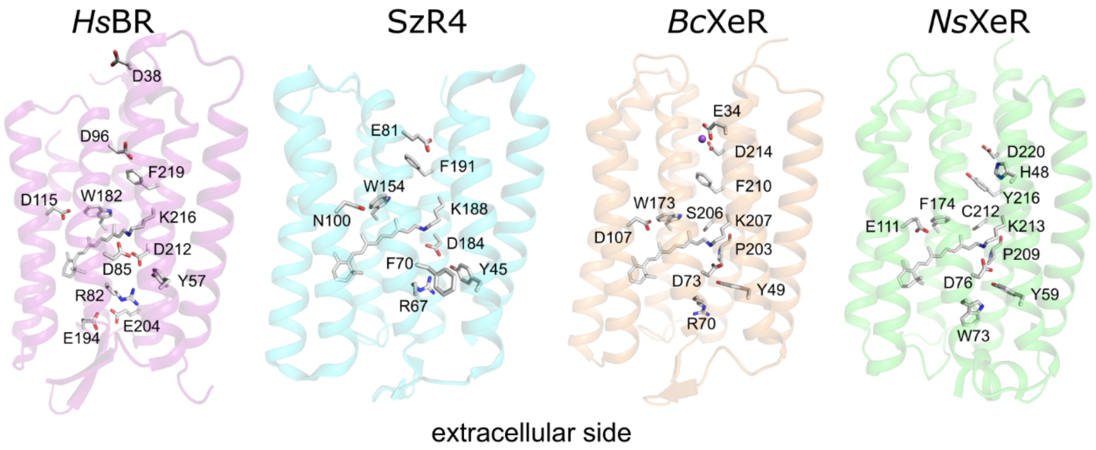

Figure 1-3: Structural comparison of the prototypical outward proton pump *Hs*BR (PDB: 1C3W) with three different inward proton pumps (SzR4 PDB: 7E4G, *Bc*XeR PDB: 7ZMY, *Ns*XeR PDB: 6EYU). Residues which are potentially relevant for the functional mechanism are shown as sticks and labeled accordingly. Water molecules are omitted. The purple sphere in the structure of *Bc*XeR shows the presence of a sodium ion. All structures are oriented in the same orientation with the N-terminus facing downward to the extracellular side. For simplification the membrane is omitted.

The question about the physiological role of inward proton transport is intriguing, but no studies addressing this question have been carried out so far. In this respect, it has to be noted that such experiments can only be carried out if the organisms, where the genes were found in, are cultivatable. Given the insights gained on inward proton transport so far, it seems that the mechanism for inward proton transport may differ among the members of this group of proteins. Nevertheless, a thorough investigation of protonation steps occurring in this protein family is needed to derive concepts for inward proton transport.

1.2 Scope of this Work

This work can be divided into two major parts: The first part aims to provide a mechanistic description of the directionality of proton transport. Here, a recently discovered microbial inward proton pump (*Ns*XeR) is characterized spectroscopically with a focus on the protonation pathway. The mechanistic insights gained on inward proton pumping are compared with the well-known concepts of outward proton pumping. Ultimately, this part aims to address one of the fundamental questions of active proton transport: What determines the direction of proton translocation?

The second part focuses on establishing new IR spectroscopic methods for the study of proton transfer. As most time-resolved IR spectroscopic techniques can only be applied to reversible systems that can be probed repeatedly, the application of time-resolved IR spectroscopy is still limited to a relatively small group of proteins. In this thesis, two novel IR absorption techniques based on quantum cascade lasers (QCL) are applied to the study of proton transfer in light-driven proteins. First, the two techniques are benchmarked using a reversible photoreaction and finally applied to the study of irreversible protein dynamics. This showcases the possibility to extend the application of time-resolved IR spectroscopy to a wider range of proteins that do not undergo cyclic (photo)reactions, which is the vast majority of enzymes.

1.3 Vibrational Spectroscopy

Any chemical transformation involves breaking and/or forming of bonds. Be it an enzymatically catalyzed substrate turnover or simply a change in protonation state of a protonatable amino acid, the observation of the fundamental molecular step requires a method with “atomic resolution” (in this context not necessarily in terms of spatial resolution). In biological systems, these fundamental chemical alterations are very small in comparison to the macromolecule, wherein they occur. Whereas structural methods provide the structural framework for the understanding of reaction mechanisms, they are often not able to resolve minute but mechanistically relevant chemical transformations or interactions. Instead, vibrational spectroscopy inherently provides chemical information at “atomic resolution” by probing the molecular vibrations of a molecule. Molecular vibrations can be investigated using infrared (IR) spectroscopy and Raman spectroscopy. IR spectroscopy is an absorption technique, relying on transitions between vibrational states of a molecule by absorption of electromagnetic radiation. Instead, the physical mechanism underlying Raman spectroscopy is inelastic scattering of photons. Consequently, not every vibration is IR and/or Raman active, leading to the so-called selection rules: a vibration is IR active when the dipole moment changes during the vibration, while it is Raman active when its polarizability changes during the vibration. In the simplest case a molecular vibration can be described as a harmonic oscillation of two point masses (atoms) connected by a mass-less spring (bond). The circular frequency ω of the vibration is given by (1), where c is the speed of light, f the force constant and μ the reduced mass. In vibrational spectroscopy, the circular frequency is typically expressed in wavenumbers ($\tilde{\upsilon}$ in units of cm^{-1}). The terms frequency and wavenumber are used interchangeably throughout this thesis. It is evident from (1) that upon isotopic substitution the frequency will shift, which can be exploited for band assignments. For a detailed description of the theoretical background of vibrational spectroscopy and how the harmonic model can be extended to include anharmonic effects, the reader is referred to ref.[41, 42].

$$\omega = 2\pi c\tilde{\upsilon} = \sqrt{\frac{f}{\mu}} \qquad (1)$$

A molecule with N atoms has $3\mathrm{N}\text{-}6(5)$ vibrational degrees of freedom, the so-called normal modes, which may give rise to a band in a vibrational spectrum. A vibrational mode with the frequency $\tilde{\upsilon}$ can be described by the displacement of atoms in a normal coordinate system. This is commonly referred to as normal mode analysis. To obtain a more illustrative description, an internal coordinate system can be introduced, where changes in distances (stretching coordinates) and angles (deformation coordinates) between atoms are used to describe the molecular vibration. Therefore, a molecular vibration or normal mode is often described as a combination of stretching coordinates and/or deformation coordinates. Usually, out of plane deformation and torsional coordinates are introduced as additional internal coordinates.[41] Depending on the introduced internal coordinates, the mass displacements during the vibration may be described as symmetric (ν_s) or antisymmetric (ν_{as}) stretching coordinates whereas deformation vibrations are often described as in-plane bending (δ), rocking (γ_r), wagging (γ_w) or twisting (γ_t) coordinates (the nomenclature used here is adapted from ref.[43]). In non-linear molecules a normal mode is usually not described by a localized vibration of a single bond, but a combination of several coordinates. In the case where a vibration of a single bond represents the major character of a normal mode, it is often considered to be a localized vibration, which is coupled to another mode[22]. Therefore, the phrasing “the vibrational mode, giving rise to a band at xxxx cm^{-1}, is caused by vibration A, which couples to vibration B” is often used in literature synonymously for “the vibrational mode, giving rise to a band at xxxx cm^{-1}, is a normal mode with character of coordinate A and coordinate B.”

From the aforementioned considerations, it is evident that macromolecules such as proteins give rise to a large number of vibrational modes. Although not every mode is IR and/or Raman active, vibrational spectra of (biological) macromolecules consisting of thousands of atoms can be very complex and therefore difficult to analyze. Therefore, the assignment of a specific band to a certain residue inside a macromolecule is a challenging task, but both techniques allow to reduce the complexity of vibrational spectra. In Raman spectroscopy, one can chose the wavelength of the incident light source as such, that it matches the electronic transition of a co-factor of the protein. In this so-called resonance Raman approach, vibrations of the co-factor are enhanced with high preference and can therefore be distinguished from Raman-active vibrational modes of the protein. This approach is limited to proteins containing co-factors absorbing in the UV/vis spectral range. Instead, reaction-induced IR difference spectroscopy is a yet simple but elegant approach to monitor only those vibrations, which are changing during the functional mechanism of the sample. After recording a spectrum in the inactive state (absorbance A^i or transmitted light intensity I^i), the reaction is induced and a spectrum is recorded while or after the system undergoes its reaction to an active state (absorbance A_a or transmitted light intensity I^a). By calculating the difference of the two spectra (2), all vibrations which are not changing during the reaction cancel each other out and the resulting difference spectrum displays only bands which have changed upon the reaction. Great care must be taken that the two spectra are collected under identical measurement conditions to fulfill $I_0^i = I_0^a$, with I_0 being the transmitted light intensity without any sample present.

$$\Delta A = A_a - A_i = log\frac{I_0^a}{I^a} - log\frac{I_0^i}{I^i} = log\frac{I^i}{I^a} \tag{2}$$

Reaction-induced difference spectroscopy can be performed in a steady-state experiment, where the reaction intermediate or product is accumulated in order to have enough time to record a spectrum. This may be achieved by shifting equilibria by e.g. temperature or pH. Technically more demanding are time-resolved experiments, where the spectral changes are followed transiently after applying the trigger to the reaction. In the easiest and most used case, the trigger is a short pulse of light when the reaction at study is intrinsically light sensitive.[41]

To obtain spectral information, a certain frequency range of interest needs to be probed. Different strategies to record spectra have been employed in the past years. Common principles used throughout this thesis are summarized in Figure 1-4. As Raman spectroscopy was not intensively used in this thesis, only IR spectroscopy is discussed in the following chapters with a focus on time-resolved methods.

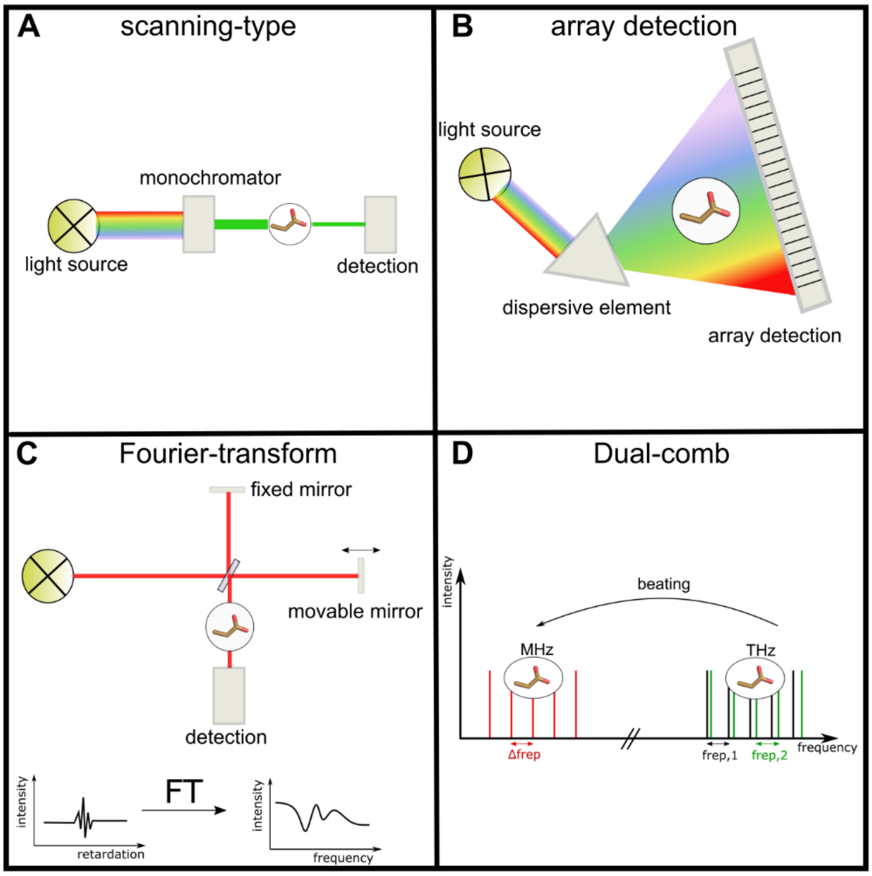

Figure 1-4: Principles of optical absorption spectroscopy. A) scanning-type spectroscopy, where a certain frequency of the emission of a polychromatic light source is selected by a monochromator and subsequently detected by the detection system. B) array detection, where multiple frequencies are detected simultaneously by an array detector. Array detection is used for resonance Raman experiments, but with a monochromatic laser as probing light source and detection of scattered light. C) Fourier-transform spectroscopy using a Michelson interferometer. D) Dual-comb spectroscopy detects the beating between two optical frequencies, which allows to retrieve spectral information without the use of a dispersive element or interferometer.

1.3.1 Fourier-Transform Infrared Spectroscopy

The small extinction coefficient of absorption bands in the infrared as compared to the UV/vis range of the electromagnetic spectrum inherently leads to small signals. While black body emitters readily provide IR radiation, it is challenging to find IR-transparent materials for optical parts, which imposes limitations on the construction of the spectrometer. Further, detectors operated at room temperature are susceptible to thermal fluctuations, which in turn increases noise. Those prerequisites demand advanced techniques, in order to achieve a sufficient SNR. Since the 1970s, Fourier-transform infrared (FTIR) spectroscopy has surpassed conventional dispersive spectrometers. Besides a high wavelength accuracy and little limitation of available photons by entrance slits (Jacquinot's advantage), a major advantage is the massively reduced time to record a spectrum as compared to dispersive spectrometers due to the increase in SNR (Fellgett's advantage).[41, 44] The following conceptual description of FTIR spectroscopy is adapted from refs.[41, 42].

Central part of the Fourier-transform spectrometer is the Michelson interferometer (Figure 1-5A). A monochromatic light wave entering the interferometer is split into two equal parts and directed to a fixed and movable mirror, respectively. The movable mirror introduces an optical path length difference γ and thereby a phase difference given by $2\pi\gamma\tilde{\nu}$, with $\tilde{\nu}$ being the wavenumber. Upon recombination, the two fields with amplitudes E_1 and E_2 superimpose and the detected intensity I is given by (3)

$$I(\gamma) \sim |E_1 + E_2|^2 = \frac{1}{2}{E_0}^2[1 + cos(2\pi\gamma\tilde{\nu})] \tag{3}$$

which contains a static signal (DC signal) and modulated signal (i.e. the interferogram, AC signal). For a continuous polychromatic light source in a real spectrometer the measured interferogram $\mathrm{S}(\gamma)$ is given by

$$S(\gamma) = \int_{-\infty}^{+\infty} B(\tilde{\nu})\, cos\, 2\pi\tilde{\nu}\gamma\, d\tilde{\nu} \tag{4}$$

where $\mathrm{B}(\tilde{\nu})$ represents the intensity of the light source modified by instrumental properties such as detector response or amplifier characteristics.

The inverse Fourier transformation relates the interferogram to the spectrum by (5).

$$B(\tilde{\nu}) = \int_{-\infty}^{+\infty} S(\gamma)\, cos\, 2\pi\tilde{\nu}\gamma\, d\gamma \tag{5}$$

However, in a real spectrometer, the path difference γ, i.e. the extension of the interferometer arm is restricted to a finite range. Mathematically, this can be modeled by multiplying the infinite interferogram with a boxcar function, which is 1 for $-\gamma_{max} < \gamma < \gamma_{max}$ and 0 outside this window. Fourier transformation of a boxcar function leads to a sinc function, which shows band broadening of the main peak and side lobes. This effect can be minimized by multiplying the interferograms with so called apodization functions.

Nevertheless, the spectral resolution is inversely proportional to the optical path length difference.

Another practical implication is that the interferogram cannot be digitized continuously, but in discrete steps. Therefore, the signal needs to be digitized with a constant spacing of datapoints. In a conventional FTIR spectrometer, a monochromatic helium-neon (He-Ne) laser is coupled into the interferometer and the interferogram is detected by a photodiode (Figure 1-5A). The sinusoidal interference pattern of the He-Ne laser (Figure 1-5B) displays zero-crossings spaced by $\Delta\gamma = \frac{\lambda}{2}$. The simultaneously detected IR signal can now be equidistantly digitized at every nth zero-crossing of the He-Ne signal. Thereby, the wavelength of the He-Ne laser itself determines the upper wavelength limit detectable (i.e. Nyquist frequency). This can be appreciated, following the Nyquist criterium, which states that a sinusoidal signal can only be determined precisely, if the signal is sampled at least twice per period (Figure 1-5B). A practical implication of this is, that digitizing only every n-th zero crossing reduces the bandwidth of the spectra, which might be beneficial for time-resolved FTIR spectra. In such a case, frequencies higher than the Nyquist frequency need to be optically or electronically filtered to avoid aliasing effects. An additional benefit of the implementation of the He-Ne laser is, that it provides an internal frequency calibration.

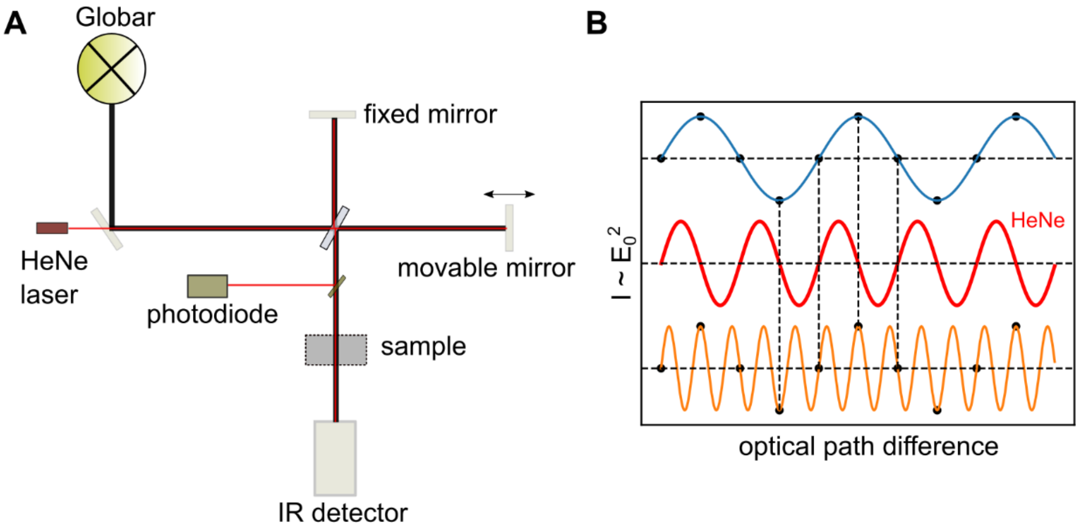

Figure 1-5: Principle of FTIR spectroscopy. A) Schematic representation of a Michelson Interferometer in an FTIR spectrometer. IR radiation is displayed in black, the visible radiation of the He-Ne Laser is displayed in red. B) Digitization scheme and Nyquist theorem, adapted from ref.[42]. Interferogram of the He-Ne laser (red), where the zero-crossings define the digitization rate of the signal (dashed vertical lines and dots). Blue and orange signals show modulations with lower and higher frequencies, respectively, as compared to the He-Ne signal. It is apparent that with the present sampling frequency the orange sine wave cannot be appropriately measured.

For time-resolved FTIR experiments two different methods have been established. In the rapid-scan approach interferograms are rapidly recorded after excitation of the sample. The time resolution is limited by the time it takes to record a full interferogram and therefore by the mechanical speed of the movable mirror as well as the optical retardation and hence the spectral resolution. The speed of the analog-to-digital converter (ADC) imposes a limitation on the spectral bandwidth as it needs to correctly sample the interferogram at a given modulation frequency. State of the art spectrometers are able to measure a single-sided interferogram within ~6 ms at 8 cm^{-1} resolution. However, the actual time resolution may be lower due to time gaps between recording subsequent interferograms and dead times between sample excitation and recording of the first interferogram. Instead, in the step-scan approach interferograms are not measured continuously, but time traces are recorded at fixed mirror positions. Therefore, the mechanical movement of the mirror is no longer limiting the time resolution. Although ns time resolution can be achieved by step-scan FTIR, often the time resolution is limited by the speed of the ADC which is usually around 5 μs. After collection of the transients at all mirror positions the data is reorganized to obtain interferograms as a function of time. In order to conduct the experiment in a reasonable time frame, the number of interferogram points needs to be reduced by decreasing the spectral bandwidth and the spectral resolution, but is at least as high as 500 points. Therefore, only highly repetitive reactions can be studied by step-scan FTIR. More detailed information on both time-resolved techniques can be found in refs.[22, 44].

1.3.2 Scanning-type IR Spectroscopy using EC-QCLs

In scanning-type spectroscopy single frequencies are selected from a polychromatic light source by a dispersive element and detected one after another. While this approach is often used in UV/Vis spectroscopy, it has its limitations in the IR spectral range, where the availability of IR-transparent materials imposes experimental constraints (cf. chapter 1.3.1). With the advent of the quantum cascade laser[45] the experimental realization of scanning-type spectrometers for the mid-IR range has been revived. In a time-resolved experiment, the changes in absorbance are monitored by measuring the transmitted (monochromatic) light intensity as a function of time before and after applying the reaction trigger (cf. equation (2)). Such a flash photolysis experiment is well established in the UV/vis range (cf. chapter 2.1)[46], but can also be realized in the mid-IR range using broadly-tunable external cavity quantum cascade lasers (EC-QCL) as measuring light source (Figure 1-6).[47] EC-QCLs have a built-in grating outside the cavity, which allows to select single frequencies from the polychromatic emission.[48] After selection of the frequency of interest, the transmitted light intensity through the sample is detected by a mercury cadmium telluride (MCT) detector. The signal is digitized by two oscilloscopes operating at different sampling rates. Using two oscilloscopes with high and low sampling rates enables to maintain a high time resolution but at the same time to cover a broader time range.[47]

In this thesis, triggering of the reaction is achieved using light excitation by a visible pulsed laser. The transmitted light intensity is detected as a function of time from ~ 1 ms before light excitation (pre-trigger) up to several seconds after inducing the reaction (post-trigger). Transient absorbance changes are calculated following equation (2). After averaging multiple acquisitions to achieve a sufficient SNR, the emission frequency is tuned in a stepwise manner (i.e. wavenumber spacing) and the process is repeated until the spectral region of interested is covered. By appending the individually measured monochromatic transients, a data matrix of time-resolved absorbance changes is constructed, which allows to display spectral characteristics as a function of time. Hence, the wavenumber spacing chosen by the user defines the apparent spectral resolution (cf. chapter 1.4.4), but not the bandwidth of the QCL emission which is much smaller (<0.01 cm^{-1}) than the spacing typically used (>1 cm^{-1}). The time resolution of the spectrometer is in the order of tens of ns given the rise time of the detection system of 10 ns ± 1 ns and the instrument response function with a FWHM of 14.9 ns ± 0.2 ns.[47]

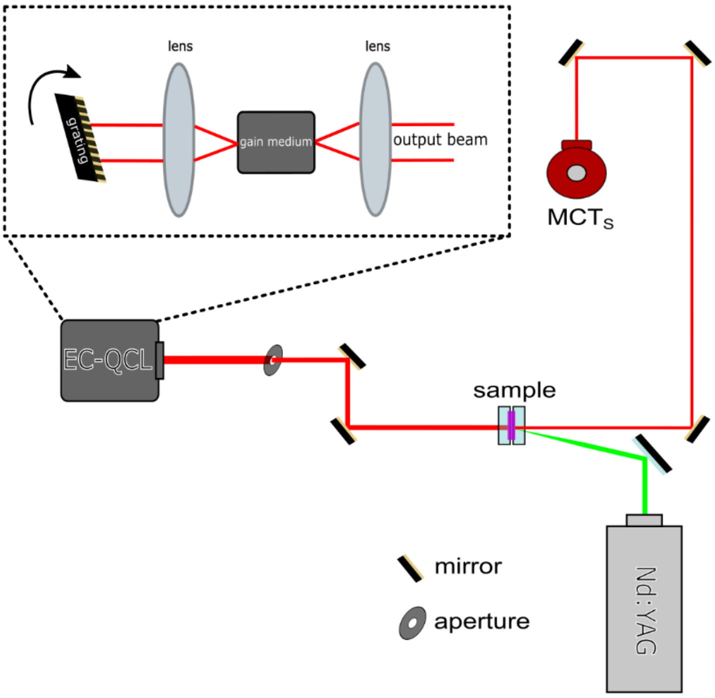

Figure 1-6: Optical layout of the scanning-type spectrometer (IR flash photolysis) using external cavity quantum cascade lasers (EC-QCLs) as light sources. The output of the QCL is attenuated using an aperture, transmitted through the sample and detected by an MCT detector. A Nd:YAG laser excites the sample by generating visible laser pulses. The zoom in shows the principle of an EC-QCL, where a grating outside the gain medium selects the desired wavenumber, adapted from[48].

1.3.3 Dual-Comb Spectroscopy

Dual-comb spectroscopy requires an optical frequency comb as light source, whose emission spectrum consists of discrete and equally spaced modes. The development of optical frequency combs was awarded with the Nobel prize in 2005 to Theodor Hänsch and

John Hall.[49] In the following section, a brief description of the fundamentals of frequency combs is given, based on the working principle of mode-locked lasers.[50, 51]

Light waves travelling back and forth in a resonator, form a set of standing waves (so called longitudinal modes) where f_m is the frequency of the mode, L the resonator length, m an integer, c the speed of light and n the refractive index (6) (cf. Figure 1-7 A).

$$f_m = \frac{mc}{2Ln} \tag{6}$$

If a sufficient number of modes with a fixed phase relation interfere, short pulses can be obtained, which are separated by their round-trip time in the cavity T (7), where v_g is the mean group velocity of the cavity.

$$T = \frac{1}{f_{rep}} = \frac{2L}{v_g} \tag{7}$$

The periodic emission of pulses in the time domain relates to a spectrum with comb lines spaced by f_{rep} in the frequency domain. In an ideal resonator, this would allow to retrieve the frequency of every comb line by $f_m = mf_{rep}$. However, caused by dispersion, the group and phase velocities in the cavity are not equal, causing a relative phase shift of the pulse envelope to the carrier wave from pulse to pulse ($\Delta\varphi_{CE}$). In the frequency domain, this leads to an offset of the frequency comb (f_{CE0}), which is illustrated in Figure 1-7 B. Therefore, for each frequency of the comb line it can be written (8):

$$f_m = f_{CEO} + mf_{rep} \tag{8}$$

As already mentioned above, achieving a fixed phase relation between the longitudinal modes is necessary to produce short laser pulses and thereby comb operation with equally spaced modes. In a mode-locked laser, this is typically achieved by passive mode-locking using a saturable absorber. However, other methodologies to obtain frequency combs are available and reviewed in ref.[50].

The working principle of quantum-cascade laser frequency combs is reviewed in ref.[52] and will only be briefly discussed below. Passive mode-locking as in classical mode-locked lasers (e.g. Ti:Sapphire lasers) is not possible in QCLs, because the upper state lifetime ($\tau \approx$ 1 ps) is much shorter than the round-trip time ($\mathrm{T} \approx$ 64 ps with L = 3 mm). However, the definition of a frequency comb is not essentially linked to the generation of high-intensity laser pulses, but the emission of equally spaced modes.[53] A QCL working in the multimode regime emits dispersed Fabry-Pérot modes. Taking dispersion into account, it can be derived that the spacing between two modes depends on their group velocity v_g (9) (see ref.[54] for the derivation of this equation).

$$\Delta f = f_{m+1} - f_m = \frac{(m+1)c}{2Ln_{m+1}} - \frac{mc}{2Ln_m} = \frac{v_g}{2L} \tag{9}$$

Following equation (9), the spacing between adjacent comb lines is proportional to the group velocity v_g and thereby depends on the group velocity dispersion (GVD). As a consequence, a low GVD in the cavity is a prerequisite for comb operation (cf. equation (7)).[54] QCLs operating in a multimode regime, emit dispersed Fabry-Pérot modes, but they can be injection-locked by additional modes, generated by a four wave mixing process (FWM). This process is not further described here, but the interested reader is referred to ref.[52] and references therein. In a pioneering study, this process was shown to create a frequency comb centered at 1430 cm^{-1} spanning up to 60 cm^{-1} with a comb line spacing of 0.25 cm^{-1}, related to the round-trip frequency of 7.5 GHz. The absence of dispersion, measured with a high-resolution FTIR spectrometer (0.0026 cm^{-1} resolution) as well as a sharp intermode beatnote (FWHM < 200 Hz) are characteristics of comb operation.[53] Driving the QCLs at higher currents broadens the optical spectrum up to 250 cm^{-1}, but at the same time broadens the intermode beatnote, indicating worse comb operation caused by the residual GVD.[52]

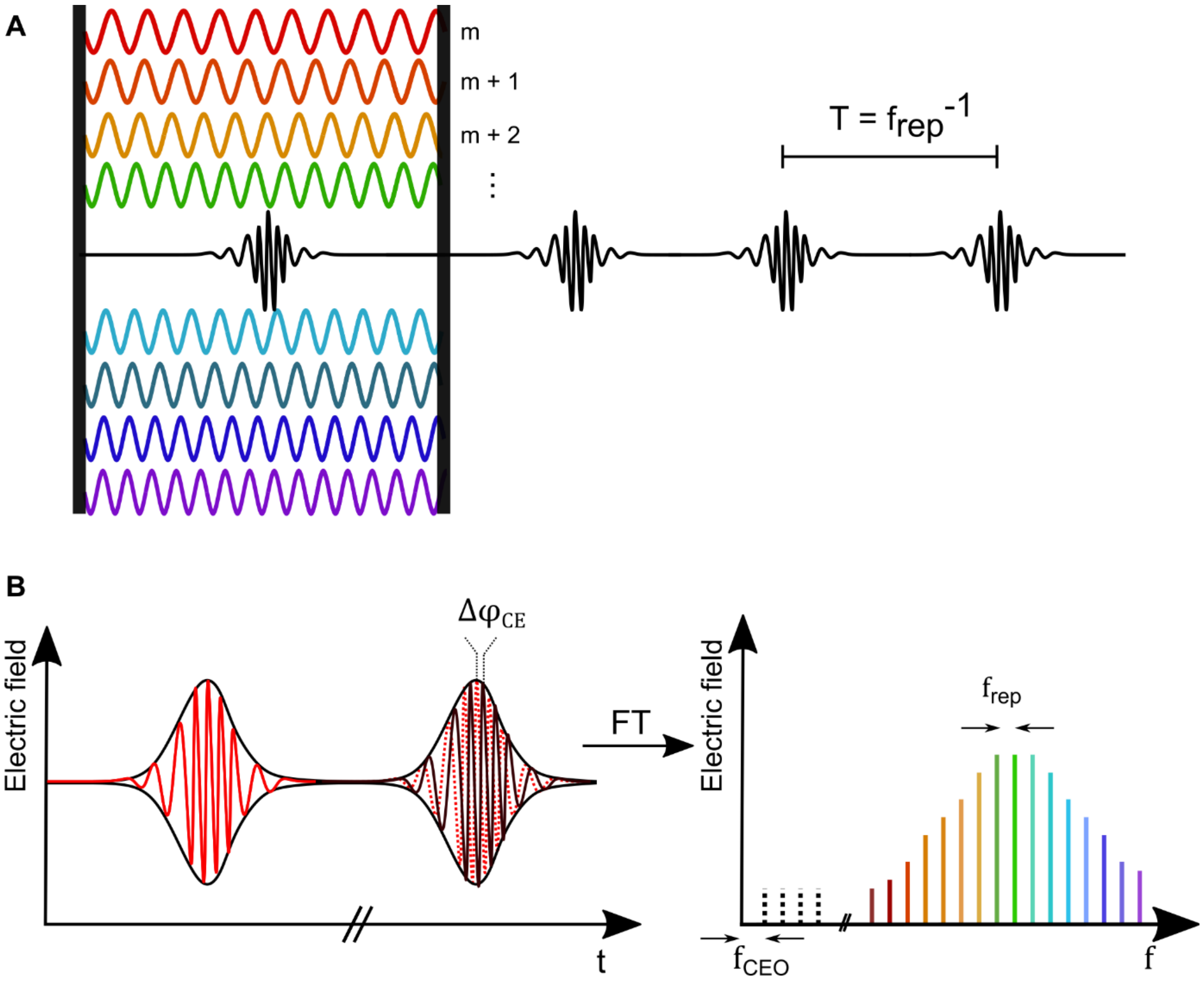

Figure 1-7: Characteristics of frequency combs. A) Schematic representation of a frequency comb in a mode-locked laser. Black vertical lines mark the laser cavity in which multiple longitudinal modes resonate. Upon mode-locking, short laser pulses are generated which leave the cavity separated by the round-trip time T. B) Schematic time-domain picture of the 2 consecutive laser pulses showing the pulse-to-pulse slip of the envelope phase with respect to the carrier phase ($\Delta\varphi_{CE}$). Fourier transformation leads to the spectral comb representation, with the comb lines spaced by f_{rep} and the carrier-envelope offset frequency f_{CEO}. Adapted from refs. [50, 51].

A promising application of frequency combs is dual-comb spectroscopy (DCS), where a multi-heterodyne detection scheme maps optical frequencies to the radiofrequency (rf) domain, which can be measured by conventional electronics. This approach enables high resolution spectroscopy without the use of a dispersive element nor moving parts and is reviewed in refs.[52, 55]. DCS in the mid-IR range employing QCL frequency combs has been demonstrated for the first time in 2014.[56] Essentially, two frequency combs with slightly different repetition rates are interfered, creating a rf comb, where each rf comb tooth is generated by a heterodyne beat of a pair of optical comb teeth. Therefore, the spacing of the rf comb (Δf_{rep}) is determined by the difference in repetition frequencies of the two optical combs (10).

$$\Delta f_{rep} = f_{rep,2} - f_{rep,1} \tag{10}$$

As depicted in Figure 1-8, the sample's absorption is thereby mapped from the optical to the rf domain and the sample's absorption is measured with a spacing of f_{rep} determining the spectral resolution (cf. chapter 1.4.4). Two configurations are possible: In the asymmetric approach, only one comb interrogates the sample and is subsequently mixed with the second comb. In the symmetric approach, both combs are transmitted through the sample. While the asymmetric approach allows to retrieve amplitude and phase information, phase information is lost in the symmetric approach, but the latter one is more robust.[55] Since the asymmetric approach is not used in the context of this thesis, it is not described further.

The optical spectral bandwidth is limited by the one-to-one mapping condition, i.e. each detected rf beat note corresponds to the beating of the n-th comb line of comb 1 with the n-th comb line of comb 2 (Figure 1-8). Mathematically this condition can be expressed as $\Delta f_{CEO} + N\Delta f_{rep} \leq \frac{f_{rep}}{2}$ with N being the number of observed beatings.[56] However, the practical limitation in QCL-based DCS is given by the analog bandwidth (BW) of the detector (11).[57]

$$N\,\Delta f_{rep} < BW \tag{11}$$

In order to resolve neighboring comb teeth, the minimum acquisition time is given by the inverse of the rf comb spacing and therefore defines the time-resolution of the instrument T_{res} (12).[57]

$$T_{res} = \frac{2}{\Delta f_{rep}} \tag{12}$$

It is evident from (11) and (12), that a high Δf_{rep} enables high time resolution but reduces the spectral bandwidth.

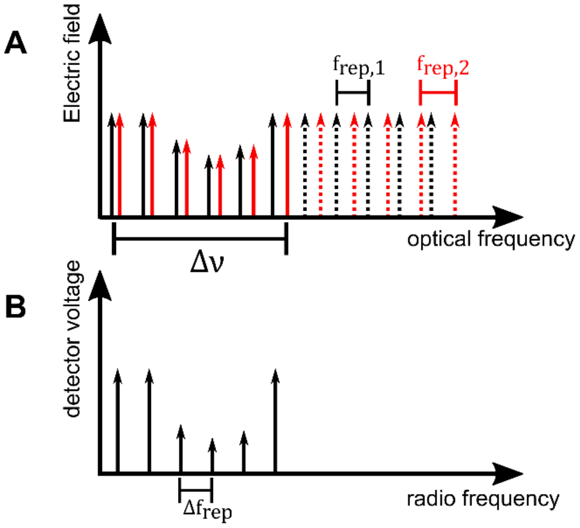

Figure 1-8: Concept of dual-comb spectroscopy. A) Two frequency combs (red and black) emitting several laser lines with slightly different repetition rates $f_{rep,1}$ and $f_{rep,2}$, create a multiheterodyne beating in the radiofrequency domain B). In B), the rf beat notes are spaced by Δf_{rep}. The spectral bandwitdh, where the one to one mapping is fullfilled is indicated by $\Delta\nu$. The reduced amplitude of the laser lines indicates the samples absorption. Adapted from ref.[55].

Due to the heterodyne detection scheme, dual-comb spectroscopy does not require any kind of dispersive element to obtain spectral information. This results in a simple and user-friendly optical layout, as can be seen in Figure 2-1.

1.4 Data Analysis

Irrespective of the method used for data collection (cf. Figure 1-4), time-resolved (optical) spectroscopy yields two-dimensional data, where the two experimental variables are wavelength (λ) or wavenumber ($\tilde{\nu}$) and time (t). A simultaneous analysis of the entire dataset is generally referred to as global analysis. Given the large amount of information, often only a thorough analysis enables the description and interpretation of the spectroscopic data. Here, two different approaches can be discriminated: 1. If a parametrized model, underlying the spectro-temporal changes, is known, fitting routines can be used to quantitatively describe parameters. 2. When no or only a class of models is known, finding the model, which best describes the dataset, provides valuable information about the physical concepts underlying the spectroscopic observations. The latter approach is usually referred to as target analysis.[58] In both cases, the choice of the model, might influence the interpretation of the data. Thus, in some cases, model-independent analysis strategies, such as lifetime density analysis (LDA) might be beneficial.[59]

In the following chapters, global analysis[58, 59] and LDA[60, 61] are briefly described. Additionally, the data treatment of the raw data of dual-comb spectroscopy is described. All fitting procedures presented in this thesis were conducted with a Python-based analysis tool, written by Dr. David Ehrenberg. The source code is available at https://github.com/deef128/trtoolbox.[61]

1.4.1 Global Analysis

In the absence of noise, the dataset of a time-resolved difference absorption experiment, can be described as the sum over all species associated difference spectra (SADS) $\Delta s_i(\lambda)$ weighted by the respective concentration $c_i(t)$ of intermediate i (13).

$$\Delta A(\lambda,t) = \sum_{i=1}^{n_{intermediate}} \Delta s_i(\lambda) c_i(t) \tag{13}$$

Here, the SADS are given by $\Delta s_i(\lambda) = s_i(\lambda) - s_0(\lambda)$, where $s_0(\lambda)$ denotes the ground state bleach spectrum, which is linked to the ground state spectrum of the sample prior to light excitation $\tilde{s}_0(\lambda)$ via the fraction cycling parameter f_c (14), which accounts for number of excited molecules.

$$s_0(\lambda) = f_c \tilde{s}_0(\lambda) \tag{14}$$

In the simplest case, it is reasonable to assume only first order kinetics, which leads to a set of linear differential equations, whose solution is a sum of exponential decays. In global lifetime analysis (GLA), the entire dataset is fitted to the sum of a sufficient number of exponential decays, set by the experimentator. The fitted amplitudes result in the so-called decay associated difference spectra (DADS). GLA models the case, where parallelly decaying reactions take place. Changing the differential equations, allows to imply different reaction models. For example, for photocycle data of photoreceptors, typically a sequential model has been used, where intermediate i interconverts into intermediate $\mathrm{i+1}$, but also branched reactions can be modeled[62]. In the case of a sequential model, the derived spectra are termed evolution associated difference spectra (EADS), which are interpreted in a way, that the i-th EADS evolves with i-1-th lifetime. If the correct model has been chosen the EADS correspond to the SADS. In any case, the experimentator biases the analysis, by choosing a certain model or number of components. Testing different models to evaluate which reaction scheme describes the data best is referred to as global target analysis (GTA). Here, a priori knowledge from different experiments can assist the analysis. An approach to aid global analysis, is singular value decomposition (SVD), which in some cases can be used to determine the number of components describing the dataset. If one reconstructs the dataset by only the significant singular values, it may also be used to reduce noise in the dataset. However, great care must be taken to not miss any relevant information.

1.4.2 Lifetime Density Analysis

Lifetime density analysis also referred to as lifetime distribution analysis (LDA) is in contrast to GTA a model-independent approach to extract kinetic information from a time-resolved spectroscopic dataset. Such a two-dimensional dataset can be described by a semi-continuous sum of n exponential decay functions (15). Here, the amplitudes $x_i(\lambda, \tau_i)$ describe the probability of a reaction taking place with a certain spectral contribution at wavelength λ and with the time constant τ_i. Note that the convolution of the spectro-temporal features with the instrument response function (IRF) is neglected below.

$$\Delta A(\lambda, t) = \sum_{i=1}^{n} x_i(\lambda, \tau_i) e^{\frac{t}{\tau_i}} \tag{15}$$

This can be rewritten in matrix notation (16), where $\mathbf{A}$ denotes the data matrix of size $n_t \times n_\lambda$, the matrix $\mathbf{D}$ contains exponential decays with the size $n_t \times n_\tau$ and $\boldsymbol{x}$ displays the matrix, containing the pre-factors for all wavelengths with the size $n_\tau \times n_\lambda$. $\mathbf{E}$ is a matrix describing the noise in the dataset.

$$\boldsymbol{A} = \boldsymbol{D} \cdot \boldsymbol{x} + \boldsymbol{E} \tag{16}$$

When (16) is solved for $\boldsymbol{x}$ by least square minimization, it is evident, that the goodness of the fit will increase, when a large number of exponential decays are allowed to contribute. In comparison to GTA, where the experimentator critically tests a relatively small number of components, LDA is more susceptible to overfitting, because the number of parameters n is very high ($n \sim 100$). As a consequence, the minimization problem needs to be regularized, which means that large fitting coefficients are being penalized. Here, Tikhonov regularization is applied, which leads to the minimization problem (17):

$$\|\boldsymbol{A}-\boldsymbol{D}\cdot\boldsymbol{x}\|_2+\alpha\|\boldsymbol{L}\boldsymbol{x}\|_2 \qquad (17)$$

On the one hand, (17) tries to minimize the residuals between the recorded and the modeled data ($\|\boldsymbol{A}-\boldsymbol{D}\cdot\boldsymbol{x}\|_2$), but at the same time, large values of $\boldsymbol{x}$ are being penalized. Here, $\boldsymbol{L}$ is identity matrix, but different matrices may be used. The regularization parameter α compromises between describing the data accurately (i.e. minimizing $\|\boldsymbol{A}-\boldsymbol{D}\cdot\boldsymbol{x}\|_2$) and having as little contributions from different exponentials as possible (i.e. minimizing $\|\boldsymbol{L}\boldsymbol{x}\|_2$). In effect, large α values smooth the data and must therefore be chosen wisely. Plotting the fitted amplitude matrix $\boldsymbol{x}$ leads to lifetime density maps, which provide a concise overview of kinetic distributions.

1.4.3 Dual Comb Data

In this section the data processing for dual-comb spectroscopy is briefly explained with a focus on the post-processing, which was performed to yield the datasets presented in 3.3. More detailed information can be found in [57], but in the meantime the processing has been updated by IRsweep to a Python-based workflow. As already mentioned in chapter 1.3.3, the reference detector is used for correction of intensity fluctuations of the QCL emission, which is not further explained here. Both detectors continuously measure the beating of the two QCL combs in the time domain. In a time-resolved measurement, each acquisition extends over >20 ms. After the signal has been digitized, the acquisition is cut into time slices of 1-4 µs which are subsequently Fourier-transformed. As already explained in 1.3.3, the length of the time slice determines the spacing of the datapoints on the time axis and hence the time resolution, but it is limited by the requirement to resolve adjacent comb teeth. After Fourier transformation, each time slice has been converted into a spectrum in the rf domain, which contains several comb lines, spaced by Δf_{rep} (Figure 1-8). The pre-trigger intensity is averaged and used to calculate the difference- transmission or absorbance. Those processing steps occur on the acquisition unit of the spectrometer, before the user starts the post-processing:

The equidistance of the frequency comb lines allows the precise determination of the relative comb line positions on the frequency axis (i.e. the frequency spacing, ~ 0.3 cm^{-1} depending on the laser module). However, the absolute frequency is not retrieved. Therefore, a calibration with a well-known standard is performed, which provides the link between the rf- and optical frequency range (Figure 1-8). For the data presented in this thesis, an FTIR spectrum of a polypropylene foil and/or a water vapor spectrum have been used. After frequency calibration, averaging of multiple acquisitions and/or spectral averaging may be performed. DCS data was spectrally averaged by a conventional moving average. Therefore, n neighboring lines on each side of the central line were averaged using a boxcar function. The spectral resolution is given by $(2n + 1)f_{rep}$ with f_{rep} being the comb line spacing. As the intensities and therefore the noise of the single laser lines of the frequency comb vary, the contribution of each laser line to the moving average is weighted by the inverse of its noise variance ($1/\sigma^2$). The variance of each laser line is derived from the pre-trigger data in a time-resolved dataset. In the last step, averaging on the time axis is performed, where the linearly spaced datapoints are logarithmically averaged to yield typically 20 datapoints per decade.

1.4.4 Spectral Resolution

As the term spectral resolution is discussed in slightly different ways for different methods, it needs to be clarified in order to avoid confusion. Spectral resolution is defined as the minimal difference between wavenumbers (or wavelengths or frequencies) at which different spectral features can still be distinguished.[63] Depending on the principle of the spectrometer, the term spectral resolution depends on different factors and may be used slightly differently.

As explained in 1.3.1 the spectral resolution of an FTIR spectrometer is determined by the extension of the movable mirror as a finite interferogram leads to broadening of bands. The spacing between spectral datapoints depends on the probed spectral range and zero-filling and may therefore be smaller than the spectral resolution. In a scanning-type spectrometer, the size of the entry and exit slit of the monochromator determines the bandwidth of the measuring light and therefore the spectral resolution.[41] However, two cases need to be distinguished: 1. The bandwidth is larger than the datapoint spacing. This resembles the aforementioned case, where the spectral resolution is determined by the size of the exit and entry slits of the monochromator. This is usually the case for FTIR spectrometers. 2. The bandwidth is considerably smaller than the datapoint spacing. In this case, the datapoint spacing practically determines the spectral resolution of the spectrometer. This scenario is the case for both QCL-based methods described in 1.3.2 and 1.3.3. If spectral averaging (i.e. averaging of neighboring spectral lines) is performed, the exact spectral resolution is not easy to define and depends on the averaging algorithm (cf. 1.4.3).

1.5 Molecular Vibrations

In this chapter the most frequently discussed vibrational modes throughout the thesis are described to aid the reader during the results part. The ambition of this chapter is not to give a complete and detailed description for all vibrational modes, but rather to describe essential features that explain experimental findings such as frequency shifts or changes in intensity. Unless indicated differently, the information on the described protein bands are taken from refs.[22, 43]. Most information about chromophore bands presented in this chapter was obtained from resonance Raman experiments on *Hs*BR, which can be analyzed in conjunction with IR data. For an extensive overview of these chromophore vibrations, the reader is referred to refs.[64, 65]. Throughout the literature, the terms bending and rocking vibration are used interchangeably for an in-plane deformation (cf. e.g. refs.[64, 66]), denoted as in-plane bending (δ) in this thesis. The bands described below are summarized in Figure 1-9.

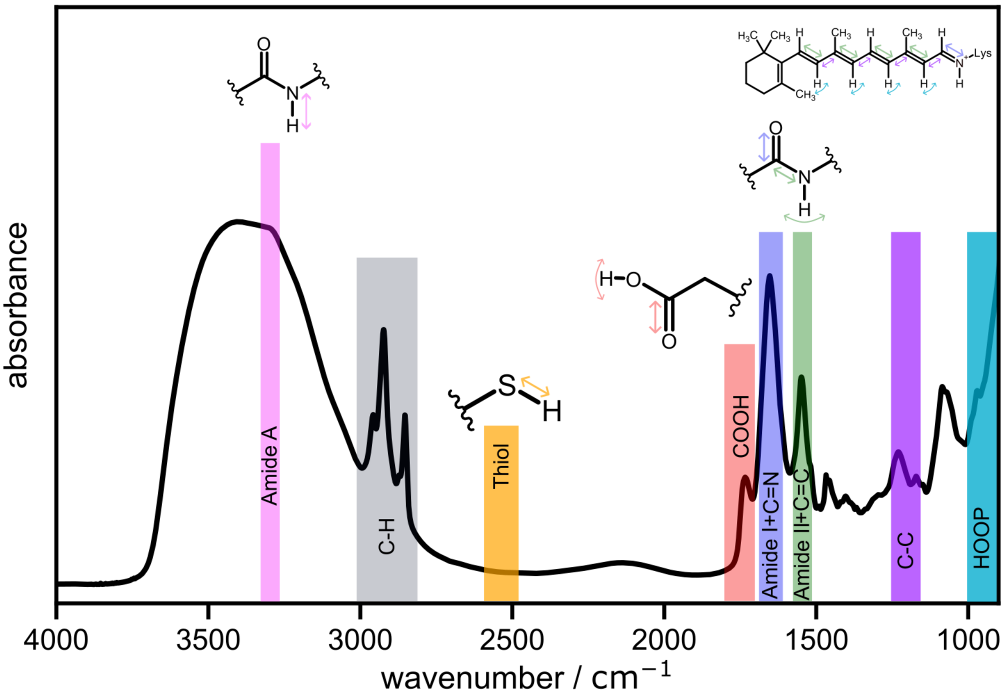

Figure 1-9: Graphical summary of the vibrational modes discussed in this thesis and the spectral range where they typically appear. Arrows indicate the dominating mass displacements of the respective vibrational mode. Minor contributions are neglected (compare to the text below). Water contributions to the spectra are not highlighted but appear in the spectral range where the amide A and amide I vibrations appear. The small broad band between 2400 and 2000 cm^{-1} is assigned to the combination mode of water. The spectrum was recorded on nanodisc-reconstituted *Ns*XeR. Therefore, the large absorbance in the COOH range can be attributed to the C=O stretching mode of the DMPC lipids.

C=C stretching vibration

The all-*trans* retinal has five ν(C=C) internal stretching coordinates, giving rise to vibrational bands between 1600-1500 cm^{-1}. In *Hs*BR the most intense band is located at around 1527 cm^{-1} and is caused by the symmetric combination of all five ν(C=C) coordinates, whereas the contribution of the ν(C=C) coordinates of the double bonds adjacent to the β-ionone ring gets smaller. The frequency of this band was shown to be linearly correlated with the UV/vis absorption maximum and can therefore be used to correlate results obtained from IR and UV/vis experiments[67].

C-C stretching vibration

Bands caused by C-C stretching modes, abbreviated as ν(C-C), occur typically around 1200 cm^{-1} and are mixed modes with ν(C-C) and in-plane bending (rocking) δ(CCH) character. Unlike the ν(C=C) modes, the ν(C-C) are localized vibrations, with e.g. the band at 1201 cm^{-1} having mostly contributions from the ν(C_{14}-C_{15}) coordinate and the band at 1169 cm^{-1} from the ν(C_{10}-C_{11}) coordinate. Such localized vibrations allow to derive detailed information about the retinal configuration. The appearance of a ν(C-C) band at 1194 cm^{-1} was shown to be indicative of a 13-*cis* configuration of the retinal in the K intermediate[68]. The intensity of the ν(C-C) bands depends strongly on the dipole of the molecule and therefore on the protonation state of the RSB. Therefore, the IR difference spectrum of the M intermediate typically does not display positive bands in this spectral range. The ν(C_{14}-C_{15}) vibration appears to be coupled stronger to the δ(NH) vibration of protonated RSB when the C_{15}=N bond is in *syn* configuration, as compared to the C_{15}=N *anti* configuration. Therefore, N-deuteration leads to stronger frequency shifts of the bands assigned to the ν(C_{14}-C_{15}) mode in the retinal when the RSB is in C_{15}=N *syn* configuration, but only minor shifts in C_{15}=N *anti.*

C=N stretching vibration

The band assigned to the protonated RSB displays ν(C=N) and δ(C=N-H) character[69]. Upon N-deuteration the contribution of the δ(C=N-H) coordinate is removed and the band has an almost pure ν(C=N) character. In other words, N-deuteration removes the coupling between the ν(C=N) and δ(N-H) vibration (*vide supra*). Consequently, the frequency difference between the protonated and deuterated RSB vibration is a measure for the coupling of the two vibrations in the protonated case, i.e. the larger the difference, the stronger the coupling. Further, it is known that vibrational coupling increases upon decreasing the energy difference of the two coupling vibrations. The higher the δ(NH) vibration is in frequency and therefore the closer to ν(C=N), the stronger the coupling. As the δ(NH) vibration shifts to higher frequencies with increasing hydrogen-bonding strength, it can be concluded that a large difference in frequency between the protonated and deuterated RSB vibration indicates a strongly hydrogen bonded RSB.

Hydrogen out-of-plane vibrations

Hydrogen out-of-plane vibrations (HOOP) or vinyl hydrogen wagging vibrations (γ_w) absorb at frequencies below ~1000 cm^{-1}. Their intensities are weak in planar polyenes but increase upon torsional deformations of the retinal polyene chain. In *Hs*BR strong HOOP bands during K have been observed at 957 and 811 cm^{-1} during K, indicating that the retinal chromophore is twisted after initial all-*trans* to 13-*cis* isomerization.[68]

Amide I vibration

The amide I vibration of the protein backbone consists mainly of the ν(C=O) with contributions from the ν(C-N) and δ(NH) coordinates, with the latter making it H/D sensitive. The H/D sensitivity varies between secondary structure motifs, because the contribution of the δ(NH) coordinate to the amide I mode may differ. The frequency of the amide I vibration shifts upon hydrogen bonding to the C=O as well as upon transition dipole coupling to neighboring amide groups. It can therefore be used to determine secondary structure elements of proteins. As the coupling delocalizes the amide I vibration, it is sensitive to global structural changes or reorientations of the protein backbone. However, amide I difference bands are often only interpreted as an indication for a protein conformational change, rather than assigned to a specific change in structure.

Amide II vibration

The amide II vibration can be described as the out of phase combination of the in plane δ(NH) coordinate and the ν(C-N) coordinate. Upon N-deuteration the amide II mode has largely ν(C-N) character and therefore shifts down by ~100 cm^{-1}. The coupling between neighboring amide II groups is less pronounced as compared to the amide I mode and therefore it is typically less sensitive to structural changes of the protein.

Amide A vibration

The amide A mode is described as a localized ν(N-H) vibration and is therefore strongly sensitive to N-deuteration. Hydrogen bond donation of the N-H downshifts the ν(N-H) frequency. Coupling to neighboring amide groups is negligible making it less sensitive to secondary structural changes but rendering the ν(N-H) vibration a good reporter for hydrogen bonding. However, the overlap with the water stretching mode may complicate experiments as well as data analysis.

Carboxylic acid vibrations

Bands associated with the ν(C=O) vibration of carboxylic residues in proteins appear typically between 1770-1710 cm^{-1}. The ν(C=O) is coupled to the δ(OH) vibration leading to a spectral blueshift as compared to the pure ν(C=O) vibration. Therefore, the carboxylic ν(C=O) vibration undergoes a redshift upon H/D exchange whose magnitude depends on the coupling of with the δ(OH) vibration. The carboxylic ν(C=O) vibration is sensitive to the medium polarity as well as hydrogen bonding. Carboxylic groups in a protein interior without any hydrogen bonding are expected to absorb around 1770-1760 cm^{-1} and display a spectral redshift upon formation of hydrogen bonds. The oxygen atom of the carbonyl bond may accept hydrogen bonds, while the hydroxyl group hydrogen can act as hydrogen bond donor. Furthermore, the hydroxyl oxygen may act as a weak acceptor. Hydrogen bonding influences the frequencies and with that it affects the coupling of the two vibrations. Therefore, it is evident that the interpretation of carboxylic ν(C=O) frequencies and shifts upon H/D exchange is not trivial and must be performed with great care. As bands caused by ν(C=O) vibrations of lipidic ester groups appear in the same spectral range, great care must be taken to distinguish these from ν(C=O) vibrations of carboxylic amino acids. The ν(C=O) vibrations of lipidic esters are usually insensitive to H/D exchange, allowing to distinguish them from carboxylic ν(C=O) vibrations.

Upon deprotonation of the carboxylic acid, the ν(C=O) vibration is converted into a ν(O-C-O$^-$) vibration, where the combination of the two C-O stretches give rise a symmetric and antisymmetric mode. The symmetric carboxylate ν_s(COO$^-$) absorbs between 1430-1350 cm^{-1} while the antisymmetric ν_{as}(COO$^-$) vibration absorbs between 1610-1540 cm^{-1}. A combination of a band caused by the ν(C=O) vibration of a protonated carboxylic acid with a band caused by a carboxylate vibration can be used as a univocal assignment to a protonation or deprotonation reaction of a carboxylic residue. However, the spectral overlap of the carboxylate bands with other bands can render an assignment complicated. Therefore, often the ν(C=O) mode of protonated carboxylic amino acids is interpreted exclusively, where a negative or positive band is interpreted as a deprotonation or protonation, respectively. Instead, differential band shapes indicate an environmental change of the carboxylic residue. Additionally, also carboxylate vibrations shift upon cation ligation and can therefore be used to derive ion binding.

S-H stretching vibration

Bands caused by the ν(S-H) vibration of cysteines in proteins occur in a spectral range between 2590 and 2480 cm^{-1}, remote from most other vibrations. Upon deuteration it shifts down by ~700 cm^{-1}. The ν(S-D) vibration is decreased in intensity as compared to the ν(S-H) vibration because of a weaker dipole moment. The ν(S-H) vibration is sensitive to hydrogen bonding and vanishes upon deprotonation. With increasing hydrogen bond donating character, the ν(S-H) frequency displays a spectral redshift. This is typically accompanied by an increase in absorption coefficient (ε_{H2O} = ~7 M^{-1}cm^{-1} (2574 cm^{-1}) vs. ε_{DMA} = 21 M^{-1}cm^{-1} (2534 cm^{-1})). Buried inside a hydrophobic part of a protein, the sulfhydryl group can form strong hydrogen bonds to polar groups (e.g. backbone carbonyls), which polarizes the S-H bond, increasing its absorption coefficient ($\varepsilon_{Protein}$ = ~150 M^{-1}cm^{-1})[70]. The sulfur atom can act as a hydrogen bond acceptor, which can lead to a small upshift in frequency by ~ 5 cm^{-1}. The ν(S-H) vibration is further sensitive to rotamers (C-S torsion) leading to spectral splits of

~ 10 cm^{-1}. The S-H bond of thiols may also establish hydrogen bonds with π-electron systems of aromatic residues [71].

2 Material & Methods

2.1 UV/vis Spectroscopy

Time-resolved UV/vis spectroscopy experiments were carried out using a commercially available setup (LKS80, Applied Photophysics, Leatherhead, Surrey, UK). The samples were excited by a laser pulse (Δt = 10 ns, λ = 532 nm, E_{exc}/A = 3 mJ/cm^2) generated by a Nd:YAG laser (Quanta-Ray, Spectra Physics) driving an optical parametric oscillator (OPO). A xenon arc lamp was used as measuring light source. Two monochromators, one in front and one behind the sample, were used to select single wavelengths from the broadband emission of the xenon lamp. A photomultiplier tube (PMT) detects the monochromatic light intensity after transmission through the sample. To cover the full photoreaction, two transients were measured for each wavelength. To obtain high SNR during the early times after pulsed excitation (ns-μs), the light-source was operated in pulsed mode, giving rise to an intense and stable light pulse of approximately 500 μs duration. A second transient was recorded with the same lamp operating in continuous wave mode, which allows to access the slower dynamics (100 μs – s). Time traces were compressed by logarithmically averaging the linearly spaced data points. To increase the SNR, 10 transients were co-averaged unless specifically noted. After the experiment, the fast and slow transients were merged, using a script written by Pit Langner (Labview, National Instruments, Austin, USA). Transients were recorded between 630 and 360 nm in steps of 5 nm (for wild-type *Ns*XeR) or 10 nm (variants). Triggering of the measurement is achieved by detection of the incoming laser pulse by a photodiode. To calculate the difference absorbance, the transmission prior to photoexcitation (10 % of the total recording time) was used as background (see equation (2)). For recording a full map, transients were recorded until 2 s after photoexcitation. Longer recording times result in software-related difficulties. Further, the emission of the xenon arc lamp is not stable for several s, which might result in signal drifts in long timescales. To avoid excitation of long-lived intermediates, the repetition rate of sample excitation was set to ensure full relaxation of the longest lived intermediate.

2.2 FTIR Spectroscopy

All FTIR experiments were carried out using a Vertex 80v spectrometer (Bruker Optics, Ettlingen, Germany) in transmission mode using standard techniques. Table 1 summarizes the settings used in the presented experiments unless differently stated in the text.

Table 1: Settings for FTIR experiments. LP: longpass, LN: liquid nitrogen cooled, AC: Alternating current, DC: Direct current.

	Steady-state	Low-T	Rapid-scan	Rapid-scan	Step-scan
Spectral bandwidth	15798 – 0 cm^{-1}	3950-0 cm^{-1}	1975 – 0 cm^{-1}	3950 – 0 cm^{-1}	1975 – 0 cm^{-1}
Spectral resolution	2 or 4 cm^{-1}	4 cm^{-1}	4 cm^{-1}	4 cm^{-1}	8 cm^{-1}
Optical filter	/	LP ~ 3950 cm^{-1}	LP ~1975 cm^{-1}	LP ~3950 cm^{-1}	LP ~1975 cm^{-1}
Scanner velocity	80 kHz	120 kHz	280 kHz	280 kHz	40 kHz
Time resolution	/	/	~10 ms	~10 ms	6.25 μs
Acquisition	double-sided	double-sided	single-sided	single-sided	single-sided
Detector settings	LN-MCT AC	LN-MCT-AC	LN-MCT AC	LN-MCT AC	LN-MCT DC

Sample excitation in steady-state difference spectroscopy experiments was achieved by using a light emitting diode (LED) with a wavelength of 530 nm. By using an automated routine, multiple scans were recorded for the protein in the dark state and under continuous illumination and automatically averaged to achieve sufficient SNR. For time-resolved measurements the sample was excited by a laser pulse (Δt = 10 ns, λ = 532 nm, E_{exc}/A = 3 mJ/cm^2) generated by a Nd:YAG laser (Minilite II, Continuum or Quanta-Ray, Spectra Physics). The excitation rate was set to allow full recovery of the longest-lived intermediate. In the case of the Minilite II, this was achieved by delaying the Q-Switch of the laser by a delay generator, while the Quanta-Ray – OPO system was run with 20 Hz and an optical shutter (NM laser products) was used to select single pulses from the laser output.

Rapid-scan experiments were performed from ~10 ms to 60 s after light excitation by an automatic routine written in OPUS. Interferograms were recorded in single-sided mode, which increases the deadtime between interferograms and therefore the time-resolution. However, since rapid-scan data were recorded to compare spectral features of the long-lived intermediate, a loss in time-resolution is justified. The first scan is recorded between 0-20 ms after light excitation, which results in a first timepoint at around ~10 ms. Towards later times, multiple scans were co-averaged for data compression. The last spectrum recorded by the automatic routine was used as background.

Step-scan experiments were conducted with an ADC frequency of 160 kHz, which results in a time resolution of 6.25 μs. 11000 linearly spaced data points were measured to cover the time range until 68 ms and subsequently logarithmically averaged. To reduce the measurement time, the repetition rate of the excitation laser was set to 0.2 Hz, which was shown to not alter the spectral signatures upon excitation of a fraction of the long-lived intermediate (Figure A. 1). In every measurement 2 coadditions per interferogram point were averaged, which results in ~90 minutes recording time per dataset. To increase the SNR, a total of 50-80 coadditions were averaged.

Low-temperature (Low-T) FTIR difference spectra were recorded with the settings summarized in Table 1. Several μL of a concentrated protein sample were placed between two BaF_2 windows separated by a 9 μm spacer. The sample was cooled to the desired temperature using a cryostat (TMHS600, Linkam Scientific Instruments, Salfords, UK). Several scans were recorded on dark-state *Ns*XeR before a 530 nm LED was used to drive the protein to a photostationary state where several scans were recorded under otherwise identical conditions. Difference spectra were manually baseline corrected by subtracting a polynomial spline with the Opus software (Bruker Optics, Ettlingen, Germany).

2.3 QCL-based IR Spectroscopy

Scanning-type time-resolved IR spectroscopy was conducted with a homebuilt setup using EC-QCLs, as essentially described in chapter 1.3.2 and refs.[47, 61]. Commercially available QCLs (MIRcat-1100-U3 and TLS41058, Daylight solutions, San Diego, USA) were used as measuring light sources. The transmitted light is detected by a mercury cadmium telluride (MCT) detector (KV104-0.5-A3/11, Kolmar Tech, Newburyport, USA) and the signal is digitized by two oscilloscopes (Picoscope 4227, Picoscope Technology, ST Neots, UK) at different sampling rates (250 MS/s and usually 1 MS/s). The linearly spaced datapoints are logarithmically averaged to 60 (20 for chapter 3.3.2 and 3.3.3) datapoints per decade and the fast and slow time traces are merged. All datasets recorded by the EC-QCL setup (except for data presented in 3.3.4) were spectrally smoothed using a Savitzky-Golay algorithm with a second-order polynomial. Unless indicated differently, two (2 cm^{-1} spacing, chapters 3.1 and 3.2) or five (1 cm^{-1} spacing, chapters 3.1.4 and 3.3) adjacent datapoints were averaged. All post-processing steps described here were performed using routines written by Pit Langner (Labview, National Instruments, Austin, USA). Light excitation of the sample is achieved by laser pulse ($\Delta t = 10$ ns, $\lambda = 532$ nm, $E_{exc}/A = 3$ mJ/cm^2) generated by a Nd:YAG laser (Minilite II, Continuum).

Dual-comb spectroscopy was carried out with a commercially available dual-comb spectrometer (IRis-F1, IRsweep, Switzerland) as described elsewhere.[57, 72] The output power of the QCLs is in the order of hundreds of mW, resulting in ~1 mW per comb tooth, which is reduced before detection by polarizers to avoid detector non-linearities. For detection, two high-bandwidth MCT detectors (PV-3TE-10.6, Vigo Systems) are used. While the sample MCT (MCT$_S$) measures the response of the sample, the reference MCT (MCT$_R$) is used to correct for intensity fluctuations of the QCLs. Digitization is achieved using an analog to digital converter (ADC) with 650 MHz analog bandwidth, 1.6 GS/s sampling rate and 12 bit resolution. A digital low pass filter (900 MHz) is used to filter out high frequency noise. Sample excitation is achieved using a Nd:YAG laser (Minilite II, Continuum or Quanta-Ray, Spectra Physics).

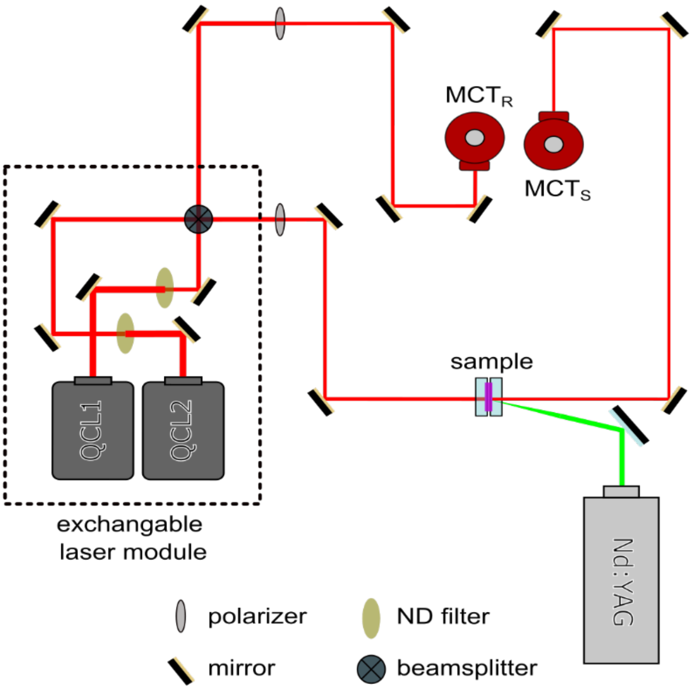

Figure 2-1: Optical layout of the commercially available IRis-F1 spectrometer by IRsweep in the amplitude sensitive configuration. The exchangeable laser module (dashed lines), where the two QCL frequency combs are positioned are pre-aligned and can be easily exchanged by the user. Two build in neutral density filter (ND filter) are used to attenuate the strong emission of the QCLs. The emission of the two QCLs is combined at a 50:50 CaF_2 beamsplitter. One part of the combined beam is focused on the reference MCT (MCT_R) while the other one is directed through the sample and focused on the sample MCT (MCT_S). A polarizer for each of the two beams is used to regulate the light intensity. In our experiments a Nd:YAG laser is used for sample excitation.

2.4 Resonance Raman Spectroscopy

Resonance Raman (RR) spectra were recorded as essentially described in ref.[73] using a LABRAM Raman microscope (JobinYvon, Bensheim, Germany). Raman scattering was probed using a 647 nm laser (diode-pumped solid-state from CrystaLaser, Reno, USA). Several µL of a highly concentrated protein sample were placed on a Quartz crucible and subsequently cooled to ~80 K using a cryostat (TMHS600, Linkam Scientific Instruments, Salfords, UK). Spectra were averaged on the same spot for several minutes until a sufficient SNR was reached. To drive the protein into a photostationary state, the sample was illuminated with a 530 nm LED before the RR spectrum was taken on the same spot where the dark-state spectrum was taken. This procedure justifies the calculation of a RR difference spectrum (Figure 3-9 D). RR spectra were manually baseline corrected by subtracting a polynomial spline using the OPUS software (Bruker Optics, Ettlingen, Germany).

2.5 Sample Preparation

Xenorhodopsin samples

The artificially synthesized xenorhodopsin gene (J07AB43_12860) from *Nanosalina* sp. was constructed into the pET27b vector via *Nde*I/*Hind*III sites, with a C-terminal His-tag (-ASH$_{10}$), which is referred to as wild-type *Ns*XeR. *Ns*XeR was expressed and purified based on the protocol published in ref.[39], but with slight modifications: *Ns*XeR was expressed in the *Escherichia coli* (*E. coli*) strain C41 (DE3) in BHI medium. Induction was achieved by the addition of 1 mM IPTG at OD$_{600}$ = 0.8-1.0 in the presence of 12.5 µM all-*trans* retinal. After harvesting, the cells were disrupted at 1.75 kbar in a cell disruptor (Constant Systems, Daventry, UK) in a buffer containing 50 mM Na_2HPO_4/NaH_2PO_4, 100 mM NaCl at pH 8.0. Subsequently, the lysate was centrifuged for 1 hour at 186,000g at 4°C. The membrane fraction was solubilized by the addition of 2 % n-dodecyl-β-maltoside (DDM) and *Ns*XeR was purified via affinity chromatography on a Ni-NTA column. The imidazole concentration was increased up to 100 mM for washing and elution was finally performed at 250 mM imidazole (50 mM Na_2HPO_4/NaH_2PO_4, 100 mM NaCl, 250 mM imidazole, pH 7.4, 0.1% DDM). Directly after elution, imidazole was removed by several washing steps in an Amicon filter (30 kDa MWCO) with imidazole free buffer (50 mM Na_2HPO_4/NaH_2PO_4, 100 mM NaCl, pH 7.4, 0.1% DDM). After the establishment of the protocol, protein expression and purification were performed by Kirsten Hoffmann (Genetic Biophysics, Department of Physics). All variants studied in this thesis, were expressed and purified by Jheng-Liang Chen (Genetic Biophysics, Department of Physics) with help by Kirsten Hoffmann.

Reconstitution into nanodiscs was performed by Jheng-Liang Chen following a standard protocol.[74] Briefly, purified *Ns*XeR was incubated with the scaffold protein MSP1D1 and DMPC (1,2-dimyristoyl-sn-glycero-3-phosphocholine) or (^{13}C) DPPC (1,2-dipalmitoyl-sn-glycero-3-phosphocholine) lipids (Avanti) at a molar ratio of 1:2:110, at 25ºC for 1h. Detergent was removed by adding SM-2 biobeads 1:1 (v/w). Subsequently the reconstituted proteo-nanodiscs were purified by gel filtration (Superdex 200 10/300 GL, buffer: 50 mM Na_2HPO_4/NaH_2PO_4, 100 mM NaCl at pH 7.4).

For UV/vis experiments nanodisc-reconstituted *Ns*XeR was diluted in a solution containing 50 mM $Na_2PO_4/NaHPO_4$ buffer and 100 mM NaCl at pH 7.4 to obtain an optical density of ~0.5 at 565 nm. Exchange to deuterated buffer was achieved by repetitive washing steps in an Amicon filter (30 kDa MWCO). The pD of the buffer was adjusted to 7.4 by measuring an apparent pH of 7 with a pH electrode, which has been calibrated using H_2O-based solutions.[75] 0.05 % DDM were added to the buffer solutions used for experiments conducted on detergent-solubilized samples. For pH-indicator experiments, the samples were washed multiple times with degassed 150 mM KCl solution in an Amicon filter and flowed with argon gas to remove any buffering compounds. Transient absorbance changes at 450 nm (pH 7) and 480 nm (pH 9) were recorded before and after supplementing the protein solution with 50 µM 6,8-dihydroxy-1,3-pyrenedisulfonic acid (DHPDS). The SNR was increased by averaging 50-100 single transients and the signal of the pH indicator was extracted by subtracting the protein signal from the protein+DHPDS signal. Great care was taken that the pH remains constant during the experiment. Preparation of the sample at pH 9 was carried out in an anaerobic tent to minimize contamination with CO_2.

For IR and RR experiments on *Ns*XeR, the buffer was exchanged to a low ionic strength buffer and the protein solution was concentrated in an Amicon filter. Several µL of protein solution were gently dried onto a BaF_2 window under a stream of dried air and subsequently rehydrated via the vapor phase by adding ~5 µL of an H_2O/Glycerol mixture next to the protein film. A second BaF_2 window, distanced by 500 µm thick spacer sealed the sample chamber. By choosing different H_2O/Glycerol mixtures, the water content in the sample can be controlled.[22] If not differently stated in the text, a buffer containing 5 mM Na_2PO_4/$NaHPO_4$,10 mM NaCl at pH 7.4 was used for *Ns*XeR and sufficient rehydration was achieved by using a H_2O/Glycerol mixture with a glycerol weight percentage of 20 %. To check, if this procedure provides sufficient rehydration and a stable pH, photocycle kinetics of IR samples were compared to UV/vis flash photolysis kinetics obtained in solution (Figure A. 2). In case of detergent-solubilized samples, the sample was washed multiple times in an Amicon filter with detergent-free buffer to reduce the content of detergent. Unless differently specified, all experiments were carried out at room temperature (20-23°C).

Others

Bacteriorhodopsin samples have been prepared from *Halobacterium salinarum* strain S9 as described in ref.[76] and were kindly provided by Kirsten Hoffmann, Dorothea Heinrich and Ramona Schlesinger (Genetic Biophysics, FU Berlin). For all measurements on *Hs*BR presented in chapter 3.3, purple membrane patches containing *Hs*BR were dispersed in a low ionic strength buffer containing 2 mM HEPES, 2mM NaCl at pH 7.4. The protein films were prepared in the same way as the xenorhodopsin samples.

Rhodopsin (rod outer segments, ROS) samples were essentially prepared as described in ref.[77] by Franz Bartl and coworkers (Humboldt Universität zu Berlin). ROS were dispersed in a buffer containing 20 mM 1,3-bis(tris(hydroxymethyl)methylamino)propane (BTP), 130 mM NaCl and 5 mM $MgCl_2$ in 100 % H_2O. For exchanging to D_2O, samples were repetitively washed with the same buffer prepared in D_2O. All time-resolved experiments were conducted at room temperature (T = 20-23°C) at pH/pD ~ 6. For trapping the Meta-I intermediate, ROS were dispersed in the aforementioned buffer at pD 9 and the experiment was conducted at T = 5°C.

Sensory rhodopsin II from *Natromonas pharaonis* (*Np*SRII) was expressed and purified as described in ref.[74] by Mariafrancesca La Greca (Genetic Biophysics, FU Berlin). *Np*SRII has been reconstituted in Nanodiscs consisting of DMPC lipids and MSP1DE3 scaffold protein and solubilized in 5 mM 2-(N-Morpholino)ethansulfonsäure (MES) buffer containing 40 mM NaCl at pH 6.

3 Results

3.1 Inward Proton Transfer Mechanism in NsXeR

Large parts of this chapter are published in:

Schubert, L., Chen, J.L., Fritz, T., Marxer, F., Langner, P., Hoffmann, K., Gamiz-Hernandez, A., Kaila, V.R.I., Schlesinger, R., Heberle, J. Proton Release Reactions in the Inward H+ Pump Xenorhodopsin, J. Phys. Chem. B ***2023****, 127, 8358-8369.*

Some of the figures presented in this chapter have been adapted with permission from the aforementioned reference. Copyright 2023 American Chemical Society.

This project was carried out in close collaboration with Jheng-Liang Chen from the Genetic Biophysics group at the Department of Physics. Expression, purification, and reconstitution of *Ns*XeR as well as mutagenesis were accomplished by Jheng-Liang Chen with helpful contributions from Kirsten Hoffmann. Most spectroscopic experiments and data analysis were performed by me. Jheng-Liang Chen conducted UV/vis flash photolysis experiments on selected mutants as well as functional assays. Florina Marxer performed the pH indicator experiments under my supervision. Data, which was not recorded by myself is labeled in the respective figure captions. MD simulations were carried out by Tobias Fritz, Ana Gamiz-Hernandez and Ville Kaila.

Despite the insights gained from structural studies as well as UV/vis spectroscopy and electrophysiological experiments (see 1.1.2), a thorough spectroscopic investigation is required to gain detailed insights on inward proton transfer at the molecular level. With UV/vis spectroscopy, the kinetics of protonation reactions at or near the retinal chromophore as well as proton transfer to and from the bulk solution can be studied (chapter 3.1.1). Time-resolved QCL-based IR spectroscopy in combination with site-directed mutagenesis is used to identify key residues involved in proton transfer with a focus on the cytoplasmic half channel (chapter 3.1.2). The broad spectral coverage of conventional FTIR spectroscopy is used to gain information on configurational changes associated with the retinal chromophore to evaluate the relevance of changes in isomerization state on vectorial proton transfer (chapter 3.1.3). Further, a cysteine residue, located in close vicinity to the retinal chromophore is studied (chapter 3.1.4). In chapter 3.2, the effect of different membrane environments on the photocycle of *Ns*XeR is evaluated.

3.1.1 Photocycle and Proton Release and Uptake

The photocycle of *Ns*XeR has been studied by means of time-resolved UV/vis spectroscopy by Shevchenko et al.[39] and Weissbecker et al.[40] Both studies proposed photocycles that were largely in agreement, but Weissbecker et al. observed a long-lived intermediate with absorption characteristics close to the ground-state absorption of *Ns*XeR, which has not been observed by Shevchenko et al. Given that the study by Shevchenko et al. was performed in a lipidic environment (nanodiscs and proteoliposomes) and the study by Weissbecker et al. in detergent-solubilized protein, the photocycle was investigated in both preparations in this thesis, which will be discussed in detail in chapter 3.2. Here, in nanodisc-reconstituted *Ns*XeR, the photocycle of *Ns*XeR comprises K, L, M and the aforementioned long-lived intermediate (Figure 3-1), which was not observed before in a lipidic membrane environment.[39] The existence of two spectrally distinct M intermediates (MI and MII), with different RSB accessibilities is considered to be of fundamental importance for vectorial proton transfer.[40] As for most microbial rhodopsins, the strongly blue-shifted absorbance maxima of the M intermediates around 400 nm are indicative of a deprotonated RSB.[9] Therefore, the rise of the MI and the decay of the MII state mark two crucial proton transfer steps occurring with time constants of 159 µs and 40 ms, respectively.

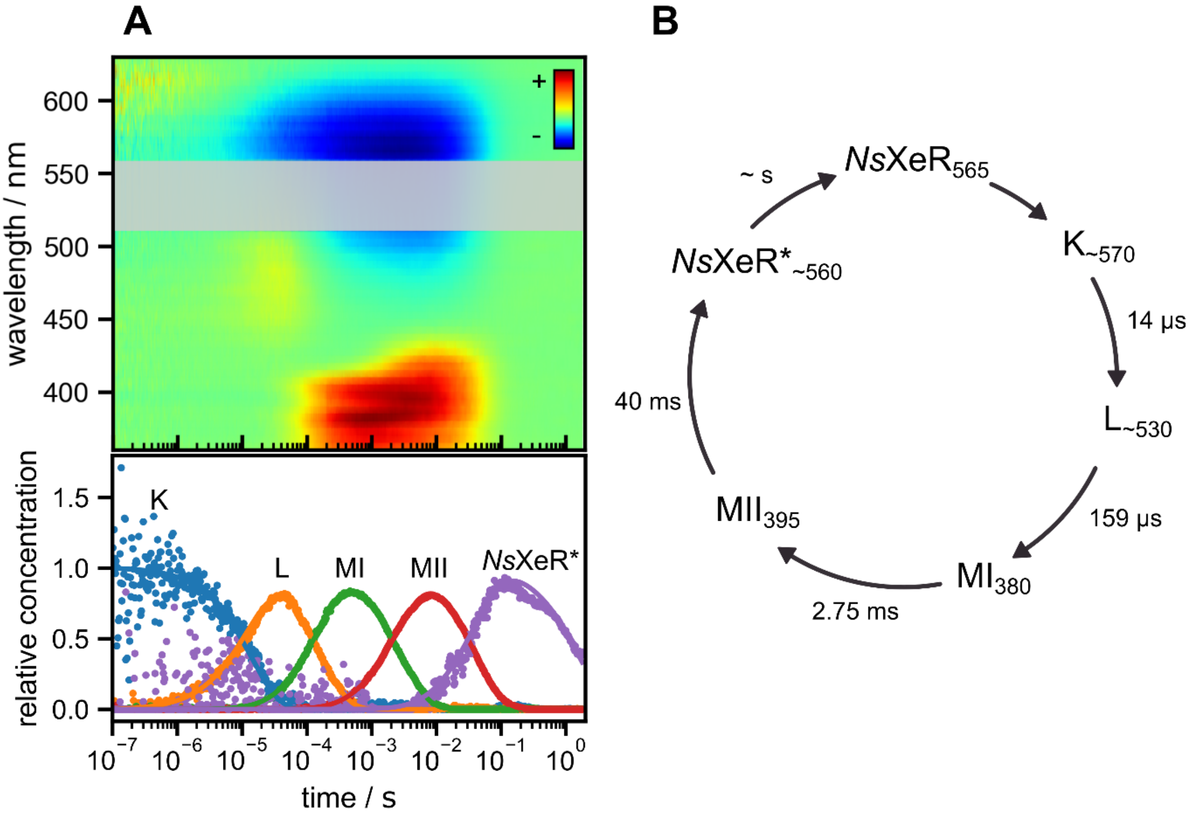

Figure 3-1: Photoreaction of *Ns*XeR studied by time-resolved UV/vis spectroscopy. A) Heatmap (top) and concentration profile of intermediates (bottom) as obtained from global analysis. The grey box indicates the wavelength range which was omitted due to scattering of the strong excitation pulse. B) Photocycle model derived from our data, in accordance with previously published data. [39, 40] Numbers in the subscript indicate absorbance maxima of the intermediates, derived from global analysis. Note that the absorbance maxima of L and *Ns*XeR* are only rough estimates, as the spectral range between 510 and 560 nm was omitted.

To further investigate the nature of these protonation steps, the photocycle kinetics in H_2O and D_2O were compared (Figure 3-2 A). By exchanging dissociable protons for deuterons, proton transfer reactions are slowed down, which is known as the kinetic isotope effect (KIE). The strength of the KIE may be more or less pronounced depending on whether the proton transfer itself is the rate-limiting step of the reaction or not.[78] Until ~50 µs, the traces at 480 and 565 nm monitoring L-state formation and *Ns*XeR dark-state depletion, respectively, superimpose. The observation that the K to L transition is not affected by H/D exchange indicates that most likely no protonation steps around the RSB occur during this transition. On the contrary, MI state formation (380 nm) as well as MII state decay (410 nm) are slowed down in D_2O. Global analysis of both datasets reveals relatively strong KIEs of 4.2 for MI rise and 3.6 for MII decay (Table A. 3). In this context, the high KIEs can be interpreted as a rate-limiting proton transfer step between the RSB and a direct proton acceptor/donor or as a multi-step protonation reaction. In *Hs*BR, a high KIE was observed for the deprotonation of the RSB, but not for the reprotonation.[78]

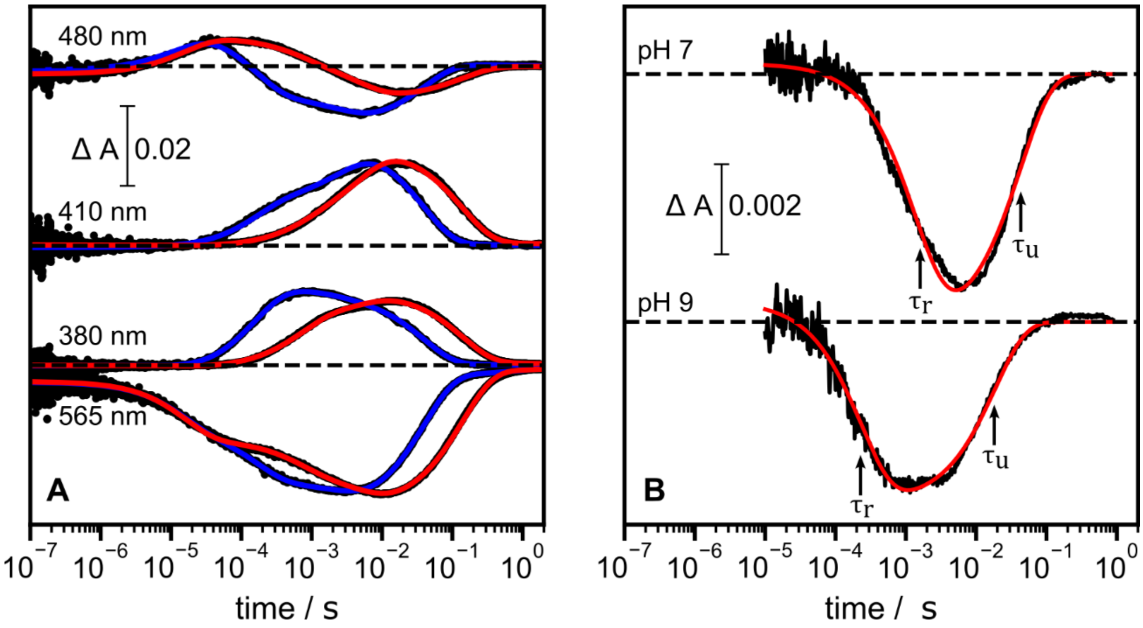

Figure 3-2: Kinetic isotope effect and proton transfer to the bulk. A) Kinetics recorded by UV/vis flash photolysis in H_2O (blue) and D_2O (red) at pH 7.4 and pD 7.4 in nanodisc-reconstituted *Ns*XeR. Raw data is shown as black dots while the colored traces represent the fits obtained from global analysis. For better kinetic comparison, the H_2O transients are scaled to match the intensity of the D_2O transients. B) Proton transfer between the protein and bulk solution monitored by the pH-sensitive dye DHPDS (black) with the fit to the sum of two exponentials (red). The pH indicator experiments were conducted on detergent solubilized (DDM) *Ns*XeR at pH 7 (top) and pH 9 (bottom). Arrows indicate the time constants for proton release (τ_r) and uptake (τ_u). The data shown in B) was recorded by Florina Marxer under my supervision. Figure adapted from ref.[79].

Proton transfer between the protein and the bulk solution can be traced by monitoring transient pH changes using a pH-sensitive dye, 6,8-dihydroxy-1,3-pyrenedisulfonic acid (DHPDS).[80] In detergent-solubilized *Ns*XeR the absorbance changes of DHPDS show transient acidification of the bulk solution. Proton release occurs with a time constant of τ_r = 1.45 ms and proton uptake with a time constant of τ_u = 43.6 ms at pH 7 (Figure 3-2 B). Proton release takes place one order of magnitude slower as compared to MI state formation (i.e. RSB deprotonation, $\tau_{L \rightarrow MI}$ = 159 µs), while proton uptake coincides with MII decay (i.e. RSB reprotonation, $\tau_{MII \rightarrow NsXeR^*}$ = 39.7 ms) (cf. Table A. 1). The delay of proton release as compared to RSB deprotonation may be explained by intermediate protonation steps and/or the dwell time of the proton at the micelle surface.[81, 82] During MII decay, direct bulk to RSB proton transfer is unlikely given the fact, that RSB reprotonation is accelerated at high pH in *Ns*XeR.[40] At pH 9, proton release and uptake are accelerated (τ_r = 237 µs and τ_u = 19 ms), too. While accelerated proton release may be explained by a base-catalyzed surface to bulk proton transfer or an accelerated internal protonation step, it is interesting to note that the accelerated proton uptake at pH 9 still coincides with RSB reprotonation at high pH[40]. Therefore, it cannot be excluded that the RSB is directly reprotonated from the bulk, but with a rate-limiting step that is accelerated at high pH. In conclusion, the kinetics of proton transfer involving the RSB as well as proton transfer between bulk solution and the protein differ from those of *Hs*BR. Time-resolved UV/vis spectroscopy provides first insights into the proton transfer mechanism and indicates strongly that internal protonation steps occur on the cytoplasmic proton release pathway, which will be investigated by time-resolved IR spectroscopy.

3.1.2 Cytoplasmic Proton Pathway

To deduce protonation steps between protonatable groups inside the protein, time-resolved IR spectroscopy in combination with site-directed mutagenesis is employed. In this respect, the spectral range between 1690 and 1800 cm^{-1} is of particular interest, as bands caused by the ν(C=O) mode of protonated carboxylic acids appear in this spectral range. In a difference experiment, positive bands are interpreted as a protonation while negative bands show a deprotonation of an aspartic or glutamic acid. Changes in hydrogen bonding result in differential band shapes (cf. chapter 1.5). In some cases, overlapping bands stemming from different carboxylic groups or lipid esters may complicate the interpretation.[22]

Based on the crystal structure of *Ns*XeR, the D220/H48 pair was suggested to act as the proton acceptor of the RSB proton.[39] UV/vis spectroscopy on the D220E and D220N variants supports the involvement of D220 on the cytoplasmic proton pathway[40], but a detailed description of the changes in protonation states of D220 is still lacking. The time-resolved difference spectra of wild-type *Ns*XeR and the D220E variant show multiple bands in the frequency range above 1690 cm^{-1} (Figure 3-3 A), where most of them are not affected by the D220E mutation. However, upon site-specific exchange of D220 by E, the prominent negative band located at 1711 cm^{-1}, which has the largest amplitude during the lifetime of MI, shifts towards 1732 cm^{-1}. Therefore, this negative band can univocally be assigned to protonated D220 in the dark state of *Ns*XeR, which gets deprotonated upon light activation. Its relatively low frequency is generally indicative of a strongly hydrogen-bonded environment.[22] Judged by the crystal structure, two possible candidates for hydrogen bonding are H48 and T91 (Figure 3-3 B). The elevated pK_a of D220 in dark-state *Ns*XeR might be explained by the interaction with H48[79] as well as a relatively unpolar surrounding (Figure 3-3 B). The upshift of the band in the D220E variant is indicative of weaker hydrogen-bonded environment of the carboxylic side chain. In the D220E variant and in wild-type *Ns*XeR the negative band associated with D220 deprotonation is already present during the lifetime of the L intermediate, which raises questions about the exact timing of D220 deprotonation.

To determine the precise timings of proton transfer involving D220, the dataset shown in Figure 3-3 A was subjected to global analysis. The species-associated difference spectra (Figure 3-4 A), reveal that the negative band centered at 1713 cm^{-1} during the lifetime of L has a shoulder located at 1703 cm^{-1}. This band appears to be negative, which is most likely caused by a baseline shift due to photothermally heated water by the excitation laser pulse[83] and can therefore actually be interpreted as a positive side band. Instead, in the spectrum representative for the MI intermediate, the band around 1711 cm^{-1} is purely negative. This indicates, that D220 undergoes a change in hydrogen bonding in L prior to its deprotonation in MI. The transients of the bands at 1709 and 1703 cm^{-1} were corrected for the heat contribution by subtracting an averaged transient above 1780 cm^{-1}, where no protein signals contribute (cf. Figure 3-4 A, broad negative signal above 1780 cm^{-1} during the L intermediate). Details of the correction procedure are shown in Figure A. 3 and Figure A. 4. The corrected transient at 1703 cm^{-1} follows the transient obtained at 480 nm by UV/vis spectroscopy, which is representative for the L intermediate (Figure 3-4 B). An exponential fit yields a time constant of $\tau_1 = 13$ µs for the rise of this side band, which is in good agreement with the time constant for the K→L transition obtained from global analysis of UV/vis data (cf. Table A. 3).

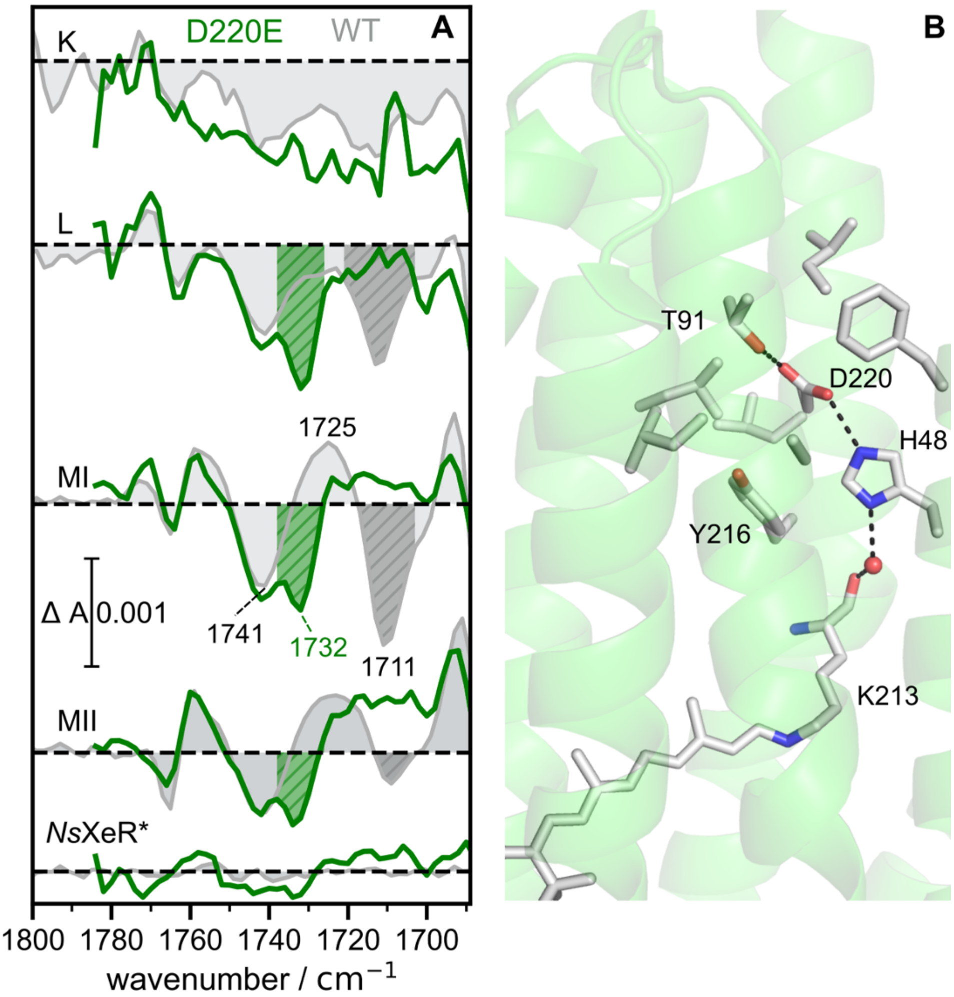

Figure 3-3: Elucidation of the role of D220 in the cytoplasmic proton pathway. A) IR difference spectra obtained by time-resolved IR flash photolysis. Grey spectra correspond to wild-type *Ns*XeR and green spectra to the D220E variant. The spectra of the variant were multiplied by a factor of 3 for better comparison. Hatched areas indicate those bands which are affected by the amino acid substitution. The spectra were extracted at time points, where the respective intermediates are predominantly accumulated as deduced from global analysis. B) Environment of D220 in *Ns*XeR. Possible hydrogen bond partners are shown as dotted black lines. Polar residues in the vicinity are labeled, several unpolar (F, L, I, A) residues in the environment of D220 are shown as unlabeled sticks [PDB: 6EYU]. Panel A adapted from ref.[79].

Likewise, the corrected band at 1709 cm^{-1} (Figure 3-4 C) is compared to the UV/vis transient recorded at 380 nm, indicative of the deprotonation of the RSB. An exponential fit yields three time constants with τ_1 = 16 μs, τ_2 = 125 μs and τ_3 = 6 ms, where the amplitude of τ_2 is about six times larger than the amplitude of τ_1 (cf. Table A. 2), which underlines that the major change (=deprotonation) is associated with the formation of MI. Taken together, the spectro-temporal changes associated with the band centered around 1711 cm^{-1}, assigned to D220, draw the following picture: D220 is protonated in dark-state *Ns*XeR and undergoes a change in hydrogen bonding with τ_1 $(\mathrm{K}\rightarrow\mathrm{L})$. D220 deprotonates with τ_2 $(\mathrm{L}\rightarrow\mathrm{MI})$, while its reprotonation takes place during the transition from MI to MII (τ_3).

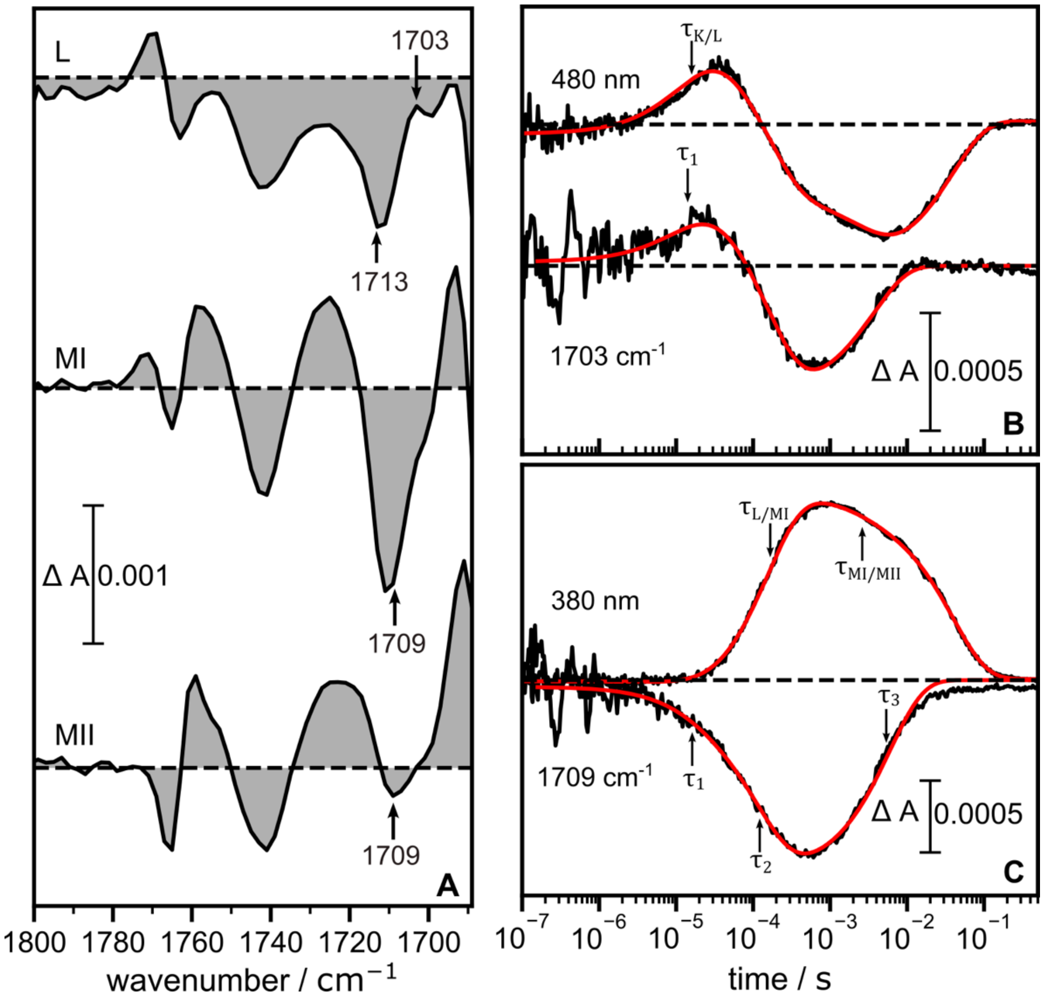

Figure 3-4: Spectro-temporal analysis of the signals associated with D220 deprotonation. A) Species-associated difference spectra derived from global analysis. B) Transient absorbance changes at 1703 cm^{-1} in comparison to the formation and decay of the L intermediate monitored at 480 nm by time-resolved UV/vis spectroscopy. C) Transient absorbance changes at 1709 cm^{-1} in comparison to the formation and decay of the MI intermediate recorded at 380 nm. The IR transients have been corrected for a heating response, as explained in detail in (Figure A. 4). Black traces in panels B) and C) represent data, while exponential fits are shown in red. Fits of UV/vis transients stem from global analysis (Figure 3-1) while the corrected IR transients were fitted to a sum of three exponentials. For comparison, UV/vis transients were scaled to match the signal size of the IR transients. Figure adapted from ref.[79].

Besides the negative band located around 1711 cm^{-1}, assigned to the deprotonation of D220, multiple other difference bands are present in the difference spectra of wild-type *Ns*XeR. The sigmoidal band at 1741 (-) and 1725 (+) cm^{-1} during the lifetime of MI (Figure 3-3) is associated with the lipidic ester vibration of the nanodiscs and will be discussed in chapter 3.2. Another differential-shaped feature located at 1763 (-) and 1771 (+) cm^{-1} during the lifetime of L undergoes a shift in frequency to 1765 (-) and 1759 (+) cm^{-1} when the M states are formed (Figure 3-5 A). Upon conservative replacement of E111 by Q, this feature downshifts to 1703 (+) and 1695 (-) cm^{-1} during the lifetime of L, as expected for a replacement of a terminal carboxyl group to a terminal carboxamide.[43] Therefore this band is unequivocally assigned to a change in hydrogen bonding of protonated E111. Upon formation of L, the carboxyl group of E111 experiences a weaker hydrogen bonding as compared to dark-state *Ns*XeR. A similar environmental change of the carboxamide is observed in the E111Q variant. The differential feature above 1765 (-) and 1759 cm^{-1} (+) during the lifetime of MI and MII are mostly absent in the spectra of the E111Q variant. Therefore, it is concluded that during the transition to the MII intermediate, E111 adopts an environment with stronger hydrogen bonding as compared to dark-state *Ns*XeR. However, the bands around 1700 cm^{-1} in the E111Q variant during MI and MII are overlapped by other strong bands and therefore not clearly discernible. A small positive band located at around 1759 cm^{-1} is still present in the E111Q variant in MI, which is most likely caused by a different residue. Based on the crystal structure, a possible hydrogen bonding partner of E111 is T81 (Figure 3-5 B). It can be concluded that E111 senses structural alterations of the protein during the L and M intermediates but does not change its protonation state. This is corroborated by the fact that the photocycle kinetics of the E111Q variant are only slightly altered (Figure 3-5 C). The homologous residue in *Hs*BR, D115, experiences a similar environmental change and was hypothesized to be responsible for sensing the transmembrane pH gradient.[84]

Since D220 gets deprotonated upon formation of MI (RSB deprotonation) and receives a proton during the MI to MII transition, another intermediate proton binding site on the cytoplasmic side needs to be discussed, which cannot be E111 as it stays protonated throughout the photocycle. A possible candidate is Y216, whose corresponding residue in *Hs*BR is F219. The Y216F variant displays strongly altered photocycle kinetics. The M state formation is slowed down by an order of magnitude and only one spectrally distinguishable M intermediate is observed (Figure 3-6 A, B). However, the Y216F variant retains its function being an inward proton pump.[79] Difference spectra of the Y216F variant in the carboxylic range resemble those of wild-type *Ns*XeR. The position of the band assigned to protonated D220, located at around 1711 cm^{-1}, is unaffected by the Y216F replacement, indicating that the direct environment of D220 in dark-state *Ns*XeR remains unchanged. The pK_a of Y216 was estimated to be >26 and therefore it is unlikely that Y216 itself acts as a counter ion to the RSB and accepts its proton.[79] The role of Y216 for the inwardly directed proton pathway in *Ns*XeR will be discussed in chapter 4.1.

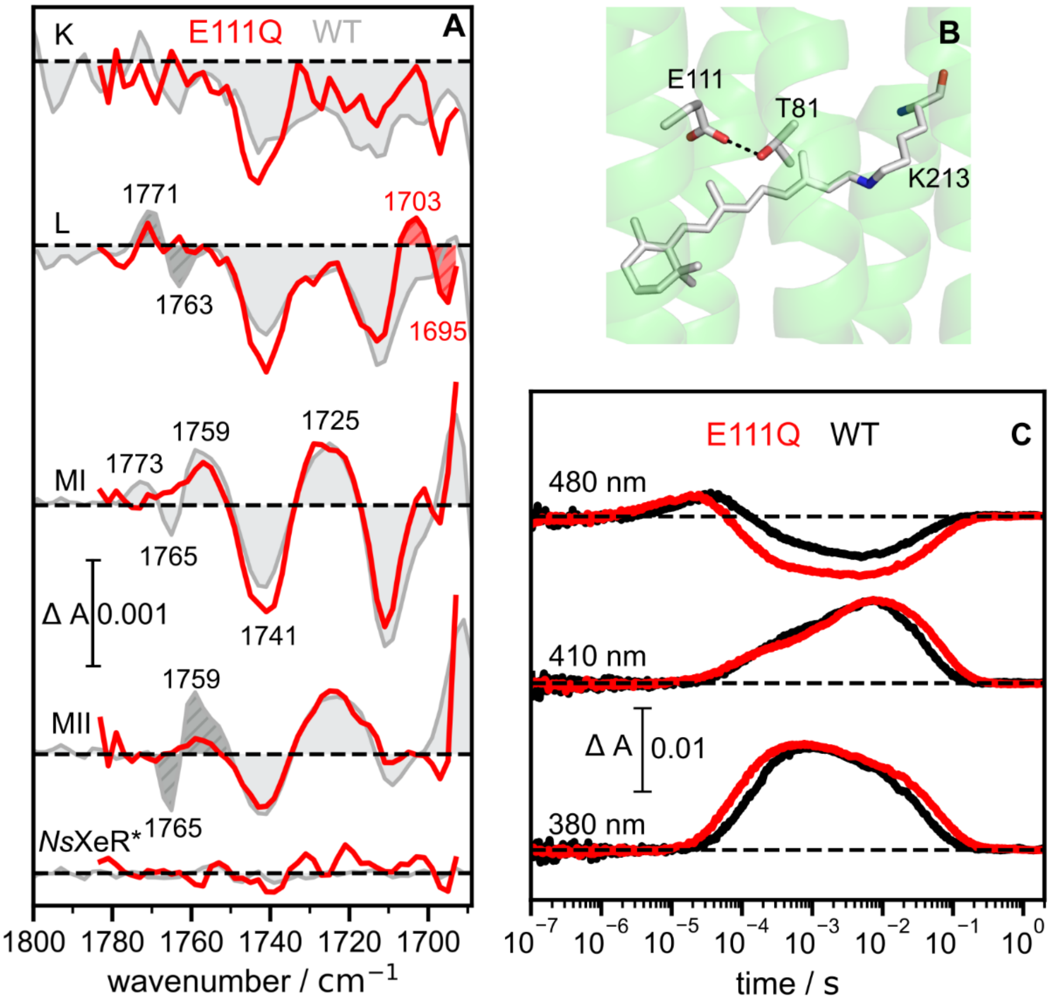

Figure 3-5: Role of E111 in the cytoplasmic proton transfer path. A) IR difference spectra obtained by time-resolved IR flash photolysis. Grey spectra correspond to wild-type *Ns*XeR and red spectra to the E111Q variant. The spectra of the variant were multiplied by a factor of 2 for better comparison. Hatched areas indicate those bands which are affected by the amino acid substitution. The spectra were extracted at time points, where the respective intermediates are predominantly accumulated, as deduced from global analysis. B) Environment of E111 in *Ns*XeR. A possible hydrogen bond to T81 is indicated by a black dotted line. [PDB: 6EYU]. C) Influence of the E111Q mutation on the photocycle kinetics. The variant data shown in C) were recorded by Jheng-Liang Chen and scaled to match the intensity of the wild-type data. Panel A adapted from ref.[79].

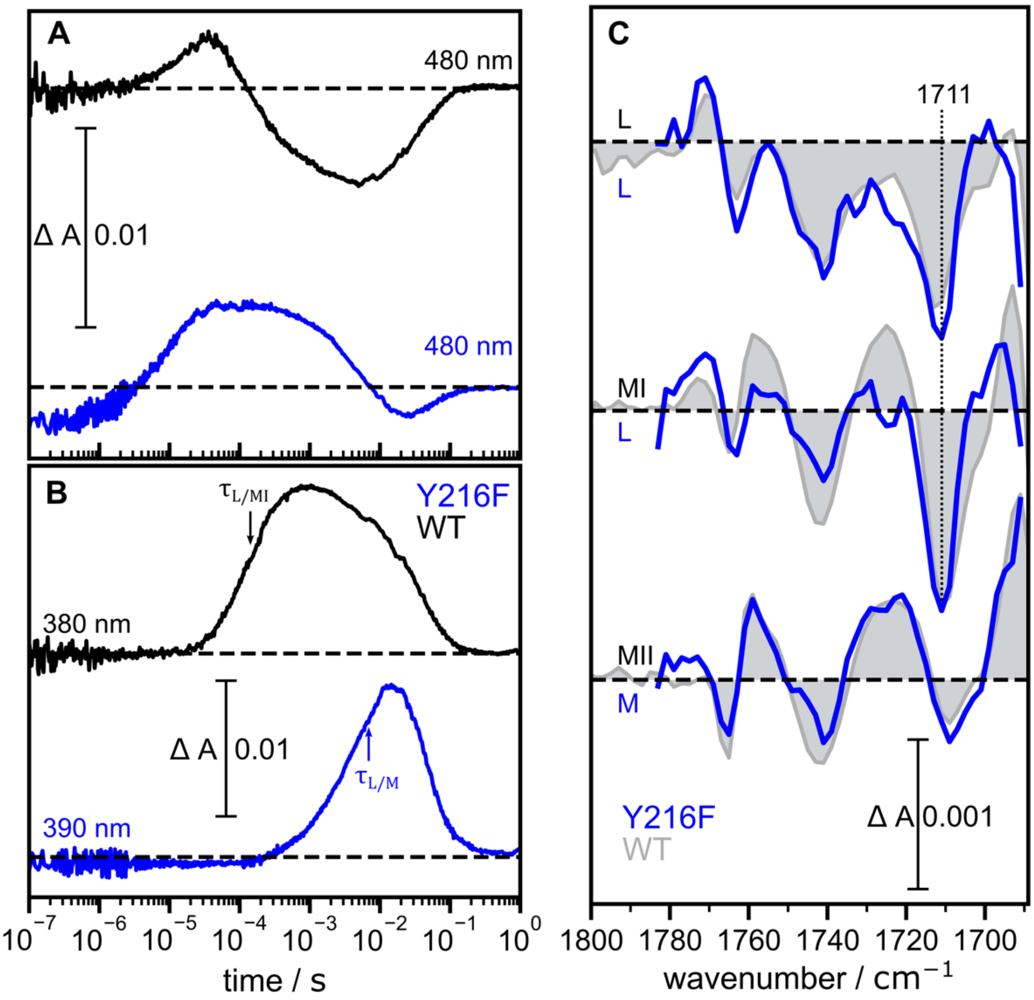

Figure 3-6: Effect of Y216F substitution on the photocycle. A) Transients recorded by time-resolved UV/vis spectroscopy at 480 nm, representative of the L intermediate. B) Transients recorded at 380 and 390 nm, indicative for the MI (wild type) and M (Y216F) intermediates, respectively. C) IR difference spectra of the Y216F variant in comparison to wild-type *Ns*XeR spectra, extracted at times, where the respective intermediates are predominantly accumulated. The spectra of the variant were multiplied by a factor of 2 for better comparison. Wild-type data is shown in black (grey) and Y216F data is shown in blue. The variant data shown in A, B were recorded by Jheng-Liang Chen and were scaled to match the intensity of the wild-type data. Figure adapted from ref.[79].

To evaluate if protein conformational changes are involved in the proton transfer mechanism of *Ns*XeR, QCL-based IR spectroscopy was performed in the spectral range between 1524 and 1690 cm^{-1}, where a large variety of vibrational bands appear (Figure 3-7). A strong negative band located at 1526 cm^{-1} can be assigned to the ν(C=C) vibration of all-*trans* retinal in dark-state *Ns*XeR, as its frequency matches the empirical correlation between the vis absorption maximum and ν(C=C) frequencies.[67] Another negative band located at 1556 cm^{-1} shows a distinct kinetic trace (Figure 3-7 B) and may be tentatively assigned to an amide II mode in the transmembrane region (cf. chapter 3.1.3). A positive band located at 1538 cm^{-1} during the lifetime of K, which is most likely caused by a retinal mode, will be discussed in chapter 3.1.3.

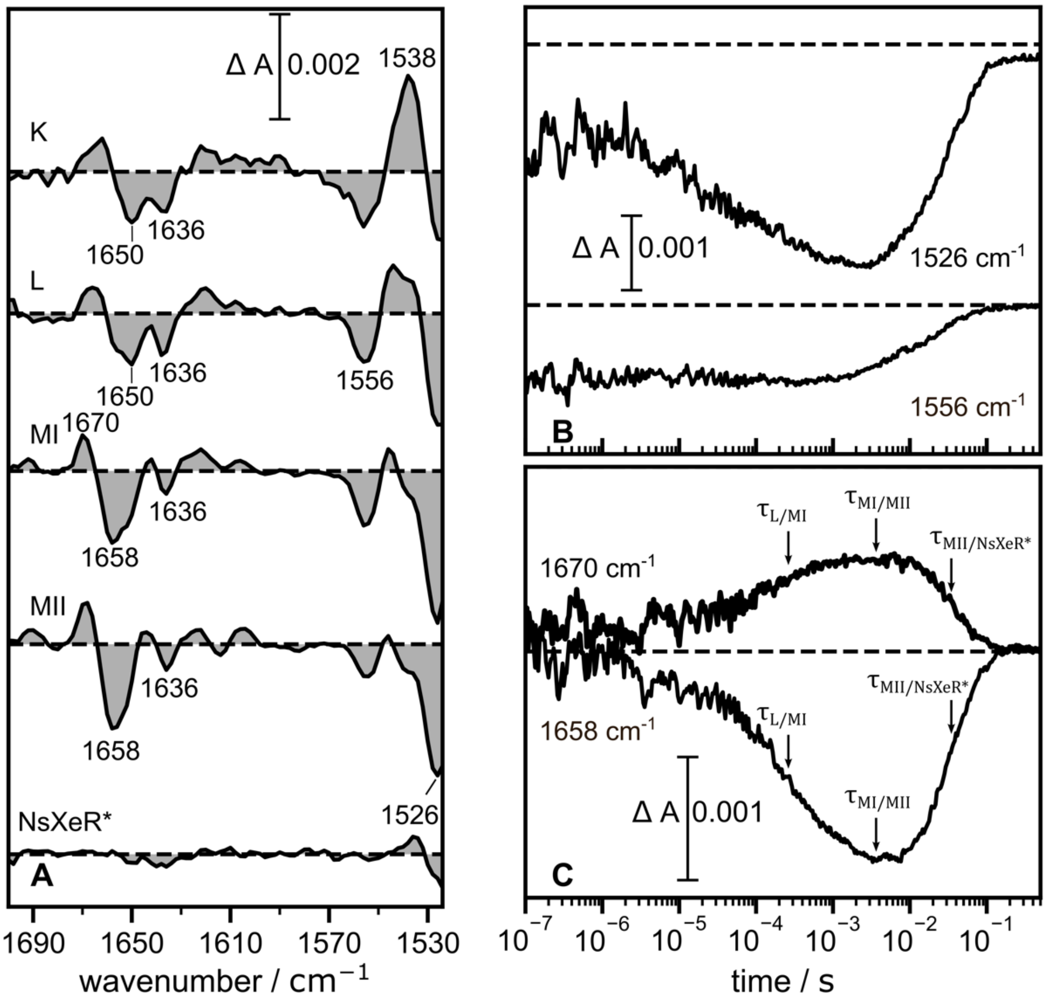

Figure 3-7: IR flash photolysis on wild-type *Ns*XeR in the frequency range between 1524 and 1700 cm^{-1}. A) IR difference spectra of *Ns*XeR intermediates. Spectra are extracted at times, where the intermediates are predominantly accumulated. The *Ns*XeR* spectrum is enlarged by a factor of 2. Most prominent bands are labeled. B) Transients of the bands at 1526 and 1556 cm^{-1}. C) Transients of the bands at 1658 and 1670 cm^{-1}. Figure adapted from ref.[79].

Bands located at 1650 (-), 1658 (-) and 1670 (+) cm^{-1} can most likely be assigned to changes of the amide I mode of the protein backbone upon structural changes of the protein. While the band at 1650 cm^{-1} is already present during the K and L intermediates, the bands at 1658 and 1670 cm^{-1} appear with the formation of MI and increase in intensity towards formation of MII. Both bands return to 0 with the decay of MII (Figure 3-7 C). As IR spectroscopy does not provide spatial information on protein structural changes, the interpretation of the relevance of the amide I modes for the proton pathway is speculative. As the KIE of the MI to MII transition is small (cf. chapter 3.1.1) and the amide I features increase in intensity during this transition, it may be speculated that this structural change is involved in the proton transfer between the RSB and D220. The relevance of the structural changes monitored by amide vibrations will be discussed in detail in chapter 4.1.

3.1.3 Vibrational Spectroscopy with Focus on the Retinal Configuration

The photoisomerization from all-*trans* to 13-*cis* retinal is the primary configurational change during the photocycle of *Hs*BR leading to vectorial proton translocation. *Hs*BR containing retinal analogues with a locked C_{13}=C_{14} bond, where no isomerization can occur, does not pump protons nor undergoes a photocycle.[85, 86] Despite the consensus about the importance of C_{13}=C_{14} isomerization for function, details about the C=N configuration and its relevance for the functional mechanism have long been a matter of debate. However, for *Hs*BR a mechanism is established, where the 13-*cis*, 15-*anti* configuration is the functionally relevant retinal isomer, pre- and post RSB deprotonation (See ref.[87] and references therein). It is an intriguing question whether the sequence of isomerization reactions of the retinal chromophore determines the directionality of proton transport. For the inward proton pumps *Po*XeR and SzR the configurational changes of the retinal chromophore upon light activation have been studied by vibrational spectroscopy, but not for *Ns*XeR (cf. chapter 1.1.2). For *Ns*XeR it was shown, that independent of pre-illumination it predominantly harbors all-*trans* retinal in the dark state, but no spectroscopic data is available addressing the isomeric composition of intermediates.[39] To aid the reader in the following chapter, the discussed structures and main assignments are summarized in Figure 3-8.

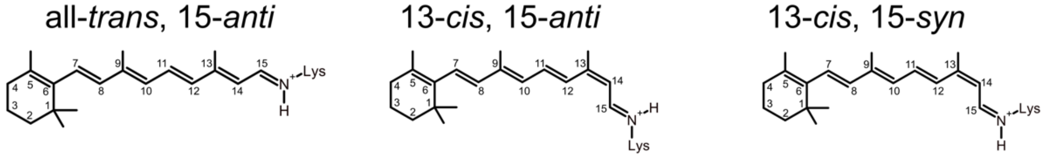

vibration	frequency / cm^{-1}	vibration	frequency / cm^{-1}	vibration	frequency / cm^{-1}
C=C	1526	C=C	1539*	C=C	1537
C-C	1242	C-C	1185	C-C	1183
C-C	1200	C-C	1155*	C-C	1157*
C-C	1168			N-H	1327*

Figure 3-8: Retinal configurations discussed in this chapter. Assignments based on FTIR difference spectroscopy described in the text are summarized below the structures. Band positions are given for FTIR spectra recorded in H_2O. Tentative assignments are marked with an asterisk. The orientation of the retinal is shown as if the protein was oriented with the C-terminus up (cytoplasmic side up). Note that such idealized structures may not accurately represent the actual geometry of the chromophore within the protein.

To decipher the retinal configuration during the photocycle of *Ns*XeR, (time-resolved) vibrational spectroscopy is employed. As already mentioned in chapter 3.1.2, the spectrum associated with the K intermediate obtained by the EC-QCL setup, shows a peculiar band pattern in the frequency range around 1500 cm^{-1}, indicative of ν(C=C) vibrations of the retinal chromophore (Figure 3-9A). While the band at 1526 cm^{-1} can be univocally assigned to the ν(C=C) mode of all-*trans* retinal in dark-state *Ns*XeR (*vide supra*), the band at 1538 cm^{-1} (+) is not in line with the correlation of the frequency of the ν(C=C) mode and the vis absorption maximum.[67] Interestingly, in *Po*XeR and ASR a likewise blue-shifted band was observed and tentatively assigned to an amide II vibration.[88, 89] To assess whether the band can be assigned to a chromophore vibration or to the amide II vibration of the protein backbone, resonance Raman spectroscopy was performed, where chromophore bands are selectively enhanced. Figure 3-9B shows resonance Raman spectra of *Ns*XeR with a focus on the spectral range indicative of ν(C=C) vibrations. It is evident that upon light illumination with a green LED (Figure 3-9B, green spectrum), the main peak at 1531 cm^{-1} is decreased, while a high-frequency shoulder evolves at around 1538 cm^{-1}. Calculating the difference of the two spectra yields a similar band pattern as observed in the IR difference spectra (cf. Figure 3-9 A and D), which allows to assign the band located at 1538 cm^{-1} to a vibration of the retinal chromophore. Notably, FTIR and Raman spectra obtained at 80K show a slight frequency upshift of the retinal modes as compared to experiments conducted at room temperature (Figure 3-9). The origin of this shift remains elusive. As the tuning range of the EC-QCL setup does not allow to probe frequencies below 1520 cm^{-1}, no information about a marker band for the K intermediate is obtained, which is expected to occur around 1510 cm^{-1}.[67] Therefore, a light-induced FTIR difference spectrum was recorded at 80 K where the K intermediate is accumulated (Figure 3-9 A). It resembles the time-resolved spectrum recorded at room temperature, but does not show a positive red-shifted band which may be attributed to a K marker band, which is in line with the difference spectrum obtained by resonance Raman spectroscopy (Figure 3-9 D). In *Po*XeR, based on low-temperature FTIR experiments, a band at 1522 cm^{-1} (+) has been assigned to the ethylenic stretching vibration of the retinal during the K intermediate, but a clear assignment by resonance Raman spectroscopy is lacking.[88] In light of this controversy, future experiments with isotopically labelled retinal chromophore may permit an univocal band assignment.

The frequency of the negative band located at 1556 cm^{-1} (Figure 3-9 A) is indicative for either a ν(C=C) mode of the retinal chromophore or an amide II vibration. Its negative sign indicates that this vibration vanishes upon light excitation and can therefore be attributed to dark-state *Ns*XeR. The rise time of this band is beyond the time resolution of the EC-QCL setup and it decays with the decay of the MII intermediate (Figure 3-7 B): The resonance Raman spectrum does not show a shoulder at around 1556 cm^{-1} nor does this band show up in the difference spectrum, which renders an assignment to a retinal mode unlikely (Figure 3-9 B, D). However, using a Raman probe laser with a wavelength of 647 nm, the pre-resonant conditions lead to a stronger resonance effect for the band at 1531 as compared to the band 1556 cm^{-1}. In turn this may influence the relative band intensities. A band in a similar position was observed for *Po*XeR, but left unassigned.[88] In *Ca*ChR1 some controversy arose about a negative band at ~1550 cm^{-1} as it was assigned to the ν(C=C) of 13-*cis* retinal in dark-state *Ca*ChR1 based on resonance Raman experiments[90], but later to an amide II mode as it remains unaffected upon using retinal isotopologues and its shift upon H/D exchange.[91] In

*Ns*XeR the band at 1556 cm^{-1} remains largely unaffected by exchanging dissociable protons by deuterons (Figure 3-10 B), which contradicts an assignment to an amide II vibration, as N-deuteration is expected to shift the vibration down to 1490-1460 cm^{-1}.[43] However, it might well be that this difference feature is caused by a region of the peptidic backbone, which is not solvent accessible and therefore H/D exchange cannot take place. In light of this, the band at 1556 cm^{-1} is tentatively assigned to an amide II vibration of the protein backbone in a solvent inaccessible transmembrane region. Additionally, the shift of the band located at 1638 to 1619 cm^{-1} (-) upon H/D exchange together with the observation of a band at 1645 cm^{-1} in the resonance Raman spectrum leads to the assignment of this band to the ν(C=N) mode of the RSB (cf. Figure 3-10 B and Figure 3-9 C). Notably, the band shape of the band in the resonance Raman spectrum with a maximum at 1531 cm^{-1} shows a slight asymmetry, already in the spectrum without additional green-light illumination (Figure 3-9C, inset). Displaying bands at 1210, 1201 and 1173 cm^{-1} which are indicative of all-*trans* retinal, the spectrum also shows smaller bands at 1184 and 1167 cm^{-1}, indicative for 13-*cis*, 15-*syn* retinal (Figure 3-9 C inset).[65] This may be explained by a dark-state heterogeneity, which was not observed in extraction experiments[39], or by photoisomerization induced by the Raman probe laser.

To get a more detailed insight on the retinal configuration during the photocycle of *Ns*XeR, time-resolved FTIR experiments using the step-scan and rapid-scan techniques are conducted. The FTIR spectra resemble those obtained with the EC-QCL setup, but provide access to a much broader spectral range from 1800-1000 cm^{-1} (cf. Figure 3-3A, Figure 3-7A and Figure 3-10 A). As the datasets recorded with two different methods are in good agreement in the spectral range between 1800 and 1524 cm^{-1}, this spectral range is not discussed here, but the focus is set on the spectral range between 1400 and 1100 cm^{-1}, where mostly ν(C-C) vibrations of the retinal chromophore appear. The difference spectra of wild-type *Ns*XeR show three negative bands located at 1242, 1200 and 1168 cm^{-1}, which can be assigned to all-*trans* retinal in *Ns*XeR dark state in analogy to *Hs*BR. A positive band arises at 1185 cm^{-1} during the K/L intermediate, which can be assigned to 13-*cis* retinal. [65, 92] This band slightly redshifts upon formation of the L intermediate to 1182 cm^{-1} and persists until the lifetime of the long-lived intermediate *Ns*XeR*. This band loses intensity during the two M intermediates, which can be rationalized by the loss in dipole moment upon RSB deprotonation (Figure 3-10A).[93] This band pattern indicates that after the initial all-*trans* to 13-*cis* isomerization, the retinal chromophore remains in a 13-*cis* configuration until recovery of dark-state *Ns*XeR.

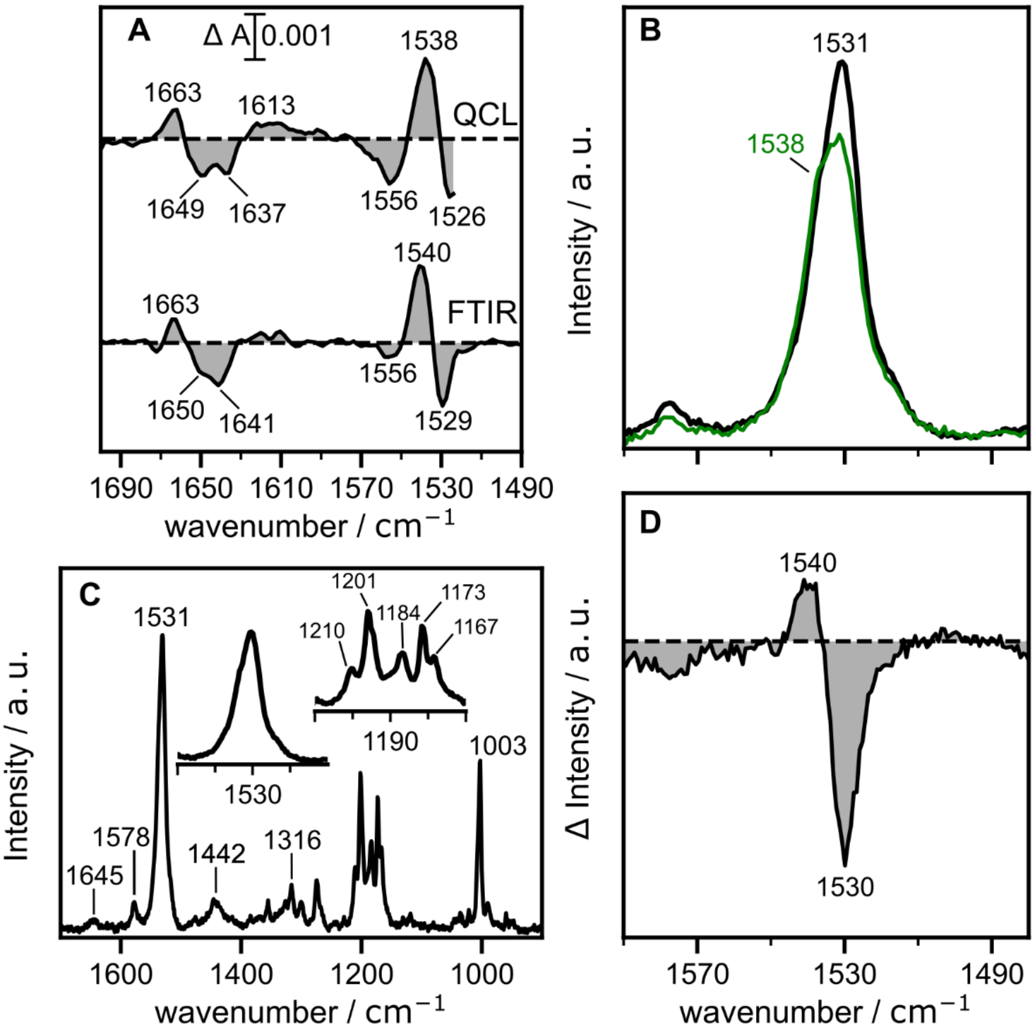

Figure 3-9: Vibrational analysis of the retinal chromophore in dark-state *Ns*XeR and the K intermediate. A) Species-associated difference spectrum of the K intermediate obtained by global analysis of the QCL dataset presented in Figure 3-7 in comparison to a low-temperature FTIR spectrum of detergent-solubilized *Ns*XeR at 80 K. The FTIR spectrum is scaled to match the intensity of the spectrum obtained by the QCL. B) Resonance Raman spectrum of dark-state *Ns*XeR (black) obtained at 80 K using a 647 nm Laser as probe light source. The green spectrum was obtained under the same conditions but with additional illumination with a 532 nm LED. The spectral range indicative for C=C stretching modes is shown. C) Resonance Raman spectrum shown in the spectral range from 1700 to 900 cm^{-1}. Insets show zoom ins for spectral regions indicative for C=C and C-C stretching modes. D) Resonance Raman difference spectrum obtained by subtracting the two spectra shown in B) without any scaling factor. All experiments were carried out at pH 7.4 in nanodisc-reconstituted *Ns*XeR except for the low-temperature FTIR (DDM solubilized). The resonance Raman spectra were recorded with help of Dr. Jacek Kozuch. Resonance Raman and FTIR spectra were manually baseline corrected using a polynomial function.

A positive band located at 1155 cm^{-1} during the K/L and 1148 cm^{-1} during the L intermediate, is present at 1157 cm^{-1} but less intense during the long-lived *Ns*XeR* intermediate (Figure 3-10C). In ChR2 a band located at 1154 cm^{-1} was assigned to the C_{14}-C_{15} stretching vibration by $^{13}C_{14}$-$^{13}C_{15}$ labeling of the retinal.[94] In analogy, the band occurring at 1155 (1148) cm^{-1} in *Ns*XeR may be tentatively assigned to the C_{14}-C_{15} stretching vibration of 13-*cis* retinal. It was shown for *Hs*BR that the C_{14}-C_{15} stretching vibration appears to be coupled stronger to the δ(NH) vibration when the protonated RSB is in the 15-*syn* configuration but only weakly in the 15-*anti* configuration. Therefore, this band was shown to be sensitive to N-deuteration of the RSB only in 15-*syn* retinal (cf. chapter 1.5).[65] In *Ns*XeR this band seems to be unaffected by H/D exchange in the K/L and L spectra (Figure 3-10C). It may therefore be concluded that the retinal isomerizes from all-*trans* to 13-*cis*,15-*anti* retinal, which persists at least until the L intermediate. Conversely, in the spectrum of the long-lived *Ns*XeR* intermediate, the band at 1157 cm^{-1} is H/D sensitive as well as the band at 1327 cm^{-1}, with the latter being tentatively assigned to the δ(NH) vibration of the RSB. The *Ns*XeR*-*Ns*XeR difference spectrum displays high similarity to the $\mathit{Hs}BR_{DA}$-$\mathit{Hs}BR_{LA}$ difference spectrum.[92] Taken together, these findings indicate, that upon formation of *Ns*XeR* the retinal has isomerized to a 13-*cis*,15-*syn* configuration. However, it cannot be deduced whether the 15-*anti* to 15-*syn* isomerization occurs during the M intermediates or upon decay of the M intermediate. In the final step of the photocycle, the retinal has to isomerize from a 13-*cis*,15-*syn* configuration back to the all-*trans*, 15-*anti* retinal. The same sequence of reactions was suggested for *Po*XeR and is further discussed in chapter 4.1.[95]

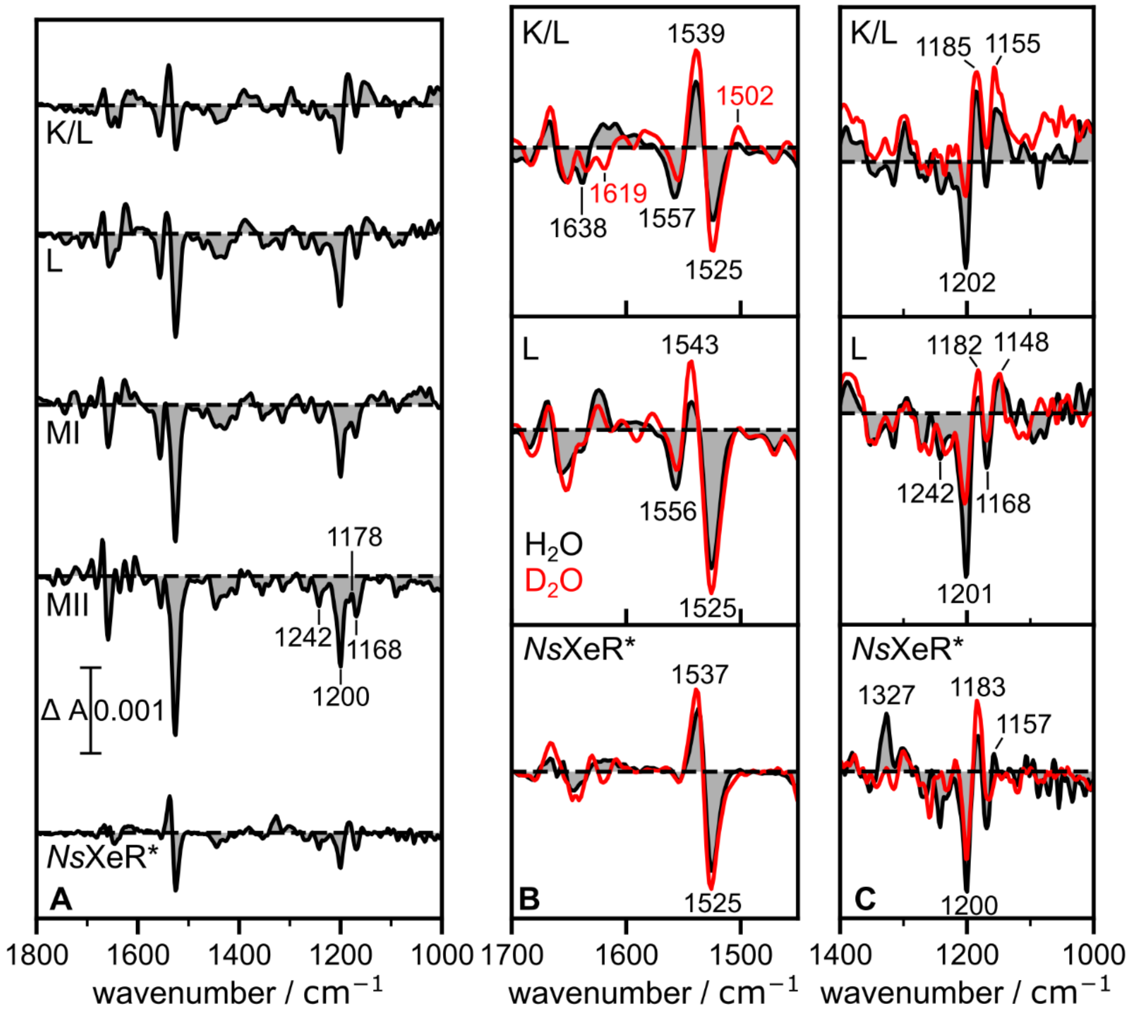

Figure 3-10: Analysis of retinal configurations in nanodisc-reconstituted *Ns*XeR by time-resolved FTIR spectroscopy. A) Step-scan spectra obtained at 6 µs (K/L), 43 µs (L), 600 µs (MI) after pulsed excitation and MII (~10 ms) and *Ns*XeR* spectra obtained by rapid-scan FTIR. The *Ns*XeR* spectrum shows the species-associated spectrum obtained by global analysis of the dataset as the raw dataset shows some baseline fluctuations. For better visualization, the MII spectrum is multiplied by a factor of 1.5 and the *Ns*XeR* spectrum by a factor of 5. B,C) Zoom in into the spectral range between 1700 and 1450 cm^{-1} and 1400-1000 cm^{-1}, respectively. Spectra for the K/L, L and *Ns*XeR* are shown for H_2O (black) in comparison to D_2O (red). The spectra recorded in D_2O were extracted at 6 µs (K/L), 60 µs (L) and 430 (*Ns*XeR*) ms after pulsed excitation to take the KIE into account. The scalebars in panel B and C are omitted, but intensities can be inferred from panel A. The spectra recorded in D_2O were not scaled for the K/L and L intermediate, but for *Ns*XeR* in order to match the signal size in H_2O. Both experiments were carried out on nanodisc-reconstituted *Ns*XeR at pH/pD 7.4. Note that the step-scan experiment was carried out at 8 cm^{-1} and the rapid-scan at 4 cm^{-1} spectral resolution.

3.1.4 C212 Responds to Light Activation

The description of protonation steps on the cytoplasmic side (3.1.2) reveals that the proton released from the RSB transiently resides at a yet unidentified residue before it reprotonates D220 in the MI-to-MII transition. While Y216 is very unlikely to act as the primary proton acceptor, H48 seems to be a promising candidate (cf. 3.1.2). However, other protonatable residues on the cytoplasmic side may be considered, too. An interesting candidate is C212, located next to K213, which binds the retinal chromophore. The homologous residue in *Hs*BR is A215, while it is S209 in ASR, T187 in SzR4, S206 in *Bc*XeR and a serine in *Po*XeR

(Table A. 1). In *Ns*XeR only one cysteine is present, which allows for a univocal assigned of the observed vibrational bands to the ν(S-H) mode of C212.

The pK_a of free cysteine is around 8.3, while it is typically higher when buried inside a protein and lower in solvent exposed regions.[96] Therefore, both protonated and deprotonated forms in dark-state *Ns*XeR need to be considered under our experimental conditions (pH 7.4). To assess the protonation state of C212 in dark-state *Ns*XeR, a steady-state FTIR spectrum is recorded (Figure 3-11A). In order to maximize the signal caused by the ν(S-H) vibration of the sulfhydryl group of C212, a sample with a high optical density was prepared, as can be judged from the strong absorbance of the amide I and amide A of the protein and ν(O-H) and δ(H-O-H) of water (Figure 3-11). Zooming into the range between 2450 and 2600 cm^{-1} reveals a very small band around 2540 cm^{-1}, which is hardly discernible on top of the large background. Performing a manual baseline correction (polynomial spline subtraction) in this spectral range reveals bands at 2541 and 2492 cm^{-1} (Figure 3-11B). Both bands may be attributed to a ν(S-H) vibration. The low frequencies are indicative of a strongly hydrogen-bonded thiol group. A second derivative spectrum shows a complex feature centered around 2541 cm^{-1} (Figure 3-11C). A detailed spectral analysis based on the band shape of the baseline-corrected spectrum, or the second derivative spectrum is not reliable at the present SNR. Taken together, the steady state FTIR experiment provides evidence that C212 is protonated in *Ns*XeR ground state. As in difference experiments (Figure 3-12A) only the band at 2541 cm^{-1} is perturbed upon light activation, the band at 2492 cm^{-1} is not discussed further. It is not clear if the two observed bands indicate a heterogeneity of the sample or the band at 2492 cm^{-1} is of different origin than a cysteine.

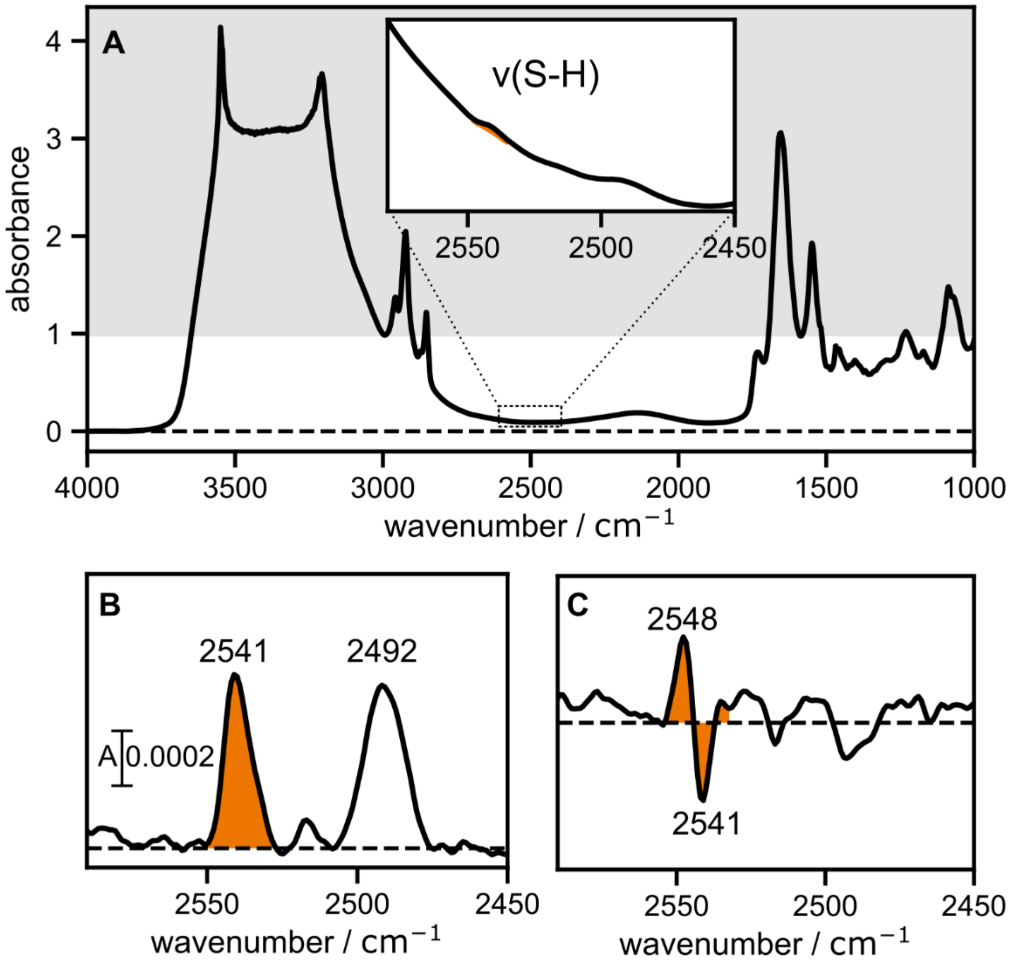

Figure 3-11: Steady-state FTIR spectroscopy of wild-type *Ns*XeR reconstituted in nanodiscs with the focus on the spectral region between 2600 and 2400 cm^{-1}, where the ν(S-H) vibration of the sulfhydryl group of cysteines typically occur. A) FTIR spectrum of a dried and rehydrated protein film of *Ns*XeR prepared for experiments in the spectral range for the ν(S-H) mode. Note the high absorbance for the amide I and amide A/water ν(O-H) mode. The data above 1 (grey shading) is not trustworthy. The inset shows a zoom into the region of interest. B) Spectrum shown in A) but manually baseline corrected. C) Second derivative spectrum of the spectrum shown in A). The second derivative was smoothed with 9 points. The spectrum was recorded with a spectral resolution of 2 cm^{-1}. The spectrum in A) was manually offset to be 0 around 3900 cm^{-1}.

Upon light-activation in a steady-state FTIR difference experiment, usually the long-lived *Ns*XeR* intermediate predominantly accumulates with contributions of the MI and MII intermediates (cf. Figure 3-16). The FTIR difference spectra of wild-type *Ns*XeR and the Y177F variant, shown in Figure 3-12A, display a similar intermediate composition as compared to the spectra shown in Figure 3-16 (full spectral range not shown). The contribution of the M intermediates may be slightly higher in the samples optimized for the analysis of cysteine vibrations, but a detailed comparison of marker bands is not possible because of the high background absorption (cf. Figure 3-11). Therefore, assigning the spectral changes of the cysteine vibration to a specific photocycle intermediate is not possible, but a first insight into the environment of C212 can be obtained. Upon light excitation, the band centered around 2540 cm^{-1} upshifts by 10 cm^{-1} in wild-type *Ns*XeR (Figure 3-12 A), reminiscent of weakened hydrogen-bond environment. In the Y177F variant, the spectral feature assigned to C212 is upshifted by ~9 cm^{-1}. This indicates that C212 is most likely hydrogen bonded to Y177 in dark-state *Ns*XeR, which is in hydrogen-bond distance (Figure 3-12 B). The relatively low frequency of the thiol vibration in the Y177F variant is still indicative of a relatively strongly hydrogen-bonded environment.[22] Inspection of the crystal structure of *Ns*XeR (PDB:6EYU) might indicate an additional intrahelical hydrogen to the backbone carbonyl of L208 (Figure 3-12 B), which will be discussed further below.

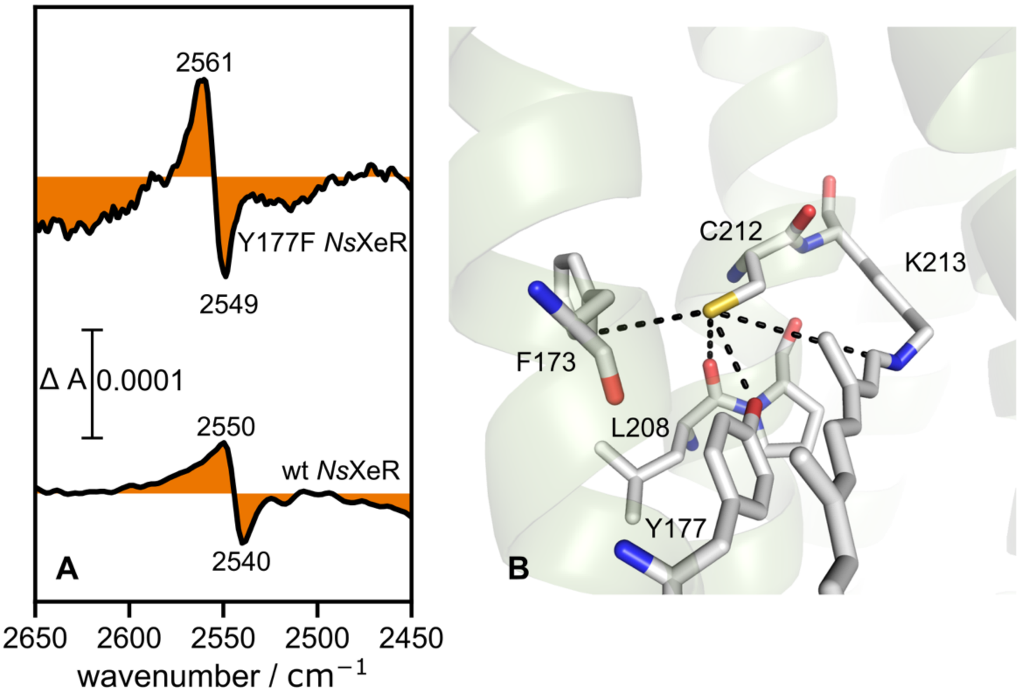

Figure 3-12: Environmental changes of C212 upon photoactivation of *Ns*XeR. A) Steady-state FTIR difference spectroscopy of wild-type *Ns*XeR (bottom) and the Y177F variant (top). In both spectra a mixture of the M and *Ns*XeR* intermediates are accumulated as judged from the fingerprint region (data not shown). The spectrum of Y177F was recorded at 2 cm^{-1} resolution while the spectrum for wild-type *Ns*XeR was recorded with 4 cm^{-1} resolution. As the baseline in this spectral region is not flat, no zero line is drawn, but the colored areas indicate a putative baseline. The Y177F spectrum was scaled to match the intensity of the band at 1200 cm^{-1} assigned to the ν(C-C) mode of all-*trans* retinal in wild-type *Ns*XeR and vertically shifted. B) Environment of C212 in dark-state *Ns*XeR. Potentially relevant interaction partners are connected via dashed lines (distances: d(S_{C212}-O_{L208}) = 3.1Å, d(S_{C212}-O_{Y177}) = 3.3Å, d(S_{C212}-N_{RSB}) = 6.4Å, d(S_{C212}-C_{F173}) = 4.0Å).

To assign the spectral changes to photocycle intermediates, time-resolved (FT)-IR experiments were conducted (Figure 3-13). Using the EC-QCL setup, the spectral range between 2590 and 2490 cm^{-1} was probed from 100 ns to 2 s after pulsed excitation. The heatmap shows a broad positive feature appearing on the millisecond timescale, which spans the entire spectral range, indicative of a baseline shift (Figure 3-13 A). To test whether this spectral feature is a response of the sample or an artefact caused by the setup, a rapid-scan FTIR experiment was conducted over a broad spectral range. Figure 3-13B shows a difference spectrum extracted at ~10 ms after pulsed excitation. In the spectral range below ~2000 cm^{-1} and above ~2300 cm^{-1} broad positive features are discernible. In fact, the 10 ms spectrum obtained by the EC-QCL setup and rapid-scan FTIR show the same response

(Figure 3-13 B inset). It is well known that transiently heated water can cause broad absorption changes in the mid-IR. However, the spectral and the kinetic response do not match those observed for transiently heated water by the excitation light source.[83] Therefore, the origin of this broad absorption feature remains elusive. To correct for this baseline shift, the dataset shown in Figure 3-13 A was smoothed with a Savitzky-Golay algorithm with 43 adjacent points and a second order polynomial (here termed oversmoothed). This removes all sharp bands but preserves the broad spectral feature and provides smoothed kinetics (Figure 3-13 C, D; blue traces). Subsequently, this “oversmoothed” dataset is subtracted from the raw dataset to yield the baseline corrected dataset (red and black traces respectively in Figure 3-13 C, D), which can be analyzed further.

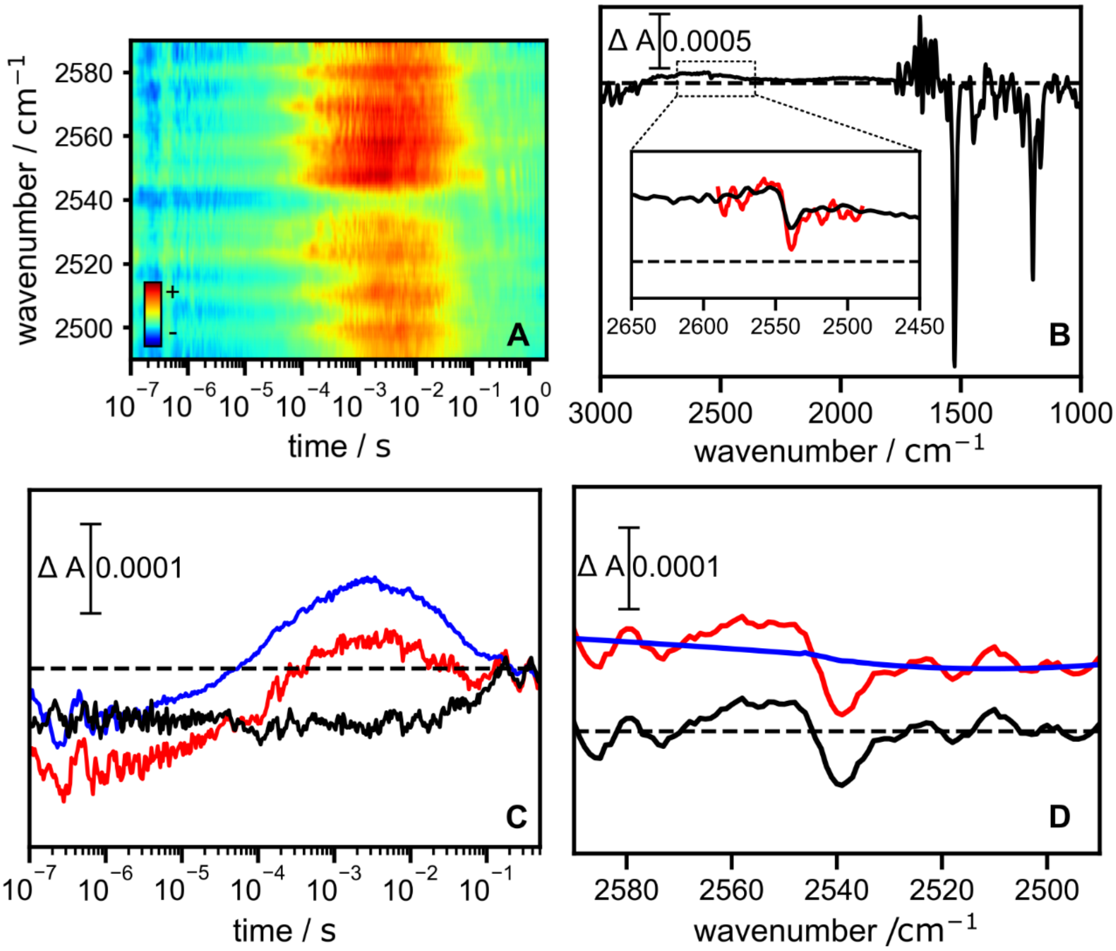

Figure 3-13: Time-resolved IR spectroscopy of the ν(S-H) vibration of C212. A) Heatmap of a time-resolved dataset acquired with the EC-QCL setup. Data was recorded between 2490 and 2590 cm^{-1} with 1 cm^{-1} spacing. Subsequently the data is smoothed with a Savitzky-Golay algorithm with 5 adjacent points and a second-order polynomial. B) FTIR difference spectrum obtained ~10 ms after pulsed excitation. The inset shows a zoom in into the cysteine region. Black: FTIR spectrum. Red: Spectrum extracted at 10 ms from the dataset shown in A). The spectrum obtained by the QCL setup was scaled by a factor of 0.8. Both spectra were not baseline-corrected. Note that the data in the amide I spectral range is not trustworthy because of the high background absorption. C, D) Depiction of the correction procedure. Red: Data extracted from dataset shown in A). Blue: Oversmoothed dataset with 43 adjacent points (Savitzky-Golay). Black: Corrected data by subtracting the oversmoothed dataset from the raw dataset. C) Transient at 2539 cm^{-1}. D) Spectra at 10 ms after pulsed excitation.

To assign the spectral changes of the ν(S-H) vibration of C212 to photocycle intermediates, spectra at 40 µs, 600 µs and 10 ms are extracted, where predominantly the L, MI and MII intermediates are accumulated, respectively (Figure 3-14). The baseline corrected dataset obtained with the EC-QCL setup (Figure 3-14, lower spectra) yields satisfying SNR from 100 µs onwards but has its limitations in the early µs timescale. Therefore, FTIR difference spectra recorded at low temperature are shown in comparison (Figure 3-14 upper spectra), which show close agreement. The accumulation of the L intermediate at 153 K (Figure 3-14 A) and the mixture of the two M intermediates at 250 K (Figure 3-14 B,C) were verified by comparing the spectral signatures in the fingerprint region (data not shown) with spectra obtained from step-scan FTIR experiments (cf. Figure 3-10). Upon formation of the L intermediate, the band centered around 2540 cm^{-1} redshifts towards ~2525 cm^{-1}, indicating the formation of a stronger hydrogen-bonded environment of the thiol group as compared to dark-state *Ns*XeR. This feature is reverted upon formation of the M intermediates, where the band blueshifts towards 2555 cm^{-1}. This indicates a weaker hydrogen bonding environment of the thiol group of C212 during the M intermediates (Figure 3-14 A-C).

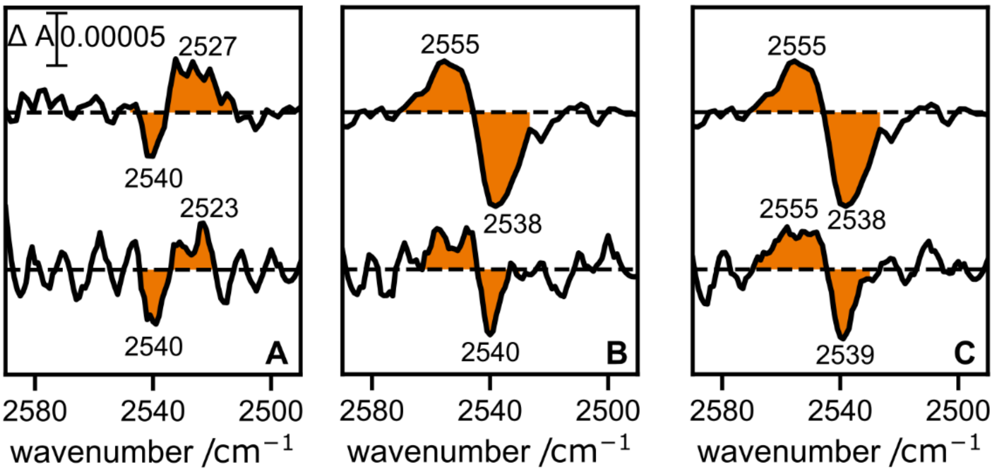

Figure 3-14: Intermediate spectra in the spectral range indicative of the ν(S-H) vibration. Lower spectra show the difference spectra obtained by the QCL setup (corrected data), while the upper spectra show steady-state FTIR difference spectra obtained at low temperature. FTIR spectra were manually baseline corrected using a polynomial function. QCL spectra were baseline corrected as described above. A) L-like intermediate spectra obtained 40 µs after pulsed excitation (EC-QCL) or at 153K (FTIR). B) MI spectrum extracted at 600 µs in comparison to an FTIR spectrum obtained at 250K, which displays a mixture of the two M intermediates. C) EC-QCL spectrum extracted at 10 ms in comparison to the same low-T FTIR spectrum as shown in B). Note that the FTIR spectra were recorded on detergent-solubilized *Ns*XeR while the EC-QCL experiments were performed on nanodisc-reconstituted *Ns*XeR. The orange shading is shown to highlight the bands as they are hardly above the noise level. All spectra are shown with the same y-scaling.

The spectral shifts of the band assigned to the ν(S-H) mode of the sulfhydryl group of C212 strongly indicate that C212 remains protonated but undergoes environmental changes throughout the photocycle of *Ns*XeR. Frequency shifts can be interpreted in terms of altered hydrogen bonding with polar groups of the protein but also changes in solvent polarity (cf.

chapter 1.5). In the case of *Ns*XeR, the relatively low frequency of the ν(S-H) band in dark-state *Ns*XeR indicates a strongly hydrogen-bonded environment. The spectral blueshift of ~9 cm^{-1} upon removal of the phenolic group of Y177, indicates strongly that Y177 and C212 are hydrogen bonded in ground-state *Ns*XeR. Given the magnitude and sign of the shift, an S-H→O-H binding motif (donor→acceptor) seems more likely, as an O-H→S-H binding motif would result in a smaller and opposite shift (cf. chapter 1.5).[22] As the light-induced upshift of the band by ~10 cm^{-1} is likewise observed for wild-type *Ns*XeR and the Y177F variant, this band feature is most likely not caused by an altered interaction between C212 and Y177. Therefore, it needs to be considered, that C212 is in hydrogen bond contact with Y177 and a second partner, whereas the interaction with the second partner is altered upon light excitation. The backbone carbonyl of L208 may be considered as a hydrogen bond acceptor (S-H→O=C) as well as the π-electron system of F173 (Figure 3-12 B). Beside the fact that the thiol group of C212 seems to be hydrogen-bonded to two partners, an exact description of the hydrogen bond contacts in dark-state *Ns*XeR cannot be given at this point. Interestingly, even bifurcated S-H→O hydrogen bonds have been observed in crystals under high pressure, but to my knowledge not in proteins under physiological conditions.[97]

The spectral redshift of the thiol vibration upon formation of the L intermediate indicates an increase in hydrogen-bonding strength to one of the possible binding partners. Based on the interatomic distances, the backbone carbonyl of L208 is likely to be in hydrogen bond contact to C212 (Figure 3-12). The spectral redshift upon formation of the L intermediate might therefore be explained by an increased intrahelical hydrogen bonding with L208 upon a structural alteration (decreasing the C212-L208 distance) of helix G. Upon RSB deprotonation, the ν(S-H) vibration experiences a spectral blueshift, indicating a less strongly hydrogen-bonded environment as compared to *Ns*XeR dark-state. Notably the spectral signature seems to be similar in MI and MII, indicating no further environmental change during this transition (Figure 3-14, lower spectra). This spectral blueshift may be explained by a weakened hydrogen bond upon increasing the distance between C212 and L208. A similar scenario was reported for hemoglobin, where an intrahelical hydrogen bond between a thiol group and a backbone carbonyl was perturbed by helical dynamics.[70] While this interpretation may explain the spectro-temporal features associated with the thiol vibration of C212, other scenarios have to be considered, too and will be discussed in chapter 4.1.

3.2 Perturbation of the Membrane Environment by the Activation of *Ns*XeR

Parts of this chapter are published in:

Baserga, F. Vorkas, A., Crea, F., Schubert, L. Chen, J.L., Redlich, A., La Greca, M., Storm, J., Oldemeyer, S., Hoffmann, K., Schlesinger, R., Heberle, J. Membrane Protein Activity Induces Specific Molecular Changes in Nanodiscs Monitored by FTIR Difference Spectroscopy, Front. Mol. Biosci. ***2022****, 9, 915328.*

The data presented in this chapter was recorded and analyzed by myself. Expression, purification and reconstitution of *Ns*XeR was carried out by Jheng-Liang Chen and Kirsten Hoffmann. The interpretation of the steady state data was done collaboratively with most co-authors presented above.

Membrane proteins typically contain hydrophobic regions, whose interactions with the long chain of lipid molecules stabilize their positioning within the lipid membrane. Unless a membrane protein is investigated in its native membrane environment, the isolated and purified protein needs to be stabilized by a membrane-mimicking system. Typically, the isolation of the membrane protein from its natural membrane or, in the case of a heterologously expressed protein, the isolation from the host cell membrane, is performed using amphipathic molecules. A broad variety of amphipathic agents such as detergents are available, but they need to be chosen with great care, as the detergent may influence structural properties of the protein, e.g. their oligomeric state. After isolation, the desired membrane protein may be studied directly in detergent or reconstituted into lipids forming proteoliposomes. While the lipid bilayer of a proteoliposome arguably models the native environment more realistically than a detergent micelle, they are less well suited for optical studies due to their strong light scattering. Instead, nanodiscs consist of a lipidic bilayer tied together by a scaffold protein and are much smaller in size (10-30 nm, cf. proteoliposomes 0.2 μm – 10 μm). Therefore, they are less susceptible to light scattering. The amphipathic scaffold protein makes the particle water soluble, and the size of the scaffold protein enables to control the size of the particle. If the lipid is chosen appropriately, the lipidic double layer may mimic a rather native membrane environment. As all of the aforementioned membrane systems require prior solubilization in detergent, solubilization is particularly critical if protein complexes or oligomeric states need to be retained. In that case it may be beneficial to circumvent solubilization using a detergent by the use of a chemically synthesized copolymer scaffold nanodisc, which simultaneously solubilizes the membrane protein of interest and forms a nanodisc.[98]

Depending on the biophysical technique used to study the desired membrane protein, each of the aforementioned membrane systems have their advantages and disadvantages. In any case, a possible influence of the membrane environment on the function of the protein needs to be considered. On the other hand, activation of the membrane protein might also perturb the lipidic surrounding. In the case of IR difference spectroscopy, vibrational bands stemming from the lipidic environment will be detected if the lipid reacts upon triggering the desired protein reaction. In the case of light-driven proteins, such perturbations may be related to transient heating of the sample upon applying the light trigger but might also stem from specific protein-lipid interactions. Lipid perturbations have been observed by monitoring the ν(C=O) vibrations of the lipid ester by FTIR spectroscopy for microbial rhodopsins[99, 100] as well as for vertebrate rhodopsin[101]. While these bands may report on functionally relevant structural changes or protein-membrane interactions, they might overlap with bands originating from carboxylic residues of the protein. Therefore, a thorough spectroscopic investigation of the protein in different membrane systems is beneficial to evaluate the impact of the membrane environment on the protein as well as obtaining univocal band assignments.

To assess the impact of the membrane environment on the function of *Ns*XeR, the photocycle kinetics in detergent-solubilized and nanodisc-reconstituted *Ns*XeR are compared (Figure 3-15 A). The characteristic transients for the photocycle intermediates show only minor deviations between the two preparations, which is manifested in almost identical time constants as derived from global analysis (Table A. 3). As the functional assay on proton pumping is performed in *E. coli* cells[79], a functional comparison is not possible. However, proton release to and uptake from the bulk solution are fundamental steps for a functional proton pump and are therefore considered to be an indirect readout of functionality. A comparison of the proton transfer reactions between protein and the bulk, monitored by the pH sensitive dye DHPDS (cf. chapter 3.1.1), reveals high similarity between the two preparations (Figure 3-15 B). The smaller signal and slightly altered kinetics in nanodisc-reconstituted *Ns*XeR may be explained by a certain buffering capacity of the nanodisc sample. Taken together, the membrane environment does not strongly influence the photocycle associated with inwardly directed proton pumping in *Ns*XeR and therefore does not seem to impair the proteins' function.

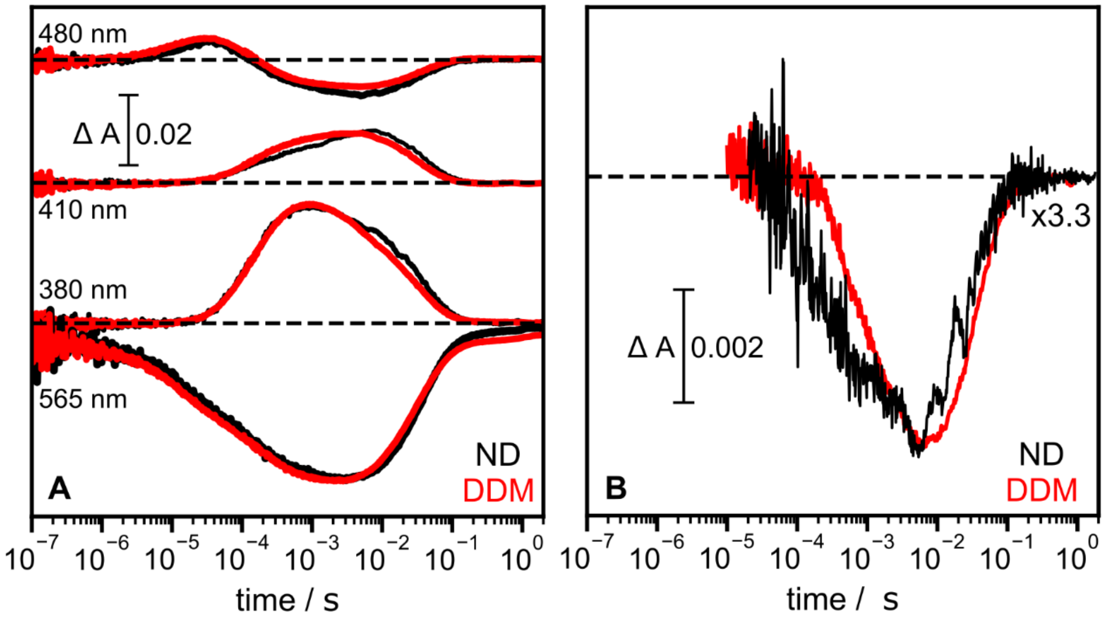

Figure 3-15: Effect of the membrane environment on the photocycle kinetics. UV/vis flash photolysis data recorded on wild-type *Ns*XeR reconstituted in DMPC/MSP1D1 nanodiscs (black) in comparison with detergent-solubilized (DDM) *Ns*XeR (red). A) Transients at characteristic wavelengths, representing the L (480 nm), MII (410 nm) and MI (380 nm) intermediates as well as the ground-state depletion (565 nm) are shown. The black transients are scaled to match the intensity of the red transients. Both experiments were conducted in a buffer containing 50 mM NaH_2PO_4/Na_2HPO_4, 100 mM NaCl at pH 7.4. B) Proton transfer to the bulk solution monitored by the pH sensitive dye DHPDS in nanodiscs (black) and DDM (red). These experiments were conducted in an unbuffered solution of 150 mM KCl at pH 7 (cf. Figure 3-2). The transient recorded in nanodiscs (black) is multiplied by a factor of 3.3. The pH indicator experiment conducted on detergent-solubilized sample was performed by Florina Marxer under my supervision. Figure adapted from ref.[79].

To test whether the activation of the protein induces molecular changes in the surrounding membrane environment, or the membrane environment affects the structural changes associated with proton pumping, we performed light-induced FTIR difference spectroscopy on detergent-solubilized and nanodisc-reconstituted samples (Figure 3-16). Under steady state illumination, the most long-lived intermediate is predominantly accumulated, but contributions from earlier photocycle intermediates may be observed. As expected from the kinetic similarity of both preparations (compare Figure 3-15), a very similar intermediate mixture is obtained in a steady-state experiment, which is confirmed by the excellent agreement of both spectra presented in Figure 3-16. Under the present conditions, the long-lived intermediate, termed *Ns*XeR* is accumulated with contributions from the M intermediates, as can be judged from the bands assigned to ν(C=C) and ν(C-C) vibrations of the retinal chromophore (cf. Figure 3-10). However, small deviations in the amide I region and the carboxylic range are discernible and are therefore discussed in detail in Figure 3-17. Note that the IR experiments presented below were performed on nanodiscs containing DPPC lipid, while those presented in Figure 3-15 and in previous chapters were performed in nanodiscs containing DMPC lipid. However, the spectral responses discussed below for

DPPC containing nanodiscs are likewise observed in DMPC containing nanodiscs (compare e.g. Figure 3-3).

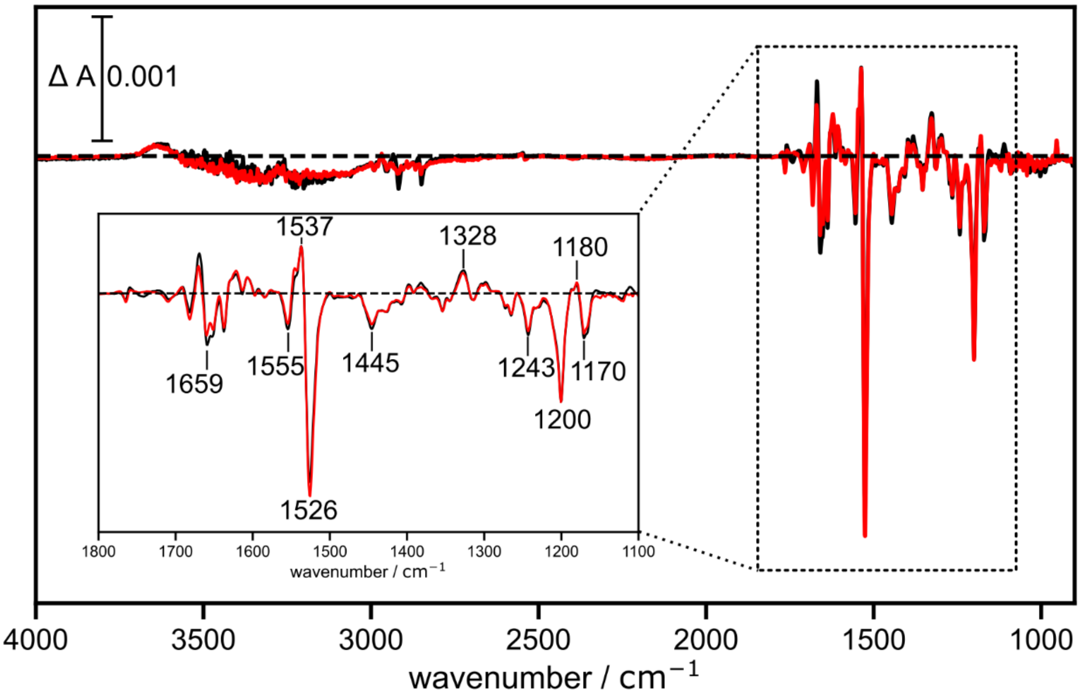

Figure 3-16: Light-induced difference spectroscopy on *Ns*XeR in different membrane environments. Steady-state light minus dark difference spectrum on wild-type *Ns*XeR reconstituted in DPPC/MSP1D1 nanodiscs (black) and solubilized in DDM (red). Continuous illumination was achieved using a 525 nm LED. The spectra were recorded with 2 cm^{-1} spectral resolution. The inset shows a magnification of the region between 1800 and 1100 cm^{-1}. The data recorded in DPPC was scaled to match the intensity of the retinal band located at 1200 cm^{-1} in the spectrum recorded on detergent-solubilized *Ns*XeR.

In the frequency range between 1800 and 1680 cm^{-1}, where the ν(C=O) vibration of protonated carboxylic amino acids typically occurs, a prominent differential feature at 1742 (-)/1725(+) is present in nanodisc-reconstituted *Ns*XeR, but absent in the detergent-solubilized sample (Figure 3-17 A). This suggests that this band feature is caused by the perturbation of the ν(C=O) vibration of the lipid ester moiety. To exclude that this band is caused by an environmental change of a carboxylic amino acid, which depends on the lipid environment, we repeated the experiment using the ^{13}C-isotopologue of DPPC (Figure 3-17C). The negative band centered at 1742 cm^{-1} shifts towards 1698 cm^{-1}, as expected from the increase in mass.[102] The corresponding positive band is not observed, possibly due to overlay with strong protein bands around 1680 cm^{-1}. Therefore, the band feature located at 1742 (-)/1725 (+) cm^{-1} is assigned to the ν(C=O) vibration of the lipid ester. The slightly altered band shape of the feature around 1770 cm^{-1}, assigned to a perturbation of E111 (cf. chapter 3.1.2), may be explained by a slightly higher accumulation of the MI intermediate in detergent-solubilized sample as compared to the nanodisc-reconstituted sample (compare Figure 3-5). Comparison of spectra recorded in DPPC- and ^{13}C-DPPC-reconstituted *Ns*XeR allows to assign the ν(C-H) vibration of the alkyl chain of the lipid. The negative bands centered at 2918 and 2849 cm^{-1} selectively downshift upon isotopic substitution (Figure 3-17 D). The baseline shift does not allow to clearly conclude whether these bands are purely negative or have a positive counterpart.

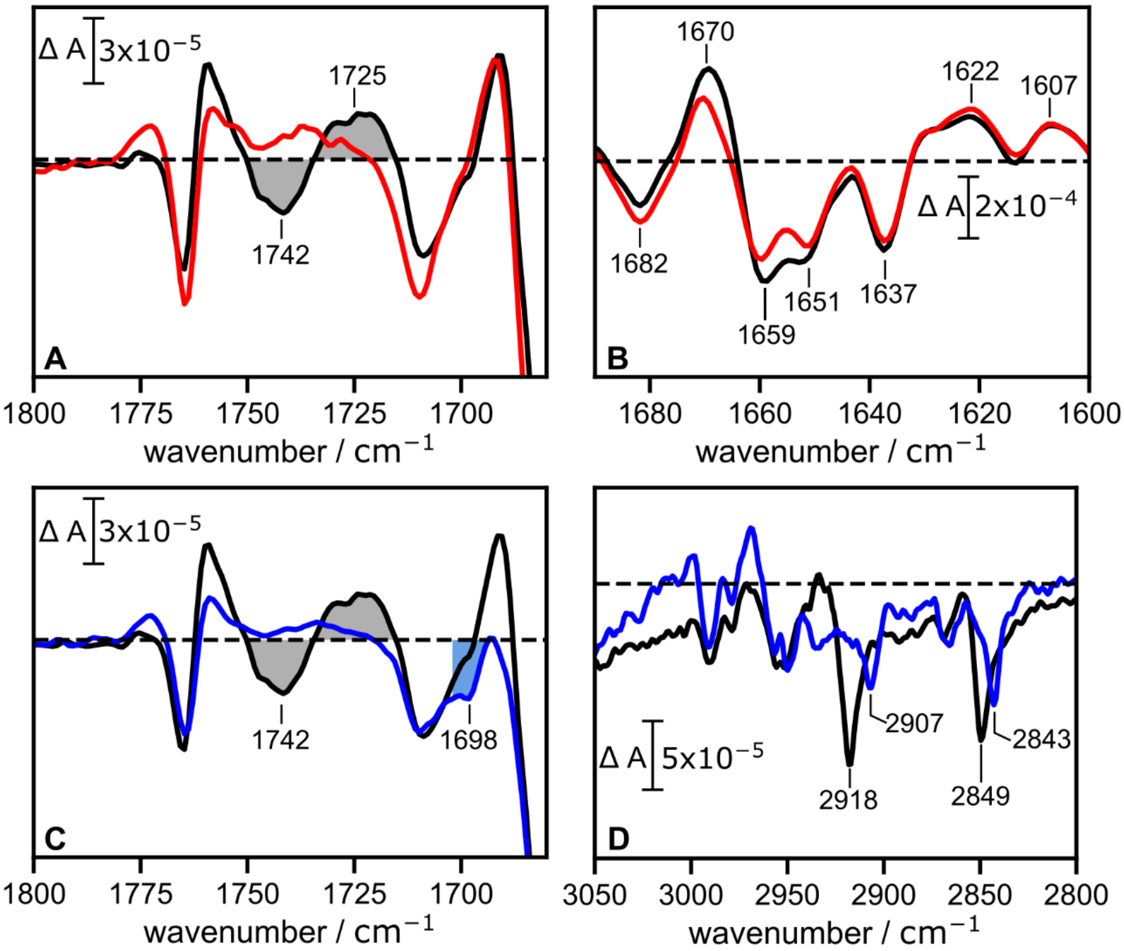

Figure 3-17: Assignment of vibrational bands associated with light-induced perturbation of the membrane environment. In all panels, black spectra stem from the same experiment shown in Figure 3-16 and represent *Ns*XeR reconstituted in DPPC-containing nanodiscs. Red spectra in panel A&B were recorded on detergent solubilized *Ns*XeR (cf. Figure 3-16). Blue spectra in panel C&D were recorded on *Ns*XeR reconstituted in nanodiscs containing ^{13}C-labeled DPPC. Good agreement between retinal bands (compare Figure 3-16, not shown for ^{13}C-DPPC labeled protein) ensure, that very similar intermediate mixtures are accumulated. The data recorded in DPPC and ^{13}C-DPPC were scaled to match the intensity of the retinal band located at 1200 cm^{-1} in the spectrum recorded on detergent-solubilized *Ns*XeR (cf. Figure 3-16). The blue spectrum in panel D is scaled by a factor of ~2 to facilitate comparison of the two spectra.

As the helical scaffold protein of the nanodisc may also respond to the activation of *Ns*XeR, this may be detected via additional difference bands in the amide I region (Figure 3-17 B). The spectra in this spectral range superimpose well but show small differences in band intensities at 1659 (-) and 1670 cm^{-1} (+) as well as very little frequency shifts. These bands are assigned to the amide I vibration of the protein backbone (cf. Figure 3-7) of *Ns*XeR reflecting protein conformational changes. Whether these small differences hint to altered structural changes depending on the membrane system cannot be concluded, as such small differences might also be explained by other factors, such as slightly different hydration levels of the protein films or marginally different accumulation of intermediates. Interestingly, in an empty nanodisc, containing DPPC and a photoswitchable lipid (AzoPC), the contribution of protein conformational changes caused by the scaffold protein upon light activation can be assessed free from any other protein contribution. Upon *cis* to *trans* isomerization of AzoPC, which leads to relatively strong lipid signals, a small negative band located at 1653 cm^{-1} has been assigned to the amide I vibration by isotopic labeling of the protein scaffold.[74] As this amide I signal is considerably smaller than the lipid bands, amide I signals are probably not observable in difference spectra of *Ns*XeR, due to overlay with stronger bands stemming from *Ns*XeR itself.

The steady-state experiments presented above do not yield any information about if and how the lipid signals are correlated with photocycle intermediates. Therefore, it is desirable to investigate these in a time-resolved fashion. Following the transients of the bands at 1743 and 1725 cm^{-1}, obtained by EC-QCL setup (cf. Figure 3-3), it is evident that both kinetics show a different behavior (Figure 3-18 A). The band located at 1725 cm^{-1} rises and decays with time constants of 280 μs and 45 ms respectively, which correlates well with MI rise and MII decay (compare Figure 3-1, Table A. 3). The transient at 1743 cm^{-1} shows a distinct transient with the rise of this band being beyond the time resolution of the EC-QCL setup. It can be fitted with three time constants yielding 52 μs, 1.4 ms and 48 ms. Whereas the first two time constants seem uncorrelated with photocycle kinetics, the latter one coincides with MII decay. To evaluate whether the changes of the lipidic bilayer are correlated with protein structural changes, the transients for the amide I vibrational mode of *Ns*XeR are compared (Figure 3-18 A). The decay of the amide I bands correlates very well with the decay of the ν(C=O) band of the lipid esters. While the rise of the band at 1725 cm^{-1} is correlated with the rise of the amide I bands, this seems not to be true for the rise of the band at 1743 cm^{-1}. To visualize the correlation of the decays of the two ν(C=O) bands, the transient at 1725 cm^{-1} can be mirrored along the x-Axis (Figure 3-18B). This illustrates how the decay of the two bands follows the same process. On the basis of this comparison, one can assume that the transient at 1743 cm^{-1} monitors two different processes: A fast process, occurring already on the sub 100 ns timescale and extending its dynamics to the millisecond time range; and a second process, which shows the same kinetic behavior as the transient at 1725 cm^{-1}. Under this assumption, a subtraction of the two kinetics leads to a transient describing the faster components only (Figure 3-18B). This can be reliably fitted with two time constants of 23 μs and 440 μs. Which processes these time constants describe remains elusive and needs to be interpreted with care, as the subtraction of the two transients convolutes the information contained at both frequencies. The origin of these spectro-temporal features associated with the lipidic ester vibrations will be discussed in chapter 4.2.

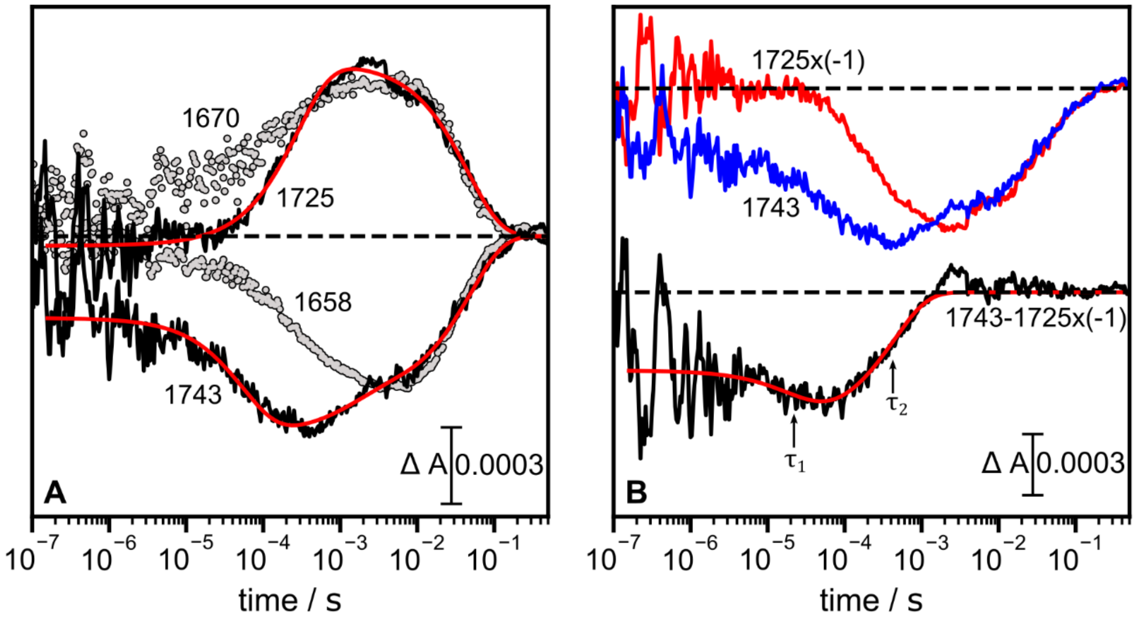

Figure 3-18: Kinetic analysis of the lipid ester vibration. A) Comparison to amide I vibrations associated with protein conformational changes. Black traces represent the transients associated with the lipid ester vibration (extracted from the same dataset presented in Figure 3-3). Both transients were corrected for the contribution of photothermally heated water (cf. Figure A. 4). Red lines represent exponential fits (cf. Table A. 2). Grey datapoints show the transients at 1658 and 1670 cm^{-1}, reflecting protein conformational changes (compare Figure 3-7 C). The transients at 1658 and 1670 cm^{-1} were scaled to match the intensity of the bands at 1725 and 1743 cm^{-1}. B) Visualization of the complex lipid kinetic at 1743 cm^{-1} (blue, same as in panel A). The transient at 1725 cm^{-1} mirrored along the 0 line (red). The black trace shows the difference between the transient at 1743 cm^{-1} and mirrored 1725 cm^{-1} kinetic. The red trace on top of the black one shows a fit using the sum of two exponentials, which yields two time constants as indicated.

3.3 Establishing QCL Spectroscopy as Tools to Monitor Non-Repetitive Protein Reactions

Large parts of this chapter are published in:

Schubert, L., Langner, P., Ehrenberg, D., Lorenz-Fonfria, V., Heberle, J. Protein conformational changes and protonation dynamics probed by a single shot using quantum-cascade-laser-based IR spectroscopy, J. Chem. Phys. ***2022****, 156, 204201.*

DCS and step-scan experiments presented here were done by me. EC-QCL experiments were conducted by Pit Langner for whom I prepared the sample and joined the experiment. Data which has been recorded by Pit Langner is labeled in the respective figure caption. *Hs*BR was kindly provided by the Genetic Biophysics lab of Dr. Ramona Schlesinger. The datasets were analyzed by myself with helpful contributions from Victor Lorenz-Fonfria and David Ehrenberg.

The investigation of a functional mechanism of an enzyme or protein aims at a profound description of structure-function relationships. While static methods such as X-ray crystallography or cryogenic electron microscopy (cryo-EM) set the basis for structural understanding, they lack information on the dynamics associated with protein function. The advent of X-ray free electron lasers (XFEL) has facilitated the development of serial crystallography, which allows to determine crystal structures of functional intermediates. This method enables the study of protein reactions at near-atomic resolution with time resolution down to femtoseconds. However, these technically demanding experiments require *a priori* knowledge of the reaction at study to select meaningful delay times.[103] For this purpose, time-resolved UV/vis spectroscopy can be used to characterize the photocycle dynamics of the crystallized protein prior to the crystallographic experiment.[104, 105] Monitoring electronic transitions of the chromophore, it is selective for structural changes at or in direct vicinity of the chromophore and might therefore miss spectrally silent transitions[106] and is intrinsically limited to chromoproteins. Instead, infrared difference spectroscopy is sensitive to all kinds of molecular vibrations in a protein. With time-resolved IR spectroscopy it is possible to link specific structural changes to reaction intermediates.[41] It can therefore not just provide appropriate time delays for serial crystallography, but also aid the molecular interpretation. Despite its high information content, time-resolved IR experiments are experimentally tedious and are often limited to the study of strictly reversible reactions.[22] The study of sub-ms dynamics became possible with the development of step-scan FTIR spectroscopy.[107] Providing a high spectral bandwidth, step-scan FTIR requires strictly repetitive systems and is therefore limited to light-driven, reversible reactions. To overcome this limitation and to mature the application of time-resolved IR spectroscopy to irreversible reactions, several new methods were developed: Employing a fast-scanning interferometer, the time to record an FTIR spectrum was reduced to the sub-ms timescale. However, this approach required extensive averaging of acquisitions to achieve sufficient SNR.[108] Using synchrotron radiation in a dispersive setup enabled the study of an irreversible photoreceptor by averaging only seven single acquisitions.[77] In contrast to such a synchrotron-based approach, setups based on quantum cascade lasers (QCLs) do not require large-scale facilities and can therefore be used as table-top spectrometers. Here, two different experimental approaches have been realized recently. A scanning-type spectrometer using tunable external cavity QCLs (EC-QCLs) allows to obtain transients at single frequencies.[47] Instead dual-comb spectroscopy (DCS) records spectro-temporal data in every acquisition by employing quantum cascade laser frequency combs and a heterodyne detection scheme (cf. chapter 1.3).[56] Although their spectral coverage is often limited as compared to FTIR-based methods (Figure 3-19), both QCL-based techniques are promising tools to study protein dynamics with (sub)µs time resolution. Obtaining data with sufficiently high SNR in a single acquisition (= single shot) renders extensive averaging unnecessary and may allow to derive reaction dynamics of irreversible reactions.[47, 57] This may not just enable a thorough spectroscopic characterization of irreversible (protein) reactions, but also provide important kinetic information for serial crystallography or time-resolved cryo-EM experiments.

In the following chapters, QCL-based dual-comb spectroscopy is applied to study functionally relevant structural changes in membrane proteins. Dual-comb spectroscopy is conceptually compared to step-scan FTIR as well as to our homebuilt EC-QCL setup in terms of applicability to the study of irreversible protein reactions. Bacteriorhodopsin from *Halobacterium salinarum* (*Hs*BR) is used as a model system because its photocycle is well characterized and most difference bands in the mid-IR are assigned to vibrational modes of the retinal chromophore, the protein backbone or amino acid side chains. Because of its strictly repetitive and fast photocycle it has been intensively studied by step-scan FTIR spectroscopy which revealed functionally relevant dynamics in the ns to ms time range.[7] For a detailed description of the photocycle of *Hs*BR, the reader is referred to chapter 1.1.1. After benchmarking the capabilities of QCL-based mid-IR spectroscopy with *Hs*BR as a model system, the EC-QCL and DCS techniques are applied to the study of the irreversible photoreaction of vertebrate rhodopsin, a prototypical GPCR.

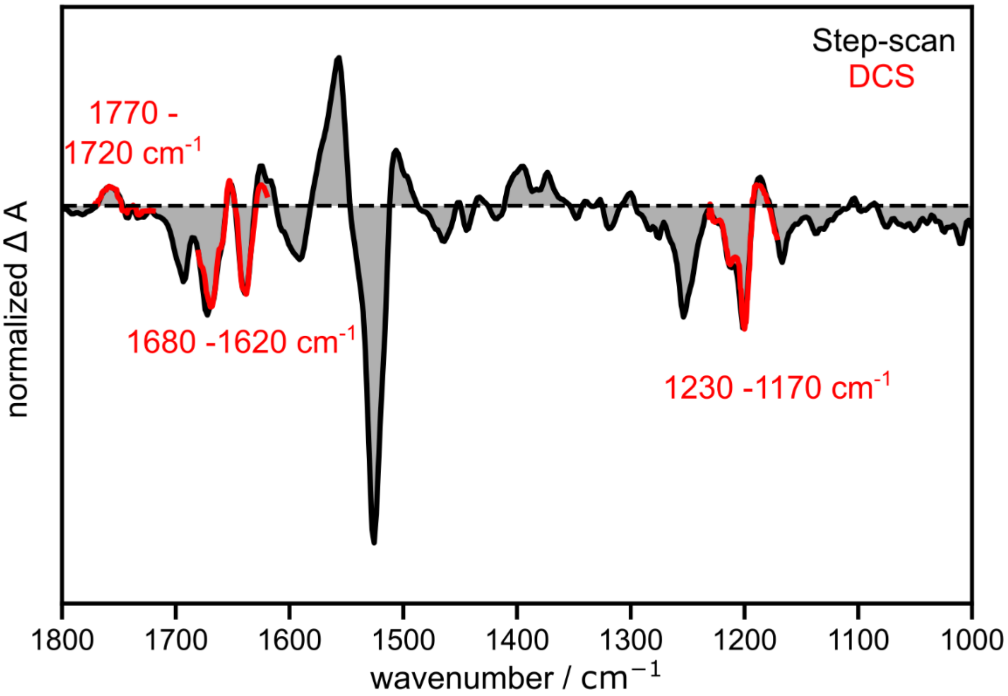

Figure 3-19: Overview on spectral coverage of DCS modules used in this thesis as compared to step-scan FTIR. Shown are difference spectra of bacteriorhodopsin from *Halobacterium salinarum* (*Hs*BR) extracted at 5.3 ms, representative of a mixture of N and O intermediates obtained by step-scan FTIR (black) and three individual DCS laser modules (red) at a spectral resolution of 4 cm^{-1}. The nominal tuning range of the EC-QCLs used in this study is limited from 1724 to 1495 cm^{-1} and 1830-1660 cm^{-1}.

3.3.1 Retinal Isomerization

During the photocycle of *Hs*BR, the retinal chromophore undergoes structural changes such as *cis-trans* and/or *anti-syn* isomerization, twisting of the polyene chain or even deprotonation of the RSB. Those structural changes give rise to changes in the electronic spectra, which have been traced by transient UV-Vis spectroscopy[109] but are also reflected in IR difference spectra as well as resonance Raman spectra[110]. In a time-resolved experiment, the kinetics of the bands assigned to ν(C-C) and ν(C=C) modes of the retinal may be analyzed in a complementary manner with the kinetics in UV-Vis experiments, which allows to establish a link between results of both experiments. While the ν(C=C) mode provides information about the energy of corresponding electronic transition of an intermediate[67], the ν(C-C) modes have been used to assign specific retinal configurations and protonation states of the RSB.[65]

In FTIR difference spectra, many vibrational bands might overlap in certain spectral regions, rendering difference spectra crowded. To differentiate bands and foster their assignment, an increased spectral resolution is sometimes required. In *Hs*BR this is for example the case for the band located at 1213 cm^{-1} (Figure 3-20), assigned by resonance Raman experiments to a ν(C-C) mode of all-*trans*, 15-*anti* retinal in light-adapted *Hs*BR.[65] The band is clearly resolved at 4 cm^{-1} resolution, but shows up only as a shoulder of the main band located at 1201 cm^{-1} at 8 cm^{-1} resolution. In FTIR spectroscopy, improving the spectral resolution by a factor of two requires doubling the path length difference, which in turn doubles the time for an experiment. While this is feasible for *Hs*BR, which is robust against photobleaching and has a fast (<1 s) photocycle, it is a challenging task for proteins with longer photocycles (e.g. ChR2[111]) and impossible for non-cyclic proteins like visual rhodopsin.[112] Instead, in DCS, time-resolved data is inherently recorded with the highest possible "spectral resolution" (cf. chapter 1.4.4), determined by the wavenumber spacing of the frequency comb lines, which is about 0.3 cm^{-1} for the laser modules used here. This is a clear advantage over FTIR or scanning methods, where an improved spectral resolution is only achieved by an increased experimental effort. However, in DCS, adjacent comb lines are typically averaged to increase the SNR on the expense of spectral resolution.[57, 61, 72] Figure 3-20 B shows spectra of the same dataset recorded by DCS but postprocessed to different spectral resolutions. Spectral averaging smooths the data and therefore increases SNR. However, this effect is not very pronounced here as the spectra show already high SNR at 2 cm^{-1}. As expected, the band at 1213 cm^{-1} is well resolved at 2 and 4 cm^{-1} spectral resolution, but less pronounced at 8 cm^{-1} resolution. However, it is evident that the band at 1200 cm^{-1} (-) slightly redshifts by 1 cm^{-1} upon spectral averaging of the DCS data. The fact, that spectral smoothing during the post-processing might affect band positions needs to be considered, when absolute band positions are quantitatively analyzed. As DCS does not come with a built-in frequency calibration (as compared to FTIR, compare 1.3.1) the spectra are calibrated using a well-known standard (here polypropylene foil or water vapor). Taken together, great care must be taken in order to choose appropriate smoothing and calibration whenever absorption frequencies and/or band shapes are quantitatively analyzed.

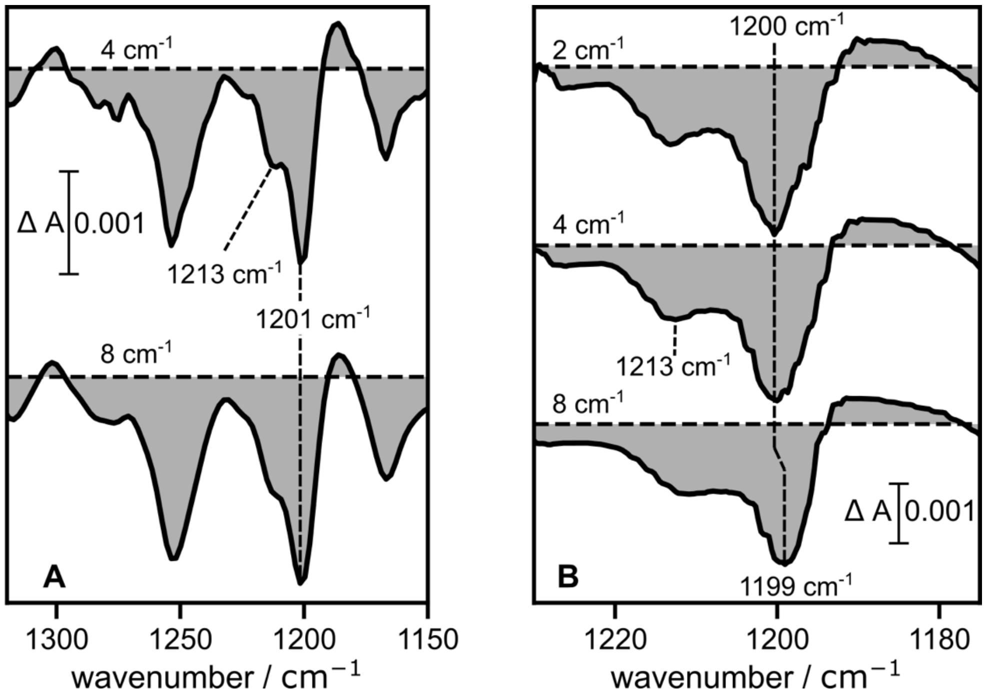

Figure 3-20: Retinal fingerprint region and comparison of spectral resolution. A) Step-scan FTIR spectra, at 4 and 8 cm^{-1} spectral resolution, extracted at 5.3 ms after pulsed excitation, reminiscent of a mixture of N and O- intermediate. B) Spectra at 5.3 ms, recorded by DCS at 0.329 cm^{-1} spectral resolution (= comb line spacing) and post-processed to a spectral resolution of 2.3 cm^{-1}, 4.3 cm^{-1} and 8.2 cm^{-1}.

3.3.2 Protein Structural Changes

The amide I band in proteins contains information about the secondary structure of a protein. In an IR difference experiment, absorption changes in this spectral range indicate protein conformational changes and/or secondary structure changes.[43] While the time-resolution allows to derive structure-function relationships, FTIR experiments typically don't provide spatial resolution, failing to assign the observed structural changes to specific regions in the system at study.

A prominent example where spectroscopic and structural data was used mutually, is the β-sheet to α-helix refolding in phytochromes.[113] In alpha-helical retinal proteins no refolding, but structural changes such as tilting of helices are observed.[26, 114] In *Hs*BR protein conformational changes were studied by low-temperature FTIR[115] and later by time-resolved FTIR at room temperature.[116] In *Hs*BR, bands located at around 1650, 1660 and 1670 cm^{-1} are assigned to the amide I mode of the protein backbone. The bands at 1650 and 1670 cm^{-1} are largest upon the formation of the N intermediate.[116, 117] It was shown that the conformational change during the M to N transition lowers the pK_a of D96 from >12 to 7.1, which leads to the reprotonation of the RSB by D96.[24]

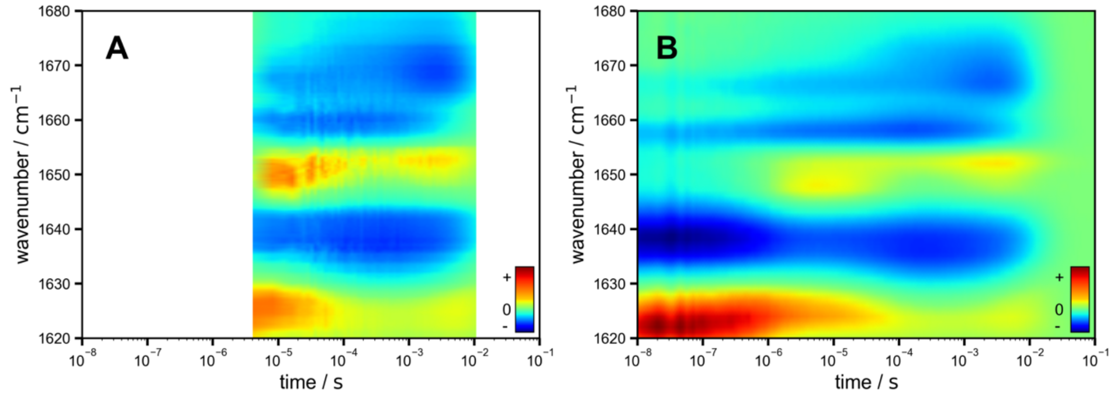

Figure 3-21: Comparison of time-resolved IR datasets obtained by DCS (A) and EC-QCL spectroscopy (B) on *Hs*BR. Heatmaps showing the spectral region between 1680 and 1620 cm^{-1}, covering mostly the amide I vibrational mode, which is indicative for structural changes of a protein. For better comparison, both plots are shown with the same time axis and color gradient. Both datasets are shown at a spectral resolution of ~4.5 cm^{-1}, while the frequency spacing of (A) is 0.3 cm^{-1} and 1 cm^{-1} for (B). The data presented in panel B has been recorded by Pit Langner. Figure adapted from ref.[61].

For the study of protein conformational changes, a DCS laser module covering the frequency range from 1680 – 1620 cm^{-1} has been used. The EC-QCL has a nominal tuning range of 1724-1495 cm^{-1} but was restricted to match the DCS frequency range. The time-resolution of DCS is limited by the requirement to resolve neighboring comb teeth in the rf domain and therefore depends on the difference in repetition frequency of the two frequency combs (see chapter 1.3.3). Instead, the time resolution of the EC-QCL is limited by the rise time of the detector.[47, 61] The upper limit for data recording is restricted by the memory of the data recorder in DCS to tens of ms.[57] Using two oscilloscopes with high and low sampling rate in the EC-QCL setup theoretically allows to measure beyond 1 s. However, the data is often not useful for times > 100 ms as the setup suffers from instabilities of the QCL emission (see 4.3). The spacing of datapoints in DCS is set by the repetition rate of the lasers, which is about 0.3 cm^{-1} in the present case. For the EC-QCL, the spacing is defined by the user and is set in this study to 1 cm^{-1} (cf. chapter 1.3).

The data recorded on *Hs*BR by DCS and the EC-QCL setup (Figure 3-21) was recorded by averaging 3000 acquisitions in DCS and 50 averages per single transient in the EC-QCL, resulting also in 3000 sample excitations. Both datasets agree nicely, showing bands at around 1624 cm^{-1} (+) and 1639 cm^{-1} (-), which have been previously assigned to the ν(C=N) mode of the RSB in the M- and ground state, respectively.[92] Bands assigned to the amide I vibration of the protein backbone occur at 1650 (+), 1660 (-) and 1670 cm^{-1} (-) (Figure 3-21, Figure 3-22).[115, 116] Comparing the spectra extracted at 20 µs, 300 µs and 5.3 ms, representative of the L, M and N/O intermediates respectively, reveals high similarity between the two datasets (Figure 3-22 A, C). Small deviations, e.g. the altered relative intensity of the band at 1660 cm^{-1} in the 5.3 ms spectrum, might stem from different procedures for spectral averaging. DCS data was recorded with 0.3 cm^{-1} spacing and subsequently spectrally averaged with a boxcar function (cf. chapter 1.4.3), while the EC-QCL data was recorded with 1 cm^{-1} spacing and post-processed by a Savitzky-Golay filter with 5 adjacent points and a second-order polynomial. Transients recorded by the EC-QCL (Figure 3-22 D) have a higher SNR than those obtained by DCS (Figure 3-22 B) and span a wider time range.

Both methods have been used to study protein conformational changes of *Hs*BR with high SNR. In comparison to step-scan FTIR, only the EC-QCL setup provides higher time resolution, but both QCL-based setups provide access to a much smaller spectral range, rendering step-scan FTIR advantageous when studying strictly repetitive systems. However, the study of non-repetitive reactions by step-scan FTIR requires to exchange the sample between every acquisition, which is experimentally challenging and demands a very high sample consumption. Because of their high emission power in a narrow spectral range, QCL-based methods have the potential to achieve a sufficient SNR with no averaging or averaging of only few single acquisitions. Successful single- or few-shot experiments were already conducted on *Hs*BR[57] and RAS proteins[72]. However, those experiments were conducted on co-factor bands, which in the case of retinal proteins are often stronger as compared to bands stemming from single amino acids and are located in a spectral range with low background absorption of the protein and water (cf. Figure 3-19).

To increase the SNR, two aspects need to be considered: First, a higher signal can be achieved by increasing the number of molecules in the beam path. Secondly, a higher background absorption of the sample decreases the number of detected photons and therefore increases the noise. In order to optimize the SNR, both aspects need to be considered. This case is particularly important in the frequency range between 1700 and 1600 cm^{-1} where the bending mode of water and the amide I mode appear.

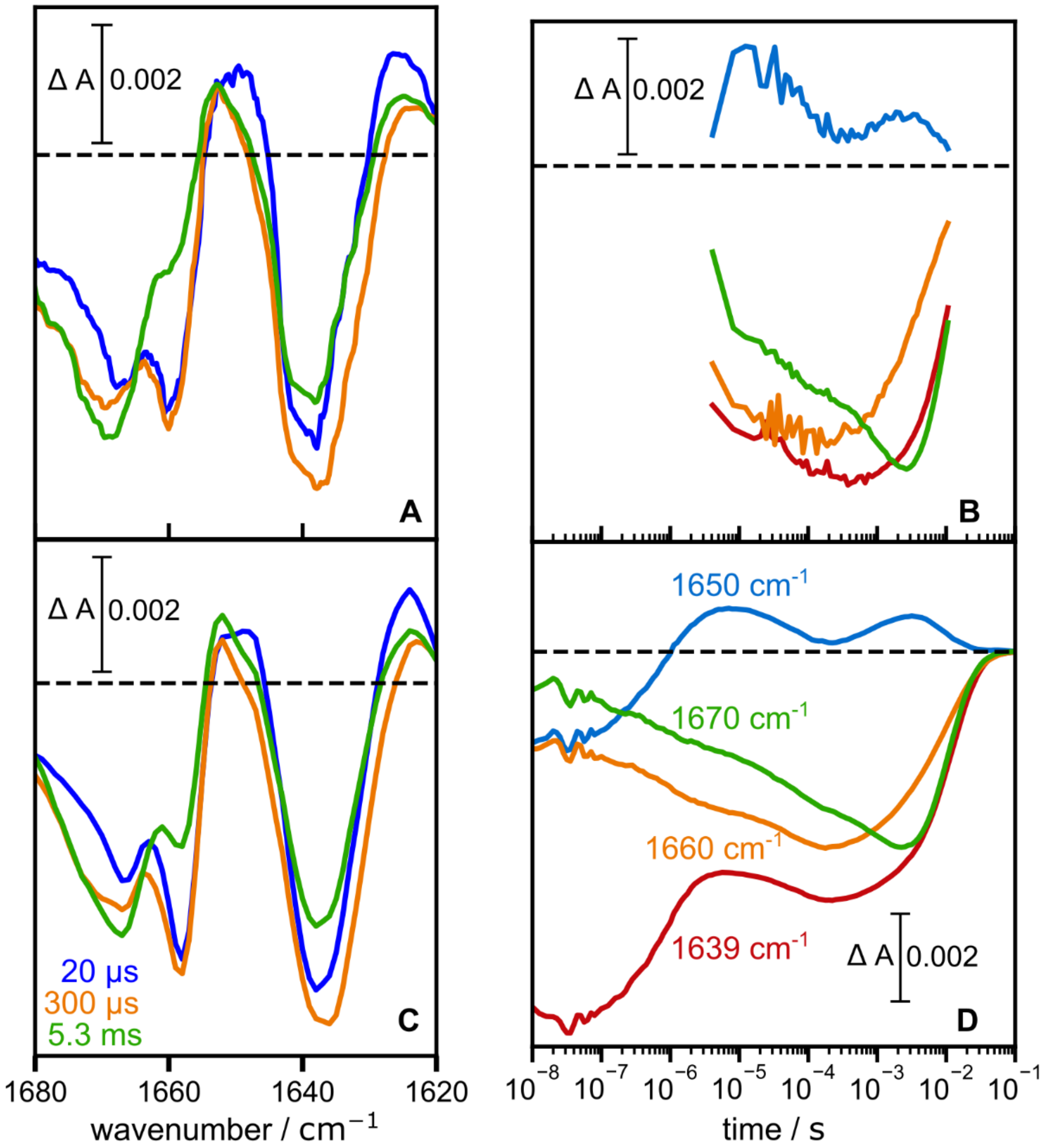

Figure 3-22: Comparison of time-resolved difference spectra and kinetics obtained by DCS (A, B) and EC-QCL spectroscopy (C, D). Spectra (A, C) extracted at 20 µs (blue), 300 µs (orange) and 5.3 ms (green) representing mostly L, M and N/O intermediates, respectively. Kinetics (B, D) at 1639 cm^{-1} (red), 1650 cm^{-1} (blue), 1660 cm^{-1} (orange) and 1670 cm^{-1} (green). Spectra and kinetics are extracted from the respective datasets in figure 4-3. The data presented in panel C and D has been recorded by Pit Langner. Figure adapted from ref.[61].

To simulate the study of a non-repetitive reaction, the cyclic photoreaction of *Hs*BR was studied, but the experiments were restricted to a single excitation of the sample (Figure 3-23), which is referred to as a single-shot experiment. The acquisition scheme of DCS allows to obtain spectro-temporal data, while the EC-QCL can only record a transient at a single frequency under single-shot conditions. When averaging ten single-shot experiments (black traces in Figure 3-23), the spectro-temporal features shown in Figure 3-22 are reproduced by the DCS setup. Under single-shot conditions, the SNR is sufficient to resolve the spectral features of the N/O state spectrum extracted at 5.3 ms after pulsed excitation, but not entirely at 300 µs (Figure 3-23 A&C). Logarithmic averaging on the time axis leads to a reduction in noise at later times. The single-shot transients at 1670 cm^{-1} (Figure 3-23 B&D) reproduce the results from multiple excitations (Figure 3-22 B&D), but the transient recorded by the EC-QCL excels the one recorded by DCS in terms of time-resolution, time coverage and SNR. The higher SNR of the EC-QCL can be rationalized by comparing both detection schemes: Assuming a comparable photon intensity on the detector element in both experiments, DCS detects several laser lines in parallel (~60 cm^{-1} with ~0.3 cm^{-1} spacing) while the EC-QCL detects only a single frequency (bandwidth < 0.01 cm^{-1}). This leads to a much higher number of photons per wavenumber and hence higher SNR in the EC-QCL setup. On the other hand, DCS data is spectrally averaged (cf. 1.4.3) which increases the SNR of a single transient. Beside the possibility of spectral averaging, spectro-temporal data obtained by DCS can also be subjected to data analysis tools such as singular value decomposition (SVD), global analysis (GA) or lifetime density analysis (LDA). Figure 3-24 illustrates how LDA can be used as a tool to extract relevant information from noisy data.

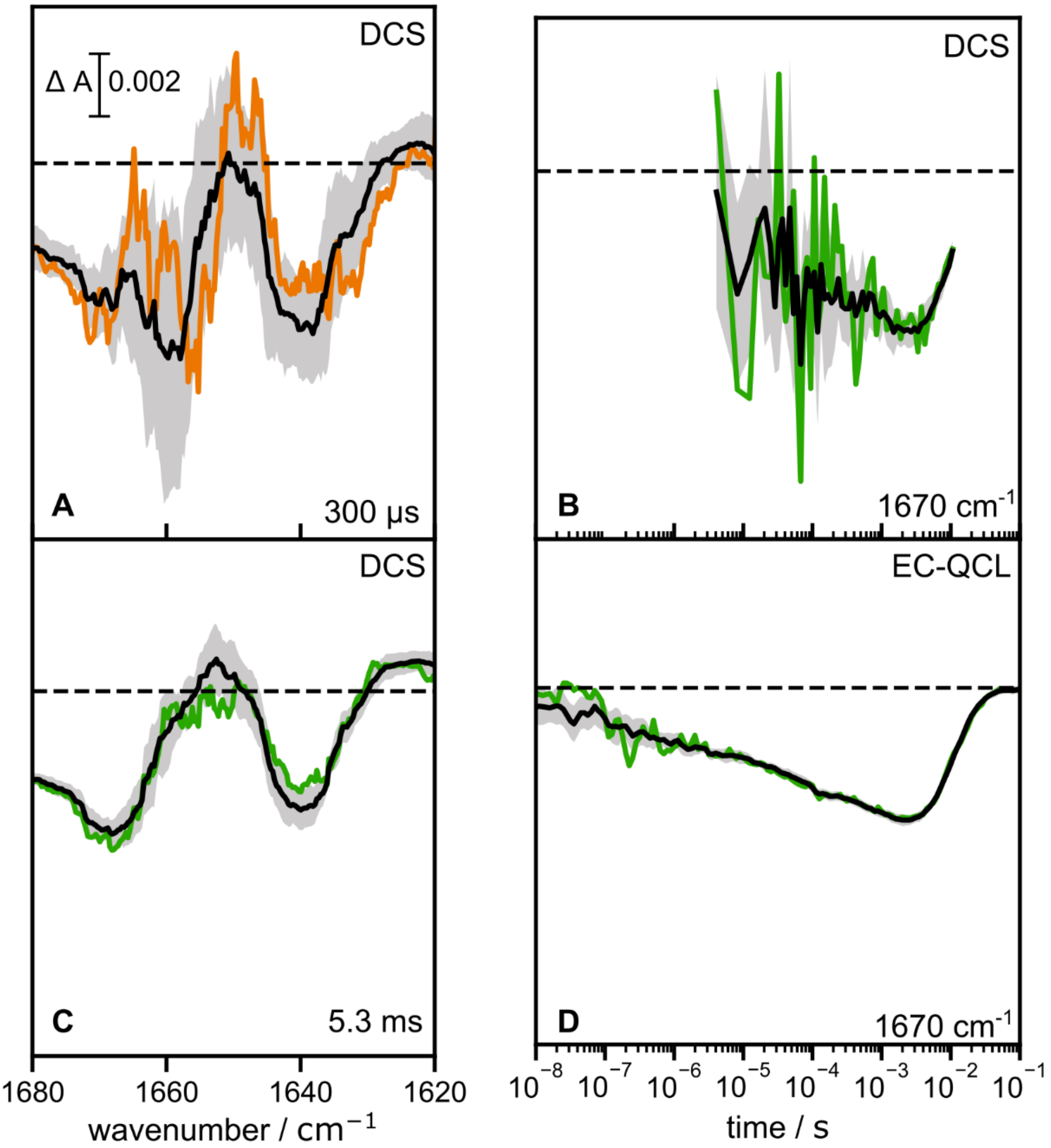

Figure 3-23: Protein conformational dynamics of *Hs*BR probed by single-shot experiments. (A, C) Difference spectra extracted at 300 µs (A) and 5.3 ms (C) obtained by DCS. (B, D) 1670 cm^{-1} kinetic obtained by DCS (B) and EC-QCL spectroscopy (D). Colored traces represent data obtained from a single-shot, black traces are the average of ten single-shot experiments and the grey shading displays the standard deviation (σ) derived from ten single-shot experiments ($\Delta A_{10} \pm \sigma$). DCS data is shown at 8.1 cm^{-1} spectral resolution. All plots show the same y-scaling. The data presented in panel D has been recorded by Pit Langner. Figure adapted from ref.[61].

The raw spectrum extracted at 300 µs (Figure 3-23 A and Figure 3-24 A), does not resolve the double band feature located at 1660 / 1670 cm^{-1}, but after denoising by LDA both bands are clearly resolved. However, such analysis tools must be used with great care, especially with noisy data and usually some knowledge from different experiments is taken into consideration. In this respect LDA is beneficial as compared to GA, because it is not based on a reaction model (compare chapter 1.4).

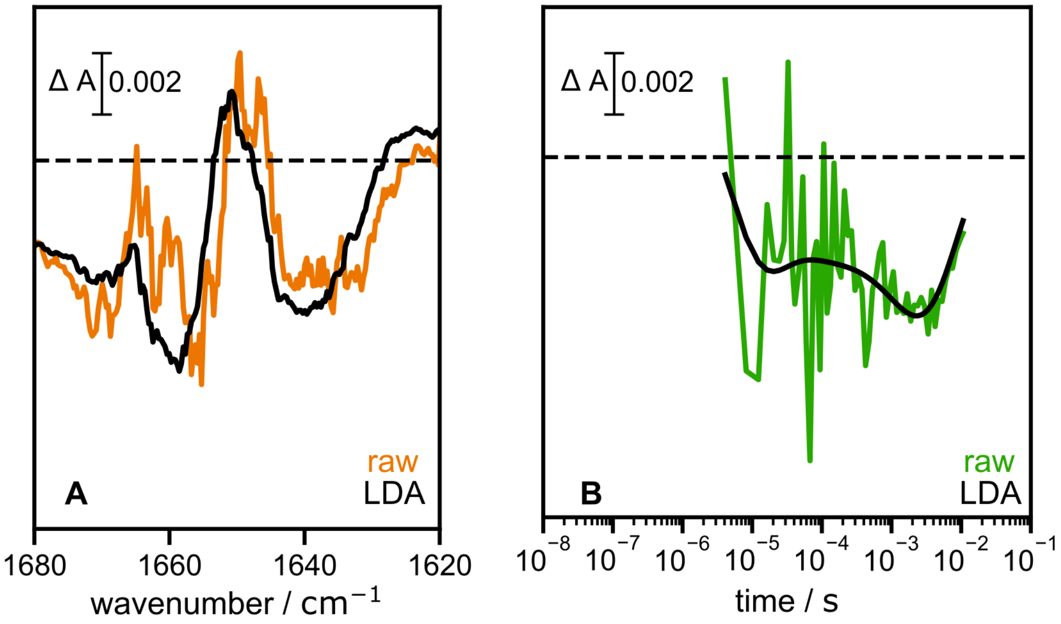

Figure 3-24: Lifetime density analysis (LDA) of DCS data. (A) Single-shot spectrum extracted at 300 µs (orange) and LDA-fitted spectrum (black). (B) 1670 cm^{-1} kinetic obtained by a single shot and LDA-fitted kinetic (black). For the LDA an alpha value of 10 was used. Figure adapted ref.[61].

3.3.3 Protonation Reactions

The characterization of the proton transfer steps by IR spectroscopy contributed to a large extent to the understanding of the functional mechanism of microbial rhodopsins. Time-resolved IR difference spectroscopy together with site-directed mutagenesis allows in some cases for an unequivocal assignment of protonation states of ionizable amino acid residues in proteins.[22] A prominent example is the proton transfer from the protonated RSB to the counter ion D85 in *Hs*BR (cf. 1.1.1). During the M-intermediate a positive band centered at 1762 cm^{-1} appears, which has been interpreted as the protonation of D85, which serves as a counter ion to the RSB in the ground state.[118] This band stays positive and therefore D85 remains protonated until the recovery of ground-state *Hs*BR. However, the band position redshifts by less than 10 cm^{-1}, which was interpreted as an environmental change of D85 during the M→N transition.[117] Because *Hs*BR has a cyclic photoreaction and can therefore be excited multiple times, such protonation dynamics have been traced already by stroboscopic and later by step-scan FTIR spectroscopy.[107, 116, 117] Difference bands originating from carboxylic ν(C=O) vibrations of single amino acids are usually much weaker than chromophore bands or amide I bands (cf. Figure 3-19), which necessitates an experimental design which allows to obtain data with sufficiently high SNR. This can usually be achieved by using longer pathlengths and therefore increasing the signal size, because the background absorption is usually weaker than in the amide I range. In this context, the use of QCLs as light sources is superior as compared to conventional FTIR spectroscopy using globars, because their high emission power permits penetration of longer pathlengths.

Here the DCS and the EC-QCL setup have been used to reproduce the spectro-temporal changes of *Hs*BR in the frequency range between 1800 - 1700 cm^{-1}, which have been well described by FTIR spectroscopy (see e.g. ref.[7] for a review). The DCS laser module provides access to a spectral range of about 1770-1720 cm^{-1}. Similarly, as in the amide I range, the nominal tuning range of the EC-QCL exceeds this spectral range but was limited here for comparison. As can be seen in Figure 3-25, the datasets from both setups agree well with each other and with data obtained by step-scan FTIR.[7] The amplitudes of the bands in DCS are slightly higher than in the EC-QCL experiment, which can be explained by slightly different sample preparation as well as slightly different excitation energies (compare Figure 3-25 A&B). The SNR of the EC-QCL dataset is higher than in DCS, which was already discussed in section 3.3.2. However, in this comparison the extent of acquisition averaging is more than 10 times higher in the EC-QCL experiment and therefore the SNR is not comparable.

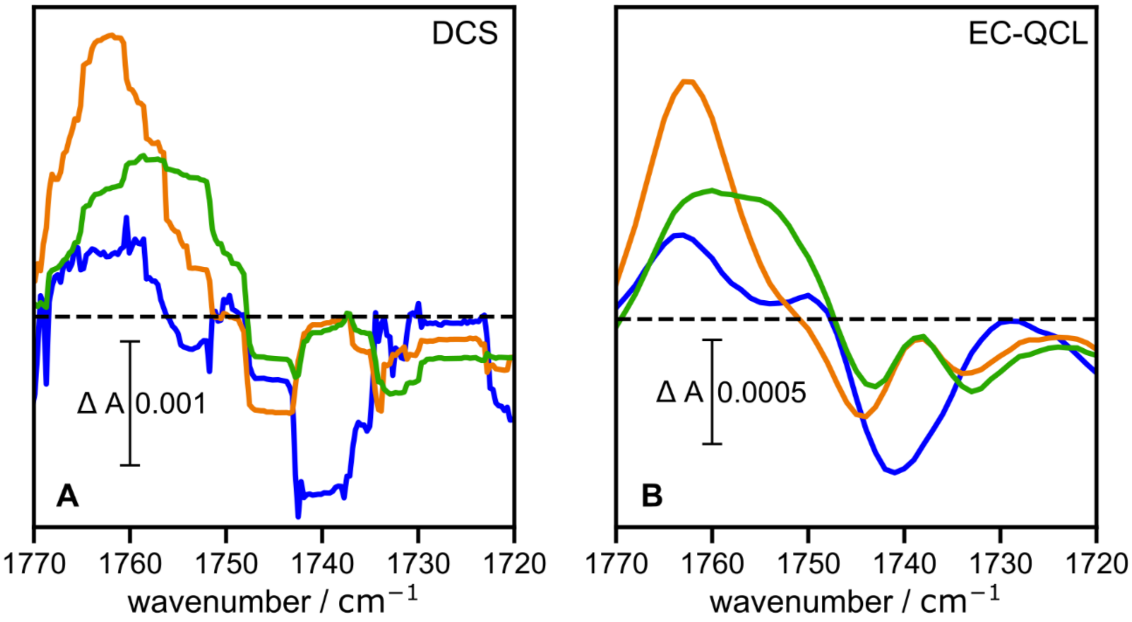

Figure 3-25: Protonation dynamics of *Hs*BR probed by DCS (A) and EC-QCL based spectroscopy (B). Difference spectra extracted at 20 µs (blue), 300 µs (orange) and 5.3 ms (green) representing mostly L, M and N/O intermediates. The DCS dataset was recorded by averaging 179 acquisitions. The EC-QCL dataset was recorded by averaging 50 coadditions per transient with a spacing of 1 cm^{-1}, leading to a total of 2500 excitations. Both datasets were postprocessed to a similar spectral resolution of ~4.5 cm^{-1}. The data presented in panel B has been recorded by Pit Langner.

The M spectra in Figure 3-25 display a prominent positive band located at 1762 cm^{-1} which redshifts during the M→N transition and is assigned to protonated D85 (vide supra). The L intermediate (blue spectrum) displays a negative band at 1742 cm^{-1}. The presence of this band led to a controversy (see ref.[23] for an overview) about a potential deprotonation of D96. This controversy arose because time-resolved measurements at room temperature did not resolve the small band centered at 1748 cm^{-1} and therefore the purely negative band at 1742 cm^{-1} was believed to stem from a deprotonation of D96.[119] However, later it was clearly shown that the negative band at 1742 cm^{-1} during the lifetime of L is a result of hydrogen bonding changes of D96&D115 and D96 deprotonates during the M→N transition.[23]

This discourse illustrates the non-trivial interpretation of carboxylic C=O bands and the importance of methods capable of achieving high SNR and spectral resolution to resolve neighboring side bands. While in the dataset, obtained by using the EC-QCL, the small band at 1748 cm^{-1} is clearly resolved, the data obtained by the DCS setup is slightly too noisy to resolve this feature (Figure 3-25). If the same number of sample excitations as in the EC-QCL experiment would have been used, the noise can be expected to decrease by a factor of ~3.7 allowing to resolve this band. In the present case this was not done because this laser module suffers from long term instabilities, which do not allow to average acquisitions over several hours.

Next, the experiment was restricted to a single acquisition as it was carried out already in the amide I range (cf. chapter 3.3.2). As can be seen in Figure 3-26 A-C, a single acquisition by the DCS setup is sufficient to resolve the spectro-temporal features associated with the protonation of D85 in *Hs*BR. In a single-shot experiment, the EC-QCL provides only a single transient, albeit with higher time resolution and SNR (Figure 3-26 D). The difference spectra presented in Figure 3-26 A, C display abrupt changes in intensity at specific frequencies. This stems from the fact that in this laser module the intensity of the laser lines varies drastically at certain frequencies. When the spectral averaging (compare chapter 1.4.3) procedure is applied, these features may arise. It shall be noted that the relatively low background absorption of the protein backbone and water in this spectral range together with the high emission power of the QCLs, allowed to have a high amount of protein in the beam path, which enables to achieve large difference signals of several mOD in this spectral range. In FTIR spectroscopy, where the background absorption in the amide I spectral range sets the upper limit for the sample thickness, the signals caused by carboxylic ν(C=O) vibrations are usually smaller.

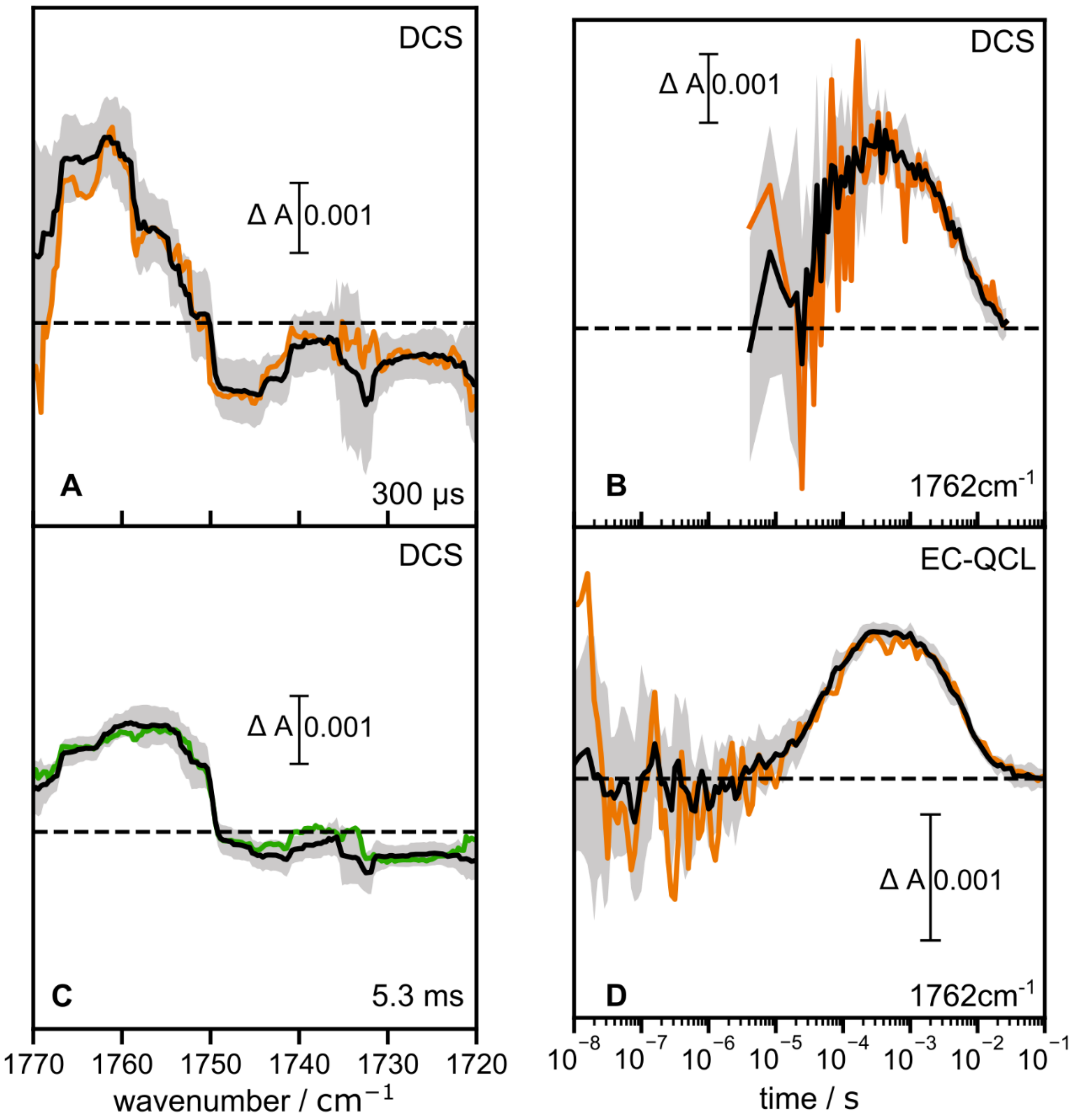

Figure 3-26: Single-shot protonation dynamics of D85 in *Hs*BR. (A, C) Difference spectra at 300 µs (A) and 5.3 ms (C) acquired by DCS. (B, D) Transients at 1762 cm^{-1} measured by DCS (B) and the EC-QCL (D). In all panels, the colored trace resembles single-shot data, while the black trace shows the average of ten single shots. The gray shading displays the standard deviation calculated from ten single shots ($\Delta A_{10} \pm \sigma$). The data presented in panel D has been recorded by Pit Langner. Figure adapted from ref.[61].

To scrutinize the reliability of the single-shot experiments, dissociable protons within the protein were exchanged to deuterons. This leads to two effects: The vibrational isotope effect (VIE), i.e., a frequency shift of certain vibrational bands and a slowing down of protonation reactions, which is termed kinetic isotope effect (KIE). Those phenomena are well described for microbial rhodopsins.[120] In bacteriorhodopsin, the L→M transition (protonation of D85 by RSB) displays a large KIE, while the M→N and subsequent transitions have a smaller KIE.[121] Figure 3-27 B, C shows the aforementioned behavior by comparing the transients assigned to the protonation of D85 in H_2O and D_2O. A KIE of 4 for the L→M transition and ~1.5 for the M→N/O transition were derived from globally fitting the dataset recorded by ten shots. Those values are in reasonable agreement in comparison to literature data, considering that the literature values stem from time-resolved UV-VIS data (See ref.[120] and references therein). It shall be noted that the analysis of KIEs depend strongly on fitting procedures and therefore can be interpreted in various ways. A more elaborate way to discuss KIEs can be achieved by the use of proton inventory plots.[78] The carboxylic ν(C=O) mode of D85 redshifts by ~10 cm^{-1}, as already demonstrated by FTIR spectroscopy.[92, 122] Our DCS setup is able to resolve this shift in a single shot (Figure 3-27A). Again, in terms of SNR the EC-QCL setup excels the DCS setup, but DCS yields spectro-temporal information which enables the analysis of the VIE, which is not possible in a single-shot experiment using the EC-QCL.

Taken together, both QCL-based spectrometers are able to resolve the protonation of a single amino acid by a single-shot experiment. While the kinetic information of the EC-QCL excels the one from DCS, the latter provides spectral information. The advantage to obtain spectral information, even in a small spectral range, is nicely illustrated with the example of D85. The ν(C=O) band rises in the L→M transition upon protonation and then undergoes a spectral redshift in the M→N transition (*vide supra*). The EC-QCL setup would not be able to resolve such spectro-temporal features in single- or few-shot experiments. Therefore, the combination of both methods may be advantageous in many cases.

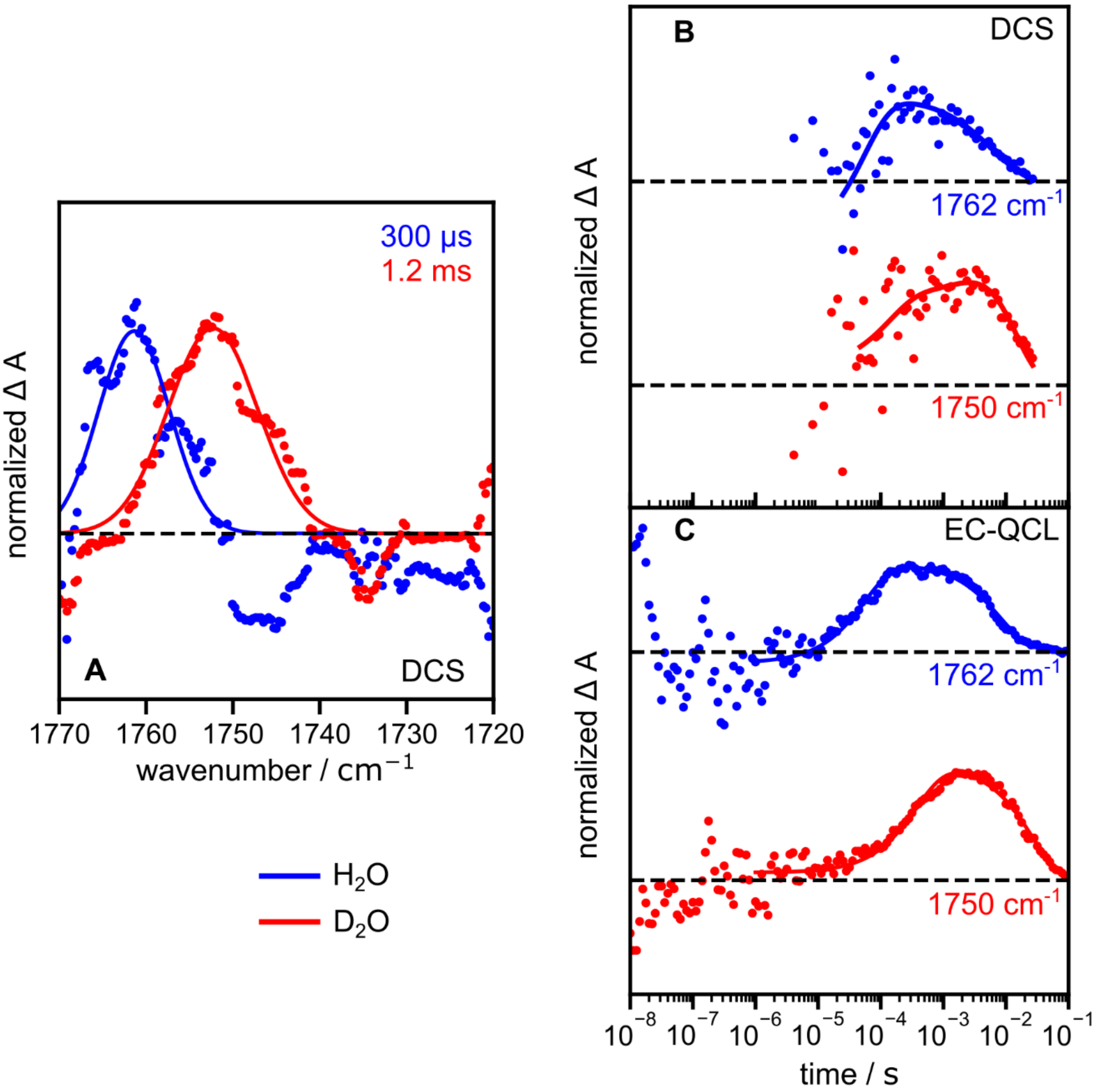

Figure 3-27: Isotope effects revealed by single-shot IR spectroscopy. (A) Difference spectra of *Hs*BR rehydrated in H_2O (blue) and D_2O (red). The blue spectrum is the same spectrum as shown in Figure 3-26 (300 µs), the red spectrum is extracted at 1.2 ms, because the M intermediate is accumulated at later times in D_2O. (B, C) Transients, showing the protonation of D85 in H_2O (blue) and D_2O (red) obtained by DCS (B) and the EC-QCL (C). In H_2O the transient at 1762 cm^{-1} and in D_2O at 1750 cm^{-1} are shown. The data presented in panel C has been recorded by Pit Langner. Figure adapted from ref.[61].

3.3.4 Monitoring Rhodopsin Activation by Single-Shot IR Spectroscopy

The experiments presented in this chapter were performed in collaboration with AG Bartl (Humboldt Universität zu Berlin), who provided the samples and introduced me to the handling of bovine rhodopsin. Experiments and data analysis were conducted by myself.

After showcasing the possibility to probe protein dynamics by single-shot IR spectroscopy on a well characterized model system (*Hs*BR, see 3.3.2 and 3.3.3), the study of an irreversible photoreaction sets the next milestone for establishing QCL-based spectroscopy for the study of biological systems. The visual pigment rhodopsin is a prototypical type-II rhodopsin and has been widely studied as a model system for G-protein-coupled receptors. Binding the 11-*cis* retinal as an inverse agonist, which is photoconverted to the full agonist all-*trans* retinal, it is simpler to study GPCR activation with visual rhodopsin as compared to ligand-activatable GPCRs. On the other hand, as compared to the study of reversible photocycles of type-I rhodopsins, their irreversible photoreaction renders a thorough spectroscopic analysis very challenging. Due to convenient isolation and purification methods, bovine rhodopsin has been studied intensively by a plethora of biophysical methods.[9]

The photoreaction of bovine rhodopsin (Rho) is reviewed in detail in ref.[9] and briefly explained below (Figure 3-28 A). Upon photon absorption, 11-*cis* retinal isomerizes to all-*trans* retinal within 200 fs with 100% selectivity and a quantum yield of 67% via photorhodopsin (Photo) to bathorhodopsin (Batho). In Batho, a large fraction (~60%) of the excitation energy is stored in a highly strained all-*trans* retinal, which is partially released by an elongation of the retinal chromophore, forming lumirhodopsin (Lumi) via the BSI intermediate. In the transition from Lumi to Meta I, the retinal chromophore relaxes further, which is believed to trigger the first global protein conformational changes, i.e. rotation of transmembrane helices 5 and 6. The positive charge of the retinal Schiff base is stabilized by a complex counter ion, consisting of E113 and E181, where E113 serves as the primary counter ion until formation of Meta I. The conformational changes associated with Meta I formation are believed to switch the main counter ion from E113 to E181. Subsequently, RSB deprotonation leads to formation of the Meta II state, which is described as an equilibrium between Meta II_a, Meta IIb and Meta $IIbH^+$ states. Proton transfer from the RSB to E113, occurring during Meta I to Meta II_a transition, precedes large-scale protein conformational changes, which are associated with Meta IIb formation. Proton uptake from the bulk solution by protonation of E134 stabilizes the active Meta II intermediate by disrupting the so-called ionic lock between R135, E134, E247 and T251. The latter step explains why Meta II formation is favored at low pH. Finally, hydrolysis of the retinal Schiff base leads to free all-*trans* retinal and the apoprotein opsin. Branching of the photoreaction may occur during the lifetime of Meta I, resulting in RSB hydrolysis via Meta III.[9] Protein backbone changes associated with Meta IIb formation comprise an elongation of TM5 as well as tilt of TM6, evident from a comparison of the crystal structures of Rho and Meta II (Figure 3-28 B).[114] During the lifetime of Meta II, the G-protein is bound on the cytoplasmic side which activates the signaling cascade.[9]

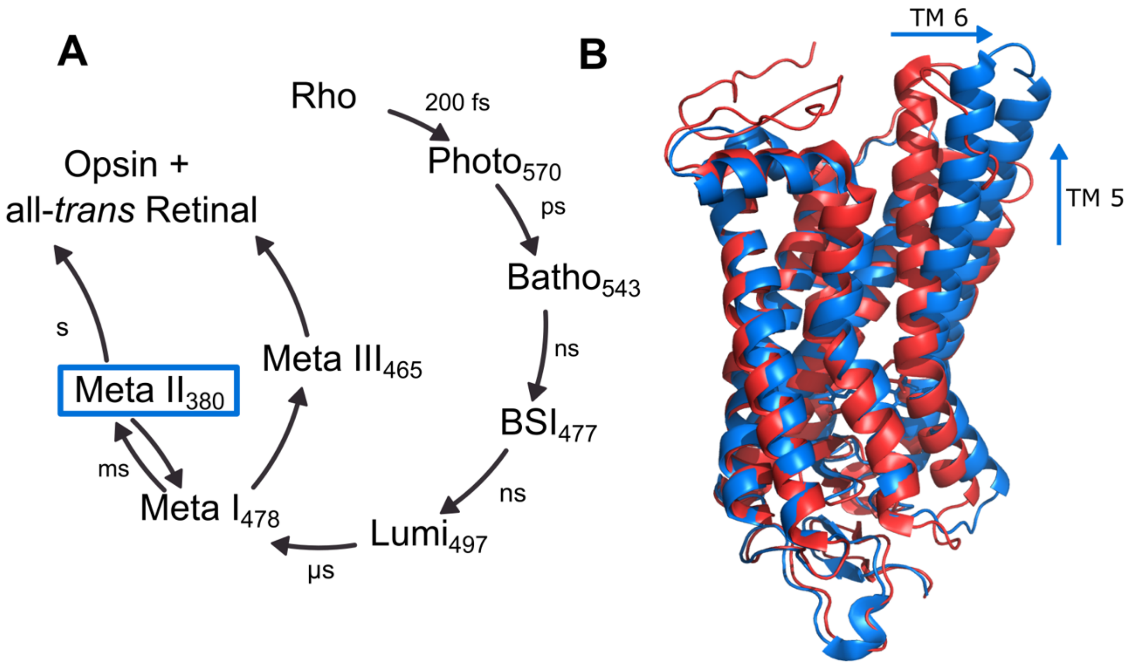

Figure 3-28: Activation of the G-protein-coupled receptor rhodopsin. A) Photocycle of bovine Rhodopsin, adapted from [9]. Subscripts indicate the absorption maxima of the intermediates. The Meta II intermediate (blue box) is the signaling state, where G-protein binding occurs. B) Structural comparison of dark-state Rhodopsin (red, PDB: 1U19) and the Meta II intermediate (blue, PDB: 3PXO). The arrows indicate the most prominent helix movements of transmembrane helix 5 and 6. The crystal structures (B) are shown with the C-terminus (cytoplasmic side) up, for the sake of consistency with microbial rhodopsins. B) is adapted from ref.[77].

Complementary to structural data, the aforementioned structural changes of the peptide backbone associated with the formation of Meta IIb, were characterized by spectroscopic methods, especially electron paramagnetic resonance (EPR) and FTIR spectroscopy. With the EPR label located at position 227 at TM5, the movement of TM6 was indirectly monitored. In a time-resolved experiment, the outward tilt of TM 6 is observed with a time constant of 1.9 ms, with formation of Meta II$_b$ at 20°C and pH 6.25 in detergent-solubilized bovine rhodopsin.[123] In FTIR spectroscopy a prominent band located at 1644 cm^{-1} was observed upon Meta II$_b$ formation and assigned to an amide I mode. As its rise coincides with the formation of Meta II$_b$, it may be interpreted as the backbone change indicative of the movement of TM6.[124]

With steady-state FTIR spectroscopy the longest-lived state or a stationary mixture of states can be investigated. Under our conditions (pH/pD ~ 6, T ≈ 20°C), the Meta II$_b$H$^+$ state is predominantly accumulated.[124] The FTIR difference spectra (Figure 3-29) reproduce already published data.[125] Most prominent bands are located at 1238 and 1555 cm^{-1} and assigned to chromophore bands.[126] The differential features at 1768 (-)/1747 (+) and 1734(-)/1745(+) have been assigned to hydrogen bonding changes of D83 and E122 respectively, whereas the negative band at 1734 cm^{-1} is a shoulder of a negative band at 1726 cm^{-1}, which is believed to be an amide I band.[127] However also a ν(C=O) vibration of a lipid ester group gives rise to difference band in that spectral range (cf. chapter 3.2).[101] The positive band at 1712 cm^{-1} has been assigned to the protonation of E113.[126] The large band located at 1644 cm^{-1} with a low-frequency shoulder has been assigned to an amide I vibration.[124, 126] The ν(C=N) vibration of protonated RSB of Rho is located at 1659 cm^{-1} and downshifts to 1623 cm^{-1} upon deuteration. Another intense negative band located at 1655 cm^{-1} (-) does not shift upon isotopic labeling of the retinal nor deuteration and can therefore be assigned to a band caused by the protein. An unequivocal band assignment of the ν(C=N) mode of the RSB of Rho is only possible with the help of ^{13}C-labeled retinal in combination with FTIR measurements at high spectral resolution and is therefore not clearly visible in our FTIR data (Figure 3-29 B).[125, 128]

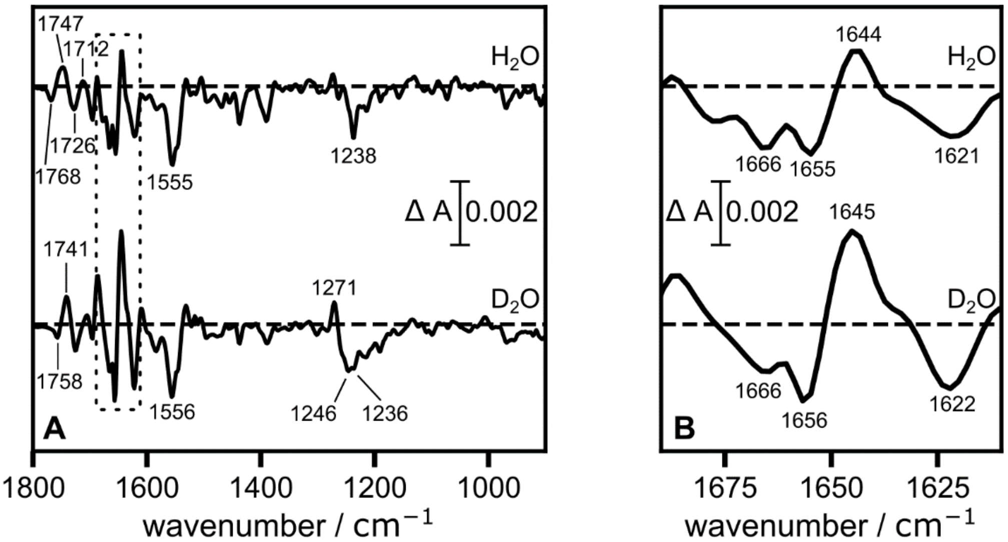

Figure 3-29: Steady state FTIR difference spectroscopy of ROS in H_2O and D_2O. Under the present conditions (pH/pD ~ 6, LED illumination λ = 532 nm, T ≈ 24°C), the Meta II state is predominantly accumulated. The difference spectrum recorded in H_2O is multiplied by a factor of 2 to facilitate the comparison of the spectra. A) Full spectrum, dashed box indicates spectral region of interest. B) Zoom into the frequency range where amide I bands occur. The spectra were recorded at a spectral resolution of 4 cm^{-1}.

To test the possibility to probe the dynamics of bovine rhodopsin as a model system for GPCR activation, the transient at 1644 cm^{-1} has been measured with the EC-QCL setup (Figure 3-30) following pulsed excitation. A positive signal, well above the noise level, arises after several ms, remaining constant until the end of data recording (Figure 3-30A). Performing the experiment on three independently prepared samples (Figure 3-30B) yields reproducible results. Fitting a mono-exponential function to the kinetic, yields time constants of 3.4, 4.4 and 9.7 ms, which is in good agreement with the kinetic information obtained from EPR experiments (*vide supra*), considering slightly different conditions.

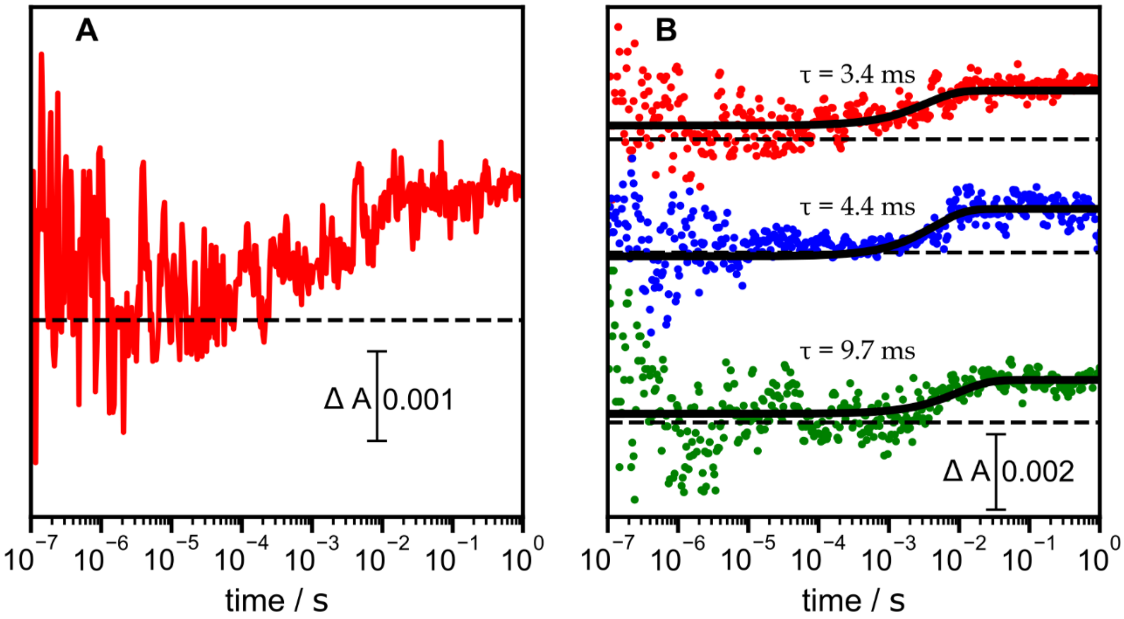

Figure 3-30: Reproducibility of single-shot experiments conducted with IR flash photolysis on ROS in H_2O recorded at 1644 cm^{-1} probing the amide I vibration A) Representative single-shot transient. B) Comparison of three independent measurements on three different samples. Colored scatter plots show raw data and black lines show mono-exponential fits, which yield the displayed time constants. Note that the red trace shows the same data as in A). To facilitate comparison, the blue and green traces are multiplied by a factor of 1.5 and 1.8, respectively, to match the intensity of the red trace. The different amplitudes are due to the use of different spacers (red: 13 µm; blue, green: 6µm).

To assess bleaching behavior under our experimental conditions, we applied ten consecutive excitations to the sample. As the visible excitation laser bleaches the rhodopsin molecules, the amplitude of the signal decreases gradually (Figure 3-31). The transients recorded after exciting the rhodopsin sample for the second and third time, resemble the transient recorded after the first excitation and are reduced in amplitude by less than half as compared to the initial amplitude (Figure 3-31 A, B). As expected, the average of acquisitions 1-3 shows a reduction in signal as well as noise as compared to the first acquisition, while the signal is absent in the average of the later acquisitions (Figure 3-31C). This illustrates that under the present conditions, only a fraction of rhodopsin molecules is bleached by the excitation laser (λ = 532 nm, E_{exc}/A = 4.5 mJ/cm^2). This holds true for samples prepared with a 13 µm (H_2O) as well as a 25 µm (D_2O) spacer. To semi-quantitatively characterize the reduction in noise upon averaging multiple acquisition, the residuals of a mono-exponential fit to a single-shot transient and a three-shot transient were compared (Figure 3-32). Under the assumption, that the fit describes the absorbance changes appropriately, the residuals of the fit reflect noise only. In fact, the fits of the single-shot and three-shot data result in very similar time constants, reassuring that the observed processes are the same and most likely no long-lived intermediate is excited. Comparing the residuals of the two fits, it is evident, that the noise is reduced when three acquisitions are co-averaged. In fact, calculating the standard deviation σ along the time axis of the residual transient (Figure 3-32) shows that the noise is reduced by a factor of 1.55, which is close to the theoretical value of $\sqrt{3}$.

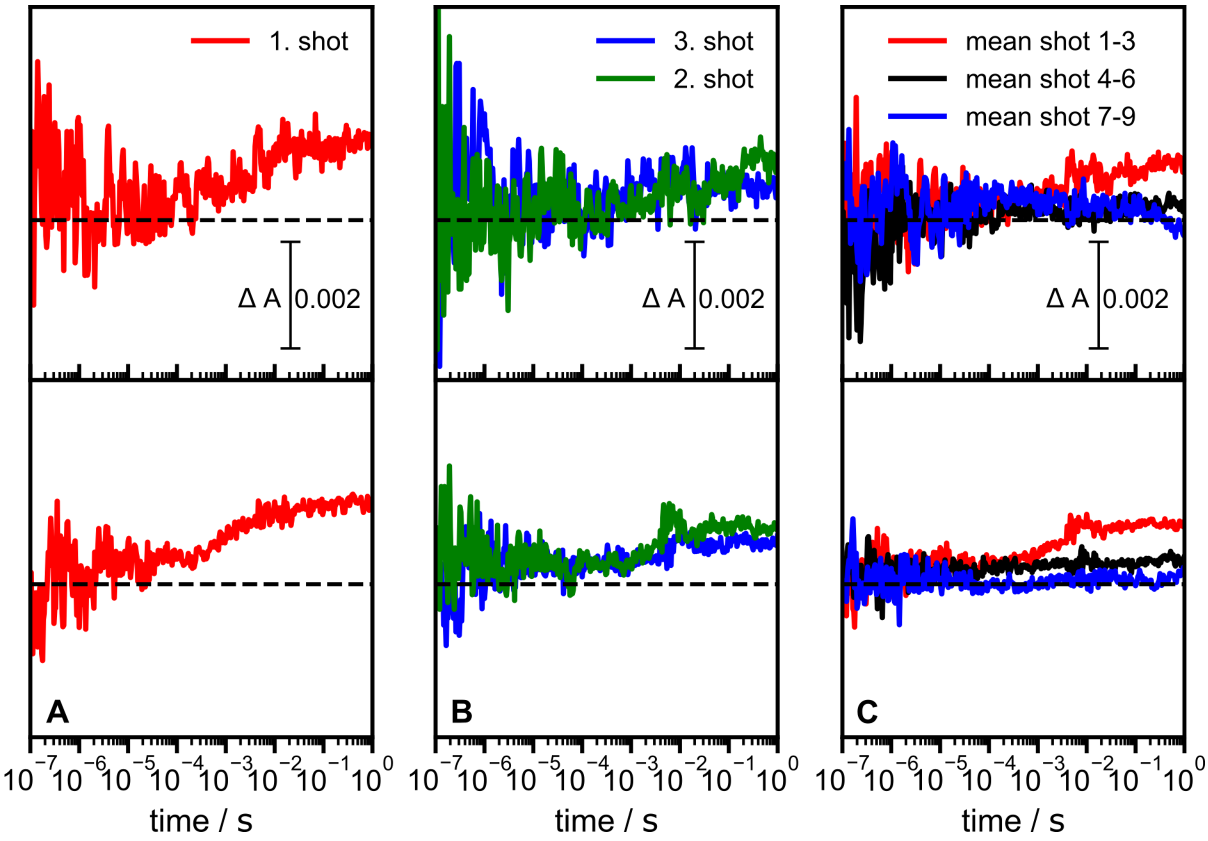

Figure 3-31: Photobleaching and acquisition averaging of multiple single-shot transients recorded on the same sample at 1644 cm^{-1}. Upper panel: Experiments conducted in H_2O with a 13 μm spacer. Lower panel: Experiments conducted in D_2O with a 25 μm spacer. A) Transient recorded after exposing the sample to the first laser excitation after preparation in the dark. B) Transients recorded after exposing the same sample to the second (green) and third (blue) laser flash. C) Transients obtained by co-averaging acquisitions 1-3 (red), 4-6 (black) and 7-9 (blue). The time between excitations was set to 8 s.

However, due to the logarithmic averaging along the time axis and the lower noise on the >ms timescale, the absolute noise reduction is more prominent in the early time scales below 100 μs. In the data shown in Figure 3-32, the signal in the ms time range is already well above noise level, rendering acquisition averaging only slightly advantageous in terms of SNR.

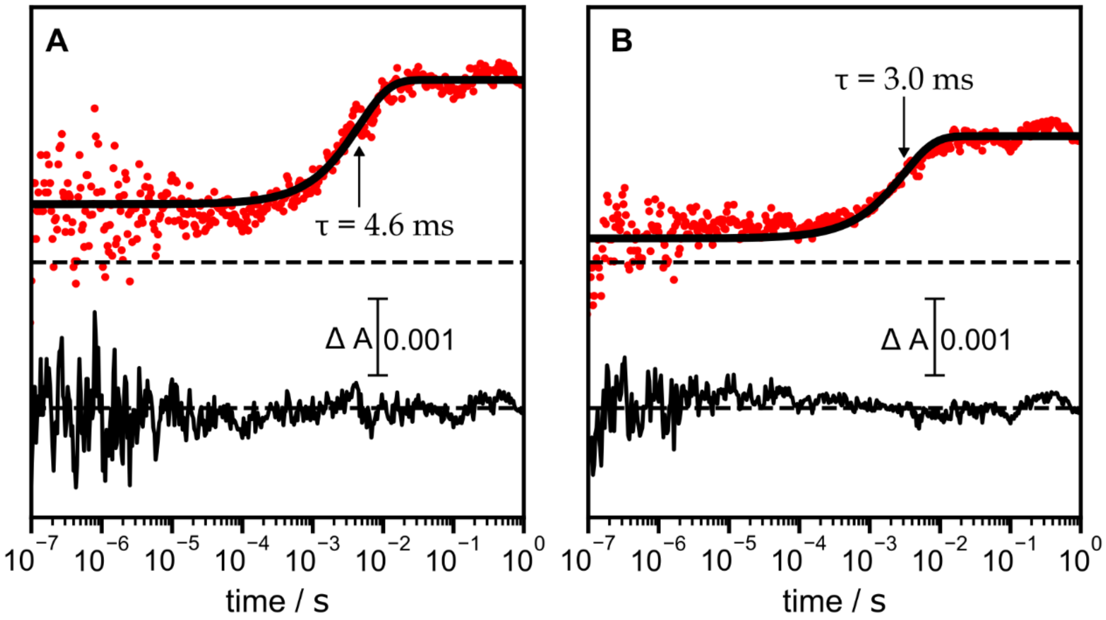

Figure 3-32: Noise reduction by averaging multiple acquisitions. A) First acquisition of the 1644 cm^{-1} transient recorded on a ROS sample in D_2O with a 50 µm spacer. B) Average of the first three shots obtained with the same sample as compared to A). Raw data is shown in red together with a monoexponential fit (black). The residuals of the fit are shown with an offset (black).

As already outlined in chapter 3.3.3, the EC-QCL setup excels in terms of SNR on a single transient but does not provide spectral information in a single-shot experiment. In order to obtain spectro-temporal information on the irreversible photoreaction of bovine rhodopsin, DCS has been employed. As the optical power is distributed over several comb lines and is therefore less intense for single laser lines as compared to the EC-QCL (cf. 3.3.2), the H_2O based buffer was exchanged to D_2O and a 25 µm spacer was used. This allows to optimize signal strength and transmitted light intensity to obtain high SNR (cf. 3.3.2). The dataset presented below was obtained by averaging the first three acquisitions of three independently prepared samples, resulting in an averaged dataset of nine acquisition (Figure 3-33). Individual single-shot datasets are too noisy and therefore not shown. To increase SNR, the DCS dataset was spectrally smoothed to a spectral resolution of 8.1 cm^{-1}. The DCS data is very noisy below 1 ms, making it impossible to assign spectral features of the Lumi intermediate (Figure 3-33A) and perform a global analysis with reliable fit results. Instead, methods such as LDA are more robust when modeling noisy data.[129] In fact LDA models the noisy data satisfactorily from 1 ms onwards. Between 1 ms and 100 ms, LDA reveals to major distributions of time constants centered around 5 ms and 60 ms, indicative for the Meta I to Meta II transition and a probably further Meta II decay, respectively. However, since the time range for the experiment ends shortly after 100 ms, the latter process is not clearly assignable. The local minima before and after those transitions most likely represent the times when Meta I and Meta II are predominantly accumulated. In order to increase the SNR, multiple spectra of the logarithmically averaged dataset were averaged, as indicated by the dashed boxes in Figure 3-33C. The time constants below 1 ms are describing the large noise in the dataset.

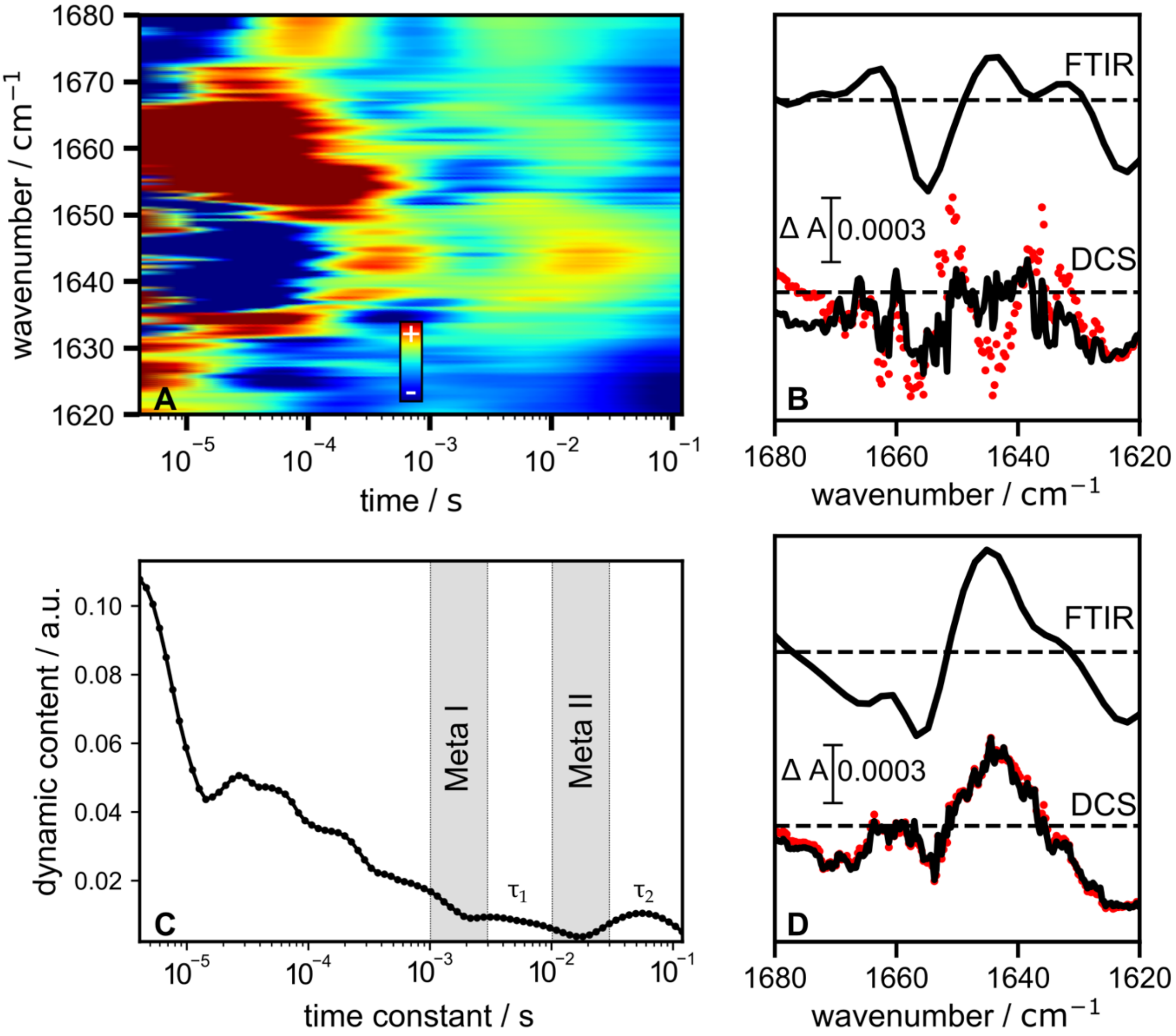

Figure 3-33: Dual-comb spectroscopy applied to the study of the rhodopsin photocycle. A) Heatmap of the absorbance changes as a function of time and wavenumber. Note that the color code is scaled to appropriately display the data in the millisecond time range. Therefore, the large noise in the µs range is out of scale. C) Dynamic content (see ref.[130] for a description) obtained by lifetime density analysis (LDA). Dashed boxes indicate representative times where the Meta I and Meta II intermediates are extracted (see B and D). In order to obtain an appropriate modelling by the LDA, time constants larger than the measurement range were allowed (up to 1 s). B) Meta I spectrum obtained by DCS (red: raw data, black: LDA fitted data) and Meta I spectrum obtained by steady-state FTIR spectroscopy at 5°C and pD~9. D) Meta II spectrum obtained by DCS (red: raw data, black: LDA fitted data) in comparison to the Meta II spectrum obtained by steady-state FTIR spectroscopy at 24°C and pD~6 (compare Figure 3-29). All experiments were carried out in D_2O. The FTIR spectra were scaled down to match the intensity of the spectra obtained by DCS.

The averaged spectrum obtained for the Meta I intermediate has a lower SNR as compared to the Meta II spectrum (cf. Figure 3-33 B, D). This can be explained by considering that roughly 10 times more datapoints were averaged to yield the Meta II spectrum. As the bands are just slightly above the noise level for Meta I, one needs to be cautious to not overinterpret spectral features. The Meta I spectrum (Figure 3-33B) displays two major bands located around 1625 and 1655 cm^{-1} and the prominent amide I band at 1644 cm^{-1} is absent. It compares relatively well to the Meta I spectrum obtained by steady-state FTIR experiments, which resembles previously published Meta I spectra in D_2O.[131] However, a thorough interpretation of band features requires a higher SNR. For Meta II (Figure 3-33D) instead, all bands are well above noise level and can be interpreted with more confidence. The spectrum resembles those from steady state experiments (cf. also Figure 3-29).[125, 131] The shoulder at 1636 cm^{-1}, which is nicely resolved at 2 cm^{-1} spectral resolution in FTIR[125], is not clearly resolved after smoothing the DCS dataset to 8.1 cm^{-1} (cf. chapter 3.3.1). A negative band located at 1670 cm^{-1} is present, whereas in literature a small negative band at around 1666 cm^{-1} was reported.[125, 131] Kinetics extracted from DCS dataset are noisy in comparison to the EC-QCL dataset and therefore not shown. Beside the limitations in terms of SNR below 1 ms, the EC-QCL setup as well as DCS are able to probe the reaction dynamics of Meta II formation occurring on the millisecond timescale. Minor spectral differences may be explained by different spectral resolutions and intense spectral smoothing of the DCS data (cf. Figure 3-20).

To illustrate that QCL-based methods are also capable of probing perturbations of single amino acids during an irreversible photoreaction, the transient at 1741 cm^{-1} is monitored by the EC-QCL setup (Figure 3-34A, cf. Figure 3-29A). It represents the absorption changes of the carboxylic ν(C=O) vibrations of D83 and E122 in D_2O, which remain protonated throughout rhodopsin activation but undergo environmental changes upon Meta II formation.[126, 127] The signal, monitored at 1741 cm^{-1} is smaller than 0.5 mOD but still above noise level from 1 ms onwards. The rise of the signal in the millisecond time range matches the rise of the band monitored at 1644 cm^{-1} and hence the Meta II formation under the present conditions (~23°C, pD 6). The apparent decay of the band at ~200 ms is observed in only one of the two transients (data of single experiments not shown). It is most likely caused by a fluctuation of the emission of the QCL and is not a signal originating from the sample. This phenomenon occurs randomly in our EC-QCL setup at times >100 ms. To correct for this, a setup with a second MCT reference detector may be advantageous, which will be discussed in chapter 4.3. Improving the sample preparation in order to increase the signal strength may enable to record spectro-temporal data by the DCS setup in the future.

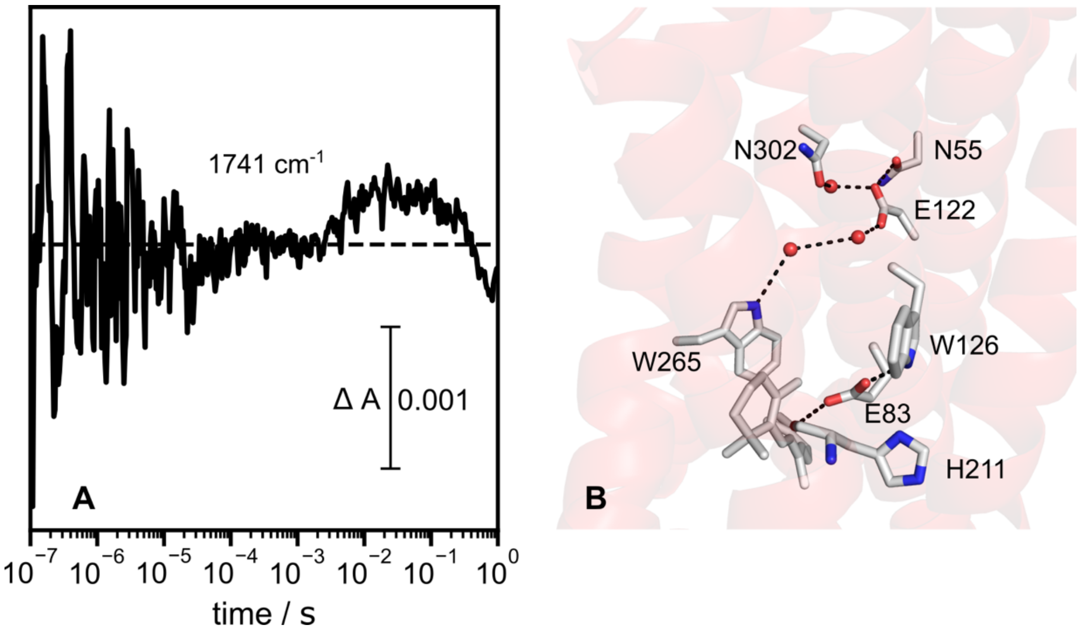

Figure 3-34: Probing perturbations of single amino acids by single-frequency single-shot IR spectroscopy. A) Transient recorded at 1741 cm^{-1} by the EC-QCL setup. The data shown is the average of two individual single-shot experiments in D$_2$O with a 50 µm spacer. The absorption changes monitored at 1741 cm^{-1} are associated with environmental changes of D83 and E122. B) Environments of D83 and E122. (PDB: 1U19). Water molecules are shown as spheres.

3.3.5 Dual-Comb Spectroscopy Applied to the Study of Slow Reactions

The experiments presented here were done in collaboration with IRsweep in Stäfa, Switzerland. DCS experiments were conducted together in Stäfa, while the rapid-scan FTIR experiment was conducted by myself in Berlin. Sample purification and reconstitution was done by Mariafrancesca La Greca (Genetic Biophysics, Freie Universität Berlin). Data analysis was performed by myself with contributions from Xinyi Huang and Raphael Horvath (IRsweep).

When studying cyclic reactions in the mid-IR, FTIR spectroscopy allows to routinely obtain broadband (>2000 cm^{-1}) spectra with millisecond to nanosecond time resolution using the rapid-scan or step-scan technique respectively.[7] Laser-based systems, such as pump-probe spectroscopy, even enable to obtain spectro-temporal data with femtosecond time resolution.[132] With the advent of tunable quantum-cascade-lasers, scanning type spectroscopy has been revived, providing access to the nanosecond to second timescale[47, 133-135]. In many cases, the reaction at study needs to be not just only reversible, but also sufficiently fast (~1 s). This is required, because either the experimental design demands to probe the same reaction repeatedly (step-scan FTIR, pump-probe or scanning type spectroscopy) and/or extensive averaging of acquisitions is necessary to achieve a satisfactory signal to noise ratio (rapid-scan FTIR, multiple probe spectroscopy[136]).[22] Instead, quantum-cascade-laser based dual-comb spectroscopy allows to record spectro-temporal data with every acquisition[56] and has achieved satisfying signal-to-noise ratios (SNR) in single-shot experiments [57, 61].Aside from individual advantages and disadvantages of the above-mentioned techniques, a common limitation for some methods is the accessible time range. In FTIR spectroscopy, nanosecond or microsecond time resolution can be achieved by the step-scan technique which is restricted to tens of milliseconds due to limited memory. Further, instabilities of the mobile mirror introduce baseline shifts mostly apparent in the time range > ms. This may be circumvented by merging two step-scan datasets with high and low acquisition rates or by performing a separate rapid-scan experiment for the ms to s dynamics.[22] Here, time-resolved multiple probe spectroscopy is superior, as it allows to detect dynamics on the picosecond to second timescale in every acquisition[136, 137]. While the transients, recorded by our external-cavity QCL, are usually not limited by memory restrictions as the data is digitized with high and low sampling rates[47], they suffer from instabilities of the laser emission on the timescale > 100 ms. To date, dual-comb spectroscopy is limited to tens of milliseconds due to memory limitations[57, 61], but a recent update increased the available acquisition time to 128 ms (cf. 3.3.4). However, a second acquisition mode with millisecond time-resolution (long term = LT) can be used and may complement a dataset recorded with high time resolution (time resolved = TR).[72] Since the realization of two experiments demands usually more sample and time, a method which has a large time coverage in a single experiment is desired. This is particularly relevant for the study of irreversible reactions.

Due to the unique detection scheme of DCS, which does not employ any dispersive element (see 1.3.3), the access to different timescales does not involve a change of hardware settings as in FTIR spectroscopy. Therefore, both measurement modes can be combined into a single acquisition, which covers microsecond to second dynamics (hybrid mode) (Figure 3-35). In the novel hybrid mode, two TR datasets are subsequently collected where spectra are measured with 4 µs sampling rate. In the same acquisition several spectra are recorded subsequently with lower sampling rate (see Figure A. 7). Data transfer from the digitizer to the computer leads to deadtimes between the datasets and spectra, which is often unproblematic as the observed slow processes do not require high time-resolution.

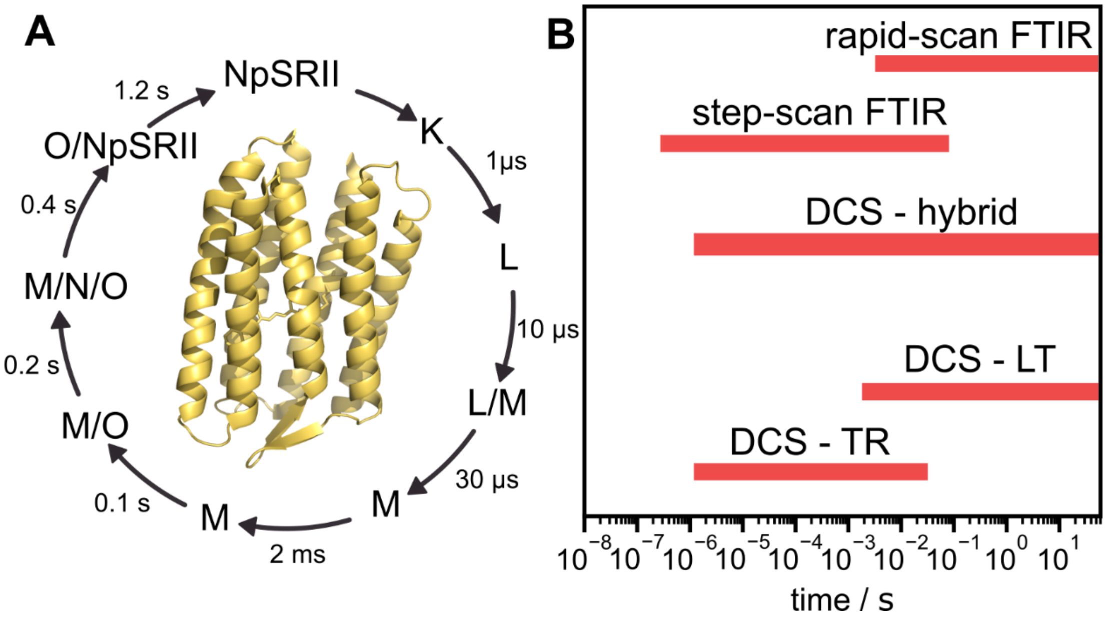

Figure 3-35: Extension of DCS to slow-cycling photoreactions. A) Photocycle of Sensory Rhodopsin II from *Natromonas pharaonis* (*Np*SRII) adapted from ref.[138] and crystal structure (PDB: 1H68). The depicted times correspond to the half times at 25°C. B) Time coverage of different measurement modes of DCS in comparison to FTIR spectroscopy.

To test and showcase this novel measurement mode, the photoreaction of sensory rhodopsin II from *Natromonas pharaonis* (*Np*SRII) has been used as a model system as its photocycle extends towards several seconds after light excitation (Figure 3-35A).[138] *Np*SRII undergoes protein conformational changes during its photocycle, which are indicated by strong amide I difference bands occurring on the µs timescale and persisting until several seconds after photoexcitation.[139] The relatively long recovery time of the photoreceptor renders the time-resolved vibrational experiment a challenging task. Using FTIR spectroscopy, slow dynamics (100 ms – s) may be studied by rapid-scan, while resolving the fast dynamics (ns-ms) requires the step-scan technique. The latter is a tedious task when a photoreaction with a slow recovery time is being probed. Under typical step-scan settings (spectral range: 1975-0 cm^{-1}, spectral resolution 8 cm^{-1}) roughly 500 mirror positions need to be probed repeatedly, usually > 50 times per mirror positions to achieve sufficient SNR.

Under the experimental conditions used here (*Np*SRII reconstituted in DMPC- MSP1DE3 Nanodiscs, 40 mM NaCl, 5mM Mes, pH 6, ~20°C), the sample has returned back to its ground state after about 20 s (τ = 4.6 s) judging from rapid-scan FTIR spectroscopy (Figure 3-36 B). With an excitation frequency of 0.05 Hz, a step-scan FTIR experiment would take 5-6 days, which demands high stability of the sample as well as the spectrometer. To reduce the measurement time, Hein et al.[139] performed step-scan FTIR at 37°C and pH 8 on *Np*SRII reconstituted in purple membrane lipids, which allowed photoexcitation at 0.5 Hz. This experiment provides reasonable data, but with data quality, which imposes limitations on the interpretation of signals below ~1 μs. Irrespective of the aforementioned challenges, intermediate spectra were recorded with satisfactory SNR in the μs-ms time range, displaying large amide I bands, located at 1663 (-) and 1643 (+). Interestingly, the band pattern in the amide I region is already present 1 ms after photoexcitation and only changes slightly in intensity, but does not display any peak shifts until completion of the photocycle.[139]

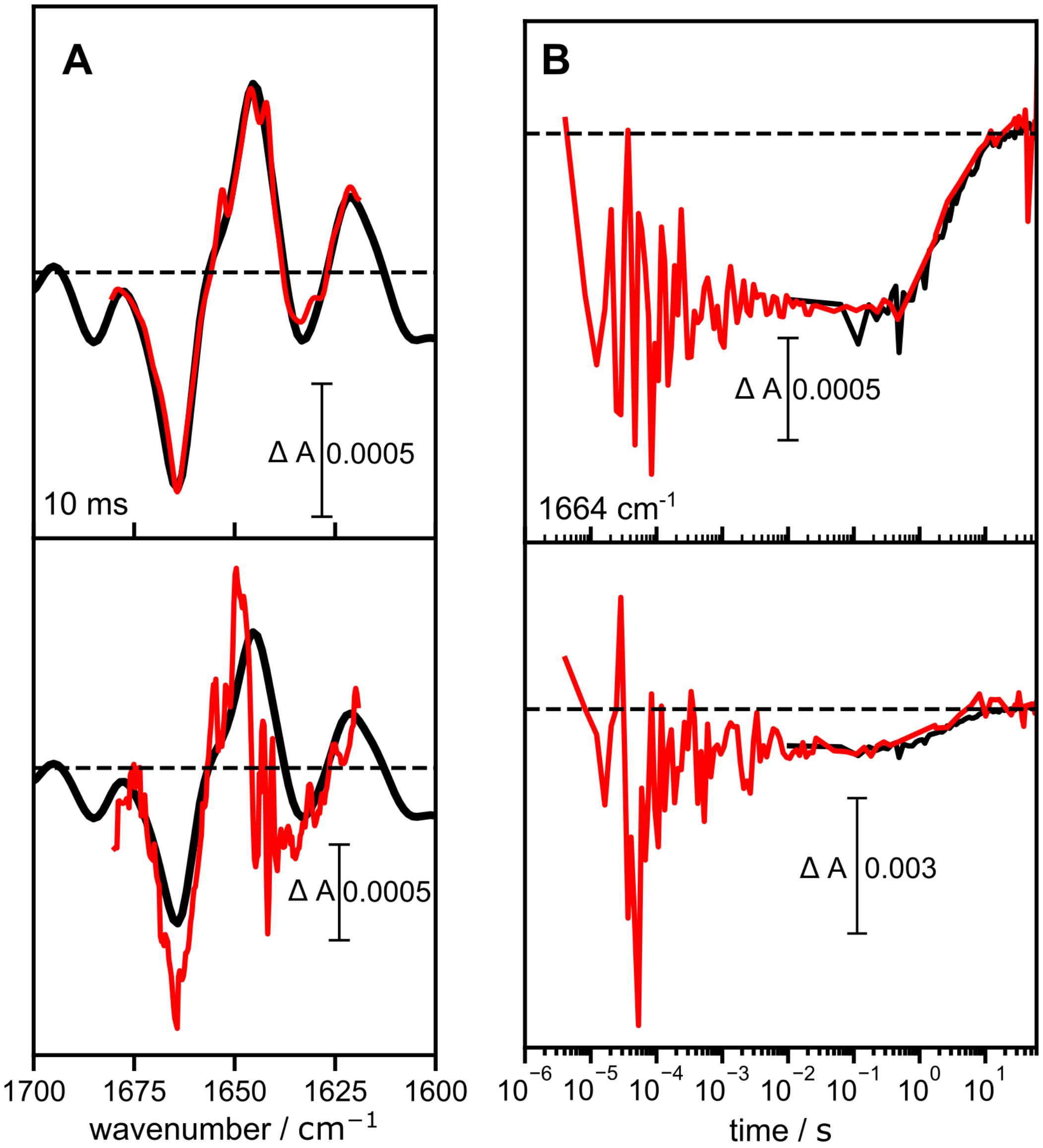

Figure 3-36: Dual-comb spectroscopy in hybrid-mode applied to the photoreaction of *Np*SRII. DCS data is shown in red, rapid-scan FTIR data in black A) Difference spectra, extracted 10 ms after pulsed sample excitation. B) Transient of the amide I band centered at 1664 cm^{-1}. Upper panel: DCS data obtained by co-averaging 41 acquisitions, smoothed to a spectral resolution of 2.8 cm^{-1}. Lower panel: DCS data obtained by a single-shot at 8 cm^{-1} spectral resolution. The FTIR data is collected by co-averaging 1140 acquisitions at a spectral resolution of 4 cm^{-1}. The DCS data was multiplied by a factor of 0.65 to match the intensity of the data obtained by rapid-scan FTIR.

The rapid-scan data recorded here (Figure 3-36, black, full spectra not shown), nicely resemble the results obtained by step-scan spectroscopy[139], but lack data below ~10 ms. Instead, DCS in hybrid mode is capable of monitoring spectro-temporal changes between 4 µs and 60 s after photoexcitation (Figure 3-36, red), albeit with a limited spectral range. Co-averaging 41 single acquisitions (which equals a recording time of about 60 minutes vs rapid-scan ~20 h), is sufficient to resolve all spectral features and provides excellent spectral and kinetic agreement with FTIR data (Figure 3-36, upper panel). As no prominent sub-ms dynamics are expected in this spectral range and do not show up in the dataset recorded by DCS, a thorough kinetic analysis to extract µs dynamics is not performed. Due to logarithmic averaging along the time axis, the noise decreases towards later times, before it increases again after ~10 s. The sudden increase of the noise is most likely caused by instabilities of the QCL. The origin of these instabilities is elusive, but was likely to be caused by an external perturbation such as electric fields from other devices located to close to the spectrometer. The increasing integration time at times > 10 ms leads to high SNR, which even allows to extract the spectro-temporal features in a single-shot experiment (Figure 3-36, lower panel).

In summary, DCS in hybrid mode extends the accessible time range of DCS from tens of milliseconds up to seconds and beyond. This is particularly useful for the study of slow-cycling systems, non-repetitive systems or even slowly reacting samples, which are not intrinsically light-activatable.

4 Discussion

4.1 Proton Pathway in *Ns*XeR and Implications for Inward Proton Transport

The photocycle of the inward proton pump *Ns*XeR has been studied by molecular spectroscopy to elucidate molecular alterations enabling inward proton translocation (see chapter 3.1). In the following section, the main findings are summarized (cf. Figure 4-1) and discussed in order to address the topic of directional proton transport.

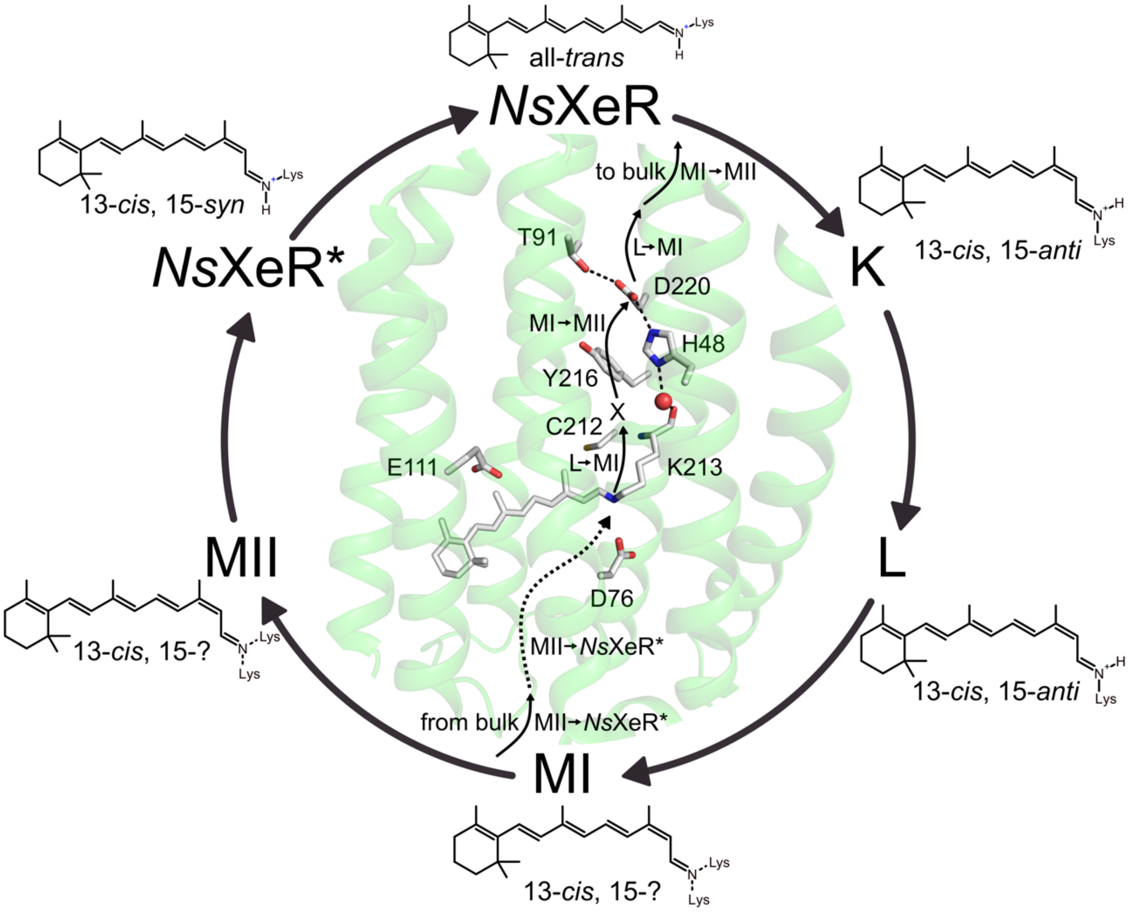

Figure 4-1: Molecular insights on inward proton transport in *Ns*XeR. Photocycle scheme assuming a sequential and unidirectional model. The configuration of the retinal chromophore is derived from FTIR experiments and the chemical structures are drawn in an idealized way. Note that the geometry of the chromophore embedded in the protein may differ to a certain extent. The configuration in the two M intermediates cannot be determined and is therefore shown with both possibilities as dashed lines. Inside: Crystal structure of *Ns*XeR (PDB: 6EYU) with relevant amino acids shown as sticks. Protonation steps observed throughout this thesis are indicated with solid arrows. The dotted arrow indicates a putative reprotonation pathway, which has not been studied extensively in this thesis. Possible hydrogen bonds are shown as dotted lines. Figure adapted from ref.[79].

The Role of the Chromophore for Inward Proton Transport

Light absorption by *Ns*XeR leads to the formation of a red-shifted K intermediate, absorbing at around 570 nm (596 nm).[39, 40] The band pattern observed by vibrational spectroscopy shows that the retinal chromophore has isomerized from an all-*trans* to a 13-*cis* configuration (see chapter 3.1.3). However, vibrational spectroscopy does not reveal a red-shifted ethylenic stretching vibration, indicative of a red-shifted K intermediate. The absence of such a K marker band and the appearance of a blue-shifted ethylenic mode absorbing at 1538 cm^{-1} raise questions about the exact retinal configuration, which can only be addressed by a thorough spectroscopic study employing isotopically labeled retinal molecules in combination with computational methods as it was performed for *Hs*BR[64, 65]. The insensitivity of the bands assigned to ν(C-C) modes upon H/D exchange during the lifetime of the K/L and L intermediates (cf. Figure 3-8) suggests that the retinal chromophore is most likely in a 13-*cis*,15-*anti* configuration[65], implying that the RSB proton is oriented towards the cytoplasmic side (Figure 4-1). With the formation of the L intermediate, the UV/vis absorption blueshifts towards 530 nm, indicative for a structural alteration at or near the retinal chromophore. As the ν(C-C) vibrations change only slightly during this transition, it can be assumed that the retinal remains in a 13-*cis*,15-*anti* configuration. Based on these findings, it is tempting to speculate that retinal isomerization already leads to a cytoplasmic orientation of the RSB proton which is engaged in a hydrogen bond network in L. This scenario sets the stage for the proton transport towards the cytoplasmic side occurring in the subsequent L→MI transition. However, for the prototypic outward proton pump *Hs*BR the retinal configuration of K and L was found to be 13-*cis*, 15-*anti*, too,[65] which likewise implies a cytoplasmic orientation of the RSB proton prior to RSB deprotonation. However, structural, spectroscopic and computational studies have shown that the RSB proton is not oriented towards the cytoplasmic side as the retinal adopts a highly twisted 13-*cis*, 15-*anti* geometry after photoisomerization.[19] During the L intermediate in *Hs*BR, the protonated RSB interacts with a water molecule, D85, and D212, which prepares proton transfer from the RSB to D85.[18, 19] In light of this, the interpretation of the RSB orientation in *Ns*XeR based on idealized retinal configurations must be considered very carefully. A first insight might be gained by the study of HOOP modes of the retinal chromophore, which are indicative of a twisted geometry of the retinal chromophore[19], but the exact chromophore geometry after light excitation may only be addressed reliably in future structural and spectroscopic studies. However, it has to be noted that among inward proton pumps, the extracellular binding pocket is distinctly different as compared to the prototypical outward pump *Hs*BR (cf. chapter 1.1.2 and Table A. 1). All inward proton pumps have in common that the extracellular binding pocket harbors only a single aspartate (D76 in *Ns*XeR, D85 in *Hs*BR), while the second aspartate (D212 in *Hs*BR) is replaced by a conserved proline (except for SzR4). Therefore, less electrostatic attraction by the extracellular side of the retinal chromophore might explain why the RSB proton is not oriented towards the extracellular but to the cytoplasmic side in inward proton pumps, as already suggested in ref.[29]

The isomeric state of the retinal chromophore during the two M intermediates cannot be addressed in detail, given the low intensities of bands associated with retinal vibrations when the RSB is deprotonated. The band pattern observed in the spectra of the long-lived intermediate *Ns*XeR* suggests a 13-*cis*, 15-*syn* configuration, reminiscent of the long-lived intermediate observed in *Po*XeR and in dark-adapted *Hs*BR.[29, 92] Therefore, it is unlikely that in *Ns*XeR 13-*cis* to all-*trans* isomerization precedes RSB reprotonation as it was suggested for SzR4 and concluded to be a key step for its inward proton transport.[34] In *Ns*XeR no indication for a branched photocycle, as it was discussed for *Po*XeR[31], was found, but in light of the similar band feature at 1538 (+)/1525 (-) cm^{-1} for the K and *Ns*XeR* intermediates a branching of the photocycle before the formation K may be considered if further evidence arises. Based on a small KIE for the M decay, it was concluded that the reprotonation of the RSB in *Po*XeR is rate-limited by the reisomerization of the retinal chromophore.[31] Instead, in *Ns*XeR the large KIEs observed for RSB de- and reprotonation indicate that proton transfer reactions itself are the rate-determining steps, but not the isomerization of the retinal. Taken together, the configurational changes of the retinal chromophore in the second half of the photocycle differ among inward proton pumps and do not provide a comprehensive explanation for inwardly directed proton transport in *Ns*XeR.

Proton Transfer between the Bulk and NsXeR Correlates with the M intermediate

Proton release and uptake to and from the bulk solution were monitored by the water-soluble dye DHPDS (Figure 3-2). At pH 7, proton release ($\tau_r = 1.45$ ms) precedes proton uptake ($\tau_u = 43.6$ ms). Proton release is retarded as compared to the formation of MI ($\tau_{L \rightarrow MI} = 159$ μs), associated with RSB deprotonation, similar as in *Hs*BR. For *Hs*BR in purple membrane it was shown that proton release precedes proton uptake and the proton diffuses along the membrane surface before it gets released to the bulk solution.[81, 140, 141] In detergent solubilized monomeric *Hs*BR, surface to bulk proton transfer occurs considerably faster with a time constant of 125 μs, but is still about 10-fold slower than RSB deprotonation.[82] Therefore, the retarded proton release as compared to RSB deprotonation in *Ns*XeR may either be explained by the dwell time of the proton at the micelle surface or internal protonation steps between the RSB and the cytoplasmic surface. Without the use of covalently bound optical probes probing proton occurrence at defined positions as used in e.g. refs.[81, 82], the exact timings of proton release from the protein entity cannot be deduced. At pH 9 proton release is accelerated ($\tau_r = 237$ μs), which may be caused by base-catalyzed surface to bulk transfer or an accelerated internal proton transfer step.

Instead, proton uptake is correlated with MII decay (i.e. RSB reprotonation, $\tau_{MII \rightarrow \mathit{Ns}XeR^*} = 39.7$ ms), implying direct RSB reprotonation from the bulk solution. Interestingly, proton uptake is accelerated at pH 9 ($\tau_u = 19$ ms) and still correlated to MII decay, which is likewise accelerated at pH 9 ($\tau_{MII \rightarrow \mathit{Ns}XeR^*} = 14$ ms)[40]. This may be explained by two possible scenarios: A) RSB reprotonation from the extracellular side occurs via internal proton transfer steps, which are rate-limiting both for RSB reprotonation and proton uptake and are accelerated at high pH. B) The RSB is reprotonated directly from the bulk solution, but this reaction is rate-limited by another reaction which is accelerated at pH 9.

D220 Mediates Cytoplasmic Proton Release

Based on a structural study together with functional assays on selected variants, D220, possibly together with H48, has been suggested to act as the cytoplasmic proton acceptor, which has found support in UV/vis spectroscopic and electrophysiological experiments.[39, 40] However, the sequence of protonation reactions involving D220 has not been elucidated. In this work, time-resolved IR spectroscopy in combination with site-directed mutagenesis, provides univocal evidence that D220 is protonated in dark-state *Ns*XeR (chapter 3.1.2). D220 experiences an environmental change with the formation of the L intermediate leading to deprotonation of D220 during the L→MI transition. Subsequently, D220 gets reprotonated during the MI→MII transition. Therefore, D220 does not act as a classical proton acceptor, but rather like a proton release group[142]. The delay between D220 deprotonation (τ_2 = 125 μs) and proton release to the bulk (τ_r = 1.45 ms) may be explained by an additional protonation step or the dwell time at the membrane/micelle surface (*vide supra*). The fact that D220 deprotonation happens simultaneously with RSB deprotonation necessitates the existence of another, yet unidentified primary proton acceptor between the RSB and D220 (indicated as X in Figure 4-1). Computational studies support an elevated pK_a of D220 in dark-state *Ns*XeR, but also suggest that the pK_a values of D220 and H48 are strongly coupled. Therefore, it may be considered that H48 acts as a proton acceptor and mediates proton transfer between D220 and the RSB, but this hypothesis needs to be tested in more detail.[79]

In *Ns*XeR, Y216 is located at an intermediate position between the RSB and D220 and may therefore be considered as a primary proton acceptor, too. In other proton pumps a phenylalanine (F219 in *Hs*BR) is conserved in this position (Table A. 1). The Y216F variant of *Ns*XeR exhibits strongly altered photocycle kinetics (Figure 3-6). The L→M transition is strongly delayed and only one spectrally distinguishable M intermediate is found, emphasizing its effect on the cytoplasmic proton release pathway. A direct interaction of Y216 with D220 in dark-state *Ns*XeR can be ruled out because the frequency of the carboxylic ν(C=O) vibration of protonated D220 is unaffected by the Y216F replacement. Therefore, the strong kinetic effect in the Y216F variant cannot be ascribed to a strongly altered pK_a of D220 in dark-state *Ns*XeR but is of different origin. No spectroscopic marker bands indicating a protonation of Y216 upon RSB deprotonation (data not shown) were found and pK_a calculations suggest, that Y216 is protonated in dark-state *Ns*XeR.[79] Therefore, it is unlikely that Y216 acts as the primary proton acceptor of the RSB. Instead, MD simulations suggest that upon D220 deprotonation, Y216 is involved in establishing a hydrogen bond network between the RSB and D220/H48 including water molecules. In the Y216F variant, alternative networks are established, which perturb the proton release pathway.[79]

The finding that deprotonation of D220 occurs simultaneously with RSB deprotonation is suggestive of a coupling mechanism of these two processes. Indeed, MD simulations suggest that D220 deprotonation leads to an influx of several water molecules, establishing contact between the RSB and D220 via Y216 and H48. These newly established hydrogen bond contacts may explain the drop in pK_a of the RSB occurring concomitantly with D220 deprotonation. Further, MD simulations indicate that the deprotonation of D220 is coupled to protein conformational changes, which will be discussed below.[79]

Protein Conformational Changes Accompany Inward Proton Transport

Two amide I bands at 1670 (+) and 1658 (-) cm^{-1} rise with the formation of MI, increase in intensity during the MI→MII transition and are reverted upon MII decay (Figure 3-7). These absorption changes can be interpreted as conformational changes of the protein backbone.[22] MD simulations observe structural changes of the protein backbone upon deprotonation of D220. The structural changes affect mainly helices D and G where E111 and K213 are located, respectively.[79] This observation is in line with the environmental changes experienced by E111 during the transitions from L→MI and MI→MII, observed by IR spectroscopy (Figure 3-5). Taken together, the difference bands associated with the protein backbone and E111, rising with the L→MI transition, support the hypothesis that deprotonation of D220 is coupled to protein conformational changes. These conformational changes may in turn be linked to water influx and possibly RSB deprotonation. However, the relatively high KIE of 4.2 for the L→MI transition suggests that a proton transfer step itself, possibly the deprotonation of D220, is the rate-limiting step for this transition, but not the conformational change.[78]

The intensity of the amide I bands and hence the protein conformational change continues to increase during the MI→MII transition, where D220 gets reprotonated by the primary proton acceptor. This temporal correlation suggests that proton transfer from the primary acceptor to D220 is linked to protein conformational changes as well. The small KIE of the MI→MII transition excludes that the proton transfer to D220 itself is the rate-determining step of this transition but suggests that a conformational change is rate limiting. At the same time the observed conformational changes may also represent the structural alterations associated with switching the RSB accessibility from the cytoplasmic to the extracellular side during the MI→MII transition as suggested in ref.[40].

In *Hs*BR proton transfer between D96 and the RSB is associated with a protein conformational change, characterized by amide I bands located at 1670 (-), 1660 (-) and 1650 (+) cm^{-1}.[116] Crystallographic, spectroscopic and simulation data suggest that the ~9 Å displacement of helix F during the N intermediate is initiated by steric repulsion of the retinal with W182 in an earlier intermediate. This leads to reorientations of L93 and F219, creating space for three water molecules bridging the gap between D96 and the RSB allowing proton transfer.[25, 26] In the inward proton pump *Bc*XeR smaller displacements of helices were observed as compared to *Hs*BR. This was rationalized by the fact that W173 (W182 in *Hs*BR) avoids steric conflict by a conformational flip. This feature is considered to be an important feature for inward proton pump as a hydrophobic gate is maintained to avoid proton backflow.[38] In *Ns*XeR a similar scenario may be considered, because W173 in *Bc*XeR (W182 in *Hs*BR) is replaced by the considerably smaller F174 in *Ns*XeR. In fact, the spectral signatures in the amide I region in *Ns*XeR differ from those in *Hs*BR and may therefore be interpreted as a different structural change.

The spectroscopic data presented in this thesis together with simulation data[79] reveal that protein conformational changes are coupled to the protonation state of D220 and are likely to be involved in proton transfer between the RSB and D220 and possibly also the accessibility switch of the RSB. The exact nature of these structural changes may be scrutinized by structural and spectroscopic methods in future experiments. Interestingly, the protein conformational change associated with the M intermediates observed by monitoring the amide I vibration correlates with spectral responses of the lipidic ester groups (discussed in chapter 4.2).

The Role of C212 in Inward Proton Transfer

In light of the observed environmental changes of C212 discussed in chapter 3.1.4, the role of C212 for inward proton pumping needs to be discussed. The thiol sidechain of C212 does not change its protonation state during the photocycle of *Ns*XeR but experiences increased hydrogen bonding upon formation of the L intermediate and a weakened hydrogen-bonding environment during the lifetime of the M intermediates. The phenol sidechain of Y177 was shown to be interacting with the sulfhydryl group of C212 in dark-state *Ns*XeR, but this interhelical interaction seems not to be responsible for the light-driven change in hydrogen bonding, which necessitates the interaction of C212 with a second binding partner. A plausible candidate is the backbone carbonyl of L208. In this case, structural alterations of helix G may affect the interaction between C212 and L208 explaining the observed shifts (cf. 3.1.4). Difference bands assigned to the amide I mode of the protein backbone observed during the lifetime of L as well as during the M intermediates (cf. chapter 3.1.2), substantiate the occurrence of structural perturbations of the helical backbone (*vide supra*). However, a perturbed intrahelical interaction is not the only possible explanation for the observed shifts. Interestingly, it was suggested by MD simulations, that deprotonation of D220 during the L→MI transition not just leads to structural changes of the protein moiety, but also to hydration of the cytoplasmic half channel (*vide supra*).[79] Therefore, the spectral shifts associated with C212 may also be related to changes in hydration, which perturb the interaction of C212 with its binding partners. Another option which can explain the observed frequency shift is a change in rotamer composition (see chapter 1.5). Here, further experiments are needed to discriminate which exact structural alterations cause the observed frequency shifts of the band assigned to the sulfhydryl group of C212.

Despite the structural perturbations observed by IR spectroscopy, other methods may shed light onto the relevance of C212 for inward proton transport in *Ns*XeR. It was shown that the C212S variant exhibits lowered pumping activity, while it was not possible to obtain properly folded and colored protein in the C212A and C212D variants[39], pointing to the residue's structural role. Interestingly, the C212S and the Y177F variant exhibit strongly altered photocycle kinetics, where mostly the decay of the M intermediate is drastically slowed down (Figure A. 6). Hence, C212 is most likely not directly involved in the proton release pathway between the RSB and cytoplasmic side, but rather affects reprotonation of the RSB. In *Bc*XeR it was shown that the homologous S206 forms a hydrogen bond with the deprotonated RSB in the M intermediate. This interaction is believed to stabilize the RSB orientation toward helix G.[38] In dark-state *Ns*XeR the sulfur atom of C212 is located 6.4 Å away from the RSB (Figure 3-12), but it may occur that structural alterations establish hydrogen bond contact between the RSB and C212 upon formation of the M intermediate. In this case, the net spectral blueshift of the C212 band upon MI formation may be rationalized by a scenario, where a stronger hydrogen bond (e.g. to L208) is lost, while a weaker hydrogen bond to the deprotonated RSB is formed. In fact, an interaction of C212 with the deprotonated RSB may rationalize the retarded M decay in the C212S and Y177F variants. In analogy to *Bc*XeR, a hydrogen bond may form between C212 and the RSB nitrogen, stabilizing the deprotonated RSB. In the Y177F and C212S variants, this interaction may be altered, affecting the pK_a of the RSB in M. In turn, this may slow down RSB reprotonation. However, this model requires further investigation. As the spectral signature of the ν(S-H) vibration does not change during the MI→MII transition, it appears unlikely that an interaction between C212 and the RSB is involved in changing the accessibility of the RSB.

Conclusion

The present study underlines the importance of D220 for inward proton transport in *Ns*XeR but elucidates an unexpected sequence of protonation steps. Proton release from D220 to the cytoplasmic side occurs simultaneously with the deprotonation of the RSB. The potential coupling of the two processes may be achieved by an allosteric mechanism, where deprotonation of D220 leads to structural changes of the protein as well as an establishment of a hydrogen bond network between the RSB and D220. This network possibly involves H48, Y216 as well as water molecules. To elucidate the role of functional water molecules during the proton release of *Ns*XeR, the vibrational analysis may be extended in future studies as it was done for *Hs*BR.[25] Notably, the pK_a of the RSB in dark-state *Ns*XeR is altered in the D220E variant[40], supporting the finding that reactions occurring at both moieties are coupled. Further, the distinctively different retinal binding pocket in inward proton pumps, could be a decisive feature for the inverted directionality, as it may enable a cytoplasmic orientation of the RSB after isomerization, as already put forward in ref.[8].

C212 undergoes environmental changes possibly upon protein structural changes and seems functionally important for the reprotonation of the RSB. The reprotonation pathway in *Ns*XeR has not been addressed by vibrational spectroscopy in this work, but it was already speculated that D76 plays an important role.[39, 40] So far it was not possible to elucidate the protonation state of D76 during the photocycle because vibrational spectroscopy was hampered by stability issues of the variants (data not shown, personal communication by Jheng-Liang Chen, Genetic Biophysics, Freie Universität Berlin). Tracking protonation changes on the extracellular side will complement the mechanistic view and may therefore allow to derive a more detailed mechanistic concept about inward proton transport in *Ns*XeR.

So far, it does not seem possible to pinpoint a single molecular feature that determines the directionality of proton transport. Therefore, the functional mechanism may rather be considered as an intricate sequence of kinetically and structurally coordinated reactions that ultimately lead to directional proton transport. This is supported by the fact, that is has not yet been possible to change the directionality of a proton pump by a single point mutation.[143]

4.2 Interaction of *Ns*XeR and its Membrane Environment

Considering the spectro-temporal data associated with the lipidic ester vibration of the lipid bilayer in nanodiscs containing *Ns*XeR (chapter 3.2), the following picture may be drawn: Upon light-absorption and beyond our time resolution, a purely negative band, located around 1742 cm^{-1} appears, which persists at least until the L intermediate (cf. Figure 3-3A, Figure 3-5A). A second process is observed, which can be described as a shift of the ground-state band from 1742 cm^{-1} (-) to 1725 cm^{-1} (+), which was already observed in steady-state experiments (Figure 3-17). The second process is correlated with the rise and decay of the MI and MII states (Figure 3-18), respectively, and therefore protein conformational changes, but also protonation dynamics (compare chapter 3.1.2). While the band assignment provides a coherent picture, the physical mechanism causing these spectral changes remains to be discussed.

Lipids are polymorphic; which means that they tend to occur in certain ordered structures (phases). Lipid molecules may change from one phase to another upon varying temperature, pressure, hydration or a combination of these and this leads to changes in the band patterns observable by IR spectroscopy.[144] Using DMPC as a lipid, which has its phase transition at 23.5°C in pure lipids and around 28.5°C in nanodiscs[145], our experiments, performed at room temperature (20-23°C), were conducted close to the transition temperatures. However, it might also occur that the presence of reconstituted *Ns*XeR in the lipid bilayer may alter the phase transitions of the lipids. Therefore, it is tempting to compare the spectral changes presented in chapter 3.2 to spectral features observed upon phase transitions. However, it is debatable whether the activation of *Ns*XeR is a stimulus strong enough to induce an actual phase transition like from the lamellar gel (L_β) to the lamellar liquid-crystalline (L_α) phase, which are the two phases commonly discussed under physiologically relevant conditions[144]. Nevertheless, as the spectro-temporal features presented in this thesis resemble some of the spectral changes reported in the literature upon thermotropic phase transitions[144, 146], the data may be discussed in terms of phase transitions, but more likely as incremental changes of lipid packing within a certain phase.

The negative band located at around 1742 cm^{-1}, occurring beyond our time resolution and extending its dynamics into the millisecond timescale (cf. Figure 3-18), may be explained by band broadening: Starting from a packing state with a relatively narrow band for the ν(C=O) vibration, light excitation may lead to a transition to a state exhibiting a broader ν(C=O) band. In a difference spectrum, such band broadening would result in a negative difference band with small positive side lobes. The kinetic trace of this negative feature is monitored at 1743 cm^{-1} (Figure 3-18) while the smaller positive sidelobes are not observed due to overlap with other features or limitations in SNR (cf. Figure 3-3). Notably, a similar temporal response was observed in *Hs*BR reconstituted in lipid vesicles by monitoring the ν(C-D) vibration of deuterated lipid alkyl chains. However, a limited spectral window did not allow to observe whether a purely negative band or a shift of the lipid band occurs.[147]

With the rise of the MI intermediate the lipid packing state may change further, which leads to a spectral redshift of the lipid band from 1742 (-) to 1725 cm^{-1} (+), observed in steady-state FTIR (Figure 3-17) as well as time-resolved datasets (Figure 3-3). In fact, for pure DMPC lipids in the gel phase, the asymmetric ν(C=O) vibration of the lipid ester group comprises components at 1742 and 1726 cm^{-1}, which are assigned to non-hydrogen-bonded species and hydrogen bonded species, respectively.[146] Reminiscent of these two components, in bovine rhodopsin a difference band with features at 1724 (-) and 1743 cm^{-1} (+) was observed. The authors concluded that in the dark state the lipid esters are hydrogen bonded causing a negative band at 1724 cm^{-1} (-). Upon light activation this hydrogen bond geometry is lost and the lipids experience a bulk-like environment, causing a positive band located at 1743 cm^{-1} (+).[101] As the difference feature in *Ns*XeR is inverted, the interpretation would be the opposite.

While such changes in packing states and hence hydrogen bonding, may explain the spectro-temporal responses, the physical mechanism by which these changes are triggered remains elusive. The fast process, which can be described as band narrowing, may be caused by transient heating upon excitation of *Ns*XeR and subsequent heat dissipation from the protein to the lipid molecules. On the other hand, the correlation of the slower process (shift from 1742 to 1725 cm^{-1}) with the rise and decay of the M intermediates suggests that the lipids are perturbed by changes occurring upon the photocycle of *Ns*XeR. Interestingly, the band patterns assigned to the ν(C=O) ester vibration and to the ν(C-H) vibration of the lipid alkyl chain in *Ns*XeR were likewise observed in empty nanodiscs containing a photoswitchable lipid (AzoPC) mixed with DPPC in a 20/80 molar ratio.[74] AzoPC can be selectively photoswitched between its *cis* and *trans* forms, exerting or reducing lateral pressure within the bilayer.[148, 149] When switching from *cis* to *trans*, which leads to a decrease in surface area and hence a decrease in lateral pressure, the ν(C=O) vibration of the lipid ester shifts from 1740 to 1722 cm^{-1}, reminiscent of the shift observed for *Ns*XeR. The reverse reaction of AzoPC (from *trans* to *cis*) leads to the inverted lipid signal, a shift from 1722 to 1740 cm^{-1}.[74] As in both directions light is applied as a trigger, it can be concluded that this differential band feature is not caused by photothermal heating, but a structural change induced by isomerization. By analogy with the model system of nanodiscs containing AzoPC, a volumetric contraction of *Ns*XeR may explain the redshift of the lipid band caused by decreased lateral pressure and hence a change in the lipid packing state. It is well known from time-resolved photothermal experiments that protein conformational changes as well as isomerization of cofactors and protonation dynamics can lead to volumetric changes of proteins[150] and therefore may induce a change in the packing state of the lipids. As volumetric changes in proteins are relatively small (typically <15 Å^3)[150], it is questionable whether this induces a significant change in lateral pressure inside a nanodisc.

With the current data, it is not possible to derive which physical mechanism leads to the perturbation of the lipid bilayer resulting in the spectral features described above. An additional uncertainty in the interpretation of this data is the possibility that lipids at the interface between the protein and the bulk may act differently as bulk lipids and lipids in nanodiscs in general[151]. In fact, MD simulations and EPR experiments show that three distinct populations of lipids exist in nanodiscs.[152] It cannot be concluded if the observed lipid signals stem from bulk lipids, interfacial lipids or a combination of both. A thorough spectral analysis of the ν(C=O) vibration of the lipid esters is further complicated by overlapping bands stemming from aspartic or glutamic acids. It is therefore desirable to study lipid bands in the absence of bands stemming from the reconstituted protein. Here, studying the ν(C-D) vibration of deuterated lipid alkyl chains is a promising approach.[147]

4.3 QCL-based spectroscopy for the Study of Irreversible Reactions

In this work, two novel IR absorption techniques based on quantum cascade lasers were used to study protein conformational changes and protonation dynamics. Both spectroscopic techniques have already been shown to achieve high SNR in a single acquisition.[47, 57] However, the time-resolved study of protein conformational changes and protonation reactions in a single-shot experiment has not been demonstrated before. Using the well-characterized photoreaction of *Hs*BR, both techniques were compared in terms of data quality with a focus on applicability to the study of non-cyclic photoreactions. As a proof of principle, protein conformational changes associated with the irreversible photoactivation of the G-protein-coupled receptor rhodopsin were measured. Both setups provide data with high enough SNR to resolve (sub)millisecond dynamics associated with receptor activation. Therefore, both techniques can be used to study irreversible photoreactions and extend the application of time-resolved IR spectroscopy from the study of light-driven cyclic reactions to irreversible protein dynamics.

Although both techniques use QCLs as light sources their experimental design is fundamentally different. The setup based on tunable EC-QCLs is a scanning type spectrometer and yields transients at selected frequencies. Repeating the experiment at several frequencies allows to retrieve spectro-temporal data. Instead, DCS provides spectro-temporal data with every acquisition (cf. chapter 1.3). Both techniques have individual advantages and disadvantages which need to be considered when the study of irreversible protein dynamics is desired: The advantage that DCS records spectro-temporal data comes with the disadvantage that the total number of emitted photons is distributed over several laser lines. This explains why the SNR of a single transient obtained by DCS is considerably lower as in the EC-QCL setup (cf. Figure 3-26). Together with the higher time resolution (ns vs μs), the EC-QCL setup may be preferred for experiments where the kinetic response of a single absorption feature is of primary interest. Conversely, the spectro-temporal data obtained by DCS may allow to follow spectral shifts or the simultaneous evolution of different bands allowing a more detailed spectroscopic characterization. The relatively narrow spectral range of the QCLs is a limitation common to both techniques when compared to an FTIR spectrometer. However, by combining several laser sources, the spectral range of EC-QCLs can be extended and almost reaches the spectral range covered by a step-scan experiment.[133] Here, the spectral range covered by a single light source as well as the number of available light sources is smaller for DCS.[57, 61, 72, 153] In light of the limited spectral range, a thorough steady-state characterization of the sample at study prior to a time-resolved experiment in a narrow spectral range may be necessary in most cases. Although both techniques allow to study protein dynamics at room temperature in a single-shot experiment, averaging a small number of acquisitions may still be advantageous in certain cases e.g., when the SNR needs to be further improved to resolve (sub)microsecond dynamics (cf. e.g. Figure 3-23 and Figure 3-32). Therefore, systems for rapidly and reproducibly exchanging the probed sample may be used in the future. Such techniques have also been employed together with conventional FTIR methods but may require higher amounts of sample.[154-157] In combination with the QCL-based methods presented here, such experimental designs may allow to further improve data quality and enable a thorough spectroscopic analysis as already showcased in ref.[134]. To progress to studies of reactions which are not intrinsically light-activatable other triggering techniques such as temperature- or pH-jump[158], or rapid mixing[159] may be considered. By employing caged compounds[72] or introducing artificial light-switchable compounds to activate the process at study[149, 160, 161], light-insensitive biological reactions may be studied in the future with high time resolution upon light activation.

Both techniques are not only useful for the study of irreversible reactions but can also be applied to the study of slow cycling reactions, a case where the step-scan FTIR technique is challenging. An example, where the EC-QCL was used to obtain data with high SNR on a slow photoreaction is presented in chapter 3.1. When studying slow reactions not just only the time resolution but also the time coverage is of interest. Data recorded by the EC-QCL setup often show drifts from 100 ms onwards, caused by fluctuations of the QCL emission (cf. chapter 3.3.4). Employing a second MCT detector to correct for these fluctuations, as it is used in DCS and in other setups employing EC-QCLs[162], may therefore be considered in future setups. The development of the hybrid acquisition mode for DCS now allows to cover dynamics from μs up to minutes in a single acquisition (chapter 3.3.5). In FTIR spectroscopy this is only possible by the combination of separate rapid- and step-scan experiments[111]. An even larger time coverage can be achieved by setups employing synchronized femtosecond lasers.[137, 163] However, such setups based on femtosecond laser systems are technically more demanding as compared to the QCL-based methods presented here.

Taken together, QCL-based spectroscopy opens up the field of time-resolved IR spectroscopy to the study of irreversible systems. Notably, the high SNR achieved by QCL-based IR spectroscopy enables to not just probe protein conformational changes by resolving relatively large bands caused by the collective amide I mode of the protein backbone, but also smaller signals caused by perturbations of single amino acids (cf. Figure 3-26 and Figure 3-34). Therefore, not just only global changes of the protein upon activation can be probed, but also localized perturbations are resolved using a single shot. With the advent of serial crystallography, a powerful tool to derive structure-function relationships in proteins has emerged[103] and has already been applied to study irreversible photoreactions.[164] Time-resolved QCL-based IR spectroscopy may not just be used to aid serial crystallography by finding appropriate time delays, but also to complement the interpretation where the crystallographic data is ambiguous.[104] In particular, with IR spectroscopy one can study the dynamics of proton transfer, a reaction of utmost importance for protein function.

References

1. Mitchell, P., Chemiosmotic coupling in oxidative and photosynthetic phosphorylation (reprint). *Biochim. Biophys. Acta* **2011**, *1807,* 1507-1538.

2. Dau, H.; Zaharieva, I.; Haumann, M., Recent developments in research on water oxidation by photosystem II. *Curr. Opin. Chem. Biol.* **2012**, *16,* 3-10.

3. Michel, H., Cytochrome c Oxidase: Catalytic Cycle and Mechanisms of Proton Pumping-A Discussion. *Biochemistry* **1999**, *38,* 15129-15140.

4. Decoursey, T. E., Voltage-Gated Proton Channels and Other Proton Transfer Pathways. *Physiol. Rev.* **2003**, *83,* 475-579.

5. Longstaff, C.; Calhoon, R. D.; Rando, R. R., Deprotonation of the Schiff base of rhodopsin is obligate in the activation of the G protein. *Proc. Natl. Acad. Sci. U.S.A.* **1986**, *83,* 4209-4213.

6. Kottke, T.; Xie, A.; Larsen, D. S.; Hoff, W. D., Photoreceptors Take Charge: Emerging Principles for Light Sensing. *Annu. Rev. Biophys.* **2018**, *47,* 291-313.

7. Radu, I.; Schleeger, M.; Bolwien, C.; Heberle, J., Time-resolved methods in biophysics. 10. Time-resolved FT-IR difference spectroscopy and the application to membrane proteins. *Photochem. Photobiol. Sci.* **2009**, *8,* 1517-1528.

8. Brown, L. S., Light-driven proton transfers and proton transport by microbial rhodopsins – A biophysical perspective. *Biochim. Biophys. Acta* **2022**, *1864,* 183867.

9. Ernst, O. P.; Lodowski, D. T.; Elstner, M.; Hegemann, P.; Brown, L. S.; Kandori, H., Microbial and animal rhodopsins: Structures, functions, and molecular mechanisms. *Chem. Rev.* **2014**, *114,* 126-163.

10. Govorunova, E. G.; Sineshchekov, O. A.; Li, H.; Spudich, J. L., Microbial Rhodopsins: Diversity, Mechanisms, and Optogenetic Applications. *Annu. Rev. Biochem* **2017**, *86,* 845-872.

11. Sahel, J.-A., et al., Partial recovery of visual function in a blind patient after optogenetic therapy. *Nat. Med.* **2021**, *27,* 1223-1229.

12. Rozenberg, A.; Inoue, K.; Kandori, H.; Béjà, O., Microbial Rhodopsins: The Last Two Decades. *Annu. Rev. Microbiol.* **2021**, *75,* 427-447.

13. Niho, A.; Yoshizawa, S.; Tsukamoto, T.; Kurihara, M.; Tahara, S.; Nakajima, Y.; Mizuno, M.; Kuramochi, H.; Tahara, T.; Mizutani, Y.; Sudo, Y., Demonstration of a Light-Driven SO_4^{2-} Transporter and Its Spectroscopic Characteristics. *J. Am. Chem. Soc.* **2017**, *139,* 4376-4389.

14. Friedrich, T.; Geibel, S.; Kalmbach, R.; Chizhov, I.; Ataka, K.; Heberle, J.; Engelhard, M.; Bamberg, E., Proteorhodopsin is a light-driven proton pump with variable vectoriality. *J. Mol. Biol.* **2002**, *321,* 821-38.

15. Oesterhelt, D.; Stoeckenius, W., Rhodopsin-like protein from the purple membrane of Halobacterium halobium. *Nat. New Biol.* **1971**, *233,* 149-152.

16. Oesterhelt, D.; Stoeckenius, W., Functions of a New Photoreceptor Membrane. *Proc. Natl. Acad. Sci. U.S.A.* **1973**, *70,* 2853-2857.

17. Racker, E.; Stoeckenius, W., Reconstitution of Purple Membrane Vesicles Catalyzing Light-driven Proton Uptake and Adenosine Triphosphate Formation. *J. Biol. Chem.* **1974**, *249,* 662-663.

18. Haupts, U.; Tittor, J.; Oesterhelt, D., Closing in on bacteriorhodopsin: Progress in understanding the molecule. *Annu. Rev. Biophys. Biomol. Struct.* **1999**, *28.*

19. Lanyi, J. K., Bacteriorhodopsin. *Annu. Rev. Physiol.* **2004**, *66,* 665-688.

20. Heberle, J., Proton transfer reactions across bacteriorhodopsin and along the membrane. *Biochim. Biophys. Acta* **2000**, *1458,* 135-47.

21. Borshchevskiy, V., et al., True-atomic-resolution insights into the structure and functional role of linear chains and low-barrier hydrogen bonds in proteins. *Nat. Struct. Mol. Biol.* **2022**, *29,* 440-450.

22. Lorenz-Fonfria, V. A., Infrared Difference Spectroscopy of Proteins: From Bands to Bonds. *Chem. Rev.* **2020**, *120,* 3466-3576.
23. Maeda, A.; Sasaki, J.; Shichida, Y.; Yoshizawa, T.; Chang, M.; Ni, B.; Needleman, R.; Lanyi, J. K., Structures of aspartic acid-96 in the L and N intermediates of bacteriorhodopsin: analysis by Fourier transform infrared spectroscopy. *Biochemistry* **1992**, *31,* 4684-4690.
24. Zscherp, C.; Schlesinger, R.; Tittor, J.; Oesterhelt, D.; Heberle, J., In situ determination of transient pKa changes of internal amino acids of bacteriorhodopsin by using time-resolved attenuated total reflection Fourier-transform infrared spectroscopy. *Proc. Natl. Acad. Sci. U.S.A.* **1999**, *96,* 5498-5503.
25. Freier, E.; Wolf, S.; Gerwert, K., Proton transfer via a transient linear water-molecule chain in a membrane protein. *Proc. Natl. Acad. Sci. U.S.A.* **2011**, *108,* 11435-11439.
26. Weinert, T.; Skopintsev, P.; James, D.; Dworkowski, F.; Panepucci, E.; Kekilli, D.; Furrer, A.; Brünle, S.; Mous, S.; Ozerov, D.; Nogly, P.; Wang, M.; Standfuss, J., Proton uptake mechanism in bacteriorhodopsin captured by serial synchrotron crystallography. *Science* **2019**, *364,* 61-65.
27. Dioumaev, A. K.; Brown, L. S.; Needleman, R.; Lanyi, J. K., Fourier transform infrared spectra of a late intermediate of the bacteriorhodopsin photocycle suggest transient protonation of Asp-212. *Biochemistry* **1999**, *38,* 10070-10078.
28. Zscherp, C.; Schlesinger, R.; Heberle, J., Time-resolved FT-IR spectroscopic investigation of the pH-dependent proton transfer reactions in the E194Q mutant of bacteriorhodopsin. *Biochem. Biophys. Res. Commun.* **2001**, *283,* 57-63.
29. Inoue, K.; Ito, S.; Kato, Y.; Nomura, Y.; Shibata, M.; Uchihashi, T.; Tsunoda, S. P.; Kandori, H., A natural light-driven inward proton pump. *Nat. Commun.* **2016**, *7,* 13415.
30. Ugalde, J. A.; Podell, S.; Narasingarao, P.; Allen, E. E., Xenorhodopsins, an enigmatic new class of microbial rhodopsins horizontally transferred between archaea and bacteria. *Biol. Direct.* **2011**, *6.*
31. Inoue, K.; Tahara, S.; Kato, Y.; Takeuchi, S.; Tahara, T.; Kandori, H., Spectroscopic Study of Proton-Transfer Mechanism of Inward Proton-Pump Rhodopsin, Parvularcula oceani Xenorhodopsin. *J. Phys. Chem. B* **2018**, *122,* 6453-6461.
32. Inoue, K., et al., Schizorhodopsins: A family of rhodopsins from Asgard archaea that function as light-driven inward H^+ pumps. *Sci. Adv.* **2020**, *6,* eaaz2441.
33. Higuchi, A.; Shihoya, W.; Konno, M.; Ikuta, T.; Kandori, H.; Inoue, K.; Nureki, O., Crystal structure of schizorhodopsin reveals mechanism of inward proton pumping. *Proc. Natl. Acad. Sci. U.S.A.* **2021**, *118.*
34. Hayashi, K.; Mizuno, M.; Kandori, H.; Mizutani, Y., Cis–Trans Reisomerization Precedes Reprotonation of the Retinal Chromophore in the Photocycle of Schizorhodopsin 4. *Angew. Chem. Int. Ed.* **2022**, *61,* e202203149.
35. Harris, A.; Lazaratos, M.; Siemers, M.; Watt, E.; Hoang, A.; Tomida, S.; Schubert, L.; Saita, M.; Heberle, J.; Furutani, Y.; Kandori, H.; Bondar, A. N.; Brown, L. S., Mechanism of Inward Proton Transport in an Antarctic Microbial Rhodopsin. *J. Phys. Chem. B* **2020**, *124,* 4851-4872.
36. Inoue, S.; Yoshizawa, S.; Nakajima, Y.; Kojima, K.; Tsukamoto, T.; Kikukawa, T.; Sudo, Y., Spectroscopic characteristics of Rubricoccus marinus xenorhodopsin (RmXeR) and a putative model for its inward H^+ transport mechanism. *Phys. Chem. Chem. Phys.* **2018**, *20,* 3172-3183.
37. Zimanyi, L.; Varo, G.; Chang, M.; Ni, B.; Needleman, R.; Lanyi, J. K., Pathways of proton release in the bacteriorhodopsin photocycle. *Biochemistry* **1992**, *31,* 8535-8543.
38. Kovalev, K., et al., Mechanisms of inward transmembrane proton translocation. *Nat. Struct. Mol. Biol.* **2023**, *30,* 970-979.
39. Shevchenko, V., et al., Inward H^+ pump xenorhodopsin: Mechanism and alternative optogenetic approach. *Sci. Adv.* **2017**, *3,* e1603187.
40. Weissbecker, J.; Boumrifak, C.; Breyer, M.; Wiessalla, T.; Shevchenko, V.; Mager, T.; Slavov, C.; Alekseev, A.; Kovalev, K.; Gordeliy, V.; Bamberg, E.; Wachtveitl, J., The

Voltage Dependent Sidedness of the Reprotonation of the Retinal Schiff Base Determines the Unique Inward Pumping of Xenorhodopsin. *Angew. Chem.* **2021**, *60,* 23010-23017.

41. Siebert, F.; Hildebrandt, P., *Vibrational Spectroscopy in Life Science*. John Wiley & Sons **2007**.

42. Griffiths, P. R.; deHaseth, J. A., *Fourier Transform Infrared Spectrometry*. Second ed.; John Wiley & Sons **2007**.

43. Barth, A., Infrared spectroscopy of proteins. *Biochim. Biophys. Acta* **2007**, *1767,* 1073-1101.

44. Smith, G. D.; Palmer, R. A., Fast Time-Resolved Mid-Infrared Spectroscopy Using an Interferometer. In *Handbook of Vibrational Spectroscopy*, Chalmers, J. M.; Griffiths, P. R., Eds. **2002**.

45. Faist, J.; Capasso, F.; Sivco, D. L.; Sirtori, C.; Hutchinson, A. L.; Cho, A. Y., Quantum Cascade Laser. *Science* **1994**, *264,* 553-556.

46. Abbruzzetti, S.; Bruno, S.; Faggiano, S.; Grandi, E.; Mozzarelli, A.; Viappiani, C., Time-resolved methods in Biophysics. 2. Monitoring haem proteins at work with nanosecond laser flash photolysis. *Photochem. Photobiol. Sci.* **2006**, *5,* 1109-1109.

47. Schultz, B. J.; Mohrmann, H.; Lorenz-Fonfria, V. A.; Heberle, J., Protein dynamics observed by tunable mid-IR quantum cascade lasers across the time range from 10 ns to 1 s. *Spectrochim. Acta, Pt. A: Mol. Biomol. Spectrosc,* **2018**, *188,* 666-674.

48. Schwaighofer, A.; Brandstetter, M.; Lendl, B., Quantum cascade lasers (QCLs) in biomedical spectroscopy. *Chem. Soc. Rev.* **2017**, *46,* 5903-5924.

49. Nobelprize.org https://www.nobelprize.org/prizes/physics/2005/summary/ (accessed 20.10.2023).

50. Diddams, S. A.; Vahala, K.; Udem, T., Optical frequency combs: Coherently uniting the electromagnetic spectrum. *Science* **2020**, *369,* eaay3676.

51. Udem, T.; Holzwarth, R.; Hänsch, T. W., Optical frequency metrology. *Nature* **2002**, *416,* 233-237.

52. Faist, J.; Villares, G.; Scalari, G.; Rösch, M.; Bonzon, C.; Hugi, A.; Beck, M., Quantum Cascade Laser Frequency Combs. *Nanophotonics* **2016**, *5,* 272-291.

53. Hugi, A.; Villares, G.; Blaser, S.; Liu, H. C.; Faist, J., Mid-infrared frequency comb based on a quantum cascade laser. *Nature* **2012**, *492,* 229-233.

54. Hugi, A. Single-mode and Comb Operation of Broadband Quantum Cascade Lasers. PhD Thesis, ETH Zürich, 2013.

55. Coddington, I.; Newbury, N.; Swann, W., Dual-comb spectroscopy. *Optica* **2016**, *3,* 414-425.

56. Villares, G.; Hugi, A.; Blaser, S.; Faist, J., Dual-comb spectroscopy based on quantum-cascade-laser frequency combs. *Nat. Commun.* **2014**, *5,* 1-3.

57. Klocke, J. L.; Mangold, M.; Allmendinger, P.; Hugi, A.; Geiser, M.; Jouy, P.; Faist, J.; Kottke, T., Single-Shot Sub-microsecond Mid-infrared Spectroscopy on Protein Reactions with Quantum Cascade Laser Frequency Combs. *Anal. Chem.* **2018**, *90,* 10494-10500.

58. van Stokkum, I. H. M.; Larsen, D. S.; van Grondelle, R., Global and target analysis of time-resolved spectra. *Biochim. Biophys. Acta* **2004**, *1657,* 82-104.

59. Slavov, C.; Hartmann, H.; Wachtveitl, J., Implementation and evaluation of data analysis strategies for time-resolved optical spectroscopy. *Anal. Chem.* **2015**, *87,* 2328-2336.

60. Dorlhiac, G. F.; Fare, C.; van Thor, J. J., PyLDM - An open source package for lifetime density analysis of time-resolved spectroscopic data. *PLoS Comp. Biol.* **2017**, *13,* e1005528.

61. Schubert, L.; Langner, P.; Ehrenberg, D.; Lorenz-Fonfria, V. A.; Heberle, J., Protein conformational changes and protonation dynamics probed by a single shot using quantum-cascade-laser-based IR spectroscopy. *J. Chem. Phys.* **2022**, *156,* 204201.

62. Maia, R. N. A.; Ehrenberg, D.; Oldemeyer, S.; Knieps-Grünhagen, E.; Krauss, U.; Heberle, J., Real-Time Tracking of Proton Transfer from the Reactive Cysteine to the Flavin Chromophore of a Photosensing Light Oxygen Voltage Protein. *J. Am. Chem. Soc.* **2021**, *143,* 12535-12542.

63. Bertie, J. E., Glossary of Terms used in Vibrational Spectroscopy. In *Handbook of Vibrational Spectroscopy*, Chalmers, J. M.; Griffiths, P. R., Eds. **2002**.

64. Smith, S. O.; Braiman, M. S.; Myers, A. B.; Pardoen, J. A.; Courtin, J. M.; Winkel, C.; Lugtenburg, J.; Mathies, R. A., Vibrational analysis of the all-trans-retinal chromophore in light-adapted bacteriorhodopsin. *J. Am. Chem. Soc.* **1987**, *109,* 3108-3125.
65. Smith, S. O.; Myers, A. B.; Pardoen, J. A.; Winkel, C.; Mulder, P. P.; Lugtenburg, J.; Mathies, R., Determination of retinal Schiff base configuration in bacteriorhodopsin. *Proc. Natl. Acad. Sci. U.S.A.* **1984**, *81,* 2055-2059.
66. Massig, G.; Stockburger, M.; Gärtner, W.; Oesterhelt, D.; Towner, P., Structural conclusion on the Schiff base group of retinylidene chromophores in bacteriorhodopsin from characteristic vibrational bands in the resonance Raman spectra of BR_{570} (all-*trans*), BR_{603} (*3-dehydroretina*l) and BR_{548} (13-*cis*). *J. Raman Spectrosc.* **1982**, *12,* 287-294.
67. Aton, B.; Doukas, A. G.; Callender, R. H.; Becher, B.; Ebrey, T. G., Resonance Raman studies of the purple membrane. *Biochemistry* **1977**, *16,* 2995-2999.
68. Braiman, M.; Mathies, R., Resonance Raman spectra of bacteriorhodopsin's primary photoproduct: evidence for a distorted 13-*cis* retinal chromophore. *Proc. Natl. Acad. Sci. U.S.A.* **1982**, *79,* 403-407.
69. Aton, B.; Doukas, A.; Narva, D.; Callender, R.; Dinur, U.; Honig, B., Resonance Raman studies of the primary photochemical event in visual pigments. *Biophys. J.* **1980**, *29,* 79-94.
70. Koziński, M.; Garrett-Roe, S.; Hamm, P., 2D-IR Spectroscopy of the Sulfhydryl Band of Cysteines in the Hydrophobic Core of Proteins. *J. Phys. Chem. B* **2008**, *112,* 7645-7650.
71. Zhou, P.; Tian, F.; Lv, F.; Shang, Z., Geometric characteristics of hydrogen bonds involving sulfur atoms in proteins. *Proteins* **2009**, *76,* 151-163.
72. Norahan, M. J.; Horvath, R.; Woitzik, N.; Jouy, P.; Eigenmann, F.; Gerwert, K.; Kötting, C., Microsecond-Resolved Infrared Spectroscopy on Nonrepetitive Protein Reactions by Applying Caged Compounds and Quantum Cascade Laser Frequency Combs. *Anal. Chem.* **2021**, *93,* 6779-6783.
73. La Greca, M.; Chen, J. L.; Schubert, L.; Kozuch, J.; Berneiser, T.; Terpitz, U.; Heberle, J.; Schlesinger, R., The Photoreaction of the Proton-Pumping Rhodopsin 1 From the Maize Pathogenic Basidiomycete Ustilago maydis. *Front. Mol. Biosci.* **2022**, *9,* 826990.
74. Baserga, F.; Vorkas, A.; Crea, F.; Schubert, L.; Chen, J. L.; Redlich, A.; La Greca, M.; Storm, J.; Oldemeyer, S.; Hoffmann, K.; Schlesinger, R.; Heberle, J., Membrane Protein Activity Induces Specific Molecular Changes in Nanodiscs Monitored by FTIR Difference Spectroscopy. *Front. Mol. Biosci.* **2022**, *9,* 915328.
75. Glasoe, P. K.; Long, F. A., Use of Glass Electrodes to Measure Acidities in Deuterium Oxide. *J. Phys. Chem.* **1960**, *64,* 188-190.
76. Stauffer, M.; Hirschi, S.; Ucurum, Z.; Harder, D.; Schlesinger, R.; Fotiadis, D., Engineering and Production of the Light-Driven Proton Pump Bacteriorhodopsin in 2D Crystals for Basic Research and Applied Technologies. *Methods and Protocols* **2020**, *51.*
77. Ritter, E.; Puskar, L.; Kim, S. Y.; Park, J. H.; Hofmann, K. P.; Bartl, F.; Hegemann, P.; Schade, U., Féry Infrared Spectrometer for Single-Shot Analysis of Protein Dynamics. *J. Phys. Chem. Lett.* **2019**, *10,* 7672-7677.
78. Brown, L. S.; Needleman, R.; Lanyi, J. K., Origins of deuterium kinetic isotope effects on the proton transfers of the bacteriorhodopsin photocycle. *Biochemistry* **2000**, *39,* 938-945.
79. Schubert, L.; Chen, J.-L.; Fritz, T.; Marxer, F.; Langner, P.; Hoffmann, K.; Gamiz-Hernandez, A. P.; Kaila, V. R. I.; Schlesinger, R.; Heberle, J., Proton Release Reactions in the Inward H^+ Pump *Ns*XeR. *J. Phys. Chem. B* **2023**, *127,* 8358-8369.
80. Heberle, J.; Oesterhelt, D.; Dencher, N. A., Decoupling of photo- and proton cycle in the Asp85-->Glu mutant of bacteriorhodopsin. *EMBO J.* **1993**, *12,* 3721-3727.
81. Heberle, J.; Dencher, N. A., Surface-bound optical probes monitor protein translocation and surface potential changes during the bacteriorhodopsin photocycle. *Proc. Natl. Acad. Sci. U.S.A.* **1992**, *89,* 5996-6000.
82. Scherrer, P.; Alexiev, U.; Marti, T.; Khorana, H. G.; Heyn, M. P., Covalently bound pH-indicator dyes at selected extracellular or cytoplasmic sites in bacteriorhodopsin. 1. Proton migration along the surface of bacteriorhodopsin micelles and its delayed transfer from surface to bulk. *Biochemistry* **1994**, *33,* 13684-13692.

83. Garczarek, F.; Wang, J.; El-Sayed, M. A.; Gerwert, K., The assignment of the different infrared continuum absorbance changes observed in the 3000-1800-cm^{-1} region during the bacteriorhodopsin photocycle. *Biophys. J.* **2004**, *87,* 2676-2682.

84. Calimet, N.; Ullmann, G. M., The influence of a transmembrane pH gradient on protonation probabilities of bacteriorhodopsin: the structural basis of the back-pressure effect. *J. Mol. Biol.* **2004**, *339,* 571-589.

85. Fang, J. M.; Carriker, J. D.; Balogh-Nair, V.; Nakanishi, K., Evidence for the necessity of double bond (13-Ene) isomerization in the proton pumping of bacteriorhodopsin. *J. Am. Chem. Soc.* **1983**, *105,* 5162-5164.

86. Sheves, M.; Friedman, N.; Albeck, A.; Ottolenghi, M., Primary photochemical event in bacteriorhodopsin: study with artificial pigments. *Biochemistry* **1985**, *24,* 1260-1265.

87. Bondar, A.-N.; Fischer, S.; Smith, J. C.; Elstner, M.; Suhai, S., Key Role of Electrostatic Interactions in Bacteriorhodopsin Proton Transfer. *J. Am. Chem. Soc.* **2004**, *126,* 14668-14677.

88. Ito, S.; Sugita, S.; Inoue, K.; Kandori, H., FTIR Analysis of a Light-driven Inward Proton-pumping Rhodopsin at 77 K. *Photochem. Photobiol.* **2017**, *93,* 1381-1387.

89. Furutani, Y.; Kawanabe, A.; Jung, K.-H.; Kandori, H., FTIR Spectroscopy of the All-Trans Form of Anabaena Sensory Rhodopsin at 77 K: Hydrogen Bond of a Water between the Schiff Base and Asp75. *Biochemistry* **2005**, *44,* 12287-12296.

90. Muders, V.; Kerruth, S.; Lórenz-Fonfría, V. A.; Bamann, C.; Heberle, J.; Schlesinger, R., Resonance Raman and FTIR spectroscopic characterization of the closed and open states of channelrhodopsin-1. *FEBS Lett.* **2014**, *588,* 2301-2306.

91. Ogren, J. I.; Yi, A.; Mamaev, S.; Li, H.; Lugtenburg, J.; Degrip, W. J.; Spudich, J. L.; Rothschild, K. J., Comparison of the structural changes occurring during the primary phototransition of two different channelrhodopsins from Chlamydomonas algae. *Biochemistry* **2015**, *54,* 377-388.

92. Bagley, K.; Dollinger, G.; Eisenstein, L.; Singh, A. K.; Zimanyi, L., Fourier transform infrared difference. spectroscopy of bacteriorhodopsin and its photoproducts*. *Proc. Natl. Acad. Sci. U.S.A.* **1982**, *79,* 4972-4976.

93. Heberle, J.; Fitter, J.; Sass, H. J.; Büldt, G., Bacteriorhodopsin: the functional details of a molecular machine are being resolved. *Biophys. Chem.* **2000**, *85,* 229-248.

94. Kuhne, J.; Vierock, J.; Tennigkeit, S. A.; Dreier, M.-A.; Wietek, J.; Petersen, D.; Gavriljuk, K.; El-Mashtoly, S. F.; Hegemann, P.; Gerwert, K., Unifying photocycle model for light adaptation and temporal evolution of cation conductance in channelrhodopsin-2. *Proc. Natl. Acad. Sci. U.S.A.* **2019**, *116,* 9380-9389.

95. Inoue, K.; Ono, H.; Abe-Yoshizumi, R.; Yoshizawa, S.; Ito, H.; Kogure, K.; Kandori, H., A light-driven sodium ion pump in marine bacteria. *Nat. Commun.* **2013**, *4,* 1678.

96. Wible, R. S.; Sutter, T. R., Soft Cysteine Signaling Network: The Functional Significance of Cysteine in Protein Function and the Soft Acids/Bases Thiol Chemistry That Facilitates Cysteine Modification. *Chem. Res. Toxicol.* **2017**, *30,* 729-762.

97. Minkov, V. S.; Boldyreva, E. V., Weak Hydrogen Bonds Formed by Thiol Groups in N-Acetyl-l-Cysteine and Their Response to the Crystal Structure Distortion on Increasing Pressure. *J. Phys. Chem. B* **2013**, *117,* 14247-14260.

98. Ganapathy, S.; Opdam, L.; Hontani, Y.; Frehan, S.; Chen, Q.; Hellingwerf, K. J.; de Groot, H. J. M.; Kennis, J. T. M.; de Grip, W. J., Membrane matters: The impact of a nanodisc-bilayer or a detergent microenvironment on the properties of two eubacterial rhodopsins. *Biochim. Biophys. Acta* **2020**, *1862,* 183113.

99. Shi, L.; Yoon, S. R.; Bezerra, A. G.; Jung, K.-H.; Brown, L. S., Cytoplasmic Shuttling of Protons in Anabaena Sensory Rhodopsin: Implications for Signaling Mechanism. *J. Mol. Biol.* **2006**, *358,* 686-700.

100. Harris, A.; Saita, M.; Resler, T.; Hughes-Visentin, A.; Maia, R.; Pranga-Sellnau, F.; Bondar, A. N.; Heberle, J.; Brown, L. S., Molecular details of the unique mechanism of chloride transport by a cyanobacterial rhodopsin. *Phys. Chem. Chem. Phys.* **2018**, *20,* 3184-3199.

101. Beck, M.; Siebert, F.; Sakmar, T. P., Evidence for the specific interaction of a lipid molecule with rhodopsin which is altered in the transition to the active state metarhodopsin II. *FEBS Lett.* **1998**, *436,* 304-308.

102. Blume, A.; Huebner, W.; Messner, G., Fourier Transform Infrared Spectroscopy of ^{13}C=O-Labeled Phospholipids Hydrogen Bonding to Carbonyl Groups. *Biochemistry* **1988**, *27,* 8239-8249.

103. Standfuss, J., Membrane protein dynamics studied by X-ray lasers – or why only time will tell. *Curr. Opin. Struct. Biol.* **2019**, *57,* 63-71.

104. Skopintsev, P., et al., Femtosecond-to-millisecond structural changes in a light-driven sodium pump. *Nature* **2020**, *583,* 314-318.

105. Mous, S., et al., Dynamics and mechanism of a light-driven chloride pump. *Science* **2022**, *375,* 845-851.

106. Chizhov, I.; Chernavskii, D. S.; Engelhard, M.; Mueller, K. H.; Zubov, B. V.; Hess, B., Spectrally silent transitions in the bacteriorhodopsin photocycle. *Biophys. J.* **1996**, *71,* 2329-2345.

107. Uhmann, W.; Becker, A.; Taran, C.; Siebert, F., Time-Resolved FT-IR Absorption Spectroscopy Using a Step-Scan Interferometer. *Appl. Spectrosc.* **1991**, *45,* 390-397.

108. Süss, B.; Ringleb, F.; Heberle, J., New ultrarapid-scanning interferometer for FT-IR spectroscopy with microsecond time-resolution. *Rev. Sci. Instrum.* **2016**, *87,* 063113.

109. Lanyi, J. K.; Váró, G., The Photocycles of Bacteriorhodopsin. *Isr. J. Chem.* **1995**, *35,* 365-385.

110. Maeda, A., Application of FTIR Spectroscopy to the Structural Study on the Function of Bacteriorhodopsin. *Isr. J. Chem.* **1995**, *35,* 387-400.

111. Lorenz-Fonfria, V. A.; Resler, T.; Krause, N.; Nack, M.; Gossing, M.; Fischer von Mollard, G.; Bamann, C.; Bamberg, E.; Schlesinger, R.; Heberle, J., Transient protonation changes in channelrhodopsin-2 and their relevance to channel gating. *Proc. Natl. Acad. Sci. U.S.A.* **2013**, *110,* E1273-E1281.

112. Vogel, R.; Siebert, F., Fourier transform IR spectroscopy study for new insights into molecular properties and activation mechanisms of visual pigment rhodopsin. *Biopolymers* **2003**, *72,* 133-148.

113. Stojković, E. A.; Toh, K. C.; Alexandre, M. T. A.; Baclayon, M.; Moffat, K.; Kennis, J. T. M., FTIR Spectroscopy Revealing Light-Dependent Refolding of the Conserved Tongue Region of Bacteriophytochrome. *J. Phys. Chem. Lett.* **2014**, *5,* 2512-2515.

114. Choe, H.-W.; Kim, Y. J.; Park, J. H.; Morizumi, T.; Pai, E. F.; Krauß, N.; Hofmann, K. P.; Scheerer, P.; Ernst, O. P., Crystal structure of metarhodopsin II. *Nature* **2011**, *471,* 651-655.

115. Ormos, P., Infrared spectroscopic demonstration of a conformational change in bacterorhodopsin involved in proton pumping. *Proc. Natl. Acad. Sci. U.S.A.* **1991**, *88,* 473-477.

116. Souvignier, G.; Gerwert, K., Proton uptake mechanism of bacteriorhodopsin as determined by time-resolved stroboscopic-FTIR-spectroscopy. *Biophys. J.* **1992**, *63,* 1393-405.

117. Braiman, M. S.; Bousche, O.; Rothschild, K. J., Protein dynamics in the bacteriorhodopsin photocycle: Submillisecond Fourier transform infrared spectra of the L, M, and N photointermediates. *Proc. Natl. Acad. Sci. U.S.A.* **1991**, *88,* 2388-2392.

118. Braiman, M. S.; Mogi, T.; Marti, T.; Stern, L. J.; Khorana, H. G.; Rothschild, K. J., Vibrational spectroscopy of bacteriorhodopsin mutants: light-driven proton transport involves protonation changes of aspartic acid residues 85, 96, and 212. *Biochemistry* **1988**, *27,* 8516-8520.

119. Chen, W.-G.; Braiman, M. S., Kinetic Analysis Of Time-Resolved Infrared Difference Spectra Of The L And M Intermediates Of Bacteriorhodopsin*. *Photochem. Photobiol.* **1991**, *54,* 905-910.

120. Resler, T.; Schultz, B. J.; Lórenz-Fonfría, V. A.; Schlesinger, R.; Heberle, J., Kinetic and Vibrational Isotope Effects of Proton Transfer Reactions in Channelrhodopsin-2. *Biophys. J.* **2015**, *109,* 287-297.

121. Le Coutre, J.; Gerwert, K., Kinetic isotope effects reveal an ice-like and a liquid-phase-type intramolecular proton transfer in bacteriorhodopsin. *FEBS Lett.* **1996**, *398,* 333-336.

122. Engelhard, M.; Hess, B.; Gerwert, K.; Kreutz, W.; Siebert, F., Light-Driven Protonation Changes of Internal Aspartic Acids of Bacteriorhodopsin: An Investigation by Static and Time-Resolved Infrared Difference Spectroscopy Using [4-^{13}C]Aspartic Acid Labeled Purple Membrane. *Biochemistry* **1985**, *24,* 400-407.

123. Knierim, B.; Hofmann, K. P.; Ernst, O. P.; Hubbell, W. L., Sequence of late molecular events in the activation of rhodopsin. *Proc. Natl. Acad. Sci. U.S.A.* **2007**, *104,* 20290-20295.

124. Zaitseva, E.; Brown, M. F.; Vogel, R., Sequential Rearrangement of Interhelical Networks Upon Rhodopsin Activation in Membranes: The Meta IIa Conformational Substate. *J. Am. Chem. Soc.* **2010**, *132,* 4815-4821.

125. Siebert, F.; Mäntele, W.; Gerwert, K., Fourier-transform infrared spectroscopy applied to rhodopsin. *Eur. J. Biochem.* **1983**, *136,* 119-127.

126. Siebert, F., Application of FTIR Spectroscopy to the Investigation of Dark Structures and Photoreactions of Visual Pigments. *Isr. J. Chem.* **1995**, *35,* 309-323.

127. Fahmy, K.; Jäger, F.; Beck, M.; Zvyaga, T. A.; Sakmar, T. P.; Siebert, F., Protonation states of membrane-embedded carboxylic acid groups in rhodopsin and metarhodopsin II: a Fourier-transform infrared spectroscopy study of site-directed mutants. *Proc. Natl. Acad. Sci. U.S.A.* **1993**, *90,* 10206-10210.

128. Ganter, U. M.; Gaertner, W.; Siebert, F., Rhodopsin-lumirhodopsin phototransition of bovine rhodopsin investigated by Fourier transform infrared difference spectroscopy. *Biochemistry* **1988**, *27,* 7480-7488.

129. Lüdeke, S.; Fonfría, V. A. L.; Siebert, F.; Vogel, R., Time-resolved rapid-scan Fourier transform infrared difference spectroscopy on a noncyclic photosystem: Rhodopsin photointermediates from Lumi to Meta II. *Biopolymers* **2006**, *83,* 159-169.

130. Ruf, J.; Bindschedler, F.; Buhrke, D., The molecular mechanism of light-induced bond formation and breakage in the cyanobacteriochrome TePixJ. *Phys. Chem. Chem. Phys.* **2023**, *25,* 6016-6024.

131. Ganter, U. M.; Longstaff, C.; Pajares, M. A.; Rando, R. R.; Siebert, F., Fourier transform infrared studies of active-site-methylated rhodopsin. Implications for chromophore-protein interaction, transducin activation, and the reaction pathway. *Biophys. J.* **1991**, *59,* 640-644.

132. Herbst, J.; Heyne, K.; Diller, R., Femtosecond Infrared Spectroscopy of Bacteriorhodopsin Chromophore Isomerization. *Science* **2002**, *297,* 822-825.

133. Stritt, P.; Jawurek, M.; Hauser, K., Application of tunable quantum cascade lasers to monitor dynamics of bacteriorhodopsin in the mid-IR spectral range. *Biomed. Spectrosc. Imaging* **2020**, *9*.

134. Klocke, J. L.; Kottke, T., A quantum cascade laser setup for studying irreversible photoreactions in H_2O with nanosecond resolution and microlitre consumption. *Phys. Chem. Chem. Phys.* **2020**, *22,* 26459.

135. Sanchez, M. L. K.; Sommer, C.; Reijerse, E.; Birrell, J. A.; Lubitz, W.; Dyer, R. B., Investigating the Kinetic Competency of *Cr*HydA1 [FeFe] Hydrogenase Intermediate States via Time-Resolved Infrared Spectroscopy. *J. Am. Chem. Soc.* **2019**, *141,* 16064-16070.

136. Greetham, G. M.; Sole, D.; Clark, I. P.; Parker, A. W.; Pollard, M. R.; Towrie, M., Time-resolved multiple probe spectroscopy. *Rev. Sci. Instrum. 83,* 103107.

137. Greetham, G. M.; Donaldson, P. M.; Nation, C.; Sazanovich, I. V.; Clark, I. P.; Shaw, D. J.; Parker, A. W.; Towrie, M., A 100 kHz time-resolved multiple-probe femtosecond to second infrared absorption spectrometer. *Appl. Spectrosc.* **2016**, *70,* 645-653.

138. Chizhov, I.; Schmies, G.; Seidel, R.; Sydor, J. R.; Lüttenberg, B.; Engelhard, M., The Photophobic Receptor from Natronobacterium pharaonis: Temperature and pH Dependencies of the Photocycle of Sensory Rhodopsin II. *Biophys. J.* **1998**, *75,* 999-1009.

139. Hein, M.; Wegener, A. A.; Engelhard, M.; Siebert, F., Time-resolved FTIR studies of sensory rhodopsin II (*Np*SRII) from *Natronobacterium pharaonis*: Implications for proton transport and receptor activation. *Biophys. J.* **2003**, *84,* 1208-1217.

140. Heberle, J.; Dencher, N. A., Bacteriorhodopsin in ice. Accelerated proton transfer from the purple membrane surface. *FEBS Lett.* **1990**, *277,* 277-280.

141. Heberle, J.; Riesle, J.; Thiedemann, G.; Oesterhelt, D.; Dencher, N. A., Proton migration along the membrane surface and retarded surface to bulk transfer. *Nature* **1994**, 379-382.

142. Brown, L. S.; Sasaki, J.; Kandori, H.; Maeda, A.; Needleman, R.; Lanyi, J. K., Glutamic Acid 204 is the Terminal Proton Release Group at the Extracellular Surface of Bacteriorhodopsin (*). *J. Biol. Chem.* **1995**, *270,* 27122-27126.

143. Marín, M. d. C.; Konno, M.; Yawo, H.; Inoue, K., Converting a Natural-Light-Driven Outward Proton Pump Rhodopsin into an Artificial Inward Proton Pump. *J. Am. Chem. Soc.* **2023**, *145,* 10938-10942.

144. Lewis, R. N. A. H.; McElhaney, R. N., Membrane lipid phase transitions and phase organization studied by Fourier transform infrared spectroscopy. *Biochim. Biophys. Acta* **2013**, *1828,* 2347-2358.

145. Denisov, I. G.; McLean, M. A.; Shaw, A. W.; Grinkova, Y. V.; Sligar, S. G., Thermotropic Phase Transition in Soluble Nanoscale Lipid Bilayers. *J. Phys. Chem. B* **2005**, *109,* 15580-15588.

146. Disalvo, E. A.; Frias, M. A., Water State and Carbonyl Distribution Populations in Confined Regions of Lipid Bilayers Observed by FTIR Spectroscopy. *Langmuir* **2013**, *29,* 6969-6974.

147. Stritt, P.; Jawurek, M.; Hauser, K., Mid-IR quantum cascade laser spectroscopy to resolve lipid dynamics during the photocycle of bacteriorhodopsin. *J. Chem. Phys.* **2023**, *158,* 154202.

148. Pritzl, S. D.; Urban, P.; Prasselsperger, A.; Konrad, D. B.; Frank, J. A.; Trauner, D.; Lohmüller, T., Photolipid Bilayer Permeability is Controlled by Transient Pore Formation. *Langmuir* **2020**, *36,* 13509-13515.

149. Crea, F.; Vorkas, A.; Redlich, A.; Cruz, R.; Shi, C.; Trauner, D.; Lange, A.; Schlesinger, R.; Heberle, J., Photoactivation of a Mechanosensitive Channel. *Front. Mol. Biosci.* **2022**, *9,* 905306.

150. Gensch, T.; Viappiani, C., Time-resolved photothermal methods: accessing time-resolved thermodynamics of photoinduced processes in chemistry and biology. *Photochem. Photobiol. Sci.* **2003**, *2,* 699-721.

151. Mörs, K.; Roos, C.; Scholz, F.; Wachtveitl, J.; Dötsch, V.; Bernhard, F.; Glaubitz, C., Modified lipid and protein dynamics in nanodiscs. *Biochim. Biophys. Acta* **2013**, *1828,* 1222-1229.

152. Stepien, P.; Augustyn, B.; Poojari, C.; Galan, W.; Polit, A.; Vattulainen, I.; Wisnieska-Becker, A.; Rog, T., Complexity of seemingly simple lipid nanodiscs. *Biochim. Biophys. Acta* **2020**, *1862,* 183420.

153. Pinkowski, N. H.; Biswas, P.; Shao, J.; Strand, C. L.; Hanson, R. K., Thermometry and speciation for high-temperature and -pressure methane pyrolysis using shock tubes and dual-comb spectroscopy. *Meas. Sci. Technol.* **2021**, *32,* 125502.

154. Rammelsberg, R.; Boulas, S.; Chorongiewski, H.; Gerwert, K., Set-up for time-resolved step-scan FTIR spectroscopy of noncyclic reactions. *Vib. Spectrosc* **1999**, *19,* 143-149.

155. Rödig, C.; Siebert, F., Monitoring fast reactions of slow cycling systems with time-resolved FTIR spectroscopy. *Vib. Spectrosc* **1999**, *19,* 271-276.

156. Schleeger, M.; Wagner, C.; Vellekoop, M. J.; Lendl, B.; Heberle, J., Time-resolved flow-flash FT-IR difference spectroscopy: the kinetics of CO photodissociation from myoglobin revisited. *Anal. Bioanal. Chem.* **2009**, *394,* 1869-1877.

157. Thöing, C.; Pfeifer, A.; Kakorin, S.; Kottke, T., Protonated triplet-excited flavin resolved by step-scan FTIR spectroscopy: implications for photosensory LOV domains. *Phys. Chem. Chem. Phys.* **2013**, *15,* 5916-5926.

158. Popp, A.; Scheerer, D.; Heck, B.; Hauser, K., Biomolecular dynamics studied with IR-spectroscopy using quantum cascade lasers combined with nanosecond perturbation techniques. *Spectrochim. Acta, Pt. A: Mol. Biomol. Spectrosc,* **2017**, *181,* 192-199.

159. Hinsmann, P.; Frank, J.; Svasek, P.; Harasek, M.; Lendl, B., Design, simulation and application of a new micromixing device for time resolved infrared spectroscopy of chemical reactions in solution. *Lab Chip* **2001**, *1,* 16-21.
160. Kohse, S.; Neubauer, A.; Pazidis, A.; Lochbrunner, S.; Kragl, U., Photoswitching of Enzyme Activity by Laser-Induced pH-Jump. *J. Am. Chem. Soc.* **2013**, *135,* 9407-9411.
161. Wranik, M., et al., Watching the release of a photopharmacological drug from tubulin using time-resolved serial crystallography. *Nat. Commun.* **2023**, *14,* 903.
162. Dekmak, M. Y.; Mäusle, S. M.; Brandhorst, J.; Simon, P. S.; Dau, H., Tracking the first electron transfer step at the donor side of oxygen-evolving photosystem II by time-resolved infrared spectroscopy. *Photosynth. Res.* **2023**.
163. Helbing, J.; Hamm, P., Versatile Femtosecond Laser Synchronization for Multiple-Timescale Transient Infrared Spectroscopy. *J. Phys. Chem. A* **2023**, *127,* 6347-6356.
164. Gruhl, T., et al., Ultrafast structural changes direct the first molecular events of vision. *Nature* **2023**, *615,* 939-944.

Appendix

Table A. 1: Sequence alignment of the prototypical outward proton pump *Hs*BR to the inward proton pump *Ns*XeR and other microbial inward proton pumps. The sequence alignment was performed using COBALT multiple sequence alignment from the National Center for Biotechnology Information (NCBI).

*Hs*BR	F42	T46	A53	Y57	R82	D85	T89	D96	D115	W182	D212	A215	K216	F219	L223
*Ns*XeR	F44	H48	S55	Y59	W73	D76	S80	A87	E111	F174	P209	C212	K213	Y216	D220
*Po*XeR	E	A	S	Y	R	D	T	L	D	W	P	S	K	F	D
*Rm*XeR	E	A	S	Y	R	D	T	A	D	W	P	S	K	F	D
*Bc*XeR	E34	A	S	Y	R	D	S	A	D	W	P	S206	K	F	D
SzR4	L	N	T	Y	R	F	S	E81	N	W	D184	T	K	F	T

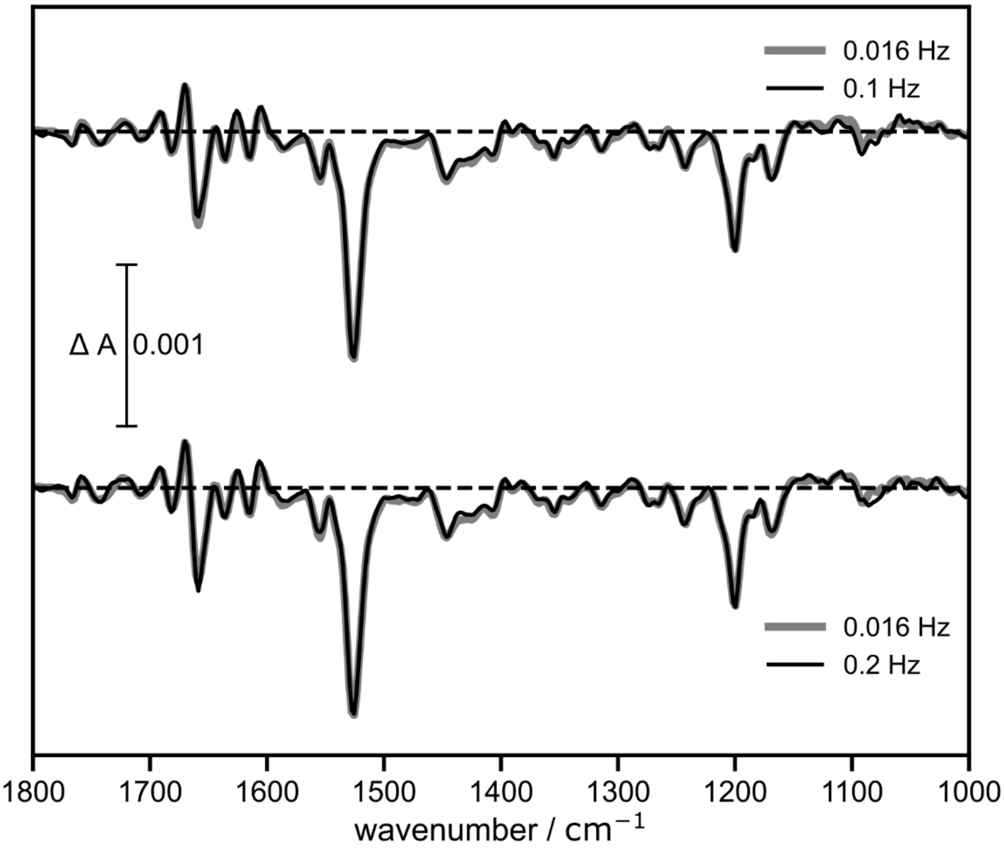

Figure A. 1: Influence of different repetition rates of the pulsed laser excitation on the spectral characteristics of MII in wild-type *Ns*XeR. Spectra obtained at ~10 ms after pulsed laser excitation in a rapid-scan experiment on nanodisc-reconstituted *Ns*XeR. No significant differences in the spectra are observed when the excitation rate is increased to 0.2 Hz indicating that the excitation of a fraction of the long-lived intermediate does not lead to the initiation of a secondary photocycle. This justifies the use of 0.2 Hz for excitation in a step-scan experiment to reduce the measurement time.

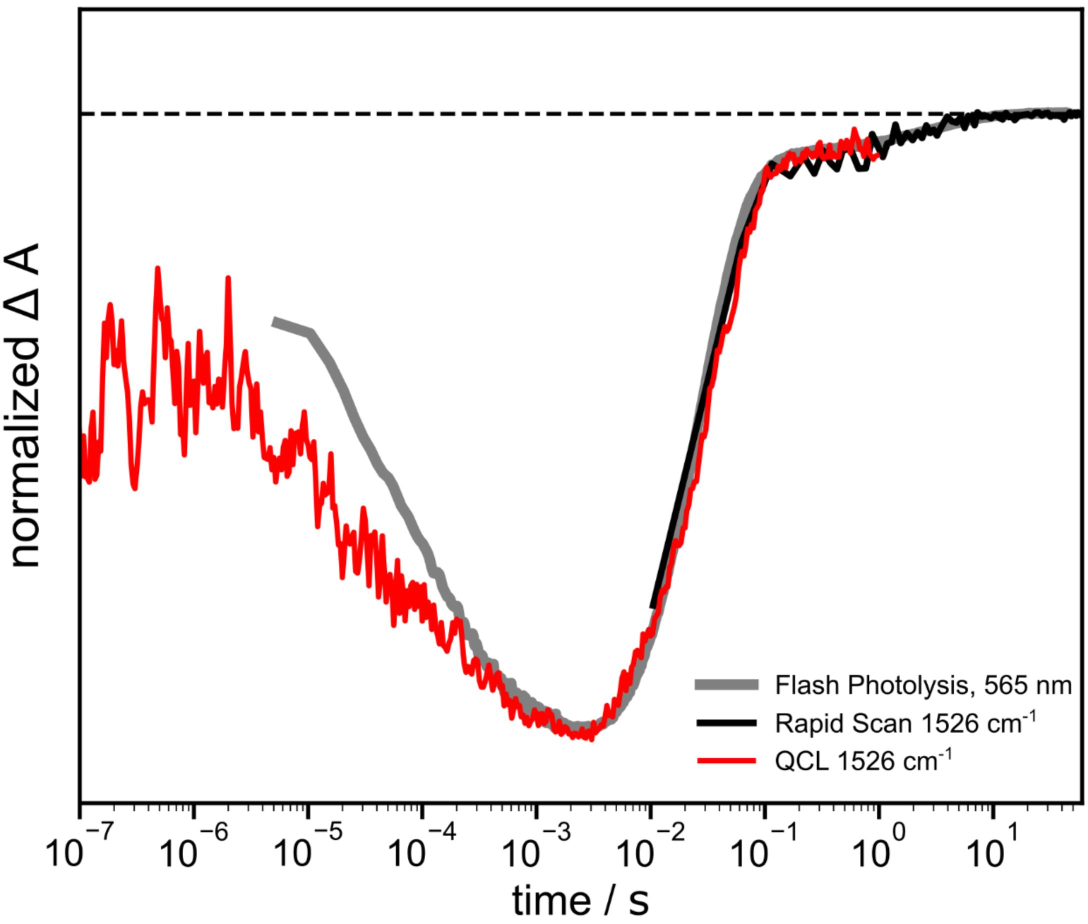

Figure A. 2: Kinetic traces monitoring the depletion of dark-state *Ns*XeR at 565 nm (grey) by UV/vis spectroscopy and 1526 cm^{-1} recorded by the EC-QCL setup (red) and rapid-scan FTIR (black). After approximately 10 s after pulsed excitation the signal has decayed back to 0. This comparison shows that drying and rehydrating of the protein film for measurements in the IR does not alter the photocycle kinetics, as compared to UV/vis experiments conducted in solution. Figure adapted from ref.[79].

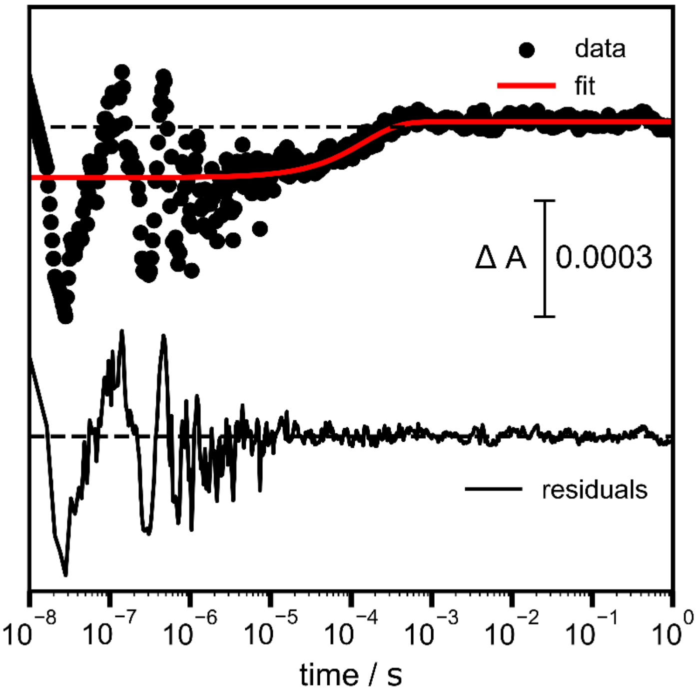

Figure A. 3: Temporal response of photothermally heated water in time-resolved experiments presented in chapter 3.1.2. The black data points show the average of the transients acquired by the EC-QCL setup between 1795 and 1781 cm^{-1}. In this spectral range, the response of photothermally heated water is small but devoid of bands stemming from carboxylic acids. The continuous red line shows an exponential fit to the data, yielding a time constant of 145 µs. The residuals of the fit are shown in black with an offset. Figure adapted from ref.[79].

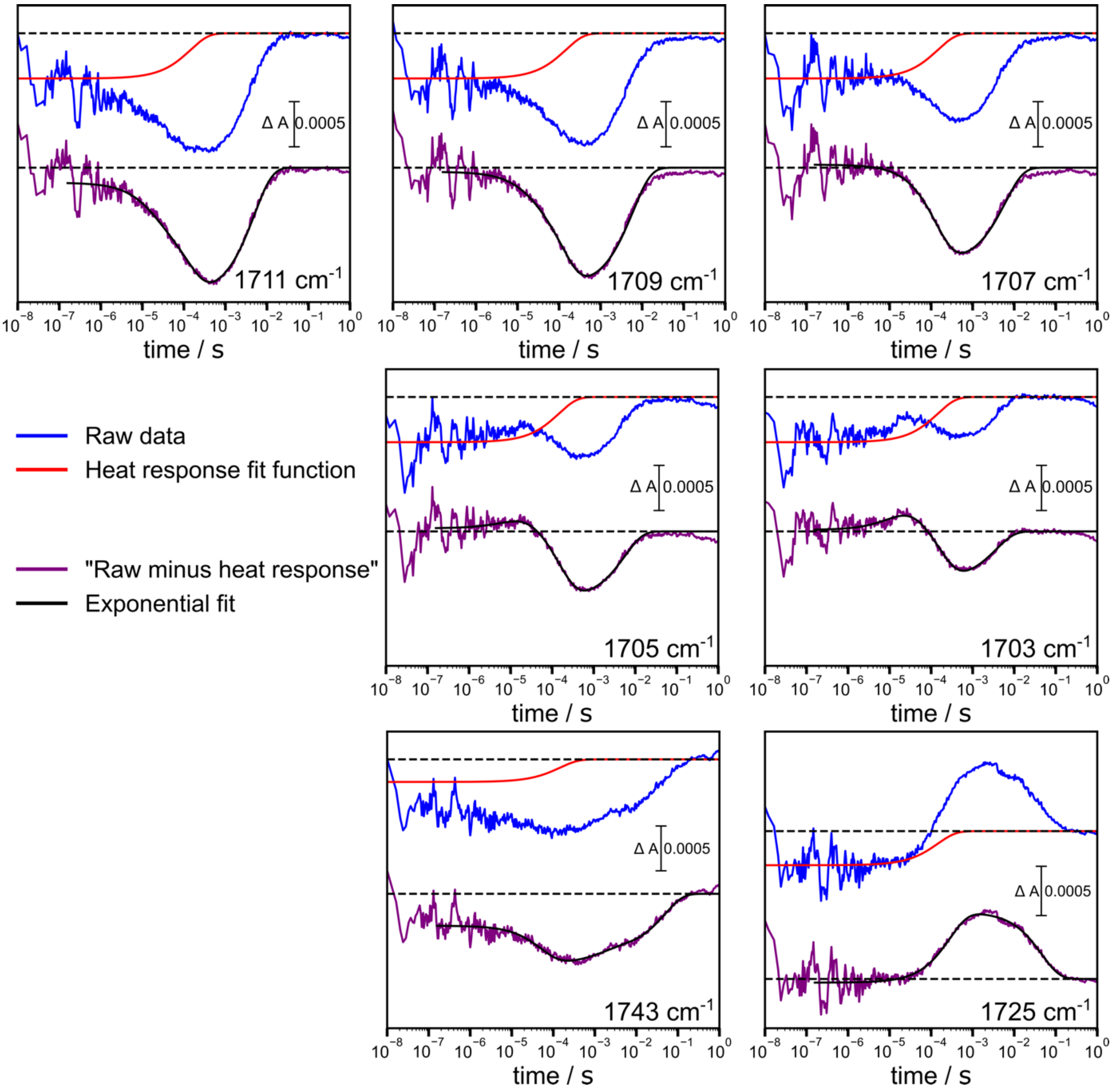

Figure A. 4: Correction of transients associated with the spectro-temporal changes of the carboxylic C=O stretching vibration of protonated D220 (1711-1703 cm^{-1}) and lipid ester vibrations (1743 and 1725 cm^{-1}). Data were obtained with the EC-QCL setup (cf. chapter 3.1.2). In all subplots, the blue traces represent the raw data while the red traces show the fit function shown in Figure A. 3 without the offset in the late ms range and scaled by a constant factor. The scaling roughly accounts for the spectral shape of the heat response i.e., increasing negative amplitude with decreasing frequency.[83] The scaling factor (SF) is chosen to be 3.5 for the transients between 1711-1703 cm^{-1} as this appropriately subtracts the negative offset signal below 1 µs (best seen for the transient at 1707 cm^{-1}). The SF was chosen to be 2.4 for 1725 cm^{-1} and 1.75 for 1743 cm^{-1}, approximated by interpolation between 1707 (SF = 3.5) and 1790 cm^{-1} (SF = 1). For removal of the heat response, the normalized heat response function is subtracted from the raw data resulting in the purple trace (raw minus heat response). Exponential fits to the corrected transients are shown in black. For all transients associated with the spectro-temporal response of the ν(C=O) mode of D220, the fit amplitude of τ_2 is higher than the fit amplitude of τ_1. However, it is apparent that the component fitted with τ_1 has a higher relative amplitude at 1711 as compared to 1709 cm^{-1} while it is completely absent at 1707 cm^{-1} and of opposite sign at 1705 and 1703 cm^{-1}. The fitting results are compiled in Table A. 2. Figure adapted from ref.[79].

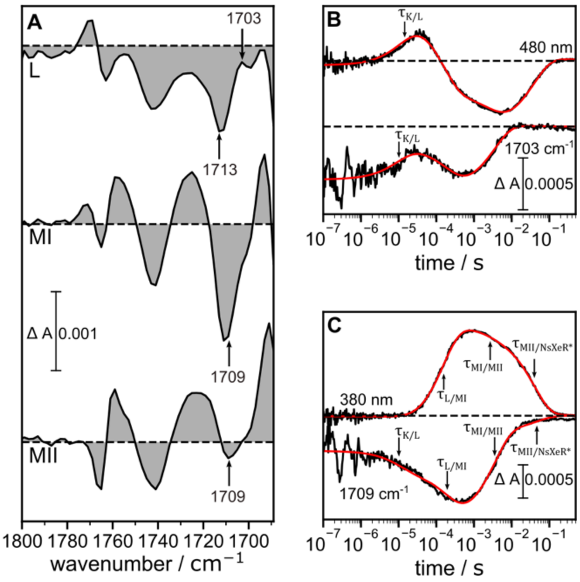

Figure A. 5: Alternative representation of Figure 3-4 with uncorrected transients. Fits stem from global analysis. Figure adapted from ref.[79].

Table A. 2: Fitting results (time constants and amplitudes) associated with the corrected transients shown in Figure A. 4.

wavenumber / cm^{-1}	τ_1 / µs	τ_2 / µs	τ_3 / ms	A_1	A_2	A_3
1795 - 1781	145	/	/	-0.000144	/	/
1743	52	1420	48.5	0.00042	-0.00016	-0.00061
1725	/	284	45.9	/	-0.00072	0.00068
1711	16	131	5.0	0.000355	0.00091	-0.00143
1709	16	125	6	0.000184	0.00110	-0.00133
1707	/	137	6.1	/	0.00109	-0.00106
1705	10	150	5.5	-0.000216	0.00101	-0.00076
1703	13	160	3.7	-0.000331	0.00089	-0.00054

Table A. 3: Time constants obtained from global analysis of flash photolysis data using five time constants and an unbranched, unidirectional photocycle. H_2O and D_2O and KIE columns refer to nanodisc-reconstituted *Ns*XeR (cf. Figure 3-1) while the column denoted with DDM refers to detergent-solubilized *Ns*XeR (cf. Figure 3-15).

	H_2O	D_2O	KIE	DDM
τ_1	14 µs	16 µs	1.1	12 µs
τ_2	159 µs	673 µs	4.2	177 µs
τ_3	2.75 ms	4.86 ms	1.8	2.42 ms
τ_4	39.7 ms	141 ms	3.6	33.6 ms
τ_5	>1 s	> 1 s	x	>1 s

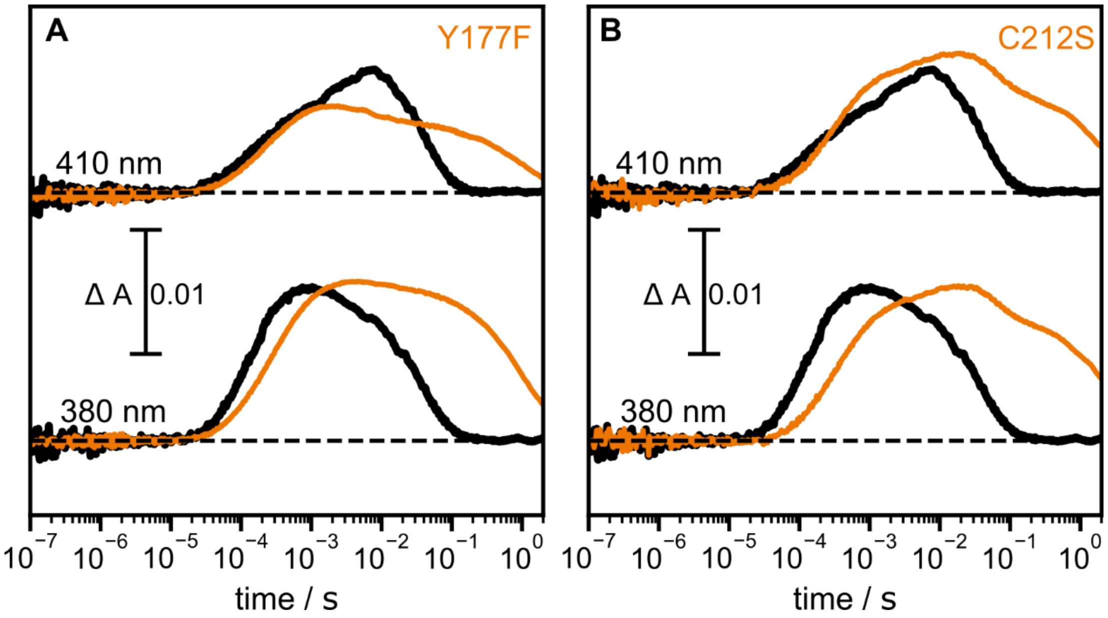

Figure A. 6: Effect of C212 perturbation or mutation on photocycle kinetics. UV/vis transients recorded at 380 nm and 410 nm, associated with the MI and MII intermediates in wild-type *Ns*XeR, respectively. A) Comparison of kinetics recorded on wild-type *Ns*XeR (black) in comparison to kinetics recorded on the Y177F variant (orange). B) Comparison of kinetics recorded on wild-type *Ns*XeR (black) in comparison to kinetics recorded on the C212S variant (orange). The data of the variants was recorded by Jheng-Liang Chen (Genetic Biophysics, FU Berlin).

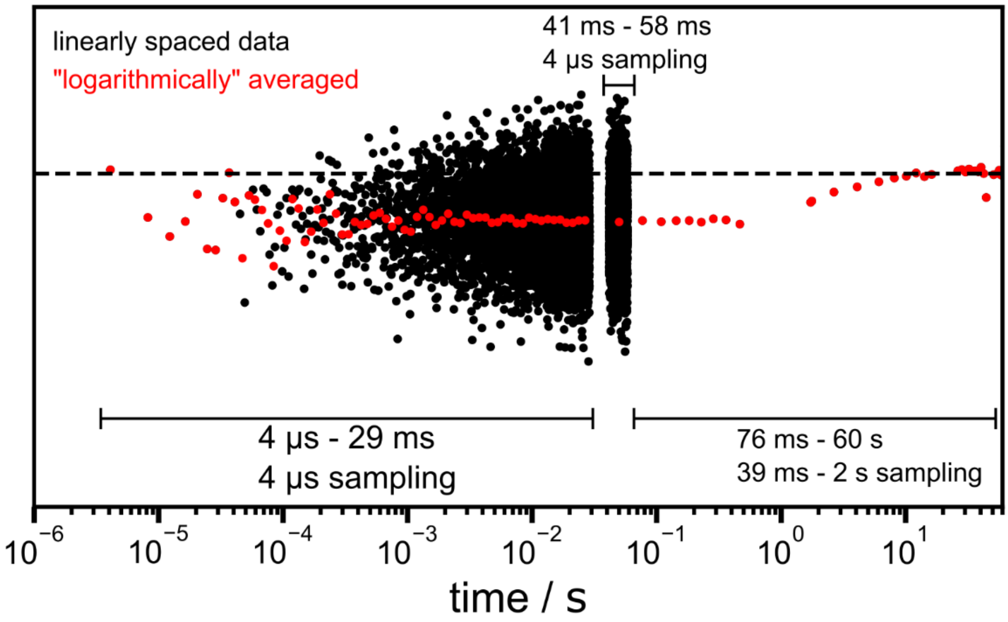

Figure A. 7: Data sampling in the hybrid mode in dual-comb spectroscopy. Data recording is synchronized to the laser trigger. In every acquisition, two time resolved data blocks are subsequently recorded with a deadtime from 29 to 41 ms in between the two datasets (black). Afterwards spectra are recorded with a lower sampling rate, which increases to 2 s at later delay times. For further data analysis the data blocks recorded with high sampling rate (black) can be (logarithmically) averaged to compress the data (red). Here, the first time resolved data block is logarithmically averaged while the second block from 41 to 58 ms is averaged to one single datapoint. The data block between 76 ms and 60 s is not postprocessed further (black data points are overlaid by red data points).

Selbstständigkeitserklärung

Ich erkläre gegenüber der Freien Universität Berlin, dass ich die vorliegende Dissertation selbstständig und ohne Benutzung anderer als der angegebenen Quellen und Hilfsmittel angefertigt habe. Die vorliegende Arbeit ist frei von Plagiaten. Alle Ausführungen, die wörtlich oder inhaltlich aus anderen Schriften entnommen sind, habe ich als solche kenntlich gemacht. Diese Dissertation wurde in gleicher oder ähnlicher Form noch in keinem früheren Promotionsverfahren eingereicht.

Mit einer Prüfung meiner Arbeit durch ein Plagiatsprüfungsprogramm erkläre ich mich einverstanden.

Berlin, den

____

(Luiz Schubert)

Acknowledgements

First of all, I would like to thank Prof. Dr. Joachim Heberle for the opportunity to join his research group to pursue my doctorate. I am thankful for his constant scientific and financial support, but most importantly for his trust, which gave me the liberty to explore Molecular Biophysics in a multi-faceted way. Secondly, I want to thank Dr. Ramona Schlesinger for her constant mentoring and fruitful collaboration. I would like to thank Prof. Holger Dau for his willingness to become the second supervisor of this thesis and for engaging in discussions during the retreats of the collaborative research center 1078. I want to thank all collaborators engaged in my projects: Victor Lorenz-Fonfria, Ville Kaila, Franz Bartl, Leonid Brown, Aba Losi and all their co-workers. Further I'd like to thank Dr. Rumiana Dimova and Prof. Dr. Stefanie Barbirz for mentoring in the framework of the International Max Planck Research School (IMPRS) on Multiscale Bio-Systems.

I want to wholeheartedly thank all past and current members of the AG Heberle, AG Schlesinger, AG Kozuch and AG Elsässer for the pleasant atmosphere you created in and outside the lab, which endured a pandemic and created plenty of nice memories, especially in Klosters. I want to particularly express my gratitude to Jheng-Liang Chen and Kirsten Hoffmann for working closely together on the xenorhodopsin project and Pit Langner for his constant support regarding setups and data analysis. I want to thank Florina Marxer and Mohamad Yahia Dekmak for having the patience to let me supervise their Bachelor and Master thesis, respectively. Federico Baserga deserves special thanks for providing not just high-caloric, but also highly appreciated scientific input. I want to thank Dr. Emanuel Pfitzner for being a role model and a great skiing companion. Thanks to David Ehrenberg for motivating me to learn python and providing the analysis toolbox, which was essential for analyzing my data. Thanks go to Ronja Paschke, Federico Baserga, Pit Langer and Jheng-Liang Chen and Aoife Murnin for proofreading my thesis. The same holds true for Jacek Kozuch, who deserves a special acknowledgement for his constant support and excitement about scientific questions.

Finally, I want to thank my lovely girlfriend Nadine for her patience and unconditional support. Clearing my head while climbing a mountain or going for a bike ride with you were vitally important for me to pursue my doctorate.